The Observation of Photon-Induced W^+W^- Production and Studies on Electron Identification with the ATLAS Experiment

by

Alexandra Fell

A thesis submitted in partial fulfillment for the
degree of Doctor of Philosophy

in the
Faculty of Science
Department of Physics and Astronomy

January 3, 2022

Declaration of Authorship

I, Alexandra Fell, declare that this thesis titled, *"The Observation of Photon-Induced W^+W^- Production and Studies on Electron Identification with the ATLAS Experiment"* and the work presented in it are my own. I confirm that:

- This work was done wholly or mainly while in candidature for a research degree at the University of Sheffield.

- Where any part of this thesis has previously been submitted for a degree or any other qualification at this University or any other institution, this has been clearly stated.

- Where I have consulted the published work of others, this is always clearly attributed.

- Where I have quoted from the work of others, the source is always given. With the exception of such quotations, this thesis is entirely my own work.

- I have acknowledged all main sources of help.

- Where the thesis is based on work done by myself jointly with others, I have made clear exactly what was done by others and what I have contributed myself.

Signed: A. Fell

_____

Date: January 3, 2022

_____

UNIVERSITY OF SHEFFIELD

Abstract

Faculty of Science
Department of Physics and Astronomy

Doctor of Philosophy

by Alexandra Fell

This thesis presents the observation of photon-induced W^+W^- production using proton-proton collision data, with a centre-of-mass energy of 13 TeV and an integrated luminosity of 139 fb^{-1}, recorded by the ATLAS detector. Particular emphasis is given on the determination of the exclusivity scale factor used to correct the theoretical prediction of elastic production to the full photon-induced process, including dissociative production and losses due to secondary scatterings. Further studies into the charged particle multiplicity of other multi-lepton final states are also presented, as a means to validate the background estimate. Finally, an outlook using the photon-induced WW process to set limits on effective field theory operators are given.

Furthermore, studies on electron identification in the ATLAS experiment are presented. The likelihood-based method, used to distinguish between prompt and non-prompt electrons, is altered to include information from two sources of non-prompt background electrons in an effort to improve the rejection of background electrons.

Acknowledgements

Contents

4

Chapter 1

Introduction

Particle physics is a branch of science that examines the most elementary particles of matter and their interactions via fundamental forces. Perhaps the most successful theory of particle physics is the Standard Model, which builds upon quantum mechanical and symmetrical principles to describe the interactions of elementary particles, via three of the four fundamental forces of the Universe.

The Standard Model has proven to be a very reliable theory that has predicted the existence of numerous particles, later discovered experimentally. However, despite its successes, the Standard Model remains an incomplete theory. It does not incorporate the fourth fundamental force of the Universe, gravity, nor does it explain how certain physical phenomena arise - such as dark matter, or matter-antimatter asymmetry, to name but a few. The unanswered questions of the Universe provide a motive to test the Standard Model, to understand its limitations, and to begin to piece together an overarching theory.

The purpose of this thesis is not to offer a comprehensive answer to the unknowns of the Universe, rather to discuss the author's efforts in helping humankind to take one step closer towards a more partial answer. This thesis will present studies of the electroweak sector using 139 fb^{-1} of proton-proton collision data, with a centre-of-mass energy equal to 13 TeV, recorded by the ATLAS experiment.

The electroweak sector is interesting to study because of its non-Abelian nature, which leads to self-interactions between the electroweak gauge bosons. Furthermore, it is subject to spontaneous symmetry breaking causing three of the four electroweak gauge bosons to acquire mass via the Higgs mechanism. This thesis will discuss the interaction between two massless photons and two massive W bosons, through the study of photon-induced W^+W^- production at the Large Hadron Collider. This process occurs when two
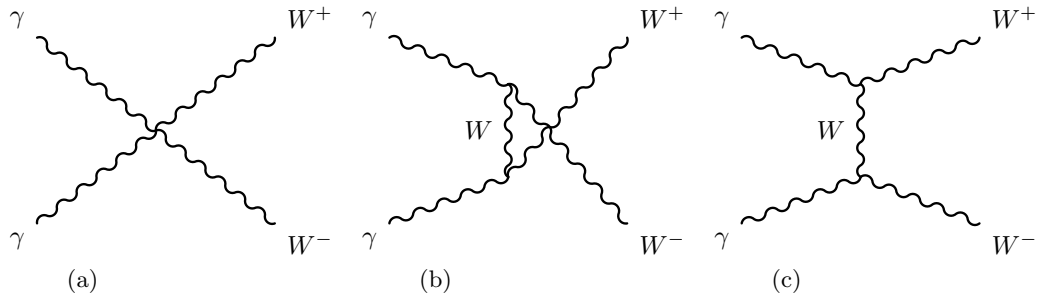
Figure 1.1: The leading order Feynman diagrams contributing to the $\gamma\gamma \rightarrow WW$ process. The process is an example of quartic and triple gauge couplings. a) Shows the quartic $\gamma\gamma WW$ coupling. The triple γWW coupling is illustrated in b) and c) [1].

incoming protons radiate off a photon each, which then go on to interact and produce two W bosons. Figure 1.1 illustrates the leading order Feynman diagrams contributing towards the $\gamma\gamma \rightarrow WW$ process. This process is an example of triple and quartic gauge boson interactions via the $\gamma\gamma WW$ and γWW vertices. The triple and quartic gauge couplings can be studied via photon-induced W^+W^- production and any deviation from the Standard Model may provide hints of new physics.

The work presented in this thesis builds upon previous studies of photon-induced W^+W^- boson production carried out by both the ATLAS and CMS collaborations in 2016 [2, 3]. The studies presented in this thesis directly contributed towards the observation of photon-induced W^+W^- production by the ATLAS collaboration [1].

Also presented are some preliminary Effective Field Theory studies on the photon-induced W^+W^- process, which examines the $WW\gamma$ and $WW\gamma\gamma$ couplings. The coupling strength of these vertices are yet to be precisely measured. If a precise measurement agrees with the Standard Model it can be used to confirm the predictions of the Standard Model. However, if there is any deviation from Standard Model predictions, this could hint towards new physics via *anomalous Triple Gauge Couplings* and *anomalous Quartic Gauge Couplings*. The effects of new physics on the $WW\gamma$ and $WW\gamma\gamma$ vertices can be parameterised using an Effective Field Theory that extends the Standard Model to include generic new physics interactions.

A general outline of the structure of this thesis is as follows: first an overview of the theoretical principles behind the studies presented will be given in Chapter 2. A short history of the development of particle physics will be given, before the Standard Model is introduced. This chapter will describe how the key principles of symmetry under-pin the form of the Standard Model and how the underlying symmetry of the electroweak sector is broken to give rise to massive electroweak gauge bosons. Then there will be a discussion on how the Standard Model can be extended with the use of Effective Field Theory, as part of a strategy to search for new physics with a model-independent

approach. Chapter 2 will conclude with a summary of the fundamental concepts of proton-proton collisions.

Next, Chapter 3 will describe the experimental setup of the Large Hadron Collider and the ATLAS experiment. Detail will be provided of each of the sub-detectors of which the ATLAS detector is composed, and a short summary of the ATLAS trigger system will also be given. Chapter 4 will describe how the data recorded by the ATLAS experiment is reconstructed into "physics objects" that can be used in a physics analysis. This chapter will focus on how information from the constituent parts of the ATLAS detector can be combined to reconstruct electrons and muons.

Chapter 5 will describe how reconstructed electrons are classified according to their origin. This chapter will describe the likelihood-based method used by the ATLAS collaboration to classify an electron candidate as either signal or background. A study, performed by the author of this thesis, will be presented that alters the nominal likelihood discriminant method to include information from different categories of background electrons. The study focuses on categorising background electrons from either light flavour or heavy flavour hadronic decays, and constructs independent likelihood discriminants for each category. Then an optimal cut is chosen for each likelihood discriminant, that optimises the rejection of background electrons from both categories. Chapter 5 concludes with a comparison between the nominal likelihood discriminant method and the new two-dimensional likelihood discriminant method.

The photon-induced W^+W^- process will be introduced in Chapter 6. This chapter will describe the mechanisms behind photon-induced W^+W^- production at the Large Hadron Collider and will discuss the results of previous measurements of this process. The main strategies of the analysis will be introduced, including an outline of the corrections that must be applied to the Monte Carlo.

Chapters 7 and 8 will describe the contribution made by the author towards the Run 2 photon-induced W^+W^- analysis. Both chapters describe corrections applied to the Monte Carlo modelling. The first correction factor to be discussed is the charged particle reweighting factor, which corrects the modelling of the charged particle distribution at low track multiplicities. Chapter 7 details studies validating the application of charged particle reweighting factor to diboson events. The second correction factor to be discussed is the exclusivity scale factor, which accounts for dissociative contributions not modelled in the simulation. Chapter 8 describes the data-driven method used to derive the exclusivity scale factor.

Chapter 9 will present a summary of the results of the Run 2 photon-induced W^+W^- analysis, performed by the ATLAS collaboration.

Finally, Chapter 10 describes preliminary studies of Effective Field Theory using the results of the photon-induced W^+W^- Run 2 analysis. This chapter describes methods used to estimate confidence limits on the free dimension-6 and dimension-8 EFT parameters, that contribute towards the $WW\gamma$ and $WW\gamma\gamma$ vertices. Initial limits are placed on the dimension-6 and dimension-8 parameters using a naive event counting technique. Then the kinematic distributions of dimension-8 operators are studied in order to refine the initial estimates. The results from these preliminary studies are compared to previously published results in order to identify the parameters that could have more stringent limits set, by a future more in-depth study.

Chapter 2

Theoretical Overview

This chapter will give a succinct summary of the theoretical concepts of particle physics, which underpin the studies presented later in this thesis. Section 2.1 will give a short history of particle physics. In section 2.2, the Standard Model of particle physics will be introduced. Section 2.3 will describe an approach for extending the Standard Model as part of a search for new physics. Finally, section 2.4 will summarise the theoretical concepts behind proton-proton collisions, which are used to test the Standard Model.

2.1 A Short History of Particle Physics

The philosophical notion that matter is composed of corpuscular particles has been around for centuries [4]. Experiments in the late-nineteenth and early-twentieth centuries provided evidence to support such ideas. The discovery of the electron by J.J. Thomson in 1897 [5] and E. Rutherford's work on the structure of the atom in 1911 [6], paved the way for the era of particle physics. The early particle model of the electron was combined with quantum mechanics and Einstein's theory of special relativity in 1928 by P. Dirac [7]. Dirac's work was further developed into a renormalisable and gauge invariant quantum field theory, known as quantum electrodynamics (QED), in the mid-twentieth century by the likes of R. Feynman, J. Schwinger, C.N. Yang, and R. Mills [8, 9]. By the 1970's, the Higgs mechanism had been postulated to explain how masses of fundamental particles arise [10, 11, 12]. Additionally, a quantum theory of the strong interaction, known as quantum chromodynamics (QCD) was formulated by H. Fritzsch and M. Gell-Mann [13, 14], using the same principles of symmetry that were used to formulate QED. By 1975, the general theoretical framework of particle physics was coined: *The Standard Model* [15].

2.2 The Standard Model of Particle Physics

The Standard Model of particle physics describes three of the four fundamental forces of the Universe and the subsequent interactions between fundamental particles. The Lagrangian of the Standard Model can be written as the sum of four separate Lagrangians:

$$\mathcal{L}_{\text{SM}} = \mathcal{L}_{\text{Gauge}} + \mathcal{L}_{\text{Fermions}} + \mathcal{L}_{\text{Higgs}} + \mathcal{L}_{\text{Yukawa}} \tag{2.1}$$

The first term, $\mathcal{L}_{\text{Gauge}}$ describes the gauge symmetries of the Standard Model that give rise to the fundamental forces carried by gauge bosons. The second term, $\mathcal{L}_{\text{Fermions}}$ describes fermionic fields that govern the fundamental particles of matter. $\mathcal{L}_{\text{Higgs}}$ describes how the gauge bosons interact with the Higgs field, provoking spontaneous symmetry breaking. The final term, $\mathcal{L}_{\text{Yukawa}}$ describes the nature and coupling strengths of interactions between fermions and the Higgs field. The implications of each term will be described in the subsequent sections below.

2.2.1 Underlying Symmetries of the Standard Model

The Standard Model is a gauge quantum field theory. The fields described by the Standard Model are gauge invariant under local $\text{SU}(3)_c \otimes \text{SU}(2)_L \otimes \text{U}(1)_Y$ symmetry transformations. The quanta of bosonic fields are integer spin particles, known as bosons. In the Standard Model, bosons convey the electroweak and strong interactions.

Each component of the gauge group corresponds to a different fundamental interaction. Table 2.1 outlines the properties of each of the fundamental interactions, corresponding to the different gauge groups. The gauge field associated with the $\text{U}(1)_Y$ symmetry is the electromagnetic field and it has one associated bosonic field, B_μ. The $\text{SU}(2)_L$ symmetry is associated with the weak interaction, and has three bosonic fields: W_μ^1, W_μ^2 and W_μ^3. The $\text{SU}(2)_L$ symmetry is a chiral symmetry and consequently weak interactions only couple to left handed fermion fields (see Section 2.2.2).

In the Standard Model, the electromagnetic and weak interactions are unified into the electroweak interaction at high energies, with an $\text{SU}(2)_L \otimes \text{U}(1)_Y$ gauge group [16]. The electroweak interaction is mediated by four gauge bosons, that arise from linear combinations of the bosonic fields. The only massless electroweak gauge boson is the photon, denoted by γ. The remaining three electroweak gauge bosons are called the W^+, W^-, and Z bosons, and acquire mass as a result of electroweak symmetry breaking (see Section 2.2.3).

Symmetry	Interaction	Bosonic Field	Mediator	Mass	Quantum Number
U(1)	Electromagnetic	1 field (B_μ)	Photon (γ)	0	Electric Charge ($Q = I_3 + \frac{Y}{2}$)
SU(2)	Weak	3 fields (W_μ^n)	W^+ boson (W^+) W^- boson (W^-) Z boson (Z)	$m_{W^\pm} = 80.4$ GeV $m_Z = 91.2$ GeV	Weak Isospin (I_3)
SU(3)	Strong	8 fields (G_μ^n)	8 Gluons (g)	0	Colour

Table 2.1: A summary of the gauge symmetries of the Standard Model and the corresponding interactions. The $SU(2) \otimes U(1)$ gauge group is unified in the Standard Model to form the electroweak interaction.

The final symmetry, $SU(3)_c$, is associated with the strong interaction. The strong interaction has eight bosonic fields, G_μ^n which are mediated by eight massless gauge bosons, known as gluons [17].

Each fundamental interaction described by the Standard Model has an associated quantum number that must be conserved. Interactions via the electroweak force must conserve both the third component of weak isospin, I_3, and weak hypercharge, Y. In electromagnetic interactions, electric charge, Q, must be conserved, where $Q = I_3 + \frac{Y}{2}$ [16]. In weak interactions, it is just the third component of weak isospin that must be conserved, and in strong interactions, a quantum number, known as colour, must be conserved.

2.2.2 The Description of Matter in the Standard Model

The Standard Model describes matter with quantum gauge fields known as fermionic fields. The quanta of these fields are half-integrer spin particles called fermions. Table 2.2 summarises the fermions in the Standard Model. They are organised into either left-handed doublets or right-handed singlets as a result of the chiral $SU(2)_L$ symmetry. Fermions have intrinsic values of the quantum numbers (Q, I_3 and Y). All left-handed fermions have a third component of weak isospin equal to $I_3 = \pm 1/2$ and all right-handed fermions have a third component of weak isospin equal to $I_3 = 0$ [17].

Fermions can be further categorised as either quarks or leptons according to which fundamental forces they interact with. Both leptons and quarks interact via the electromagnetic and weak interactions, however, only quarks interact via the strong interaction. There are three generations of both leptons and quarks, which differ only by mass.

The Standard Model also predicts each fermion has an associated antiparticle that is opposite in charge and chirality. Antiparticles have identical mass as their partner particle.

Interactions	Generation			Q	I_3	Y
	1st	2nd	3rd			
Quarks electromagnetic weak strong $\}$	$\begin{pmatrix} u \\ d' \end{pmatrix}_L$	$\begin{pmatrix} c \\ s' \end{pmatrix}_L$	$\begin{pmatrix} t \\ b' \end{pmatrix}_L$	+2/3 -1/3	+1/2 -1/2	+1/3 +1/3
electromagnetic strong $\}$	u_R d_R	c_R s_R	t_R b_R	+2/3 -1/3	0 0	+4/3 -2/3
Leptons electromagnetic weak $\}$	$\begin{pmatrix} \nu_e \\ e \end{pmatrix}_L$	$\begin{pmatrix} \nu_\mu \\ \mu \end{pmatrix}_L$	$\begin{pmatrix} \nu_\tau \\ \tau \end{pmatrix}_L$	0 -1	+1/2 -1/2	-1 -1
- electromagnetic weak $\}$	ν_{eR} e_R	$\nu_{\mu R}$ μ_R	$\nu_{\tau R}$ τ_R	0 -1	0 0	0 -2

Table 2.2: A summary of the fundamental particles of matter, known as fermions and their corresponding quantum numbers. Fermions have half-integer spin and can be classified as either quarks or leptons.

There are six quarks in the Standard Model. Each generation consists of one up-type quark and one down-type quark. The up-type quarks are called: up, charm and top. Each up-type quark has an electrical charge of +2/3. The down-type quarks are called: down, strange and bottom. Each down-type quark has an electrical charge of −1/3. Left-handed quark doublets are formed from one up-type, with $I_3 = +1/3$, and one linear combination of down-type quarks[1], with $I_3 = -1/2$. Right-handed quark doublets have $I_3 = 0$. All quarks also have a conserved quantity known as colour, which can be either red, green or blue. They only exist in bound colourless states. Three quarks, each with different colour, are known as baryons; whilst the bound states of a quark and its respective anti-quark, are known as mesons. Quarks can interact via the strong or the electroweak force.

There are six leptons in the Standard Model, with one charged lepton and one neutral lepton, known as a neutrino, in each generation. The charged lepton in the first generation is called an electron. In the second generation, the charged lepton is called a muon, and in the third generation it is called a tau. All charged leptons have an electrical charge of $Q = -1$, and interact via the electroweak force. The third component of weak isospin of left-handed charged leptons is $I_3 = +1/2$, and they form a doublet with their corresponding neutrino, which carry a third component of weak isospin of $I_3 = -1/2$. Right-handed leptons carry no third component of weak isospin. Neutrinos do not carry electrical charge and are colourless, therefore left-handed neutrinos only interact via the

[1]down-type quarks mix according to the CKM matrix which describes quark flavour changing via the weak interaction [18].

weak force; whilst the hypothesised right-handed neutrinos do not interact with any of the forces described by the Standard Model [17].

2.2.3   Spontaneous Electroweak Symmetry Breaking

The underlying $SU(2)_L \otimes U(1)_Y$ symmetry of the electroweak force is spontaneously broken to give rise to the massive W^+, W^- and Z gauge bosons, that carry the weak force [19]. This symmetry breaking occurs via the Higgs mechanism, which introduces a scalar field, known as the Higgs field, Φ. The Higgs field is a doublet and carries a hypercharge of $Y = +1$, a third component of weak isospin equal to $I_3 = -1/2$, and no electric charge. It is present throughout the whole of space and has a potential:

$$V(\Phi) = \mu^2 \Phi^\dagger \Phi - \frac{1}{2}\lambda(\Phi^\dagger\Phi)^2, \mu^2 > 0 \tag{2.2}$$

In the Standard Model, the Higgs potential has a non-zero value it at its minima, which gives rise to spontaneous electroweak symmetry breaking. This occurs for $\mu^2 < 0$ and $\lambda > 0$, where the lowest energy state of the Higgs field has a non-zero expectation value equivalent to:

$$v = \sqrt{2}\mu/\lambda \tag{2.3}$$

Where v is the vacuum expectation value of the Higgs field and is a free parameter in the Standard Model. It has been measured experimentally to have the value of 246 GeV [20].

At energies below the electroweak scale, the symmetry is broken resulting in three components of the Higgs field being absorbed into the mass terms of the weak gauge bosons, and one remaining massive scalar component, otherwise known as the Higgs boson [21]. The Masses of the resulting bosons are:

$$M_H = \lambda v \tag{2.4}$$

$$M_W = e\frac{v}{2}\sin\theta_W \tag{2.5}$$

$$M_Z = \frac{M_W}{\cos\theta_W} \tag{2.6}$$

Where θ_W is the Weinberg angle that describes the mixing between the bosonic fields, B_μ and W_μ [17].

The Higgs field does not interact electromagnetically and as a result, the gauge boson of the electromagnetic interaction, the photon, does not acquire mass.

2.2.4 Yukawa Couplings

The Higgs field also couples to fermionic fields, inducing mass for fermions. The fermions' coupling strength to the Higgs field is dictated by Yukawa couplings which, are free parameters in the Standard Model [16]. The masses of fermions in the Standard model are directly proportional to the Yukawa couplings:

$$m_f = y_f \frac{v}{\sqrt{2}} \tag{2.7}$$

Where y_f is the Yukawa coupling and it defines the strength of the coupling between the fermion and the Higgs field, and v is the vacuum expectation value of the Higgs field.

2.2.5 Achievements and Limitations of the Standard Model Measurements

The Standard Model is the most successful theory of particle physics, with many of its predictions withstanding experimental rigour. Figure 2.1 shows a summary comparing the theoretical predictions of different Standard Model processes to experimental measurements by the ATLAS collaboration. In general, there is very good agreement between the theoretical predictions and experimental measurements. However, not all measurements are statistically significant and some measurements are more precise than others. A primary objective for experimental physicists is to test the Standard Model by precisely measuring all predicted processes.

Despite the extent of the success of the Standard Model, it is known to be incomplete. As previously mentioned, the Standard Model provides no explanation for the gravitational force; nor does it explain the origin of experimental observations of dark matter or neutrino masses [23, 21, 24]. It is now widely believed that the Standard Model is a low-energy limit of a more fundamental theory and that new processes, involving new particles, will be discovered at higher energies. It is anticipated that physics beyond the Standard Model will unify all fundamental forces of nature and offer explanations for the Standard Model's shortcomings.

The focus of this thesis is to examine the Standard Model through the study of self-interactions between electroweak gauge bosons. These self-interactions can involve either three or four electroweak gauge bosons and are known as *Triple Gauge Couplings* or *Quartic Gauge Couplings*. The topic of this thesis is photon-induced W^+W^- boson production and therefore only $WW\gamma$ and $WW\gamma\gamma$ gauge couplings will be discussed.
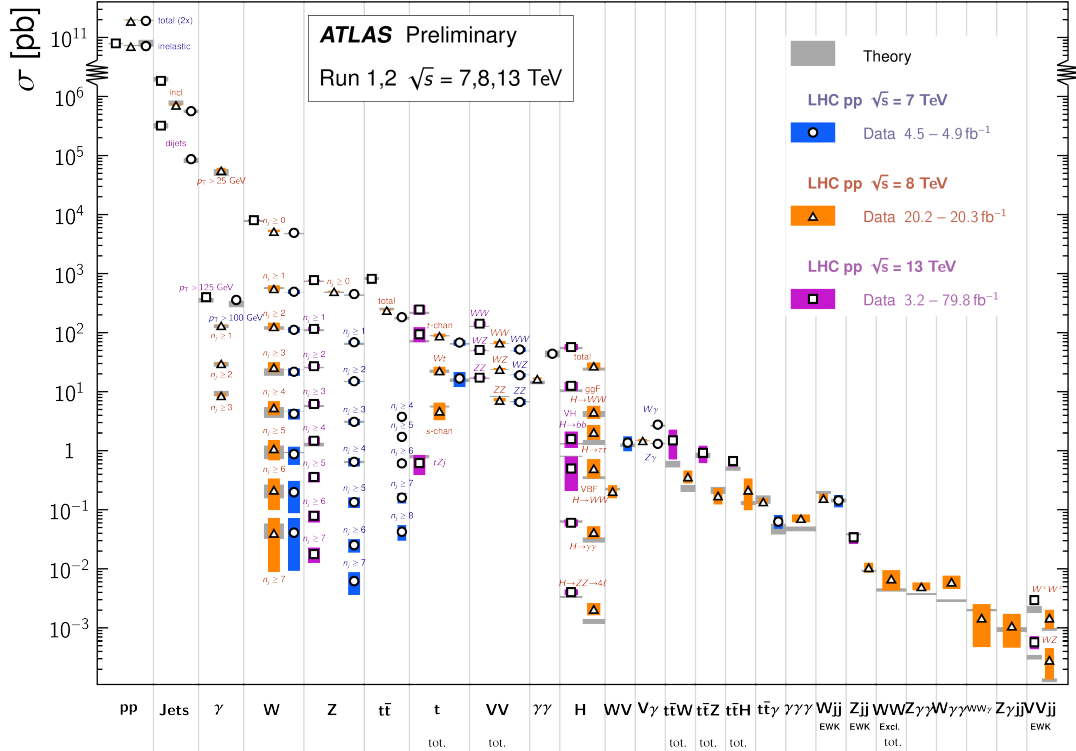
Figure 2.1: A summary of the total and fiducial cross sections for Standard Model processes, measured by the ATLAS collaboration. This plot shows experimental measurements from both Run 1 and Run 2 data-taking periods and compares to the theoretical expectations. Not all measurements shown are statistically significant [22].

The Standard Model's predictions of triple and quartic gauge couplings are yet to be measured with a high level of precision. A better understanding of Standard Model's limitations can be achieved by performing precise measurements of these interactions. Any evidence that experimental data does not precisely agree with the theoretical predictions could be a hint towards new physics at higher energy scales. New physics could have some small effects noticeable at lower energies - lower energies which are currently accessible experimentally. These small effects can be parameterised by EFT (discussed in Section 2.3).

The triple and quartic couplings in the Standard Model arise as a result of gauge invariance. However, the effective Lagrangian includes *anomalous* triple and quartic couplings which are independent of the Standard Model couplings [25, 26]. They are constructed to assess possible deviations from the Standard Model. The additional operators included in the effective Lagrangian must respect the $U(1)_Y$ and $SU(2)_L$ symmetries and conserve charge and parity separately.

2.3 Effective Field Theory - An Extension of the Standard Model

It is hypothesised that new physics at higher energy levels, could have effects (either directly or indirectly) at energies that are currently accessible experimentally. These effects can be studied using the model-independent approach of EFT. EFT parameterises the effects of new physics at lower energies by extending the Standard Model. This thesis makes use of the formalism given in References [27] and [28]. The remainder of this section will summarise the key concepts discussed in these papers.

The effective Lagrangian is written as:

$$\mathcal{L}_{eff} = \mathcal{L}_{SM} + \sum_i \frac{c_i}{\Lambda_i^{d-4}} \mathcal{O}_i + ... \tag{2.8}$$

Where Λ_i is the energy of scale at which new physics can be directly observed, d is the dimension of the additional EFT operator, c_i is a free parameter with units of inverse power of mass, and $\mathcal{O}_i$ is an operator of higher dimension. The additional operators included in EFT are suppressed by inverse powers of the high energy scale, Λ_i, and are invariant under the gauge symmetries of the Standard Model. Therefore, in the limit of $\Lambda_i \to \infty$ the additional EFT operators are entirely suppressed and the Standard Model Lagrangian is restored.

The effects of operators of the lowest dimension dominate the effective Lagrangian. Nearly all operators in the Standard Model are of dimension-4[2], whilst the dimension-6 and dimension-8 operators, included in EFT, are included to encapsulate the effect of new physics. At the low-energy limit, the dimension-6 and dimension-8 operators are suppressed by $1/\Lambda^2$ and $1/\Lambda^4$, respectively. The dimension-6 operators are part of the Warsaw basis [29], and the dimension-8 operators part of the Eboli model [30].

There are 8 dimension-6 operators and 13 dimension-8 operators that describe the effects of $WW\gamma$ and $WW\gamma\gamma$ anomalous couplings. The additional dimension-6 operators contributing towards these vertices are: $\mathcal{O}_W$, $\mathcal{O}_{HDD}$, $\mathcal{O}_{HW}$, $\mathcal{O}_{HB}$, $\mathcal{O}_{HWB}$, $\mathcal{O}_{Hl3}$, $\mathcal{O}_{ll3}$, and $\mathcal{O}_{H\square}$[3]. Each dimension-6 operator is associated with a free parameter, c_i, which governs the coupling strength of the operators. The additional dimension-8 operators are $\mathcal{O}_{M,i}$ and $\mathcal{O}_{T,i}$. With the coupling strength of each operator governed by a free parameter, $f_{M,i}$ and $f_{T,i}$, respectively.

---

[2]Dimension-5 operators lead to the violation of baryon and lepton numbers and are not discussed in this thesis

[3]The $\mathcal{O}_{H\square}$ operator is highly suppressed and there are other processes that are more sensitive to this parameter.
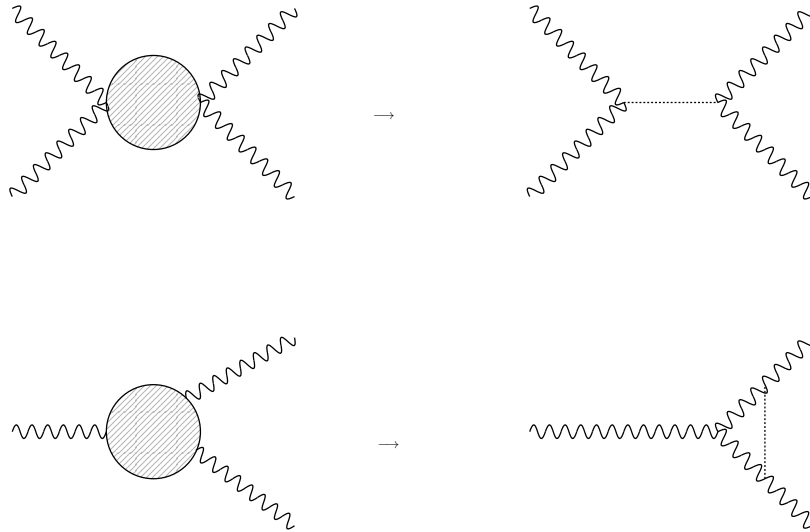
Figure 2.2: Two Feynman diagrams showing anomalous quartic gauge couplings (top) and anomalous triple gauge couplings (bottom). The anomalous coupling is represented by the hatched circle and possible ways in which a possible new heavy boson is represented by the dashed line. It is possible that the anomalous gauge couplings are low-energy limits of a new heavy boson coupling to the Standard Model gauge bosons. For the anomalous quartic gauge coupling a new heavy boson could enter at tree level. Whilst for the anomalous triple gauge coupling, a new heavy boson could only enter via a loop, which would suppress its contribution.

Figure 2.2 shows two possible scenarios of new physics, in which a new heavy boson could be exchanged between three or four known gauge bosons. In such a case, the anomalous quartic gauge coupling describes the direct exchange of a new heavy boson, whereas the exchange of the new heavy boson is suppressed via a loop for the anomalous triple gauge coupling [27].

In the Standard Model, the cross section of diboson vertices is much greater than the cross section of triple or quartic vertices, making instances of these events rare. This provides some experimental challenges to studying triple and quartic gauge couplings, at energy levels that are currently accessible. However, if new physics is present, it is possible that the enhanced anomalous triple or quartic gauge coupling may increase the number of triple or quartic boson events observed. Once observed, more can be learnt about the nature of the new physics by understanding which operator, and thus which vertex, is enhanced the most [30].

EFT provides a method to search indirectly for new physics by searching for events that only have Standard Model particles in their final state. This means any new heavy particles exchanged in the interaction are virtual and can be produced off-mass shell. Thus lower energies are needed for such studies in comparison to the energies needed for direct searches of new heavy particles.

2.4 The Physics of Proton Collisions

Both the Standard Model and any extensions to the Standard Model can be studied via particle accelerators. This thesis makes use of data from the Large Hadron Collider[4], which is a proton-proton collider. Protons are composite particles comprised of three quarks bound together by gluons. The gluons are in a constant cycle of fluctuation - producing virtual quark anti-quark pairs which later annihilate. At high energies, the gluons carry a large fraction of the proton's total momentum and the constituent particles of the proton become asymptotically free [31]. A consequence of this, is that the quarks and the gluons can be considered to be independent particles, known as partons. Any of which can interact with a parton from another incoming proton. In an inelastic proton-proton collision, there is the hard scatter interaction between two partons from different protons and additional underlying event activity. The underlying event incorporates interactions from: initial and final state radiation, additional parton-parton interactions in the same event, and from interactions between partons not participating in the hard scatter interaction [32].

The distribution of the partons inside a high energy proton is very hard to model and it cannot be characterised via perturbative QCD calculations. Instead, the structure of the proton is estimated by fitting probability density functions to experimental data [33]. Known as parton distribution functions, $f_q(x, Q^2)$, the experimental data is parameterised as a function of the longitudinal fraction of momentum, x, for a given value of four-momentum transferred squared by the scattering process squared, Q^2. The parton distribution functions are calculated for a given value of momentum transferred, according to the DGLAP equations [34, 35]. The parton distribution functions are dependent on the energy of the partons and thus the centre-of-mass energy the protons are given by the experimental setup. Figure 2.3 shows the parton distribution functions for low ($Q = 10$ GeV) and high ($Q = 10^4$ GeV) energies. It illustrates that for low energies, the quarks carry the majority of the proton's momentum whereas for high energies, the majority of the proton's momentum is carried by the gluons.

In addition to QCD parton splittings described above, the constituent partons of a proton can interact via the electroweak force. The DGLAP equations can be altered to include the QED parton splitting in order to find the photon parton distribution function $f_\gamma(x, Q^2)$. The photon parton distribution function describes the flux of photons radiated from the proton, within the scope of the Equivalent Photon Approximation (described in Section 2.4.2) [37].

---

[4]The Large Hadron Collider is introduced with more detail in Chapter 3 Section 3.1
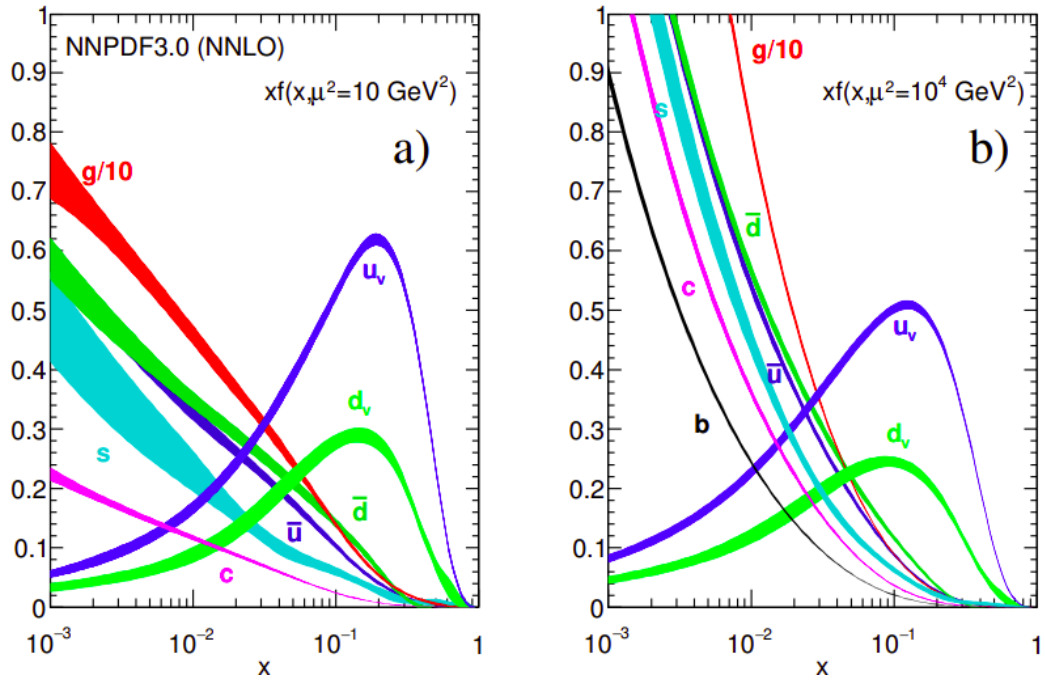
Figure 2.3: Parton distribution functions for the low energy scale (left) and high energy scale (right) [36].

The photon parton distribution function can be written as the sum of elastic and inelastic proton scattering:

$$f_\gamma(x, Q^2) = f_\gamma^{(el)}(x, Q^2) + f_\gamma^{(inel)}(x, Q^2) \tag{2.9}$$

The inelastic component corresponds to interactions between the constituent partons that result in a loss of quark and antiquark momentum. Photons that arise as a result of splitting from other partons $(q, \bar{q}, \gamma, g)$ are included in the inelastic component. The elastic component includes elastic interactions from constituent parton photons that do not result in a loss of quark and antiquark momentum, and includes interactions such as $\gamma \to q\bar{q}$. Figure 2.4 shows a comparison of the elastic, inelastic and total photon parton distribution functions for the low energy scale ($Q = 10$ GeV). The inelastic photon parton distribution function is at its largest for low values of x, and it falls off rapidly for increasing values of x. The elastic photon parton distribution has a more gentle decrease for increasing values of x. This means the total photon parton distribution function is dominated by the inelastic photon parton distribution function for low values of x. For high values of x it is dominated by the elastic photon parton distribution function.

2.4.1 Calculating Cross Sections

The Standard Model and any extensions to the Standard Model are mainly tested via measuring the cross sections of particle collisions. A cross section, denoted by σ, is a
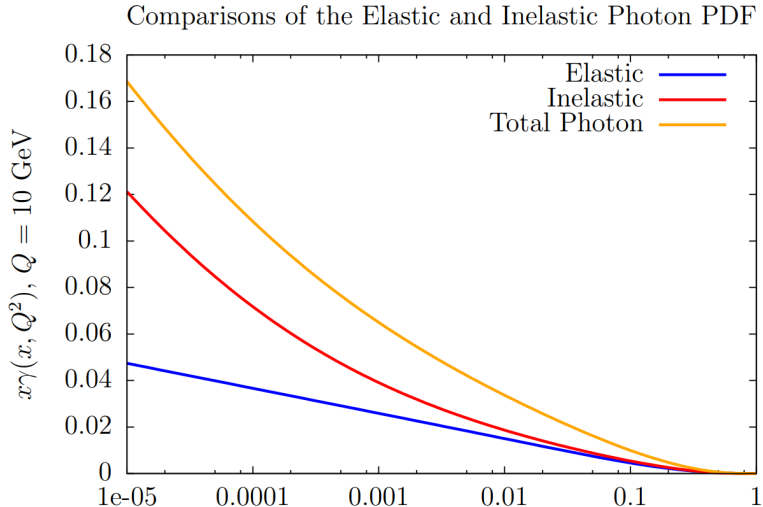
Figure 2.4: The photon parton distribution function for the low energy scale (Q = 10 GeV) [37].

way of quantifying how likely it is that a particular physics process will occur. It is given as a unit of area and calculated from the probability of the initial state particles interacting, according to the coupling strengths of the Standard Model, to produce final state particles.

The cross section of a physics process with two initial state protons, p_1 and p_2, and a particular final state, X can be separated into two distinct parts: the cross section of the hard scatter parton interaction, $\hat{\sigma}_{q_1,q_2 \to X}(\alpha, Q^2)$, and the probability to find the parton inside the proton, which is governed by the parton distribution functions:

$$\sigma_{p_1,p_2 \to X} = \int dx_1 dx_2 \sum_{q_1,q_2} f_{q_1}(x_1, Q^2) f_{q_2}(x_2, Q^2) \cdot \hat{\sigma}_{q_1,q_2 \to X}(\alpha, Q^2) \qquad (2.10)$$

The cross section of the hard scatter interaction, $\hat{\sigma}_{q_1,q_2 \to X}(\alpha, Q^2)$, is dependent on the coupling strength of the particular interaction, α, and the four-momentum transfer squared, Q^2 [38]. In hadron colliders, the cross section of the hard scatter interaction is mainly dependent on the strong coupling constant, $\alpha_s = g_s^2/4\pi$. Perturbation theory uses a power series expansion of α_s to calculate the hard scatter cross section. Each term in the perturbative series corresponds to virtual loops and the emission of real quarks and gluons via radiation.

Cross section calculations become more precise with each additional term that is included in the perturbative series. Theoretical cross section calculations typically quote the order of magnitude it is calculated to. The lowest order calculation is called Leading Order (LO), this corresponds to just one term in the perturbative series. The next level of precision is called Next-to-Leading Order (NLO), with two terms in the perturbative
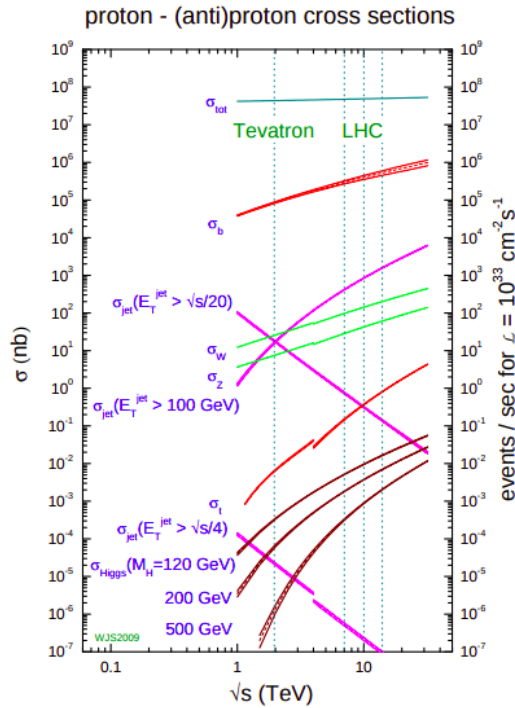
Figure 2.5: Cross sections of Standard Model processes initiated by proton-proton collisions, as a function of the centre-of-mass energy, $\sqrt{s}$. [40].

series. The trend continues with one additional term added to the series each time. The perturbative series converges towards the true value of the cross section, which can be measured experimentally. Without including the higher order terms, the theoretical cross section calculation will either underestimate or overestimate the true value of the cross section [39]. Figure 2.5 shows the cross sections of numerous physics processes from proton-proton collisions, as a function of the centre-of-mass energy of the protons. The total inelastic cross section of the proton-proton collision is much larger than any of the cross sections for a specific process.

2.4.2 The Equivalent Photon Approximation

This section will now describe how the cross section of photon-induced processes can be calculated using the Equivalent Photon Approximation [41].

In 1925, Fermi proposed that protons moving at a velocity close to the speed of light experience a deformed electromagnetic field. As the velocity of a charged particle draws near to the speed of light, its electromagnetic field become more transverse in respect to the direction of travel. Consequently, the electromagnetic field of the relativistic charged particle cannot be distinguished from the electromagnetic field of a quasi-real photon, in the laboratory frame of rest. A quasi-real photon has a low virtuality which means
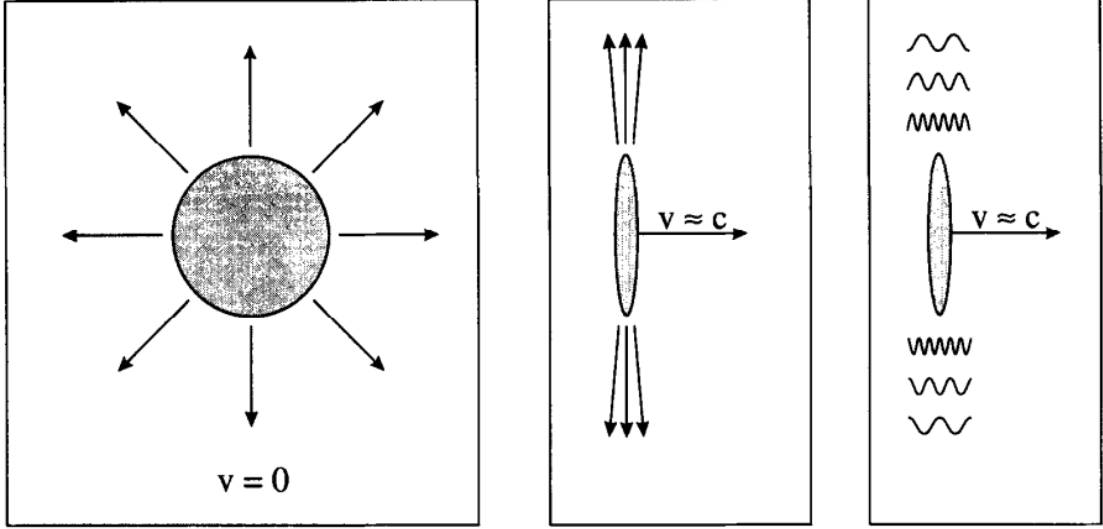
Figure 2.6: This diagram illustrates the concept of Lorentz contraction of the electromagnetic field of a relativistic charged particle, as first proposed by Fermi. As the charged particle's velocity approaches the speed of light the electromagnetic field contracts and can be approximated as photons moving parallel to the charged particle [43].

the four-momentum transferred is much less than the invariant mass of W boson pair ($Q^2 \ll m_{WW}^2$) [42]. In the Equivalent Photon Approximation, the electromagnetic fields of the incoming protons can be thought of as equivalent photons moving parallel to the protons, see Figure 2.6. The Equivalent Photon Approximation can be used to calculate the cross section of photon-induced W^+W^- production by viewing the process as an interaction of the equivalent photons' flux. The following integral shows how the cross section can be calculated for two incoming protons, p_1 and p_2 [44]:

$$\sigma^{EPA}_{p_1 p_2 \to p_1^{(*)} X p_2^{(*)}} = \int \int P(x_1) P(x_2) \sigma_{\gamma\gamma \to WW}(m_{WW}^2) dx_1 dx_2 \qquad (2.11)$$

Where $P(x_1)$ and $P(x_2)$ express the equivalent photon flux of the incoming protons, x_1 and x_2 denote the fractions of energy transferred from the protons to the photons, $\sigma_{\gamma\gamma \to WW}$ is the cross section of the QED sub-process, and m_{WW} is the invariant mass of the W boson pair.

The product of x_1 and x_2 can be found by dividing the invariant mass of the W boson pair by the square of the centre-of-mass energy of the initial state protons:

$$x_1 x_2 = \frac{m_{WW}}{s} \qquad (2.12)$$

22

2.4.3 W^+W^- Production Mechanisms

The topic of this thesis is photon-induced W^+W^- production. The Feynman diagram of this process is shown in Figure 2.7. Photon-induced W^-W^+ production occurs when photons are radiated off the incoming protons, which then go on to interact forming two opposite-signed W bosons. A W boson pair can also be produced via the direct collision of the incoming protons' constituent quarks or gluons. If the protons are radiated off the incoming protons, the process is elastic. Inelastic photon-induced W^+W^- production occurs when the photons are radiated off the proton's constituent partons, and at least one of the protons breaks up as the photon is radiated off. The production mechanisms for photon-induced W^+W^- production are discussed in more detail in Chapter 6 Section 6.2.

(a)
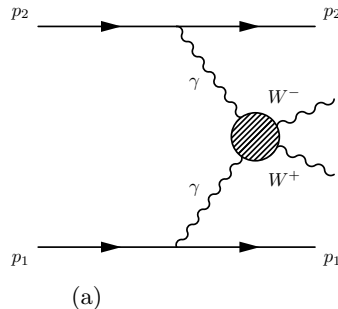
Figure 2.7: The Feynman diagram for photon-induced W^+W^- production [1].

The main background to photon-induced W^+W^- production is quark- and gluon-induced W^+W^- production. Figure 2.8 shows the leading order Feynman diagrams for quark- and gluon-induced W^+W^- production. Figure 2.8(a) and Figure 2.8(b) show quark-induced W^+W^- production in the t-channel and the s-channel, respectively. Figure 2.8(c) shows non-resonant gluon-induced W^+W^- production, and Figure 2.8(d) shows resonant gluon-induced W^+W^- production. These processes are collectively known as inclusive W^+W^- production, and are the largest source of background in the $\gamma\gamma \to WW$ analysis (presented in Chapter 6).

The theoretical cross section of photon-induced W^+W^- production can be calculated using the Equivalent Photon Approximation, and it is much smaller than the theoretical cross section of inclusive W^+W^- production (this is illustrated in Figure 2.1). The experimental methods used, to measure the photon-induced W^+W^- cross section, and to suppress the inclusive W^+W^- will be discussed in Chapter 6.
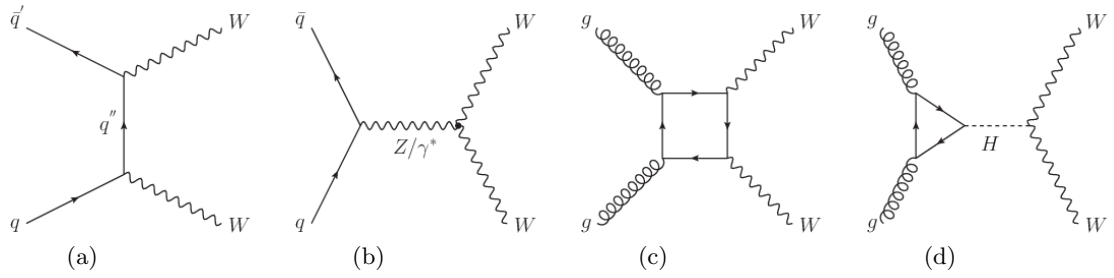
Figure 2.8: Feynman diagrams showing examples of quark- or gluon-induced W^+W^- production at the LHC. These processes are the primary background to photon-induced W^+W^- production [45].

2.4.4 Event Simulation

It is infeasible to analytically calculate the cross sections of physics processes when taking into account all parts of the productions. For a specific physics process, produced via proton-proton collisions, the total cross section depends on: the partonic cross section, the probability density functions, the underlying event, and the parton shower. So instead, theoretical predictions are made using computer simulations. Physics events are generated using Monte Carlo techniques [46] which model the hard scatter event and the underlying event separately.

Parton shower programs use a perturbative method to include higher order QCD corrections. Gluon emissions and splittings are randomly generated in an iterative fashion to simulate the parton showers [47]. The parton shower program simulates hadronisation using phenomenological models that group the partons together into colourless hadrons. The underlying event is also generated using non-perturbative phenomenological models.

The physics events are generated with tools, which return truth-level information. Truth-level information details the four momenta of the final state particles and it can be used as the input for a detector simulation. The detector is simulated using GEANT4 [48, 49], and the output can be passed through reconstruction algorithms (see Chapter 4) to create physics objects. The information supplied at this stage is known as reco-level information and can be directly compared to recorded data.

Chapter 3

The ATLAS Detector at the Large Hadron Collider

The European Centre for Nuclear Research (CERN) is located on the French-Swiss border on the outskirts of Geneva. It is home to the Large Hadron Collider (LHC), a 26.7 km-long circular proton-proton collider located 100 m underground. The LHC has four collision points, each associated with their own major independent experiment. There are two specialised experiments, LHCb [50] which is designed for studying flavour physics, and, ALICE [51], which is purposed for studying heavy ion collisions. The remaining two experiments, ATLAS [52] and CMS [53] are general-purpose detectors, capable of both performing precision measurements, and searching for physics beyond the Standard Model. The data analysed in this thesis is collected by the ATLAS detector. The LHC and ATLAS detector are summarised in 3.1 and 3.2 respectively.

3.1 The Large Hadron Collider

The LHC is built inside the tunnel that was originally excavated for the Large Electron-Positron (LEP) collider, which was operational between 1989 and 2000 [54]. The circular tunnel has a 26.7 km circumference and is buried 100m underground. At the start of the 21st Century the tunnel was re-purposed for proton-proton collisions [55]. The data presented in this thesis makes use of proton-proton collisions, although, the LHC is also capable of heavy ion collisions.

The LHC first collected data in 2009 until 2013, in a period known as Run 1; during this time, the machine reached a maximum centre-of-mas energy of $\sqrt{s} = 8$ TeV. The LHC was then shut down for two years as part of a planned upgrade. The second operational
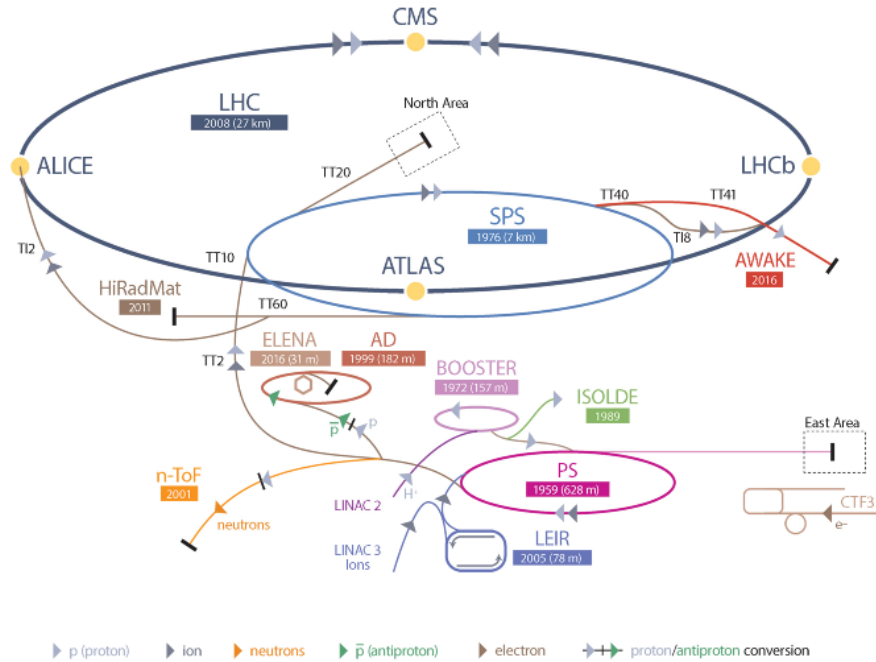
Figure 3.1: A schematic diagram of the LHC and CERN's wider accelerator complex. A series of smaller accelerators are used accelerate the protons up to the target centre-of-mass energy before the beam is injected into the LHC [56].

run, known as Run 2, took place between 2015 and 2018; a time during which the proton beams achieved a maximum centre-of-mass energy of $\sqrt{s} = 13$ TeV.

In order to achieve high centre-of-mass energies, the protons are accelerated over several stages, first using smaller accelerators to gradually increase the protons' energy before they are injected into the LHC. Figure 3.1 shows a schematic diagram of the accelerator complex at CERN. The acceleration process begins with LINAC2. At this first stage, the protons pass through a series of conductors that are alternately charged positive and negative [57]. The alternating charge of the conductors causes the protons to be pushed away from the positively charged conductors whilst also being pulled towards the negatively charged conductors, resulting in acceleration. Once the protons have reached an energy of 50 MeV they are moved into the proton synchrotron booster [58]. Once inside the proton synchrotron booster, the proton beam is accelerated by an alternating electromagnetic field, whose frequency is varied such that the protons maintain a constant circular path and hence gain energy. Next, the protons are injected into the proton synchrotron, in order to reach an energy of 25 GeV [59]. The proton beam undergoes a final stage of acceleration, before entering the LHC, inside the super proton synchrotron, where it is accelerated to have a centre-of-mass energy up to 450 GeV [60]. Inside the super proton synchrotron, the protons in the beam are separated into bunches as a consequence

of the acceleration. The bunches are separated by 25 ns. The bunch separation remains constant as the beam leaves the super proton synchrotron and enters the LHC, where the protons are accelerated up to the TeV-range. The LHC can accommodate up to 2808 bunches of protons, with each bunch approximately composed of 10^{11} protons [55, 32].

The proton beam is split into two separate beams that travel in opposite directions inside individual beam pipes. The trajectory of each beam is maintained by superconducting dipole magnets, cooled down to 1.9 K. The superconducting dipole magnets are interspersed with eight 400 MHz radiofrequency cavities. This setup allows the protons to be accelerated up to beam energies of 6.5 TeV. Quadrupole magnets focus the beam at the interaction points, narrowing the beam width and increasing the proton density, thus increasing the number of proton-proton collisions. The use of quadrupole magnets to focus the beam means that the beam dimensions can be described using Gaussian distributions [61].

The number of proton-proton collisions per second is defined as the instantaneous luminosity $\mathcal{L}$. For two bunches composed of N_1 and N_2 protons with a frequency, f, and with vertical and horizontal beam dimensions, $\sigma_x \sigma_y$, the instantaneous luminosity is:

$$L = \frac{f N_1 N_2}{4\pi \sigma_x \sigma_y} \qquad (3.1)$$

The LHC was designed to reach an instantaneous luminosity of 10^{34} cm^{-2}s^{-1}, however, over the course of Run 2 the LHC exceeded this by delivering a peak luminosity of 2.1×10^{34} cm^{-2}s^{-1}. This equates to a total number of proton-proton collisions, otherwise known as the integrated luminosity, of 156 fb^{-1}.

Figure 3.2(a) shows the cumulative integrated luminosity over time. The green area indicates the total integrated luminosity delivered by the LHC. The yellow area indicates the total integrated luminosity recorded by the ATLAS detector; this includes events that pass the level-1 and high level trigger (see Section 3.2.5). The blue area indicates the total integrated luminosity that is "good for physics". Events recorded by the ATLAS detector are categorised as "good for physics" if they pass the data quality criteria. The data quality criteria ensure events are rejected if they are linked to a problem with either the detector, trigger, reconstruction or processing stage. The ratio of the total integrated luminosity recorded by the ATLAS detector and the total integrated luminosity that is "good for physics" is quantified by the data quality efficiency [62].

The dataset recorded when the ATLAS detector is continuously recording is known as an ATLAS run, which can be sub-divided into luminosity blocks. Luminosity blocks are periods of time for which the conditions of the instantaneous luminosity, the conditions
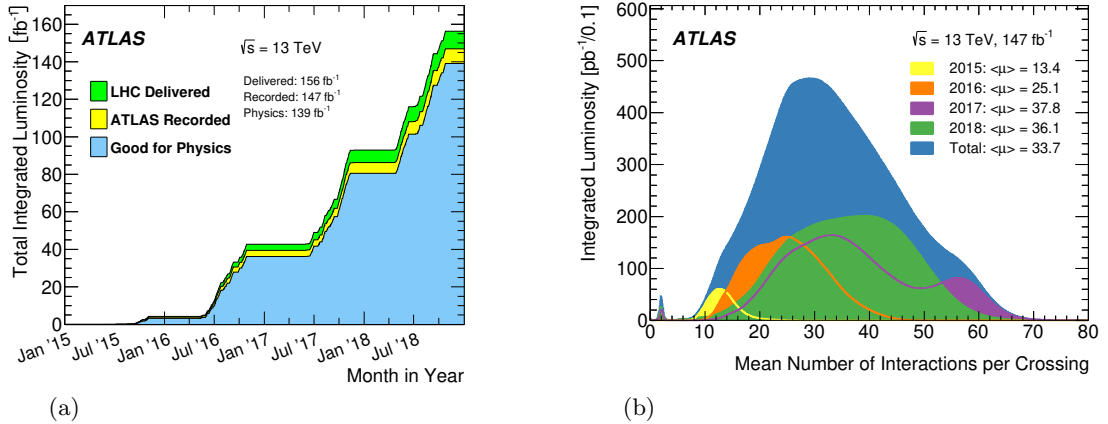
Figure 3.2: a) Shows the cumulative luminosity against time for Run 2. The total luminosity delivered to the ATLAS experiment by the LHC is shown in green, whilst the total recorded by the ATLAS detector is shown in yellow. The blue graph shows the total luminosity suitable for physics analysis after passing a data quality assessment [62]. b) Shows the mean number of interactions per crossing, weighted to the luminosity for the Run 2 data set [62].

in the detector, the trigger and the data quality are constant. The length of time for each luminosity block can vary although they are typically about 60 s in length. Luminosity blocks are used to define Good Run Lists (GRLs), which detail the data that has been labelled "good for physics". A physics analysis uses GRLs to ensure only data of the best quality is used.

After data quality measures have been applied, the ATLAS experiment was able to use 139 fb^{-1} of the data recorded in Run 2.

The large luminosity delivered by the LHC could only be achieved by increasing the number of interactions per bunch crossing (denoted by μ) a quantity also known as pile-up. Figure 3.2(b) illustrates the mean number of interactions for each year in Run 2 and shows that for the whole of Run 2 the average number of interactions per bunch crossing was equal to 33.7. In an ideal world, the pile-up would be kept as close to unity as possible. However, high pile-up is an unavoidable consequence of the high luminosity needed to ensure enough data is collected to study an individual physics process. Without enough proton-proton interactions the number of collisions would be too infrequent to conduct a meaningful study. Increased pile-up presents challenges to the detectors located on the LHC; as more activity in the detectors makes it harder to reconstruct events and distinguish between the interaction of interest and concurrent interactions. High pile-up can be addressed by optimising the trigger system (see Section 3.2.5) and the reconstruction processes (see Chapter 4).
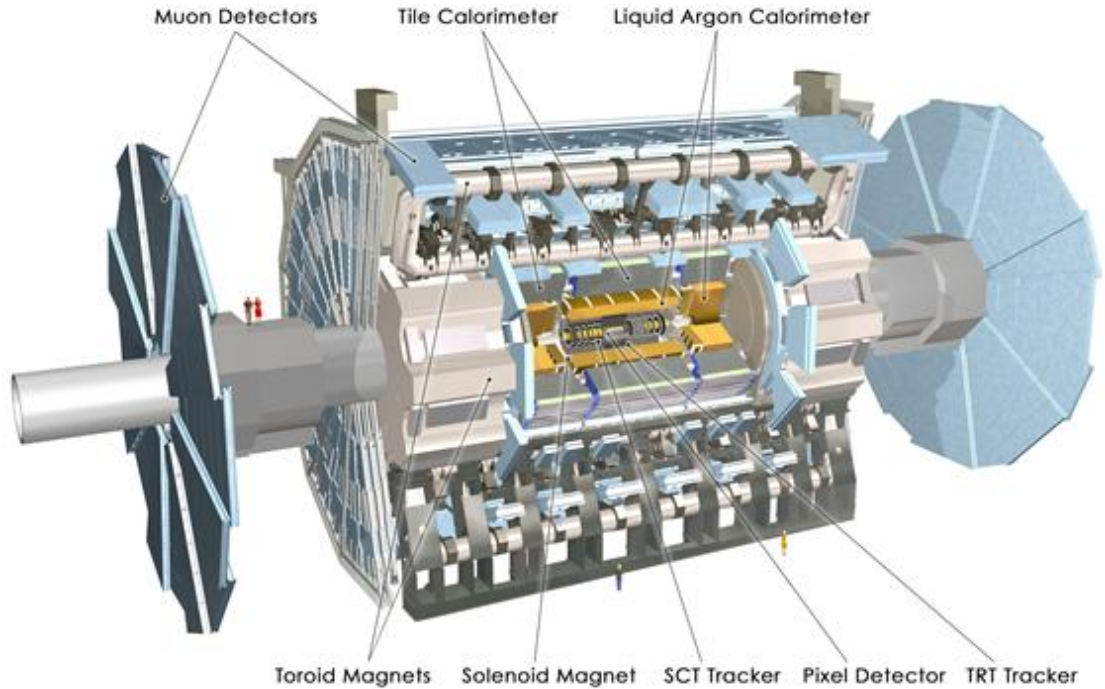
Figure 3.3: A cutaway diagram of the ATLAS detector, including labels of the constituent sub-detectors and people for scale [52].

3.2 The ATLAS Detector

The ATLAS detector is one of two general-purpose detectors located on the ring of the LHC and it is the detector used to collect the data presented in this thesis. The ATLAS detector is in a cavern 100 m underground at CERN's Meyrin site in Switzerland. It has a barrel-shape and is 44 m long with a diameter of 25 m - it is the largest volume particle detector ever made. The design features of the detector enable it to identify all particles in the Standard Model [52]; with the exception of neutrinos, which do not interact with the detector so are accounted for via calculating the missing transverse energy in a collision event. The detector itself is shown in Figure 3.3 and is made up of several layers of sub-detectors, namely, the inner detector, the electromagnetic calorimeter, the hadronic calorimeter and the muon spectrometer. The sub-detectors will be detailed further in the subsequent subsections of this chapter.

3.2.1 The Detector Geometry and Coordinate System

Before moving on to detail the sub-detectors, it is important to first define the coordinate system used to reference the ATLAS detector, and to define relevant quantities that will be referred to regularly throughout this thesis.
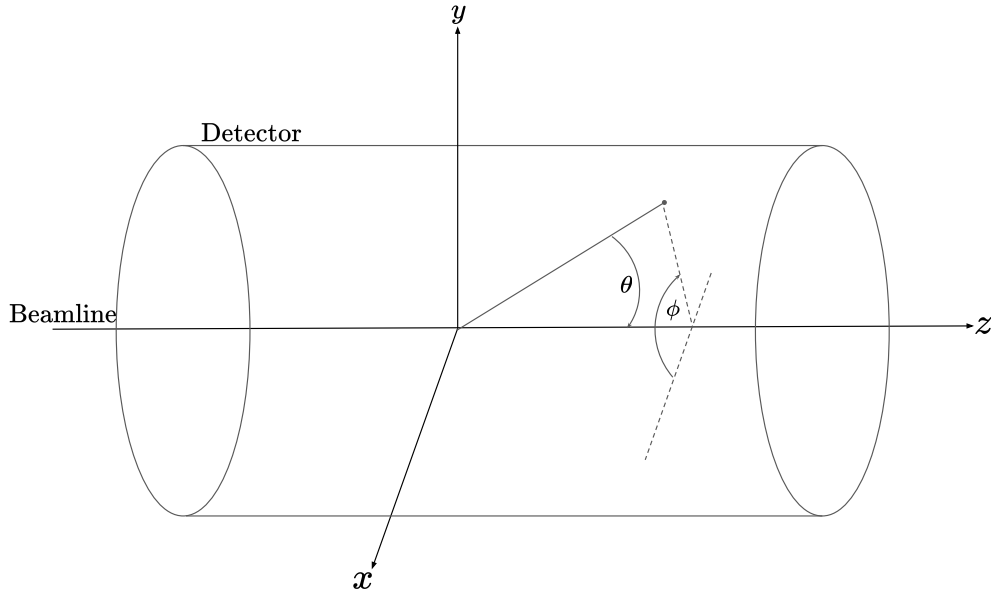
Figure 3.4: A diagram showing the geometry of the ATLAS detector.

The total momenta of the protons colliding inside the ATLAS detector is known, however the distribution of the momenta across the constituent partons is not known. Since each parton only has a fraction of the total momenta, the outgoing particles are boosted in the $z-$direction, thus the transverse momentum, p_T, is Lorentz invariant and so, it is a crucial variable used to describe the kinematics of the system. The transverse momentum is the projection of the momentum on to the $x - y$ plane of the detector and it is defined as:

$$p_T = \sqrt{(p_x)^2 + (p_y)^2} \tag{3.2}$$

The geometry of the barrel-shaped ATLAS detector lends itself to a right-handed cylindrical coordinate system, see Figure 3.4. The positive $z-$direction is clockwise along the beam pipe, the azimuthal angle around the $z-$axis is denoted by ϕ, and the polar angle from the beam axis is denoted by θ. The polar angle, θ, is not invariant under Lorentz transformations so is generally replaced by rapidity, y, or pseudorapidity, η. Changes in rapidity or pseudorapidity are invariant under longitudinal Lorentz transformations. These quantities are often used to describe the trajectories of particles in the detector as they allow the particle system to be studied in the centre-of-mass frame rather than the detector-frame. Additionally, the rapidity and pseudorapidity are equivalent for massless particles [32]. Rapidity and pseudorapidity are defined as:

$$y = \frac{1}{2} \ln \left(\frac{E + p_z}{E - p_z} \right) \qquad \eta = -\ln \left(\tan \left(\frac{\theta}{2} \right) \right) \tag{3.3}$$

30

Where E is the total energy of the particle and p_z is the particle's momentum in the $z-$direction. Consequently, the trajectory of particles in the detector is often described in the (η, ϕ) plane.

Another Lorentz invariant quantity is the angular separation, ΔR, and is defined as:

$$\Delta R = \sqrt{(\Delta \eta)^2 + (\Delta \phi)^2} \tag{3.4}$$

ΔR is used to measure distances in the detector, such as the distance between two reconstructed objects or the spread of electromagnetic showers in the electromagnetic calorimeter [32].

3.2.2 The Inner Detector

The inner detector is a tracking detector designed to reconstruct the tracks of charged particles over the complete azimuthal angle and for pseudorapidity, $|\eta| \leq 2.5$. This section will detail the components of the inner detector, whilst Chapter 4 Section 4.1.2 will detail the algorithms used to reconstruct tracks.

The inner detector is 6.2 m long and has a diameter of 2.1 m. It is surrounded by a solenoid coil that applies a $2\,\text{T}$ axial magnetic field, which bends the path of the charged particles such that a precise measurement of the particle's momentum and charge can be taken. Figure 3.5 shows a cutaway view of the inner detector. It can measure particles with momenta as low as 100 MeV, although constraints on reconstruction times and efficiencies usually mean higher threshold of $p_T \geq 400$ MeV has to be applied for the reconstruction to be feasible [63]. The inner detector is the closest sub-detector to the beam axis and it has three constituent parts: the pixel detector, the semiconductor tracker and the transition radiation tracker.

3.2.2.1 The Pixel Detector

The pixel detector is the closest detector to the beam pipe, its primary purpose is to measure the spatial coordinates of charged particles as they enter the ATLAS detector. The pixel detector comprises of three layers of pixels in the barrel region, inserted at 50.5 mm, 85.5 mm and 122.5 mm away from the beam pipe. There are also three layers of pixels in each end cap. Each pixel is $250\,\mu\text{m}$ thick and covers an area of $50\times 400\,\mu\text{m}^2$. There is a total of 80 million channels in the pixel layers, with each pixel having a resolution of $10\,\mu\text{m}$ the radial direction and $115\,\mu\text{m}$ in the azimuthal direction. The pixel detector covers pseudorapidities of $|\eta| \leq 2.5$.
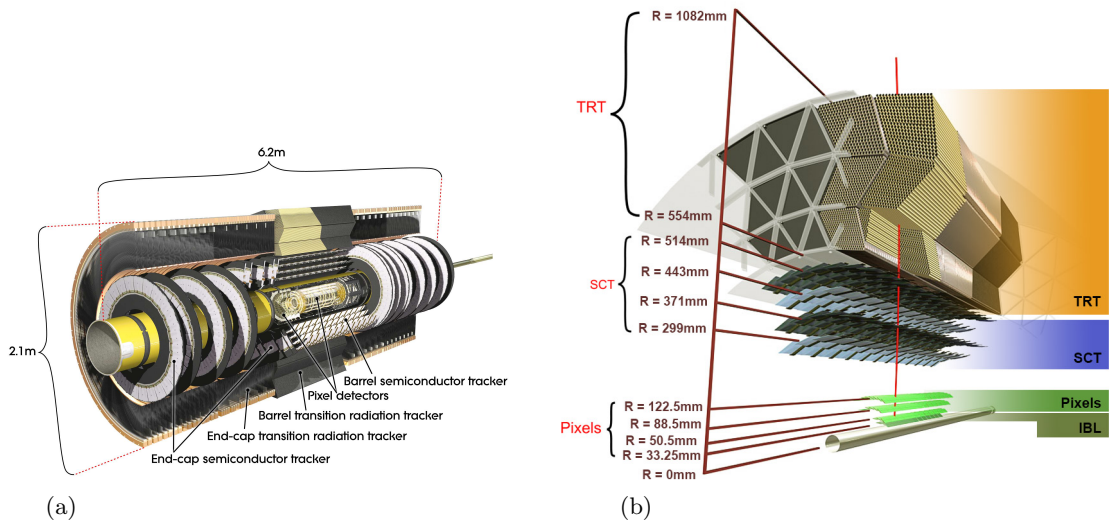
Figure 3.5: The ATLAS inner detector. a) Shows a cutaway view of the inner detector.
b) Shows a more detailed view of structure of the inner detector in the radial direction [64].

The pixel detector was upgraded to include and extra layer, known as the insertable B-layer, in the long shutdown period between Run 1 and Run 2. The insertable B-layer was inserted at a radius of 33.25 mm, and was added to deal with higher track multiplicities and pixel occupancy as a result of increasing the luminosity at the LHC [64].

3.2.2.2   The Semiconductor Tracker

The semiconductor tracker surrounds the outside of the pixel detector and provides information about charged particles as they advance through the ATLAS detector. The semiconductor tracker has $60\,\mathrm{m}^2$ of silicon strips spread across four cylindrical barrel layers, and nine planar layers at each end cap. The four barrel layers of the semiconductor tracker are located at $299\,\mathrm{mm}$, $443\,\mathrm{mm}$ and $514\,\mathrm{mm}$ away from the beam pipe, and each layer covers a pseudorapidity range of $|\eta| \leq 2.5$. The semiconductor tracker has a readout strip every $80\,\mathrm{\mu m}$, to allow for accurate position tracking of the charged particle. The strips are orientated such that they are parallel to the beam line in the barrel and radial on the end cap disks. In both the barrel and the end cap, two sensors are rotated by an angle of $40\,\mathrm{mrad}$ to one another, this improves the accuracy of the position measurements of the hits [65]. The semiconductor tracker has a transverse resolution of $17\,\mathrm{\mu m}$ and a longitudinal resolution of $580\,\mathrm{\mu m}$.

3.2.2.3   The Transition Radiation Tracker

The transition radiation tracker is the final part of the inner detector, sitting at $554\,\mathrm{mm}$ away from the beam pipe. The transistion radiation tracker is built from drift tubes,

32

known as straws. The straws have a 4 mm diameter and are separated by a dielectric material. They are made out of an insulating material with an aluminium cathode deposited on top and there is a central wire anode running through the middle of each straw. The straws are filled with either Xenon or Argon gas and a potential difference of 1.5 kV is applied between the anode and cathode. Charged particles passing through the transition radiation tracker produce an electric current that can be read out as a signal, either by ionising the gas or inducing transition radiation photons from the dielectric material, which go on to ionise the gas. The number of transition radiation photons are proportional to the relativistic γ-factor and are of the order of the keV-scale. Such photons are more likely to be emitted by less massive particles. Thus the transition radiation photons produced a higher signal amplitude than the gas ionised as a direct result of the charged particle. The transition radiation tracker is able to distinguish between low-threshold and high-threshold hits which enables it to provide information on the type of the particle passing through the detector as well as tracking information. For example, electrons have a smaller mass than charged hadrons, so are more likely to generate high-threshold hits along their trajectories [66].

The transition radiation tracker has 50,000 straws in the barrel, parallel to the beam axis and measuring 144 cm each. There are 250,000 straws in the end-caps, arranged radially and measuring 37 cm long. There are separate readouts for each half of the barrel so the transition radiation tracker can only provide measurements in the $R - \phi$ plane, although the transition radiation tracker does extend to a pseudorapidity of $|\eta| = 2.0$. The intrinsic resolution of the transition radiation tracker is 130 μm which is obtained by using the drift time to determine the drift circles. This is the lowest resolution of the three components that make up the inner detector. However, each charged particle passing through the transition radiation tracker will generally produce 30 hits, dramatically improving the spatial resolution of the track trajectories.

3.2.3 The Calorimeters

The ATLAS detector has two sampling calorimeters that encompass the inner detector and covers a pseudorapidity range of $|\eta| < 4.9$. Firstly, there is the electromagnetic calorimeter which is designed to measure the energy of particles that interact electromagnetically. Followed by the hadronic calorimeter which is designed to measure the energy of particles that interact via the strong force. Both sub-detectors that make up the calorimeter system use layers of absorbing and active material. As a particle passes through the absorbing material, it triggers a series of particle decays into a shower of secondary particles, until its energy is completely degraded. The layers of active material enable the energy deposited to be read out. This not only provides information on the energy of

the particle, but also the direction and dimensions of the shower of secondary particles, which can in turn be used to determine the nature of the incident particle. For instance, electromagnetic showers are typically entirely contained in the electromagnetic calorimeter and are much narrower and shallower than hadronic showers that can span across both the electromagnetic and hadronic calorimeters [67].

The characterisation of electromagnetic and hadronic showers uses three variables that quantify the lateral width and longitudinal depth of the particle showers inside the calorimeter. The Moilière radius, R_M, is used to quantify the lateral width of the shower, it is defined as the radius of a cone that contains 90% of the shower's energy. The radiation length, X_0, is used to quantify the longitudinal depth of electromagnetic showers, it is defined as the distance in which, the energy of a charged particle is reduced by a factor of e due to radiation losses, such as Bremsstrahlung. The analogous quantity for hadronic showers is known as the Nuclear Interaction Length, λ. The Moilière radius, the Radiation Length and the Nuclear Interaction Length are all dependent on the atomic number of the calorimeter material [67].

The electromagnetic and hadronic calorimeters are split into three sections - the central barrel section, and two end-caps, illustrated in Figure 3.6. The calorimeter system of the ATLAS detector is engineered to contain the showers produced by electrons, photons, pions, kaons and other hadrons. The calorimeter system is designed to fully contain the showers of high energy particles produced in the proton-proton collisions and consequently ensures there is minimal noise in the muon spectrometer.

3.2.3.1   The Electromagnetic Calorimeter

The electromagnetic calorimeter is a sampling calorimeter that encloses the inner detector. It uses liquid argon, cooled at -183°C as an active material, sandwiched between lead absorption plates. The lead absorption plates have a high density and short radiation length; properties that lend themselves to containing electromagnetic showers in a compact calorimeter system. The electromagnetic calorimeter makes use of an accordion-shaped geometry, in order to provide complete azimuthal symmetry and avoid any cut-off of signal between neighbouring electrodes. Electrodes are interleaved with the lead absorbing plates and have a 2 kV potential difference applied. Electromagnetic showers are triggered as particles, such as electrons or photons, cascade through the liquid argon and undergo successive pair production and Bremsstrahlung interactions. The electromagnetic showers cause excitation and ionisation of the liquid argon and resulting charges drift towards electrodes which are then in turn, read out as an electronic signal [68].
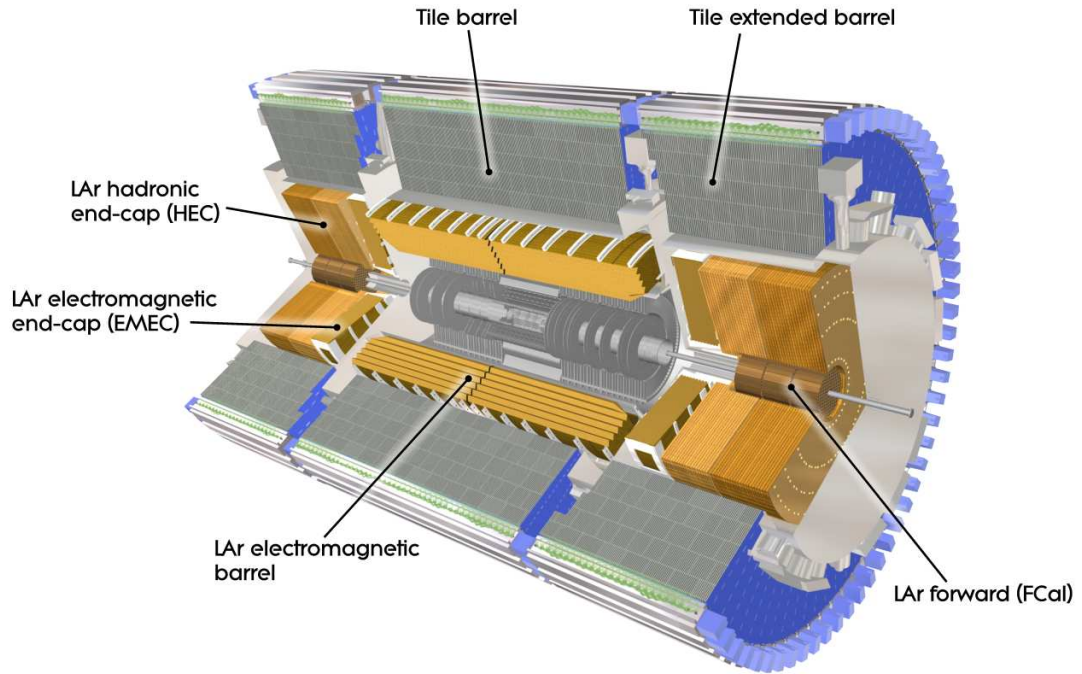
Figure 3.6: A cut-away diagram of the ATLAS calorimeter system [52].

The electromagnetic calorimeter is comprised of a presampler layer followed by three further layers. The presampler is $11\,\text{mm}$ thick and covers a pseudorapidity range of $|\eta| < 1.8$. It is segmented in intervals of pseudorapidity, $\eta = 0.2$, and its main purpose is to correct for energy losses upstream of the electromagnetic calorimeter. After the presampler layer, the barrel component of the electromagnetic calorimeter begins. The barrel component covers a pseudorapidity range of $|\eta| < 1.475$. It is $6.4\,\text{m}$ long, has an inner diameter of $2.8\,\text{m}$ and extends to an outer diameter of $4\,\text{m}$. Figure 3.7(a) illustrates the layered structure of the barrel component [52].

The first of the three layers is known as the front layer and covers a pseudorapidity range of $|\eta| < 1.4$ and $1.5 < |\eta|$. The front layer has a granularity of $\Delta\eta \times \Delta\phi = 0.003 \times 0.01$, the very fine lateral segmentation in pseudorapidity enables the $\pi^0 \rightarrow \gamma\gamma$ process to be distinguished from prompt photons. The next layer is called the middle layer and is the thickest part of the electromagnetic calorimeter, approximately $16\ X_0$. It is in this region where the electromagnetic showers deposit the most energy. The granularity of the middle layer is $\Delta\eta \times \Delta\phi = 0.025 \times 0.025$. The final layer is the back layer, which has a granularity of $\Delta\eta \times \Delta\phi = 0.05 \times 0.025$. The back layer is used to measure the tails of high-energy electromagnetic showers and also plays a central role in differentiating between electromagnetic and hadronic energy deposits. In total, the barrel component has a total thickness of $22\ X_0$ [69]. The varying granularities of the layers helps to develop the shower shape and to build an accurate picture of how the energy is distributed.

35
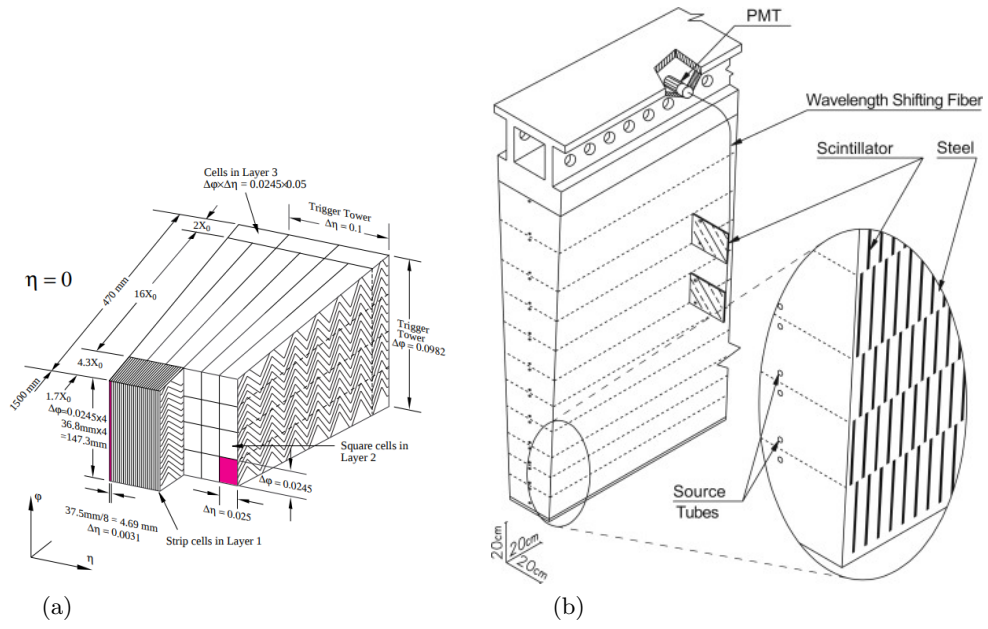
Figure 3.7: a) Shows a sketch of a electromagnetic calorimeter module which consists of several layers with varying granularity. b) Shows a single hadronic tile calorimeter module [52].

The electromagnetic end-caps cover a pseudorapidity range $1.375 < |\eta| < 3.2$ and are divided into an inner and outer end-cap. The inner end-caps have the same three layers as the central barrel component, whereas the outer end-cap has two layers with a coarser azimuthal granularity. The electromagnetic end-caps have a total thickness of 24 X_0 [69]. The gap between the barrel component and the electromagnetic end-caps is called the transition region ($1.37 < |\eta| < 1.52$). It is an area with reduced detection and energy reconstruction capabilities.

The electromagnetic calorimeter has a fine granularity over the full acceptance range of the inner detector, for pseudorapidities of $|\eta| < 2.5$. This helps to match tracks to energy deposits, a crucial aspect of particle identification. Beyond the acceptance of the inner detector, the granularity of the electromagnetic is reduced to $\Delta\eta \times \Delta\phi = 0.1 \times 0.1$.

3.2.3.2 The Hadronic Calorimeter

The hadronic calorimeter is located around the electromagnetic calorimeter and is designed to contain the showers triggered by hadrons, which typically have a more variable particle multiplicity than electromagnetic showers. Hadrons predominantly interact via the strong interaction. Like electromagnetic showers, the initial hadron causes a cascade of secondary particles which develop inside the calorimeter. Hadronic shower signatures often include energy deposited in the electromagnetic calorimeter, due

36

to pions decaying electromagnetically, followed by a long tail of energy deposited in the hadronic calorimeter from strong interactions.

Like the electromagnetic calorimeter, the hadronic calorimeter is separated into three segments: the central barrel and two end-caps. The central barrel of the hadronic calorimeter is known as the tile calorimeter and it is a sampling calorimeter constructed from layers of steel absorption plates and plastic scintillator tiles. Hadronic showers passing through the scintillating material produce light which is carried by wavelength-shifting fibres and read out via photomultiplier tubes. The tile calorimeter is partitioned into a barrel part, which covers a pseudorapidity range of $|\eta| < 1.0$ and an extended barrel part, which covers a pseudorapidity range of $0.8 < |\eta| < 1.7$. Both the barrel and the extended barrel are divided into three longitudinal layers that are 1.5 λ, 4.1 λ and 1.8 λ deep. The segmentation of the tile calorimeter is coarser than that of the electromagnetic calorimeter, for small values of pseudorapidity there is $\Delta\eta \times \Delta\phi = 0.1 \times 0.1$ which reduces to $\Delta\eta \times \Delta\phi = 0.2 \times 0.1$ for increasing values of pseudorapidity [52].

The end-caps of the hadronic calorimeter are divided into two distinct parts, the hadronic end-caps, which cover a pseudorapidity of $1.5 < |\eta| < 3.2$ and the forward calorimeter, for larger values of pseudorapidity, $3.1 < |\eta| < 4.9$. Both the hadronic end-caps and the forward calorimeter use liquid argon as the active material to measure the energy deposited in this region of the detector. The hadronic end-caps use copper plates as the absorption material. The geometry of both the hadronic end-caps and the forward calorimeter, is similar to that of the electromagnetic end-caps. They consist of 32 wedge-shaped modules arranged in a wheel-like structure. The forward calorimeter is split into three layers, the first layer uses copper as the absorption material is sensitive to electromagnetic showers, whilst the outer two layers use tungsten plates between the liquid argon to record energy deposited by hadronic showers [68, 70].

3.2.4   The Muon Spectrometer

Muons do not interact with the material in the calorimeters of the ATLAS detector, so a specifically designed muon spectrometer surrounds the calorimetry system, in order to provide tracking and momentum measurements of these leptons [71]. The muon spectrometer provides information that is complimentary to that provided by the inner detector, in order to measure muons with momenta in the range of 3 GeV to 1 TeV. The ATLAS detector has one toroidal magnet through the barrel and one in each end-cap, which apply a 0.5 T magnetic field to deflect muons travelling through the muon spectrometer in the $r - z$ plane. Four muon tracking chambers are installed between the coils of the barrel toroid magnet and on either side of the end-cap toroid magnets.

There are three layers of muon drift tube chambers which cover a pseudorapidity range of $|\eta| < 2.7$. The flux of incoming particles increases with pseudorapidity and in the outer regions of the muon system $(2.0 < |\eta| < 2.7)$ the radiation is too high for drift tubes, so a layer of cathode strip chambers is used instead. The cathode strip chambers consist of strips of multi-wire proportional chambers. Inside the barrel region, the muon drift chambers are rectangular in shape, however they have a trapezoidal geometry inside the end-caps in order to tessellate into a circular shape. There are three discs in each end-cap, known as the small wheel, the big wheel and the outer wheel [52].

Resistive plate chambers are gaseous parallel-plate detectors, designed to have good time and spatial resolution. They sit next to the muon drift chambers in the barrel region to identify potential muon tracks and act as a fast trigger of the detector. Thin gap chambers are also used to identify potential muon tracks. Thin gap chambers have anode and cathode readouts and are placed in the end-cap region for pseudorapidities up to $|\eta| < 2.4$. Both the resistive plate chambers and the thin gap chambers have a fine time resolution which is utilised to in the first level of the trigger system.

3.2.5   The Trigger System

The number of proton-proton collisions the ATLAS detector is capable of detecting vastly exceeds the readout and storage capabilities, consequently a trigger system is used to reduce the number of events recorded to more manageable levels. As mentioned in Section 3.1, the LHC splits the proton beam up into bunches, separated by 25 ns, this equates to a bunch crossing frequency of 40 MHz, which is reduced to 200 Hz by the trigger system.

The trigger system [72] has two parts: the level-1 trigger, which is hardware based, and the high level trigger, which is software based. The level-1 trigger makes a decision on whether to discard an event based on either the energy depositions in the calorimeter system or the track segments in the resistive plate chambers and thin gap chambers, located in the muon spectrometer. The level-1 trigger only has access to a reduced granularity of these sub-dectectors, but uses the information available to define regions of interest in $\eta - \phi$ space. If a region of interest passes the conditions of the level-1 trigger, it is passed onwards to the high level trigger, where a more detailed analysis of the event takes place. The high level trigger is able to reprocess the event using the full granularity of the detector and can choose between using information about the event as a whole or selecting specific isolated regions of the detector. The high level trigger uses reconstructed objects to both build events and select based on the trigger. The rate of production of some event signatures exceeds output rate of the trigger system. For these

cases, only a certain fraction are recorded and a prescale factor is applied to account for the limitations in recording. Once events have passed all stages of the trigger system, they are permanently stored at the CERN computing facility and distributed across the world to smaller national computing facilities using the computing grid.

Chapter 4

Event Reconstruction

The particles that travel through the ATLAS detector, as a result of the proton-proton collisions, interact with the various sub-detector systems. The interactions between the particles and the sub-detectors produce electronic signals that are recorded. This chapter will describe how the raw data collected by the each component of the detector is used collectively to reconstruct the properties of the final particles involved in each physics event. Known as physics objects, these properties are used in physics analyses to identify and categorise particles. Accurately reconstructing events is crucial for providing background estimates and for correctly interpreting results. First, the reconstruction of tracks and vertices will be discussed in Section 4.1. Next, the parameterisation of the proton beam parameters will be detailed in Section 4.2. The analysis presented in this thesis applies requirements on the number of tracks surrounding the primary vertex so clearly defining these quantities is fundamental for subsequent chapters in this thesis. Finally, Section 4.3.2 and Section 4.4 will describe how particle tracks are combined with information from the calorimeters and the muon spectrometer to reconstruct electrons and muons.

4.1 Track and Vertex Reconstruction

The location of a proton-proton collision inside the ATLAS experiment is known as the interaction vertex, and the path of a charged particle moving through the ATLAS detector is known as a track. Every proton-proton collision has an associated vertex but often only one of the vertices in an event is of interest to a physics analysis. It is called the primary vertex, and is usually identified as the one with the largest scalar sum of the transverse momenta associated to it. This section will first discuss how the design of the ATLAS detector lends itself to parameterise the qualities of a track, before

summarising the methods used to reconstruct the tracks and vertices that occur as a result of proton-proton collisions.

4.1.1   Track Parameters

As a charged particle moves through the inner region of the ATLAS detector, it travels through a uniform solenoidal magnetic field and hence follows an approximate helical path. A perfect helix cannot be used to describe the track since the particle undergoes scattering and energy losses as it travels through the detector. A track can be defined by a number of parameters, namely η, ϕ, q/p, d_0 and z_0, which are defined below [73].

Psuedorapidity, η and azimuthal angle, ϕ, quantify the location of the tracks within the ATLAS detector. The variable q/p is the ratio of charge to momentum of the reconstructed track. d_0 is the transverse impact parameter, and is defined as the distance of the closest approach of the track to the beam line in the transverse plane. z_0 is the longitudinal impact parameter, defined as the distance along the z-axis between the primary vertex and the point at which d_0 is evaluated. The impact parameters are used during the track fitting stage of the track reconstruction algorithms. They are used to distinguish between tracks of interest in a physics analysis. Figure 4.1 shows how the geometry of the track is used to define the impact parameters.

A fully reconstructed track will normally have impact parameters calculated with respect to the primary vertex. However during track reconstruction, the impact parameters are often estimated using either the nominal interaction point of the ATLAS detector or the beam spot instead. Where the beam spot is defined as the area in which proton-proton collisions occur, and is parameterised by the three-dimensional distribution of reconstructed event vertices[1]. For the photon-induced W^+W^- analysis discussed in this thesis (see Chapter 6), the impact parameters are calculated with respect to the beam spot.

4.1.2   Track Reconstruction

A track is defined as the trajectory of a charged particle travelling through the ATLAS detector. Track reconstruction makes use of the information recorded in the pixel detector and the semiconductor tracker. Hits are defined from the location of energy deposits above a given threshold, in the silicon pixels or strips. They are translated into three-dimensional space points which indicate the areas of the detector that the charged particle has traversed. A space point is built when at least one hit is found in a single

---

[1]The beam spot is discussed in more detail in Section 4.2.
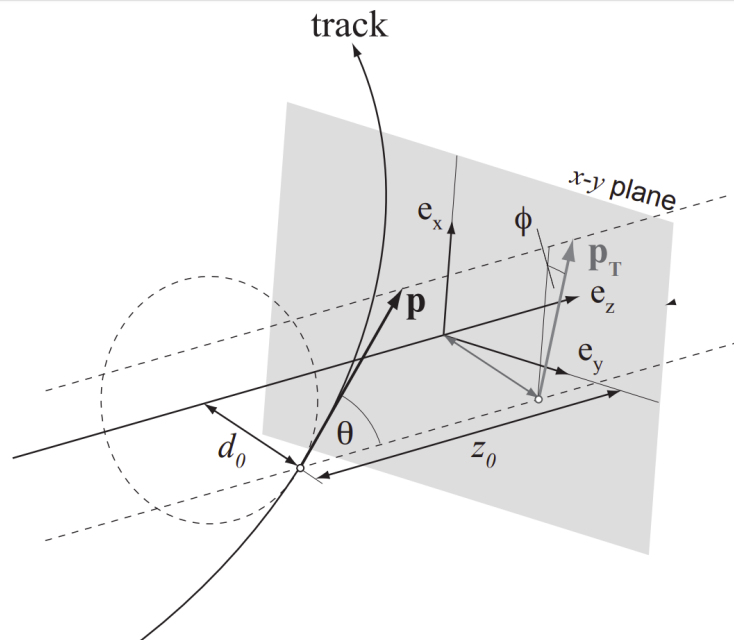
Figure 4.1: A diagram illustrating the geometry of the track parameterisation [74].

pixel module or when two hits are found in a single semiconductor tracker module [75]. Track reconstruction algorithms are used in order to infer this trajectory from a number of space points. Track reconstruction can be challenging in a high pile-up environment as the high particle multiplicity can cause some of these space points to be incorrectly associated to a particle trajectory.

Track reconstruction algorithms are used to turn the information provided by the space points into fully reconstructed tracks [76]. The reconstruction happens in two steps, first there is pattern recognition followed by track fitting. In the first phase, the reconstruction algorithms identify a number of hits emanating from a single particle trajectory. Next, the parameters of the track are determined by passing the collection of hits through one of three track fitting algorithms. Each track fitting algorithm assumes a perfect helical trajectory in a uniform magnetic field and each algorithm takes a different approach to track reconstructing. One algorithm is used for reconstructing tracks that only leave hits in the transition radiation tracker. This algorithm is mainly used to identify photons conversions into electrons and will not be discussed further in this thesis. The remaining two algorithms, known as the *inside-out* and *outside-in* algorithms, aim to match the space point information from the silicon detectors with hits found in the transition radiation tracker. Both of these algorithms are able to reconstruct tracks for $|\eta| = 2.5$.

The inside-out algorithm is the primary algorithm for reconstructing tracks from the proton-proton interaction point and it begins when three hits, in neighbouring layers, are recorded across the pixel detector and the semiconductor tracker. If the three hits pass initial cuts on the transverse momentum and then the impact parameters, they are

deemed to be a consistent with a valid track and are collected together as a seed. A seed is also required to match a fourth hit from a hit from a different detector layer in order to kick-start the pattern finding stage. The requirement of a fourth hit improves the fraction of seeds that can be reconstructed into tracks of good quality [77]. The inside-out algorithm was optimised for Run 2 to reconstruct tracks with a transverse momentum of $p_T > 100$ MeV. The algorithm extrapolates from the pixel detector and the semiconductor tracker towards the transistion radiation tracker, while considering the magnetic configuration of the detector in order to match the track seed with hits found in the transition radiation tracker. The additional hits found in the transition radiation tracker are matched to the seed track using a Kalman filter [78]. Any ambiguous tracks are removed by rejecting the poorest fitting track candidate [76].

The outside-in algorithm works in the opposite direction and extrapolates back from hits in the transition radiation tracker, towards the space points defined by the silicon detectors. The outside-in algorithm is applied after the inside-out algorithm. There is no requirement placed on the impact parameters of the track and tracks can be reconstructed down to $p_T > 50$ MeV. The purpose of this algorithm is to reconstruct trajectories that do not appear to come from the interaction point. This is particularly useful for identifying tracks from b- and c- hadron decays and for reconstructing the secondary vertices used in b-tagging techniques [79], as well as rejecting electrons that originate from photon conversions.

The quality of the track reconstruction algorithms is assessed by measuring the track reconstruction efficiency. The track reconstruction efficiency is measured using simulated Monte Carlo samples, as a function of pseudorapidity or transverse momentum. It is measured using primary tracks - defined to be charged particles with a mean lifetime $\tau > 300\,\text{ps}$, originating from either the proton-proton collision, or from short-lived particles produced from the proton-proton collision. There are two track selections, defined as [76]:

1. **Loose** requirements are:

   - $p_T > 400$ MeV
   - $|\eta| < 2.5$
   - Number of silicon hits ≥ 7
   - Number of shared modules ≤ 1
   - Number of silicon holes ≤ 2
   - Number of pixel holes ≤ 1

2. **Tight-Primary** requirements are:
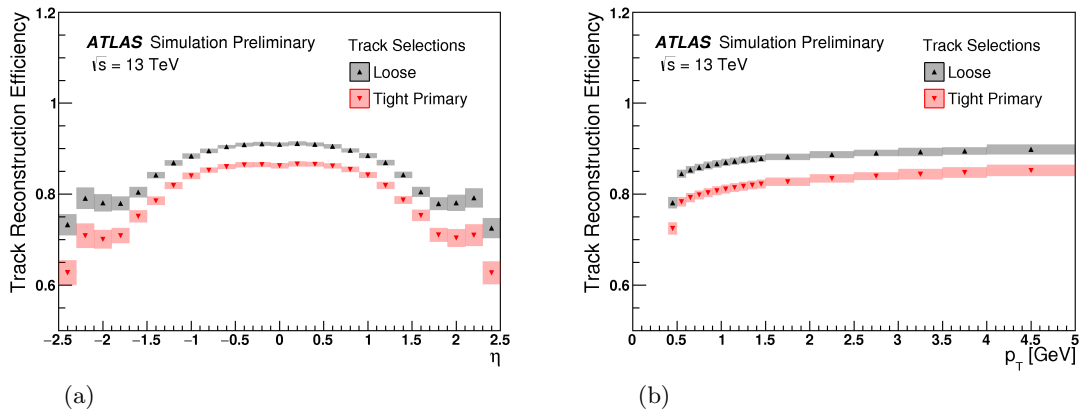
Figure 4.2: The track reconstruction efficiency for both Loose and Tight Primary tracks. a) Shows the efficiency as a function of η. b) Shows the efficiency as a function of p_T [81].

- All of the Loose requirements
- Number of silicon hits ≥ 9 (if $|\eta| \leq 1.65$)
- number of silicon hits ≥ 11 (if $|\eta| > 1.65$)
- One insertable B-layer or next-to-innermost-pixel-layer hit
- No pixel holes

The track reconstruction efficiency is defined as the ratio of the number of primary tracks matched to a reconstructed track, over all primary tracks. The track reconstruction efficiency is calculated from the primary tracks at truth-level or in the Monte Carlo generator. In general, the track reconstruction efficiency is lower for the Tight-Primary track selection than the Loose track selection due to the stricter requirements. However, the Tight-Primary selection rejects more fake tracks by its nature, where a fake track is the name given to a track reconstructed using a hit pattern that does not originate from a primary or secondary particle [80]. The differences in track reconstruction efficiency between the Loose and Tight-Primary selections are shown in Figure 4.2 as a function of pseudorapidity and transverse momentum. The reconstruction efficiencies are at their highest for central values of pseudorapidity. The reduction in track reconstruction efficiency for $|\eta| > 1$ is a consequence of more detector material for the charged particles to traverse. The track reconstruction efficiency increases as a function of transverse momentum, until $p_T \geq 5$ GeV, where the efficiency begins to level off.

4.1.3 Vertex Reconstruction

A vertex is defined as the origin of a particle interaction. Vertices can be sub-categorised into primary and secondary vertices, which denote the positions of inelastic proton-proton
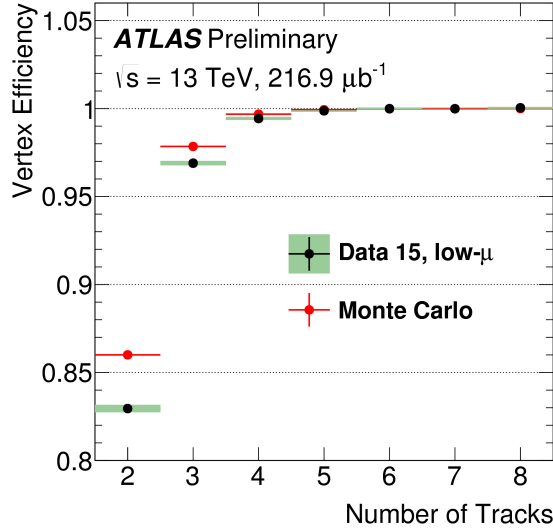
Figure 4.3: This plot compares the vertex reconstruction efficiency for low pile-up data and Monte Carlo as a function of the number of tracks [83].

collisions and the positions where long-lived particles decay, respectively. Like track reconstruction, vertex reconstruction takes place in several stages, namely, vertex finding and vertex fitting. The initial stage makes use of a group of reconstructed tracks that pass the track selection criteria to extrapolate back towards the beam pipe and select a seed position of the vertex. Each seed vertex requires at least two tracks with $p_T > 100$ MeV. Then an iterative fitting process is performed using a χ^2 minimisation technique to remove less suited tracks. Tracks which vary by more than seven standard deviations are removed and the candidate vertex position is recalculated. Once a vertex position is found, any poor track candidates are removed and are used in subsequent vertex reconstruction procedures [82].

Once a track has been matched to a vertex, the impact parameters can be calculated which are then used to discriminate between primary and secondary tracks.

The efficiency of vertex reconstruction is quantified by the ratio of the number of events with a reconstructed vertex to the number of events with a least two reconstructed tracks [83]. The efficiency to reconstruct a primary vertex is near 100% for events with four or more reconstructed tracks in a low pile-up environment, as shown in Figure 4.3. However, the vertex reconstruction efficiency is adversely affected by increased pile-up. This is due to nearby proton-proton interactions making it harder to resolve the point the tracks emerge from [80].

4.2   Beam Parameters

The area in which proton-proton collisions occur can be defined by parameterising the three-dimensional distribution of reconstructed event vertices. This parameterisation is known as the beam spot and represents the instantaneous luminosity of the proton beams. The average position of a proton-proton collision is given by the coordinates of the centre of the beam spot, measured with respect to the ATLAS coordinate system [84]. The size of the interaction point between the two proton beams is intrinsically linked to the transverse and longitudinal widths, σ_{ib}, of the beam spot, where i corresponds to the transverse or longitudinal plane, and b corresponds to each beam (1 or 2). The beam spot widths are assumed to have a Gaussian distribution. They depend on two parameters for both the transverse and longitudinal directions. The first parameter is the emittance, ϵ_{ib}, which describes how confined the beam particles are. The second parameter is the amplitude function, β_{ib}, which describes the aspect ratio of an ellipse. The beam spot widths are given by:

$$\sigma_{ib} = \sqrt{\epsilon_{ib}\beta_{ib}} \tag{4.1}$$

The beam spot widths cannot be measured directly at the interaction point, however they can be extracted using synchrotron-light or wire-scanner beam profile measurements from other locations in the accelerator system.

The distribution of particles within each bunch of protons follows a Gaussian distribution and is given by:

$$\rho_b(x, y, z, t) = \frac{N_b}{\sqrt{(2\pi)^3}\sigma_{xb}\sigma_{yb}\sigma_{zb}} \times e^{-\frac{(x-\bar{x}_b)^2}{2\sigma_{xb}^2} - \frac{(y-\bar{y}_b)^2}{2\sigma_{yb}^2} + \frac{(z\pm ct)^2}{2\sigma_{zb}^2}} \tag{4.2}$$

Where N_b is the number of protons in a particular bunch, and $\bar{x}_b$ and $\bar{y}_b$ correspond to the average position of a proton-proton collision in the transverse and longitudinal planes [85].

The attributes of the beam spot are constantly reconstructed and monitored online via the high level trigger and are regularly communicated to the LHC control.

4.3   Electron Reconstruction and Identification

Electrons are a common final state particle produced as a result of proton-proton collisions inside the ATLAS experiment. Furthermore, they are one of two final state particles that
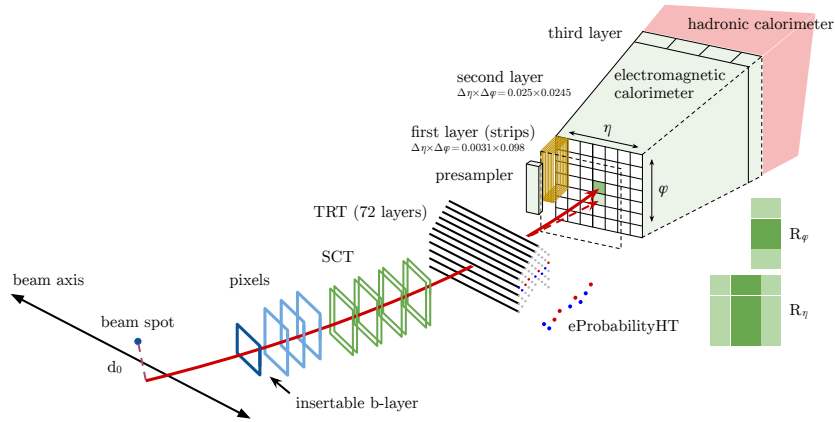
Figure 4.4: A schematic diagram showing the trajectory of an electron (solid red line) travelling through the inner detector and the calorimeters. The trajectory of a photon produced as a result of an electron interacting with the detector material is also shown (dashed red line) [86].

provide a key signature of the photon-induced W^+W^- process presented in this thesis. The signals produced by an electron travelling through the ATLAS detector are used to reconstruct the electron's properties such that it can be used in a physics analysis. The reconstruction and identification of electrons is notably challenging due to energy losses caused by Bremsstrahlung as the electron interacts with the detector material. Bremsstrahlung, combined with the effects of photon pair production, leads to multiple tracks within the inner detector and distinct shower shapes inside the electromagnetic calorimeter. These recognisable characteristics are used by the reconstruction and identification algorithms that are outlined in this section[2].

4.3.1 Electron Reconstruction

An electron is reconstructed in the ATLAS detector if electromagnetic energy deposits left in the calorimeter system are matched to a track inside the inner detector. Figure 4.4 shows the how an electron travel through the inner detector and calorimeter systems. There are three stages to electron reconstruction; first clusters of calorimeter cells containing electromagnetic energy are identified, next the inner detector tracks are reconstructed, as described in Section 4.1.2. Then finally the reconstructed tracks are matched to the electromagnetic clusters to form an electron candidate.

---

[2]Only the reconstruction and identification of electrons within the acceptance of the inner detector will be discussed since this thesis does not make use of electrons within the forward region of the detector. Conjointly, different algorithms are used to reconstruct and identify electrons in the forward region of the detector which will not be discussed in this thesis.

4.3.1.1 Topological Clusters

The electron reconstruction process begins by making use of a collection of dynamically-sized clusters of cells from the electromagnetic and hadronic calorimeters. These dynamically sized clusters, known as topoclusters, are formed using spatial-significance patterns generated by particle showers inside the calorimeters [87]. An algorithm, known as the 4-2-0 alogrithm, is used to grow the topocluster around a seed cell. A seed has a cell significance of $|\zeta_{cell}^{EM}| \geq 4$ and cannot be located in either the presampler or the first layer of the electromagnetic calorimeter. The cell significance is the ratio of the energy of a given cell, E_{cell}^{EM} to the expected noise of that same cell, $\sigma_{noise,cell}^{EM}$.

$$|\zeta_{cell}^{EM}| = \frac{E_{cell}^{EM}}{\sigma_{noise,cell}^{EM}} \tag{4.3}$$

The cell significance of all the cells surrounding the seed cell is checked and the cluster grows by adding a neighbouring cell that has a cell significance $|\zeta_{cell}^{EM}| \geq 2$. This process of growth continues iteratively, with each new cell added becoming the seed cell in the following iteration. A growing cluster of cells is known as a protocluster. Two protoclusters are combined if they share a cell. Once all cells meeting the growth significance requirement have been added, there is one final round of growth, adding all neighbouring cells without a significance requirement. If the final topocluster has more than one local maxima[3] then it is split into separate topoclusters, with each new cluster centred around one maximum cell.

Only the energy of the topocluster that has been deposited in the electromagnetic calorimeter, not including any energy deposited in transition region ($1.37 < |\eta| < 1.52$), is used for electron reconstruction [88]. Energy deposited in the presampler or first layer of the electromagnetic cluster is also added to find the electromagnetic energy of the cluster. The ratio of electromagnetic energy of the cluster to the total energy of the cluster is called the EM fraction, f_{EM}. Only clusters with $f_{EM} > 0.5$ and $E^{EM} \geq 400$ MeV are considered for selecting an electromagnetic topocluster. This is criteria is used to help reject against clusters formed as a result of pile-up.

4.3.1.2 Track-to-Cluster Matching

Tracks in the inner detector are reconstructed as described in Section 4.1.2. Initially, tracks a fitted to a pion hypothesis, assuming the trajectory of the track follows a perfect

---

[3]A local maxima is defined to be a cell with $E_{cell}^{EM} > 500$ MeV with at least four neighbouring cells which do not have an energy greater than the central cell.

helical path [76]. Tracks that fail this fit are fitted again, if there is only a small separation in pseudorapidity between track and electromagnetic cluster. The new fit considers up to 30% more energy loss due to Bremsstrahlung and therefore now assumes a non-perfect helical path [88]. Then re-fitted tracks undergo an ambiguity resolution to reduce the number of tracks that share space-points and are ranked in order of track quality [76]. The fit for the final track candidates are extrapolated out to the transition radiation tracker. Electron candidates are the combination of reconstructed track matched to an electromagnetic cluster.

4.3.1.3 Superclusters

The topological clusters from the same electron are collected together to form a super-cluster, in order to account for energy deposited in the detector by Bremsstrahlung and secondary electromagnetic showers. First a seed cluster is selected by ranking all electromagnetic topoclusters in order of transverse energy. Each cluster is then checked against the following criteria [89]:

- The cluster must not already be assigned to a different supercluster

- $E_T > 1$ GeV

- The reconstructed track, matched to the electromagnetic cluster, is required to have at least four hits in either the pixel detector or the semiconductor tracker

Once a seed cluster has been selected, the supercluster is grown by adding satellite topoclusters that are within a 3×5 or 5×12 cell window (correspinding to 0.075×0.125 and 0.125×0.300 in $\Delta\eta \times \Delta\phi$, respectively) around the weighted barycentre of the seed cluster. The smaller cell accounts for energy deposited by secondary electromagnetic showers and the larger cell accounts for energy deposited by Bremsstrahlung. The supercluster is matched to tracks using the same method as described in Section 4.3.1.2. This results in a fully reconstructed electron that can be used in a physics analysis.

4.3.2 Electron Identification

The electron reconstruction process does not discriminate between reconstructed electrons from different origins, therefore a further step is needed to identify the origins of the reconstructed electron candidates. This additional step is known as electron identification and enables physics analyses to distinguish between prompt and non-prompt electrons. Where prompt electrons are produced as a direct result from the hard-scatter vertex or

from a decay of a heavy resonance such Higgs, W, Z boson decays. And non-prompt electrons emnate from semileptonic decays of heavy quarks, misidentified hadrons or from photon conversions. Signals left in the detector by background electrons originating from photon conversions or hadronic decays, can often be misidentified as prompt electrons due to interactions with the detector material initiating electromagnetic showers. The electron identification process is designed to reject electron candidates from background processes without compromising the selection of prompt electrons.

Electron identification takes a likelihood-based approach, in which a likelihood function is built from the electron candidate's properties [86]. Variables describing the reconstructed track and the longitudinal and lateral development of the electromagnetic cluster in the calorimeter system are used to determine if a candidate electron is classed as prompt or non-prompt. The likelihood approach offers an increased electron identification efficiency for the same level of background rejection as hard cuts because it is able to utilise the information contained in the tails of the discriminating variables' distributions. Further discussion of the electron identification process is given in Chapter 5.

4.3.3   Electron Efficiency

The electron efficiencies are measured using $Z \rightarrow ee$ and $J/\Psi \rightarrow ee$ events using the tag-and-probe technique [86]. $J/\Psi \rightarrow ee$ decays are used to measure the efficiencies in the low p_T range of 4.5 GeV $< p_T <$ 15 GeV whilst $Z \rightarrow ee$ events can measure the efficiencies for events up to 110 GeV. The tag-and-probe technique applies a strict selection to one of the two electrons produced when the Z or J/Ψ resonance. The first electron with the strict requirement applied is called the tag, and the second electron is known as the probe. The electron pair are required to have opposite electric charge and an invariant mass within 10 GeVof the mass of the resonance. A probe electron is regarded as a correctly reconstructed electron if the electron candidate track is within a cone of $\Delta R = \sqrt{(\Delta \eta^2 + \Delta \phi^2)} < 0.2$. The probe electrons are blended with background signals, such as photon conversions, or misidentified hadrons, and the proportion of background contamination and true electrons is estimated by fitting background and signal analytical models to the data.

The electron reconstruction efficiency is calculated with respect to the electromagnetic clusters found in the electromagnetic calorimeter. It is defined as:

$$\epsilon_{reco} = \frac{N_{reco}}{N_{cluster}} \qquad (4.4)$$

Where N_{reco} is the number of reconstructed electron candidates and $N_{cluster}$ is the number of electromagnetic candidates. The probe electrons that contribute towards

N_{reco} are electromagnetic clusters that must be associated with a track, whilst the probe electrons that contribute towards $N_{cluster}$ are electromagnetic clusters with or without associated tracks.

The electron identification efficiency is calculated with respect to the reconstructed electron candidate and is defined as:

$$\epsilon_{ID} = \frac{N_{id}}{N_{reco}}$$
(4.5)

Where N_{reco} is the number of probe electrons reconstructed from electromagnetic clusters with an associated track and N_{id} is the number of probe electrons that satisfy a particular identification criteria.

The electron efficiencies are measured separately in data and Monte Carlo. It is important for the Monte Carlo simulation to accurately reflect the electron efficiencies achieved in data, so that physics analyses can produce reliable results. Sometimes mismodelling of tracks or of electron shower shapes in the calorimeter can lead to small disagreements between data and Monte Carlo. Consequently, the electron efficiencies measured in the Monte Carlo detector simulation is corrected to match the performance of data. This is implemented in the form of a scale factor defined as the ratio of the efficiency measured in data to the efficiency measured in simulation [86].

4.3.4 Electron Isolation

Whilst the reconstruction and identification processes provide some insight into the origins of the candidate electrons, it can still be difficult to differentiate between prompt and non-prompt electrons. A better distinction between the prompt and non-prompt electrons can be made using the amount of activity recorded by the detector in an area around the electron candidate. For instance, electrons produced via non-prompt decays from c- and b-hadrons are surrounded by many more tracks and more energy deposits in the calorimeter than prompt electrons but may still be reconstructed as if they were true prompt electrons. In such a case, the electron is referred to as a misidentified or fake electron. In order to reduce the probability of this from happening requirements known as isolation requirements are placed on the number of additional tracks in the inner detector and the extra energy deposits in the calorimeter, in a region surrounding the reconstructed electron [90].

Variables are defined for both the track and calorimeter isolation requirements. They are used to calculate the amount of detector activity in a cone, with a radius of ΔR, surrounding the electron candidate. The track isolation variable, $p_T^{varcone}$, takes a variable

cone size depending on the transverse momenta, of the electrons and sums the transverse momenta of all of the tracks associated with the primary vertex that satisfy a particular track quality requirement. Consequently the sum does not include any tracks from additional proton-proton collisions. Nor does it include any[4] of the tracks associated with the reconstructed electron. The cone size is reduced for increasing values of transverse momentum. Since tracks are the trajectories of charged particles travelling through the detector, the track isolation variable does not contribute any additional information about nearby neutral particles. The calorimeter isolation variable, E_T^{cone} is the sum of the transverse energies of positive energy topological clusters calibrated to the electromagnetic scale. As for the track isolation variable, the calorimeter isolation variable does not include the candidate electron's transverse energy contribution in the sum. However, unlike for the track isolation variable, the calorimeter isolation variable does include contributions from additional proton-proton collisions, therefore these energy deposits are corrected for each individual event [86].

Most physics analyses lay out their own set of isolation requirements for electrons. The isolation requirements can make use of either one or both of the isolation variables. Strict isolation requirements, combined with the electron likelihood discriminant is an effective method for suppressing background electrons.

4.3.5   Electron Trigger

The reconstruction and identification of electrons occurs online at both the level-1 trigger and the high level trigger. The level-1 trigger is hardware-based. It makes use of signals recorded in areas $\Delta\eta \times \Delta\phi \approx 0.4 \times 0.4$ inside both the electromagnetic and the hadronic calorimeters to form regions of interest. The level-1 trigger passes events on to the high level trigger only if they pass a certain transverse energy threshold, which varies as a function of pseudorapidity. This enables the energy responses in different regions to be accounted for.

Each specific trigger menu has isolation requirements that the electron candidate must pass. Additionally, the L1 trigger can provide a veto on the hadronic leakage by failing events that have a high fraction of energy deposited in the hadronic calorimeter.

There a several stages of the electron trigger in the high level trigger which are designed to reduce the number of background electron candidates recorded. The high level trigger is software-based and makes use of fast electromagnetic calorimeter algorithms to build clusters within the regions of interest formed by the level-1 trigger. Requirements are

---

[4]The sum excludes both the primary electron track and any that might be associated due to Bremsstrahlung that were matched during the electron reconstruction stage.

placed on the amount of energy deposited in the hadronic calorimeter, the transverse energy of the cluster, the transverse momentum of the associated track and the shower shape variable, R_η [90]. The next stage builds more precise electromagnetic calorimeter clusters using methods discussed in Section 4.3.1 which are then matched to precision tracks within $|\Delta\eta| < 0.05$ and $\Delta\phi < 0.05$. A likelihood-based identification of the electron candidates is the final stage of the high level trigger. The online identification process of the high level trigger is very similar to the offline process described in Section 4.3.2 but the momentum lost due to Bremsstrahlung, $\Delta p/p$ is not included in the calculation. Once an event has passed the high level trigger, it is reconstructed offline and stored permanently.

4.3.6 Electron Energy Calibration

The electromagnetic showers produced in the electromagnetic calorimeter are used to measure the energy of reconstructed electrons and photons. The energy scale and resolution of prompt electrons plays an important role for precision measurements, therefore the electron energy scale must be calibrated accurately. The measured electron energy may need to be corrected due to lateral leakage of energy deposits outside of the cluster of cells in the calorimeter or due to longitudinal leakage caused by energy deposits occurring outside of the electromagnetic calorimeter. Instrumental effects and loss of energy before the electron passes through the calorimeter system may also contribute towards an inaccurate energy measurement. There are three main steps involved in calibrating the electron energy in the central region of the ATLAS detector ($|\eta| < 2.47$). The first involves applying a data-driven correction to the data in order to reduce the effects caused by the non-uniform response of the detector. This is used to correct the differences seen between data and simulation due to variable responses of the longitudinal layers in the electromagnetic calorimeter. The second correction is a multivariate calibration based on simulation that is applied to both Monte Carlo and data. This correction uses information from the inner detector and accounts for the energy lost between the proton-proton interaction point and the reconstructed cluster in the electromagnetic calorimeter. The final correction fine-tunes for any remaining energy scale disagreements between the Monte Carlo and data using $Z \rightarrow ee$ events [91].

The difference in response, for a given pseudorapidty region, of the energy scale between data, E_i^{data}, and Monte Carlo, E_i^{MC}, is parameterised as:

$$E_i^{data} = E_i^{MC}(1 + \alpha_i) \tag{4.6}$$

Where α_i describes the divergence from the optimal calibration for that region.
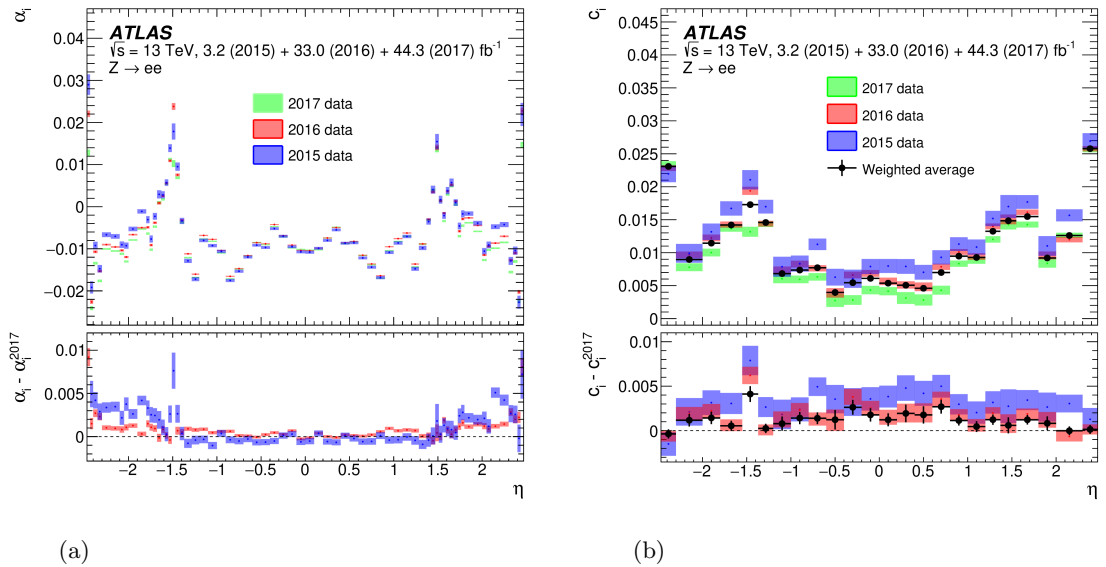
Figure 4.5: (a) The energy scale factors α_i as a function of η (b)The additional constant term c_i', as a function of η. The shaded areas indicate the statistical uncertainties [89].

The energy resolution difference between data and Monte Carlo can be described as:

$$\left(\frac{\sigma(E)}{E}\right)_i^{data} = \left(\frac{\sigma(E)}{E}\right)_i^{MC} \otimes c_i' \tag{4.7}$$

Where c_i' is an effective constant term for the given psuedorapidty region and $\otimes$ denotes the sum in quadrature.

The energy scale corrections, α_i and the additional constant terms, c_i', are estimated using $Z \to ee$ events in a template method. Figure 4.5 shows the measured values as a function of pseudorapidity for 2015, 2016 and 2017 data. There is some variation of α_i over the years due to changing temperatures of the liquid argon in the electromagnetic calorimeter and increasing instantaneous luminosity. This is reflected in measurements of c_i' and so to compensate for this, a weighted average of the c_i' values for the different years is applied to the total data set [89].

4.4 Muon Reconstruction and Identification

Muons do not interact with the detector material in the same way as electrons. Since muons are charged particles, like electrons, they do leave tracks inside the inner detector which is used to measure their transverse momentum. However, unlike electrons, they do not deposit a noticeable amount of energy in the calorimeter systems. Instead, muons leave hits inside the muon spectrometer. The muon spectrometer is formed of three

components: a central component which surrounds the outer edges of the ATLAS barrel, and a big and small wheel located at each end-cap. There is a toroidal magnetic field applied to the muon spectrometer which provides complimentary measurements of the transverse momentum. Muon reconstruction combines the information recorded by the inner detector with the that recorded by the muon spectrometer to produce precise muon measurements [92].

4.4.1 Muon Reconstruction

Muon reconstruction combines two independent reconstruction processes from the inner detector and the muon spectrometer. The tracks left by muons in the inner detector are reconstructed using the same methods as for any other charged particle (see Section 4.1.2). The process of reconstructing a muon using the muon spectrometer begins by forming track segments from hit patterns inside each muon chamber. Track segments from a single muon drift tube or cathode-strip chamber are added together and fitted to find a track candidate. The reconstructed tracks from the inner detector are then matched to those reconstructed in the muon spectrometer using a χ^2 fit. The statistical combination of both track candidates forms the muon candidate. The momentum of the muon is inferred from the curvature and coordinates of the reconstructed track. The tracks reconstructed in the inner detector and the muon spectrometer are then combined and re-fitted to ensure the muon candidate agrees across the two sub-detectors.

4.4.2 Muon Identification

To identify between a prompt and non-prompt muon[5], a series of quality requirements are placed on a candidate muon. The quality requirements aim to exploit the differences between prompt and non-prompt muons in order to reduce background signals whilst ensuring prompt muons are selected with a high efficiency. A candidate muon originating from a light charged meson, such as a kaon or a pion, is an example of a non-prompt muon. A light charged meson has a long lifetime ($\tau \sim 10^{-8}$s) and may decay into muons between leaving the inner detector and entering the muon spectrometer. As a result, the measurements of the candidate muons from the inner detector may not be compatible with measurements in the muon spectrometer, leading to a poor fit quality of the combined tracks.

---

[5]Prompt muons are produced as a direct result from the hard-scatter vertex or from a decay of a heavy resonance such Higgs, W, Z boson decays. Non-prompt muons emnate from semileptonic decays of heavy quarks or misidentified hadrons

A candidate muon is judged on the number and location of hits in the inner detector and the muon spectrometer, the track fit quality, and on the compatibility between measurements performed in the inner detector and the muon spectrometer. The following variables are used to discriminate between prompt and non-prompt muons [93]:

- q/p *significance* - This is the absolute value of the difference in the charge-to-momentum ratio of muons measured in the inner detector and the muon spectrometer.

- ρ' - This is the absolute difference between the transverse momentum measured in the inner detector and the muon spectrometer, divided by the transverse momentum of the combined track.

- χ^2 - The normalised χ^2 of the combined track fit.

The ATLAS collaboration uses four muon identification selections, based on the variables described in the previous paragraph. The four selections are intended to meet the needs of the many physics analyses in the collaboration and are known as Loose, Medium, Tight and High-p_T. The Loose selection criteria ensures muons with high quality tracks are selected and as a result maximises the reconstruction efficiency. The default muon selection is Medium as this selection aims to reduce the systematic uncertainties associated with the reconstruction and calibration of muons. The Tight requirement selects a high purity of prompt muons however this leads to some reduction on the muon reconstruction efficiency. Finally, the High-p_T selection is used to select muons with a high momentum. This selection is only used for tracks with a transverse momentum greater than 100 GeV and is mainly used by physics analyses searching for new high mass resonances.

4.4.3 Muon Efficiency

As with the electron reconstruction efficiency, the muon reconstruction efficiency makes use of the tag-and-probe technique. The efficiency is measured using samples of preselected $Z \to \mu\mu$ or $J/\Psi \to \mu\mu$ decays, which contain a high purity of prompt muons. One of the two muons, known as the tag muon, is then selected by the muon trigger and must pass the Medium requirements. The other muon acts as the probe muon and is reconstructed independently. The muon pair are required to be products of a Z of J/Ψ decay and as such, a requirement is placed on their an invariant mass. Figure 4.6 shows the muon reconstruction efficiencies are consistently high. For Tight selection the muon reconstruction efficiency is greater than 95% which increases to be around 99% for the Medium and Loose selections. There is some drop in efficiency for pseudorapidity equal to 0 since support structures and services for the detector mean there is not the space
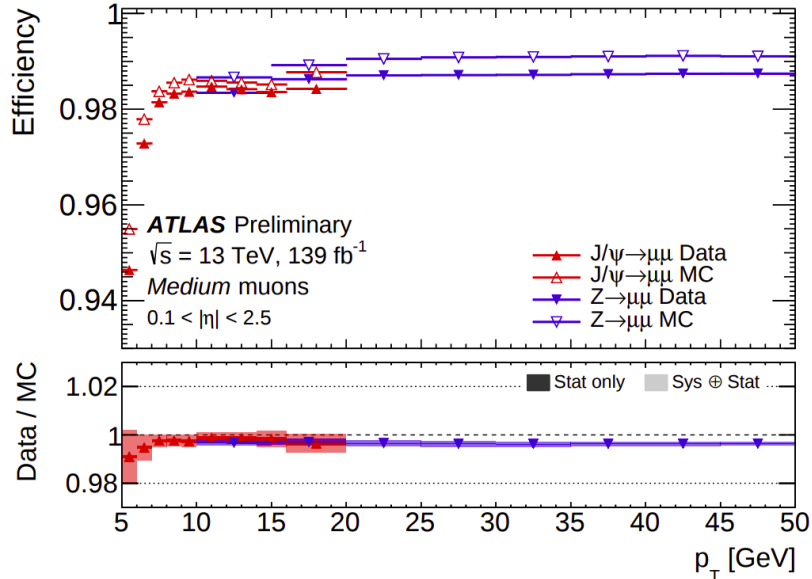
Figure 4.6: The reconstruction efficiency for muons of Medium quality as a function of p_T, in the region of $0.1 < |\eta| < 2.5$. This plot compare $Z \to \mu\mu$ and $J/\Psi \to \mu\mu$ events from both the full Run 2 data set and Monte Carlo [93].

to fully cover this region with muon chambers. An additional region with a reduced reconstruction efficiency is found in the transition region between the barrel and the end-cap $(1.37 < \eta < 1.52)$, since the muon chambers do not entirely cover this region.

The muon reconstruction efficiency is measured separately in data and in Monte Carlo and the Monte Carlo is corrected using a reconstruction efficiency scale factor. This is a necessary correction because the Monte Carlo simulation only provides an estimate of the amount of detector material traversed by a muon and hence the predicted amount of energy lost by the muon as it travels is often mismodelled. This results in the misalignment of the hit patterns inside the muon spectrometer and the tracks left in the inner detector, leading to the muon candidate being rejected at the statistical combination step. The muon scale factors are calculated for for each muon Quality in bins of pseudorapidity and transverse momentum.

4.4.4 Muon Trigger

Like electrons, the reconstruction and identification of muons occurs online at both the level-1 trigger and high level trigger. The level-1 decision is founded on information received from the calorimeters and muon trigger chambers. The level-1 muon trigger looks for muons with a high transverse momentum by looking at the muon candidate's hit pattern [94]. From the level-1 decision a region of interest, of size 0.1×0.1 in $\Delta\eta \times \Delta\phi$ in the resistive plate chambers and 0.03×0.03 in $\Delta\eta \times \Delta\phi$ in the thin gap chambers.

Each region of interest is passed on to the high level trigger and fast reconstruction algorithms are performed in the first stage. The second stage of the high level trigger is the precision stage, in which reconstruction algorithms, similar to the offline algorithms described in Section 4.7. The precision stage can be carried out in only the regions of interest defined by the level-1 trigger, or across the whole acceptance range of the detector. The first option is used most commonly as it is quicker and less CPU-intensive, but the latter option can help find additional muons not flagged by the level-1 trigger.

4.4.5 Muon Momentum and Scale Resolution

Some physics analyses require knowledge of the muon momentum scale down to the per mille level and knowledge of the muon momentum resolution down to the percent level. However, Monte Carlo does not provide the level of detail necessary, therefore a number of corrections must be applied to the momentum scale and resolution of the simulation. The corrections applied to the muon momentum and scale resolution are calculated independently and then combined together. This is because the muon reconstruction in the inner detector and the muon spectrometer is done independently. Muons traveling through the detector lose energy proportional to the amount of detector material traversed. The exact amount of material a muon traverses to reach the muon spectrometer is not known[6] and so data-driven corrections are applied to account for the energy losses associated with this. Furthermore, the momentum resolution of the reconstructed muon is influenced by a number of factors. Namely, statistical fluctuations in energy loss due to material traversed by the muon, variations of the magnetic field, multiple scattering and uncertainties related to the spatial resolution and misalignment of the muon spectrometer. The corrections are derived for different regions of pseudorapidity and transverse momentum, as the factors affecting the momentum resolution have a different dependence on transverse momentum. The muon momentum scale and resolution are measured using $J/\Psi \to \mu\mu$ and $Z \to \mu\mu$ decays [92].

4.5 Event Data Models

The ATLAS collaboration uses a system known as the Event Data Model to effectively process and analyse the recorded data and simulated Monte Carlo, without using excessive amounts of computing resources [95]

---

[6]Muons traverse the inner detector and the calorimeters with a lot of cabling which is held together with a combination of welds, solders, screws and glue. It is very difficult to understand exactly how this material is distributed and how it affects the muons travelling through the detector.
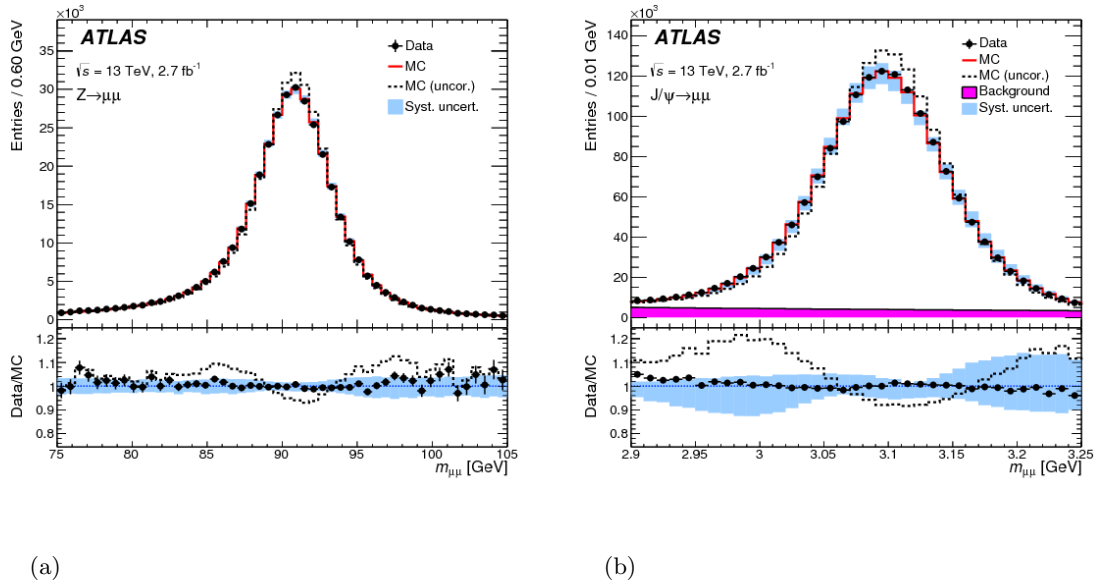
Figure 4.7: a)The dimuon invariant mass distribution of $Z \to \mu\mu$ for 2015 data and Monte Carlo. b) The dimuon invariant mass distribution of $J\Psi \to \mu\mu$ for 2015 data and Monte Carlo. In both plots, the dashed black line indicates the uncorrected Monte Carlo, the continuous red line indicates the corrected Monte Carlo and the black markers indicate the data [92].

Physics events are generated using Monte Carlo generators and are passed through a detector simulation. The detector simulation can either be a full simulation or a fast simulation depending on the needs of the physics analysis. A full simulation is performed using GEANT software and is more extensive and time consuming than a fast simulation [48]. The fast simulation still uses GEANT software to simulate the inner detector and muon spectrometer, however calorimeter systems are simulated using a parameterised calorimeter response using the ATLAS Fast II (AFII) software [96]. Once the Monte Carlo events have been passed through the detector simulation, they are known as Raw Data Objects (RDOs), and are comparable to the raw data recorded by the ATLAS detector. Both the raw data and the RDOs contain a large amount of information - approximately 1.6 Mb/event [97].

The raw data and the RDOs are sent to the CERN data centre, where they are reconstructed into physics objects and written as Event Summary Data (ESD). ESD contains detailed information about the reconstructed physics objects for all events. ESD includes information on all reconstructed hits and tracks, and energy deposits in calorimeter cells. ESD files are approximately 1500 kb/event and they are mainly used for detector and reconstruction performance studies.

The ESD files can be use to write Analysis Object Data (AOD) files, which contain higher level reconstructed objects such as electrons and muons. AOD files contain less information on the hits left in the inner detector and the energy deposited in

the calorimeters than the ESD files, as a result, the AOD files are smaller and are approximately 150 kb/event. AOD files contain enough information to conduct a physics analysis and are the data format of choice for most physics analyses. AOD files can be stored on the disk-drives of smaller computing facilities located at universities and research institutions across the world. They are easily accessible and can be used by all members of the ATLAS collaboration [98].

The size of the AOD files can be reduced further, to only contain information tailored to individual physics analyses. The reduced files are known as Derived Analysis Object Data (DAOD) and are of the order of 10 kb/event[7]. DAOD files can be processed faster than AOD files and have the advantage that they can be processed locally rather than on the CERN computing grid.

The processing of both data and Monte Carlo is performed using a framework called Athena, developed by the ATLAS collaboration [99]. Athena is used in each step of the experiment's workflow. It is used for the reconstruction of physics objects, simulation of events, and in the analysis stages. Initially, the Run 2 data set was processed with a version of Athena called Release 20.7. Then in 2017, improvements were made to both the software framework and the object reconstruction. Which resulted in a new version, called Release 21.0, that was introduced for the remainder of Run 2.

The resulting ESD, AOD or DAOD files, used in physics analyses are labelled with ATLAS Metadata Interface (AMI) tags [100]. The AMI tags are used to identify the parameters used to process each individual file. Data files are labelled with r-tags and p-tags, which catalogue the reconstruction and pile-up parameters, respectively. In addition to r-tags and p-tags, Monte Carlo files are labelled with e-tags, which catalogue the event generation parameters . Monte Carlo files are also labelled with s-tags or a-tags, which catalogue the simulation parameters. s-tags are used for GEANT full simulations and a-tags are used for AFII fast simulations. The numbers that follow the tags document the unique software configuration, such as a particular athena release.

Monte Carlo campaigns are used to reflect the data recorded throughout Run 2. A particular Monte Carlo campaign will reflect the trigger settings and pile-up conditions for a given data taking period. The first campaign is called MC16a and reflects the data recorded in 2015 and 2016. MC16a is identified with the AMI-tag r9364. Data recorded in 2017 is reflected in the MC16d campaign and is identified with r10201. Finally data recorded in 2018 is reflected in the MC16e campaign and is identified with r10724.

---

[7]The size of the DAOD file depends on the nature of the derivation.

Chapter 5

Electron Identification

This chapter will further build upon the outline of electron identification techniques, described in Chapter 4 Section 4.3.2. First, Section 5.1 will provide a more detailed description of the likelihood discriminant method, used by the ATLAS collaboration to distinguish between signal and background electrons. Then, Section 5.2 will discuss how an electron is classified as either signal or background with the help of a Bayes' classifier. Section 5.2 will also discuss the advantages and disadvantages of the current likelihood discriminant method used by the ATLAS collaboration. Finally, Section 5.3 will present a study, performed by the author, which aims to improve the rejection of background electrons. This study categorises electrons based on their origins and constructs independent likelihood discriminants for each electron category. The information from the independent likelihood discriminants is combined in order to find an optimum cut that maximises the rejection of background electrons, from each category. This study focuses on distinguishing between signal electrons and background electrons that originate from either light flavour or heavy flavour hadronic decays. Since this study uses two categories of background electrons, the optimal likelihood discriminant cut can be thought of as a two-dimensional cut and the new likelihood discriminant method is hence known as the "two-dimensional" likelihood discriminant method.

5.1   The Electron Likelihood Discriminant Method

This section will outline the method used by the ATLAS collaboration to identify electrons. The ATLAS experiment uses a likelihood discriminant to discriminate between signal electrons and electrons from background sources. The likelihood discriminant is constructed from the likelihood functions of signal and background electrons. An electron is classed as signal if it is prompt. In other words, if the electron is produced

as a direct result of the hard-scatter interaction or from a decay of a heavy resonance, such as a Higgs, W or Z boson decay. A background electron is described as non-prompt and typically originates from semi-leptonic decays, misidentified hadrons or from photon conversions. The method described in this section, will be referred to as the "nominal likelihood discriminant method", in Section 5.3.

5.1.1 Constructing Likelihood Functions

The likelihood functions are built from the probability density functions of the discriminating variables, listed in Table 5.1. Most discriminating variables make use of the detector design. For instance, the fine segmentation inside the electromagnetic calorimeter allows for the shape of an electromagnetic shower and its distribution of energy to be recorded with enough detail that small differences between showers can be resolved. The longitudinal and lateral ratios of energy deposited in each layer of the electromagnetic calorimeter and the first layer of the hadronic calorimeter, provide an insight into the development of the electromagnetic shower, and hence an indication towards the origin of the electron candidate.

The discriminating variables are measured using the tag-and-probe method (see Chapter 4 Section 4.3.3). Some of the discriminating variables have a wider distribution than the Monte Carlo, or the distribution can be shifted towards the shape of a background distribution. This is an effect of inaccuracies in the detector simulation software that leads to poor modelling of the shower shape development in the detector. To account for this, the ATLAS collaboration apply data-driven corrections to the Monte Carlo, which alter the width of the distribution or shift the distribution into agreement with the data[1]. This is done to ensure the that the operating points derived from Monte Carlo have similar performance to what is observed in data [101].

The distributions of the $d_0/\sigma(d_0)$ and f_1 variables are shown in Figure 5.1, for both data and Monte Carlo. The distributions compare data taken in 2015 with the MC16a Monte Carlo campaign, and are measured with Loose probes with $E_T < 15 >$ GeV, in order to reduce the contribution from background electrons in the data distribution. The $d_0/\sigma(d_0)$ distribution is shown in Figure 5.1(a). The number of events is underestimated by the Monte Carlo for for $d_0/\sigma(d_0) < 1$, however, the width of the distribution agrees well with the data so no data-driven corrections are applied. The distribution of the f_1 variable is shown in Figure 5.1(b). Due to inaccuracies in the modelling, the Monte Carlo distribution is shifted towards higher values of f_1, than the data. For this reason, a data-driven correction is applied to bring the modelling inline with the data. It is

---

[1]The data-driven corrections are applied to the Monte Carlo distributions of: $\Delta\eta_1$, $\Delta\phi_{res}$, f_1, f_3, R_η and $w_{\eta2}$.

Type	Description	Name	LF	γ	HF	Usage
Hadronic leakage	Ratio of E_T in the first layer of the hadronic calorimeter to E_T of the EM cluster (used over the range $|\eta| < 0.8$ or $|\eta| > 1.37$)	R_{had1}	x	x		LH
	Ratio of E_T in the hadronic calorimeter to E_T of the EM cluster (used over the range $0.8 < |\eta| < 1.37$)	R_{had}	x	x		LH
Third layer of EM calorimeter	Ratio of the energy in the third layer to the total energy in the EM calorimeter. This variable is only used for $E_\mathrm{T} < 80$ GeV, due to inefficiencies at high E_T, and is also removed from the LH for $|\eta| > 2.37$, where it is poorly modelled by the simulation.	f_3	x			LH
Second layer of EM calorimeter	Lateral shower width, $\sqrt{(\Sigma E_i \eta_i^2)/(\Sigma E_i) - ((\Sigma E_i \eta_i)/(\Sigma E_i))^2}$, where E_i is the energy and η_i is the pseudorapidity of cell i and the sum is calculated within a window of 3×5 cells	w_η	x	x		LH
	Ratio of the energy in 3×3 cells over the energy in 3×7 cells centred at the electron cluster position	R_ϕ	x	x		LH
	Ratio of the energy in 3×7 cells over the energy in 7×7 cells centred at the electron cluster position	R_η	x	x	x	LH
First layer of EM calorimeter	Shower width, $\sqrt{(\Sigma E_i(i - i_{\max})^2)/(\Sigma E_i)}$, where i runs over all strips in a window of $\Delta\eta \times \Delta\phi \approx 0.0625 \times 0.2$, corresponding typically to 20 strips in η, and $i_{\max}$ is the index of the highest-energy strip, used for $E_\mathrm{T} > 150$ GeV only	w_{stot}	x	x	x	C
	Ratio of the energy difference between the maximum energy deposit and the energy deposit in a secondary maximum in the cluster to the sum of these energies	ΔE_{ratio}	x	x		LH
	Ratio of the energy in the first layer to the total energy in the EM calorimeter	f_1	x			LH
Track conditions	Number of hits in the innermost pixel layer	n_{Blayer}		x		C
	Number of hits in the pixel detector	n_{Pixel}		x		C
	Total number of hits in the pixel and SCT detectors	n_{Si}		x		C
	Transverse impact parameter relative to the beam-line	d_0		x	x	LH
	Significance of transverse impact parameter defined as the ratio of d_0 to its uncertainty	$d_0/\sigma(d_0)$		x	x	LH
	Momentum lost by the track between the perigee and the last measurement point divided by the momentum at perigee	$\Delta p/p$	x			LH
TRT	Likelihood probability based on transition radiation in the TRT	eProbabilityHT	x			LH
Track–cluster matching	$\Delta\eta$ between the cluster position in the first layer and the extrapolated track	$\Delta_{\eta 1}$	x	x		LH
	$\Delta\phi$ between the cluster position in the second layer of the EM calorimeter and the momentum-rescaled track, extrapolated from the perigee, times the charge q	$\Delta\phi_{res}$	x	x		LH
	Ratio of the cluster energy to the track momentum, used for $E_\mathrm{T} > 150$ GeV only	E/p	x	x		C

Table 5.1: This table shows the discriminating variables used in the electron identification algorithms. The column entitled "Rejects" shows which variables are capable of rejecting electrons originating from light flavour decays(LF), electrons originating from photon conversions (γ) and electrons originating from heavy flavour decays (HF). The column entitled "Usage" indicates if a particular variable is used in the likelihood calculation (LH) or as a selection criterion (C) [86].
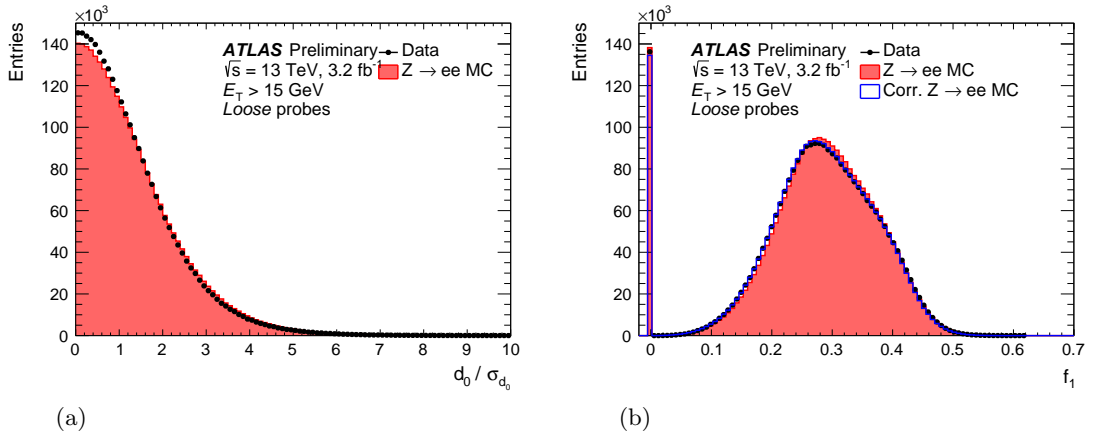
Figure 5.1: Distributions of two of the discriminating variables used in the electron identification method. The distributions are shown for data taken in 2015 and the MC16a Monte Carlo campaign. They are measured using Loose probes with $E_T > 15$ GeV in orde to reduce the background contribution in the data. a) Show the distribution of the $d_0/\sigma(d_0)$ variable. No data-driven corrections are applied to the $d_0/\sigma(d_0)$ variable. b) Shows the distribution of the f_1 variable. A data-driven correction is applied to the Monte Carlo distribution of the f_1 variable in order to account for inaccuracies in the modelling. [101]

worth noting that the f_1 variable can have negative values as a result of fluctuations due to pile-up and electronic noise leading to negative cell signals in the electromagnetic calorimeter; this is the origin of the underflow bin [87, 89].

The probability density functions are produced from the normalised distribution of each discriminating variable. Each probability density function undergoes a smoothing process to reduce the possibility of statistical limitations arising from unfilled bins or random statistical fluctuations. This is done using a non-parametric model, known as kernel density estimation smoothing. For a given discriminating variable, x, the shape of the probability density function, $f(x)$, is estimated by the sum of kernel functions, K [102]:

$$f(x) = \frac{1}{Nh} \sum_{i=1}^{N} K\left(\frac{x - x_i}{h}\right)$$ (5.1)

Where N is the number of events in the distribution, h is the bandwidth of the kernels and x_i is a set of data points. The kernel function is chosen to be a Gaussian with a nominal width of one. The width of the kernel function is increased if a region of low statistics is encountered.

The likelihood function, for either signal or background, is given by the combined product of the smoothed probability density functions constructed from each of the discriminating variables.

$$\mathcal{L}_{S(B)}(\bar{x}) = \prod_{i=1}^{n} P_{S(B),i}(x_i) \quad , \quad \bar{x} = (x_1, ...x_n)$$ (5.2)

Where $\bar{x}$ is the vector of discriminating variables for a particular electron candidate and $P_{S(B),i}(x_i)$ is the probability density for each variable, i, for either signal, S, or background, B.

5.1.2 Monte Carlo Samples

The signal probability density functions are made using simulated $Z \rightarrow ee$ events generated using a Monte Carlo sample generated with the Powheg-Box v2 [103, 104, 105, 106, 107] program and interfaced with the Pythia v.8.186 parton shower [108]. The event generation utilised the CT10 parton distribution set [109] with the matrix element. The parton showering and hadronisation was modelled using the AZNLO [110] tune and the CTEQ6L1 [111] parton distribution functions.

The background probability distributions are constructed from simulated two-to-two processes such as multijet production, $qg \rightarrow q\gamma$, $q\bar{q} \rightarrow g\gamma$, electroweak processes and top-quark production. The background samples are generated using Pythia v.8.186 with the A14 tune and the NNPDF2.3LO [112] set of parton distribution functions. A filter that enriches the background samples with electrons is applied. The filter excludes muons and neutrinos originating from the hard scatter interaction and also requires particles deposit more than 17 GeV of energy in the calorimeter, in a $\Delta\eta \times \Delta\phi = 0.1 \times 0.1$ sized region. The latter requirement ensures events selected by the filter leave highly localised energy deposits in the detector - a signature trait of electrons. Finally, the contribution from prompt electrons originating from W boson and Z boson decays, are removed using truth-level information, to increase the concentration of background electrons in the samples [86].

5.1.3 The Likelihood Discriminant

A likelihood discriminant is found for each electron candidate and is defined as:

$$d_{\mathcal{L}} = \frac{\mathcal{L}_S}{\mathcal{L}_S + \mathcal{L}_B} \tag{5.3}$$

The likelihood discriminant is the basis of the electron identification process. The discriminant, $d_{\mathcal{L}}$, is defined such that it peaks sharply at one for prompt signal electrons and at zero for background electrons. The likelihood discriminant is defined in bins of transverse energy and pseudorapidity.

The likelihood discriminant is used to define specific cuts, known as operating points, that correspond to specific purities of prompt signal electrons in a sample. The ATLAS
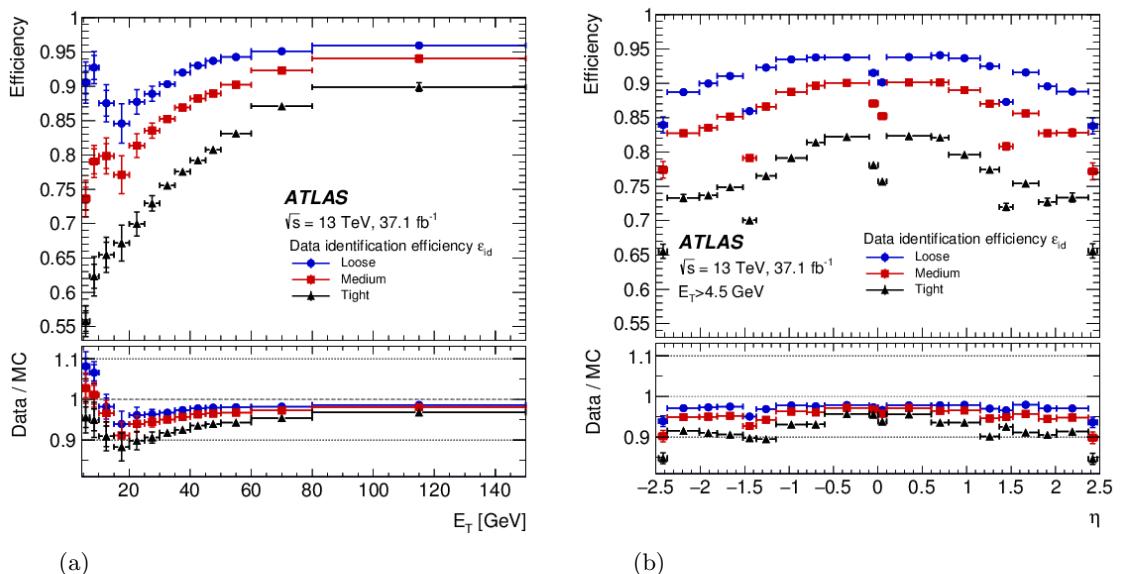
Figure 5.2: The electron identification efficiencies for each operating point measured using $Z \to ee$ events. a) shows this as a function of E_T and b) shows this as a function of $|\eta|$. The Loose operating point is shown in blue, the Medium operating point is shown in red and the Tight operating point is shown in black. The bottom panel shows the Data to Monte Carlo ratio [86].

collaboration makes use of three electron identification operating points: Loose, Medium and Tight, which broadly correspond to 80%, 90% and 95% signal efficiency, respectively[2]. Each operating point is optimised in 10 bins in pseudorapidity and 11 bins in transverse energy. Binning the likelihood discriminant in such a way, also enhances the ability to discriminate between electrons with varying characteristics. Figure 5.2 shows how the electron identification efficiencies vary across the bins for each operating point.

The likelihood discriminant typically has a sharply rising peak, which makes it impractical to select the identification operating points without applying very hard cuts. This is illustrated in Figure 5.3(a). The distribution of the likelihood discriminant is transformed logarithmically, in order to improve readability:

$$d'_{\mathcal{L}} = -\tau \ln \left(d_{\mathcal{L}}^{-1} - 1 \right) \tag{5.4}$$

where τ is a fixed parameter, and by default it is equal to 15 [102].

The transformation spreads out the distribution of discriminant making it easier to select a value of the discriminant corresponding to each operating point. The log transformed likelihood discriminant distribution is shown in Figure 5.3(b). An electron is classified as

---

[2]The target signal efficiency of each operating point varies across bins of pseudorapidity and transverse energy.
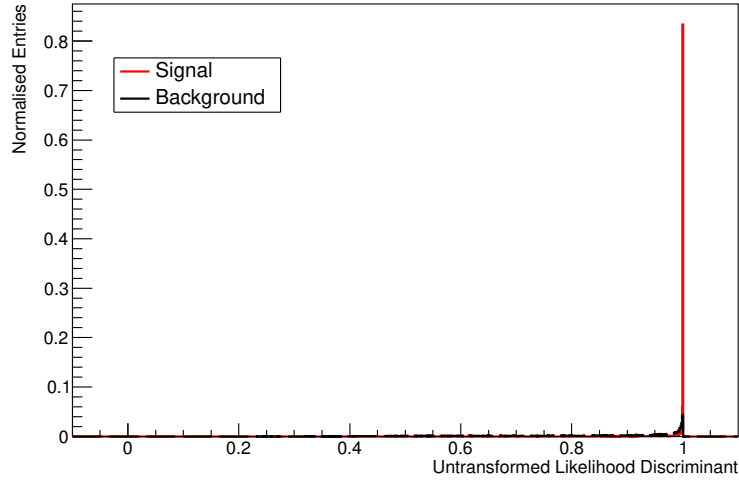
(a)
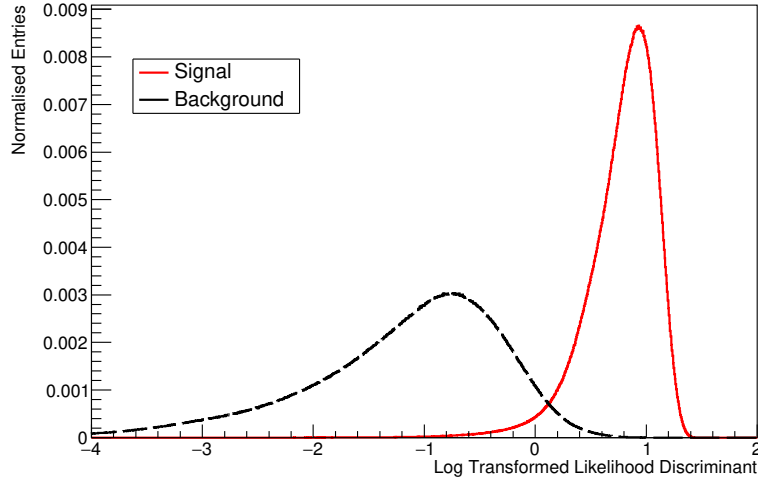
(b)

Figure 5.3: a) The untransformed likelihood discriminant distribution. b) The log transformed likelihood discriminant distribution, used for electron identification. Both plots show the simulated prompt signal electrons in red, and simulated non-prompt background electrons in black.

signal if its value of $d'_{\mathcal{L}}$ is greater than the value associated with a given operating point [86].

Both the probability density functions and the likelihood discriminant are defined in bins of pseudorapidity and transverse energy. The boundaries of the pseudorapidity bins are given in Table 5.2. The binning is chosen such that it reflects the detector geometry and acceptance, and the variable bin widths reflect changes in the detector material. The bin boundaries of transverse energy are given in Table 5.3. The binning in transverse energy is different for the probability density functions and the likelihood discriminant.

Bin Boundaries in $|\eta|$								
0.00	0.60	0.80	1.15	1.37	1.52	1.81	2.01	2.37 2.47

Table 5.2: The boundaries in pseudorapidity used to define the bins of both the probability density functions and the likelihood discriminant [86].

	Bin Boundaries in E_T [GeV]											
PDFs	4.5	7	10	15	20		30		40			∞
LH Discriminant	4.5	7	10	15	20	25	30	35	40	45	80	150 ∞

Table 5.3: The boundaries in transverse energy used to define the bins of the probability density functions (PDFs) and the likelihood discriminant (LH Discriminant) [86].

The binning for the probability density functions is chosen because the shape of the probability density functions does not change much over a ~ 10 GeV interval. On the other hand, a finer binning is required for the likelihood discriminant in order to obtain a smooth variation of electron identification efficiency, as a function of transverse energy. This is because the rate of non-prompt electrons falls very rapidly with increasing values of transverse energy, so finer binning helps to ensure a smooth distribution [86].

5.2 Classifying Electrons as Signal or Background

A Bayesian classifier is used to decide if an electron candidate is classed as signal or background. Bayes' theorem gives the probability of a hypothesis, H, given the observed data:

$$P(H|data) = \frac{P(data|H)P(H)}{P(data)} \qquad (5.5)$$

The probability of the hypothesis, $P(H)$, and the probability of the data $P(data)$ are known. The probability of the data given the hypothesis, $P(data|H)$ is the posterior probability and can be interpreted as a likelihood function [113].

Consider two hypotheses:

1. that the electron candidate is identified as signal, with a probability $P(S)$

2. that the electron candidate is identified as background, with a probability $P(B)$

In which case, Bayes' classification rule can be written as:
If $P(S|data) > P(B|data)$, then the electron candidate is classified as signal.
If $P(B|data) > P(S|data)$, then the electron candidate is classified as background.

(a)
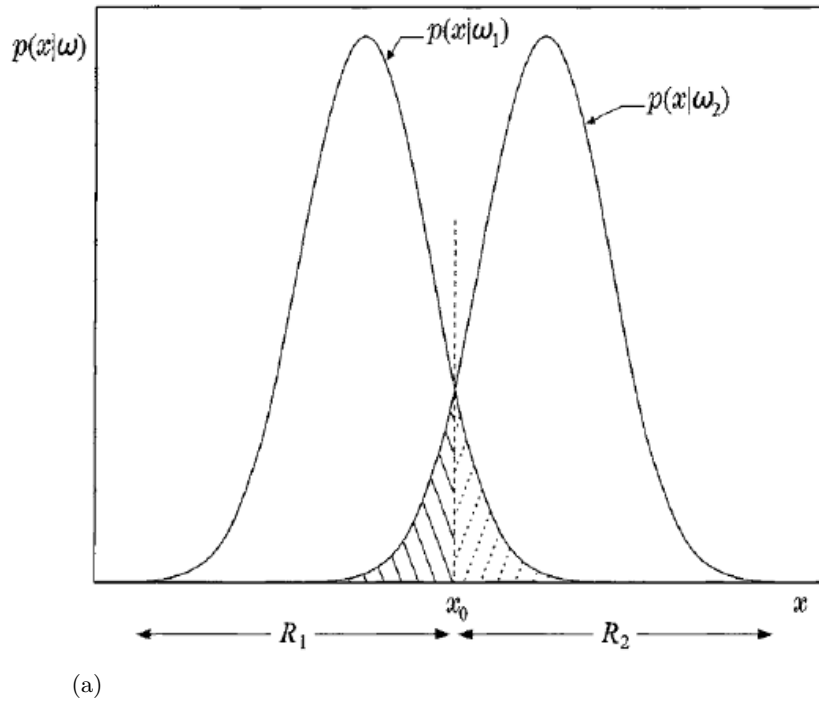
Figure 5.4: The decision boundary between two regions of equal probability, formed by the Bayesian classifier. The shaded regions indicate the decision errors associated with the Bayesian classifier [114].

Which, following the relation given in Equation 5.5, can be equivalently expressed as:
If $P(data|S)P(S) > P(data|B)P(B)$, then the electron candidate is classified as signal.
If $P(data|B)P(B) > P(data|S)P(S)$, then the electron candidate is classified as background.

Now assuming the probability of signal is equal to the probability of background, Bayes' classification rule can be simplified to statements only involving the likelihood functions:
If $P(data|S) > P(data|B)$, then the electron candidate is classified as signal.
If $P(data|B) > P(data|S)$, then the electron candidate is classified as background.

Figure 5.4 illustrates the two regions given by the Bayesian classifier if the probability of signal is equal to the probability of background. There is a an area of overlap between the two regions which exemplifies the decision errors associated with the Bayesian classifier. In the application of classifying electrons as either signal or background, this area corresponds to the probability of classing a signal electron as background or vice versa. The minimum classification error probability of the decision to classify an electron as signal is:

$$\frac{P(data|S)}{P(data|B)} > 1 \tag{5.6}$$

This is known as the Neyman-Pearson Lemma [115]. Taking the natural log of Equation 5.6 gives:

$$\ln P(data|S) - \ln P(data|B) > 0 \tag{5.7}$$

In some instances, there can be a different level of importance between the two types of classification errors. In such cases, a weight can be assigned to quantify the error associated with each decision. For example, the error associated with choosing the signal classification can be quantified by the number of candidate electrons misclassified as signal, w_S. Additionally, the error associated with choosing the background classification can be quantified by the number of electron candidates misclassified as background, w_B. Now the Bayes' classification rule can be re-written once more, to include the weights[3] associated with each type of error:

If $P(data|S)w_S > P(data|B)w_B$, then the electron candidate is classified as signal

If $P(data|B)w_B > P(data|S)w_S B$, then the electron candidate is classified as signal

Now the minimum error probability can be expressed as:

$$\frac{P(data|S)}{P(data|B)} > \frac{w_B}{w_S} \tag{5.8}$$

$$\ln P(data|S) - \ln P(data|B) > \ln \frac{w_B}{w_S} \tag{5.9}$$

A cut is placed on the likelihood discriminant at the point of the minimum error to decide if an electron candidate is classified as signal or as background.

5.2.1 Advantages and Disadvantages of the Likelihood Discriminant Method

The likelihood discriminant method used by ATLAS to identify electrons, leads to better identification efficiencies than a cut-based method because it combines information from all of the discriminating variables. For instance, a candidate electron may fail a cut-based selection due one particular variable, however the same candidate electron may be classified as signal under the likelihood discriminant method, if the combination of the discriminating variables is more signal-like than background-like. Additionally, the likelihood discriminant method allows for the use of discriminating variables with similar distributions of background and signal. For example, the f_1 variable, defined as the ratio of the energy in the first layer of the electromagnetic calorimeter to the

---

[3]The weights, w_S and w_B are numbers and are different from the probability distributions, $P(S)$ and $P(B)$ given in the second expression of the Bayes' classification rule. Under the assumption of an equal probability of signal and background, $P(S) = P(B)$, w_S and w_B play the role of *loss* functions. The optimum classification decision is found by minimising the loss functions [115]
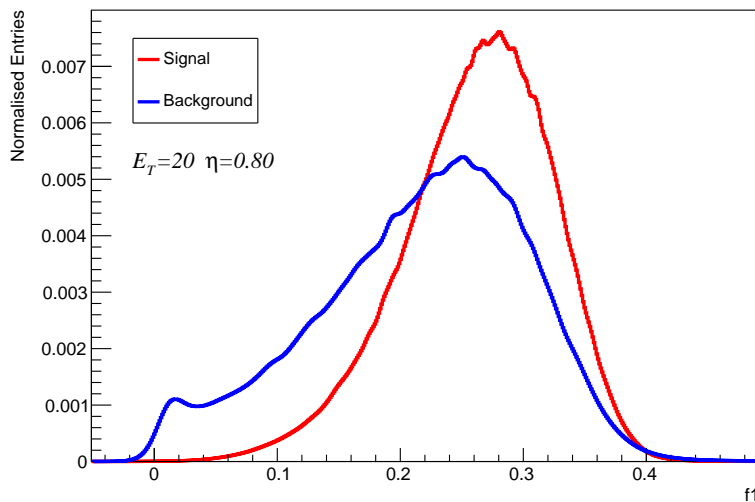
Figure 5.5: This plot shows the f_1 probability density function for $|\eta| = 0.80$ and $E_T = 20$ GeV. The distribution of prompt signal electrons is shown in red and the distribution of background electrons is shown in blue. The differences in the tails of the distribution can be used to discriminate against background electrons in the likelihood discriminant method.

total energy in the electromagnetic calorimeter, has a similar shape for both signal and background electrons. Figure 5.5 shows the distributions of signal and background for f_1. Placing a cut on this distribution will lead to a large reduction in the identification efficiency. Despite the similarities in the distributions, there are still some differences that can be used to differentiate a signal electron from a candidate electron. The likelihood discriminant method enables the information from the tails of distributions, such as f_1, to be used in the classification decision [86].

The likelihood discriminant method has advantages over an alternate cut-based method, however, it is not perfect and could be improved further. The background probability density functions used to discriminate signal from background, are constructed from Monte Carlo samples dominated by dijet events, as detailed in Section 5.1.2. This makes the likelihood discriminant method very good at rejecting against djet events but does not mean it is as effective for other sources of background electrons. In other words, the likelihood discriminant method is very effective at rejecting background electrons in physics analyses with a similar background composition as the Monte Carlo samples used to construct the likelihood. However, it is less effective in physics analyses that have a different composition of background electrons. The remainder of this chapter will present studies, performed by the author, on how the likelihood discriminant method could be improved by categorising background electrons according to their origin.

5.3 The Two-Dimensional Likelihood Discriminant Method

The two-dimensional likelihood discriminant method expands on the nominal likelihood discriminant method by categorising background electrons according to their origin, before constructing independent likelihood discriminants. The studies presented in this section focus on categorising background electrons as originating from either light flavour hadronic decays or from heavy flavour hadronic decays. The two independent likelihood discriminants are constructed for each category of background electrons, and then they are combined on a two-dimensional plane. A two-dimensional cut is found, such that the rejection of background electrons from each category, is optimised. Below, the development of this method will be described, then, Section 5.3.5 will compare the rejection achieved by the nominal likelihood discriminant method and the new two-dimensional likelihood discriminant method.

5.3.1 Classifying Electrons

Truth-level information is the information used to generate Monte Carlo events and it is used to classify electrons as either signal, background from light flavour hadronic decays, or background from heavy flavour hadronic decays. Electrons from different origins can be selected from the Monte Carlo samples using truth-level information. This ensures pure samples of signal electrons and background electron, from either light or heavy flavour hadronic decays, can be selected. The selected electrons from each category, can also be mixed to form any admixture of electrons [4], which is useful for comparing the performance of the two-dimensional likelihood discriminant method with the nominal likelihood discriminant method (see Section 5.3.5). The following definitions of the different electron categories are determined using an algorithm that classifies particles by matching truth-level tracks to reco-level tracks using hits in the inner detector.

If the truth-level information states a candidate electron is an isolated electron, then it will be classed as signal. Signal electrons are selected using the same $Z \rightarrow ee$ Monte Carlo samples used for the nominal likelihood discriminant method, as described in Section 5.1.2. The same sample of signal electrons is used for the construction of both of the new independent likelihood discriminants.

The two-dimensional likelihood discriminant method considers background electrons from two categories. The first category is background electrons originating from light flavour hadronic decays. A candidate electron is classified as a background electron originating from a light flavour hadronic decay if the truth-level information states that

---

[4]The studies presented in this thesis do not scale the admixtures of electrons to luminosity.

it originates from a hadron or it does not originally come from an isolated electron. Background electrons originating from light flavour hadronic decays are selected from the same dijet Monte Carlo sample used in the nominal likelihood discriminant method, described in Section 5.1.2. The new two-dimensional likelihood discriminant method uses the truth-level selection to ensure a pure sample of background electrons from light flavour hadronic decays is selected. However, the nominal background Monte Carlo sample has a ratio of $0.99 : 0.01$[5] of electrons originating from light flavour hadronic decays to electrons originating from heavy flavour hadronic decays, at reco-level, therefore the sample of background electrons originating from light flavour hadronic decays bares strong similarities to the background sample used in the nominal likelihood discriminant method.

The second category is background electrons originating from heavy flavour hadronic decays. A candidate electron is classified as a background electron originating from a heavy flavour hadronic decay, if the truth-level information states that it is a non-isolated electron originating from either a charm or a bottom meson. Background electrons originating from heavy flavour hadronic decays are selected using a Monte Carlo sample with a higher concentration of such electrons, than found in the nominal background Monte Carlo sample. A $t\bar{t}$ dilepton Monte Carlo sample is used to select background electrons from heavy flavour hadronic decays. The $t\bar{t}$ dilepton Monte Carlo sample has a ratio of $0.96 : 0.04$[6] of electrons originating from light flavour hadronic decays to electrons originating from heavy flavour hadronic decays, at reco-level. The truth-level selection, described above, is used to ensure a pure sample of background electrons originating from heavy flavour hadronic decays is selected.

The $t\bar{t}$ dilepton Monte Carlo sample is generated from the PowhegBox v2 [103, 104, 105, 106, 107] program interfaced with the Pythia8.230 [116] parton shower and the A14 tune [117]. The events are modelled at next-to-leading order with the NNPDF3.0NLO [112] set of parton distribution functions.

Only Monte Carlo samples from the MC16e campaign are used in the the studies of the two-dimensional likelihood discriminant. Appendix A lists all Monte Carlo used in this study in detail.

Additionally, the two-dimensional likelihood discriminant method makes use of slimmed DAODs[7] that correspond to the 2018 data taking period. The nominal signal and background Monte Carlo samples, given in Section 5.1.2, and the $t\bar{t}$ dilepton background sample enriched in heavy flavour hadronic decays, are slimmed so that they only contain

---

[5]This ratio is integrated over all bins of E_T and η.

[6]This ratio is also integrated over all bins of E_T and η.

[7]DAOD stands for *Derived Analysis Object Data*. It is the final data format of Monte Carlo samples used in most physics analyses at the ATLAS experiment

the bare information needed to construct the likelihoods. Using slimmed Monte Carlo samples reduces both the size of the samples and the time taken to produce the likelihoods. This enabled the likelihoods to be produced locally rather than on CERN's computing grid.

5.3.2 Differences in the Likelihood Discriminant Distribution

The probability distributions for the discriminating variables differ for each category of electrons. Figure 5.6 shows the probability density functions of the $d_0/\sigma(d_0)$ and R_η variables for the three categories of electrons. The different shapes of the discriminating variables are reflected in the likelihood discriminant for each category of electrons. The $d_0/\sigma(d_0)$ variable is good at distinguishing background electrons from heavy flavour hadronic decays from other sources of electrons. Conversely, the R_η variable is good at differentiating background electrons from light flavour hadronic decays and other categories of electrons.

Figure 5.7 shows the normalised distribution of the nominal likelihood discriminant, integrated over all bins of pseudorapidity and transverse energy, for the three categories of electrons. The distribution of the likelihood discriminant for background electrons originating from heavy flavour hadronic decays lies between the distributions of signal electrons and electrons originating from light flavour decays. The overlap between the distribution of signal electrons and electrons originating from heavy flavour hadronic decays is greater than the overlap between the distribution of signal electrons and electrons originating from light flavour hadronic decays. The nominal dijet Monte Carlo sample, used to construct the nominal likelihood discriminant, has a higher fraction of background electrons from light flavour hadronic decays than background electrons from heavy flavour hadronic decays. Consequently, the nominal likelihood discriminant is not very good at discriminating against background electrons from heavy flavour hadronic decays. Therefore, a likelihood discriminant cut, optimised for the nominal dijet background, can misclassify background electrons originating from heavy flavour hadronic decays as signal.

Table 5.4 shows the optimum likelihood discriminant cuts of the nominal method, obtained from the Neyman-Pearson Lemma. Also included in the table are the efficiencies of each category of electrons for each electron identification operating point. The efficiencies of background electrons originating from heavy flavour hadronic decays are considerably higher than than the efficiencies of background electrons originating from light flavour hadronic decays. As a result, there is a sizeable number of background electrons from heavy flavour hadronic decays passing the likelihood discriminant cut and being classed
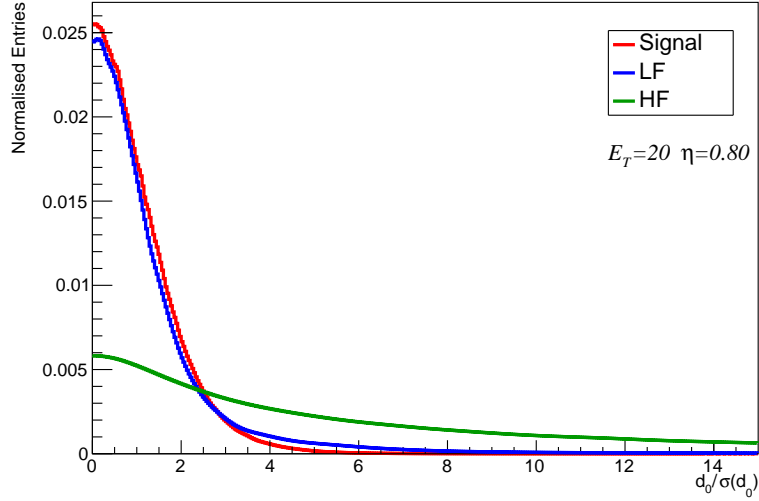
(a)
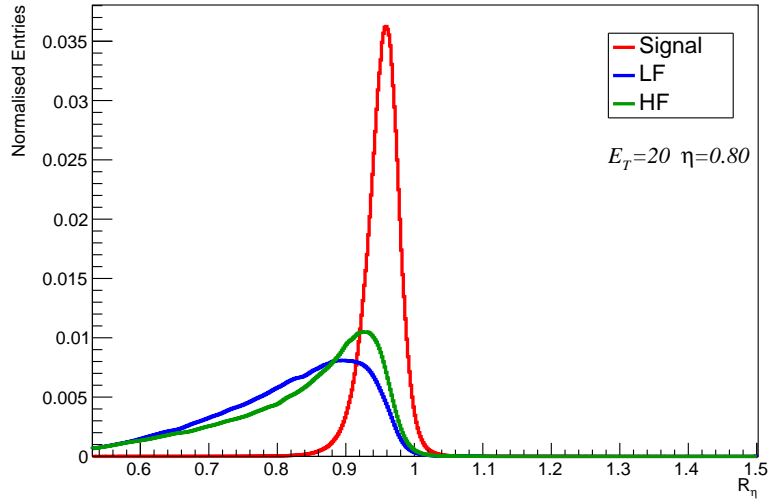
(b)

Figure 5.6: The probability density functions of a) $d_0/\sigma(d_0)$ and b) R_η for $|\eta| = 0.80$ and $E_T = 20$ GeV. The distribution of signal electrons (Signal), selected from a $Z \rightarrow ee$ Monte Carlo sample, is shown in red. The distribution of background electrons originating from light flavour hadronic decays (LF), selected from the dijet Monte Carlo sample, is shown in blue. The distribution of background electrons originating from heavy flavour hadronic decays (HF), selected from a $t\bar{t}$ Monte Carlo sample, is shown in green.

Nominal Likelihood Discriminant

Figure 5.7: This plot shows the normalised distribution of the nominal likelihood discriminant, integrated over all bins of $|\eta|$ and E_T. The distribution of signal electrons (Signal), selected from a $Z \to ee$ Monte Carlo sample, is shown in red. The distribution of background electrons originating from light flavour hadronic decays (LF), selected from the dijet Monte Carlo sample, is shown in blue. The distribution of background electrons originating from heavy flavour hadronic decays (HF), selected from a $t\bar{t}$ Monte Carlo sample, is shown in green. The HF distribution lies between the LF and Signal distributions which means some background electrons originating from heavy flavour hadronic decays will be classified as signal under the nominal likelihood discriminant method.

Operating Point	Efficiency [%]			Discriminant Cut
	Signal	LF	HF	
Loose	95.0	2.0	23.0	0.18
Medium	90.0	0.7	13.2	0.38
Tight	80.0	0.2	6.1	0.56

Table 5.4: The optimal likelihood discriminant cuts of the nominal method, integrated over all $|\eta|$ and E_T bins, at each electron ID operating point and their corresponding efficiencies for each category of electrons: signal , background electrons from light flavour hadronic decays (LF), and background electrons from heavy flavour hadronic decays (HF).

as signal electrons. Therefore the likelihood discriminant cuts cannot be considered optimal for cases with a higher fraction of background electrons originating from heavy flavour hadronic decays, than in the nominal background sample.

5.3.3 Constructing the Two-Dimensional Likelihood Discriminant

The two-dimensional likelihood discriminant method begins by constructing two independent likelihood discriminants - one constructed using a background sample of electrons originating from light flavour hadronic decays, known as the "light flavour likelihood

discriminant". The other is constructed using a background sample of electrons originating from heavy flavour hadronic decays, and is known as the "heavy flavour likelihood discriminant". The two new likelihood discriminants are constructed using the same method as the nominal, see Section 5.1. However, the data-driven corrections, mentioned in Section 5.1.1, are not applied in this study. Each likelihood discriminant is built using the same discriminating variables as used in the nominal likelihood discriminant method, see Table 5.1. Additionally, both of the new likelihood discriminants are constructed using the same signal likelihood function as used in the nominal method. However, the background likelihood function is replaced by the likelihood function of background electrons from either light flavour or heavy flavour hadronic decays. As such, Equation 5.3 can be re-written as:

$$d_{\mathcal{L}_{LF(HF)}} = \frac{\mathcal{L}_S}{\mathcal{L}_S + \mathcal{L}_{LF(HF)}} \tag{5.10}$$

Both the light flavour likelihood discriminant and the heavy flavour likelihood discriminant undergo the logarithmic transformation used in the nominal likelihood discriminant method, see Equation 5.4.

Figure 5.8(a) shows the normalised distribution of the light flavour likelihood discriminant, integrated over all bins of of pseudorapidity and transverse energy. This distribution is shown for: signal electrons, selected from a $Z \rightarrow ee$ Monte Carlo sample, in red, background electrons originating from light flavour hadronic decays, selected from the dijet Monte Carlo sample, in blue, and for background electrons originating from heavy flavour hadronic decays, selected from a $t\bar{t}$ Monte Carlo sample, in green[8]. Figure 5.8(b) shows the normalised distributions of the heavy flavour likelihood discriminant, integrated over all bins of of pseudorapidity and transverse energy, for the same categories of electrons. The light flavour likelihood discriminant, shown in Figure 5.8(a), shows a strong resemblance to the nominal distributions shown in Figure 5.7. This is because the nominal likelihood discriminant is constructed with a background sample that contains a high concentration of background electrons originating from light flavour hadronic decays, therefore there are strong similarities between the nominal likelihood discriminant and the light flavour likelihood discriminant. The heavy flavour likelihood discriminant, shown in Figure 5.8(b), provides a better discrimination between signal electrons and background electrons originating from heavy flavour hadronic decays, than is achieved by the nominal likelihood discriminant, in Figure 5.7.

---

[8]The full truth-level selection for each category of electrons is given in Section 5.3.1.

Light Flavour Likelihood Discriminant

(a)

Heavy Flavour Likelihood Discriminant

(b)
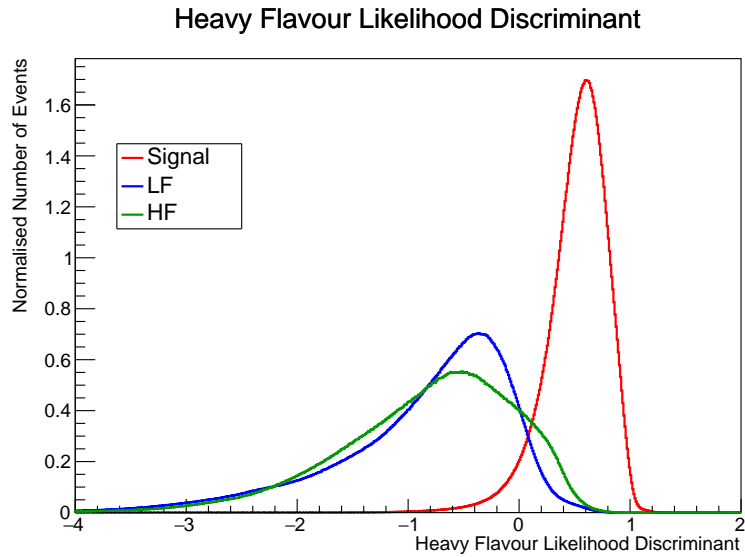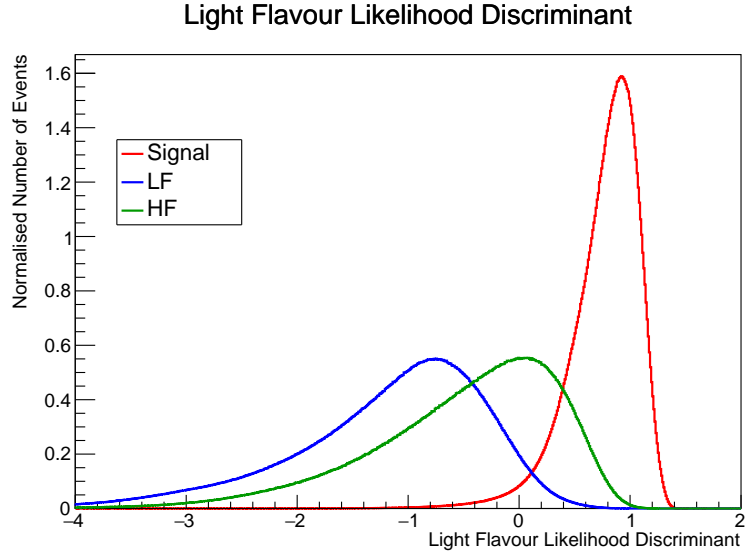
Figure 5.8: The normalised distribution of the two new likelihood discriminants, integrated over all bins of $|\eta|$ and E_T. The distribution of signal electrons (Signal), selected from a $Z \rightarrow ee$ Monte Carlo sample, is shown in red. The distribution of background electrons originating from light flavour hadronic decays (LF), selected from the dijet Monte Carlo sample, is shown in blue. The distribution of background electrons originating from heavy flavour hadronic decays (HF), selected from 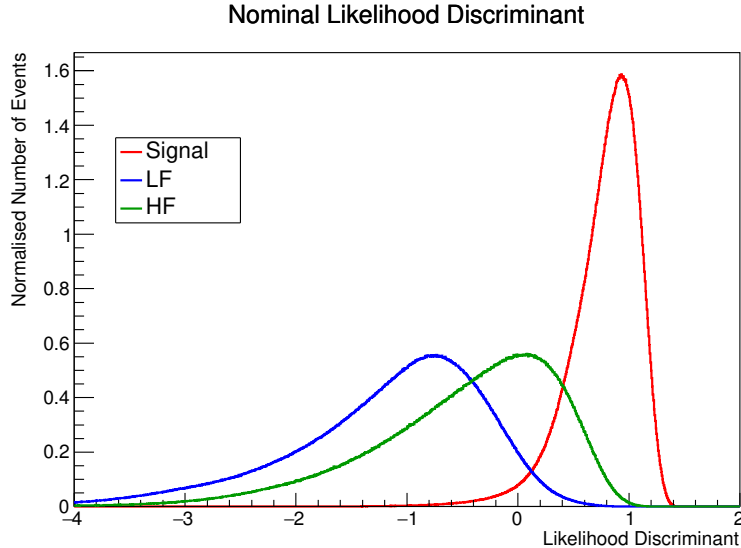a $t\bar{t}$ Monte Carlo sample, is shown in green. a) Shows the light flavour likelihood discriminant and b) Shows the heavy flavour likelihood discriminant.

Using the Neyman-Pearson Lemma, given in Equation 5.9, an optimal cut can be defined for both the light flavour and the heavy flavour likelihood discriminants:

$$\ln P(data|S) - \ln P(data|LF) > \ln \frac{w_{LF}}{w_S} \qquad (5.11)$$

$$\ln P(data|S) - \ln P(data|HF) > \ln \frac{w_{HF}}{w_S} \qquad (5.12)$$

Where LF and HF correspond to background electrons originating from light flavour and heavy flavour hadronic decays, respectively. And w_S, w_{LF} and w_{HF} correspond to the classification error associated with each category.

The optimum cuts are shown for both the light flavour likelihood discriminant, and the heavy flavour likelihood discriminant, integrated over all pseudorapidity and transverse energy bins in the top and middle parts of Table 5.5. Also shown are the efficiencies of each category of electrons at the given identification operating point. The light flavour likelihood discriminant has very similar efficiencies of each electron category as the nominal likelihood discriminant (see Table 5.4). The heavy flavour likelihood discriminant offers a reduced efficiency, and thus an increased rejection, of background electrons originating from heavy flavour decays when compared to the nominal likelihood discriminant. Although, there is a reduction of electrons originating from heavy flavour hadronic decays being classed as signal, there is an increase of the number of electrons originating from light flavour hadronic decays passing the discriminant cut. The overall effectiveness of the discriminant cut depends on the composition of the background sample. For a background sample with a high proportion of electrons from heavy flavour hadronic decays, it is more important to be effective at discriminating against background electrons from heavy flavour hadronic decays than background electrons from light flavour hadronic decays.

A more thorough way to decide if a candidate electron can be classified as signal is to ensure both of the inequalities, given in Equations 5.11 and 5.12, are satisfied. Now a two-dimensional likelihood discriminant can be constructed by considering a plane with the light flavour likelihood discriminant along one axis and the heavy flavour likelihood discriminant along the other. Figure 5.9 shows the two-dimensional distribution of the heavy flavour likelihood discriminant against the light flavour likelihood discriminant, integrated over all bins of pseudorapidity and transverse energy. The two-dimensional distribution of signal electrons, selected from $Z \rightarrow ee$ Monte Carlo samples is shown in red, and the two-dimensional distribution of background electrons originating from light flavour hadronic decays, selected from a dijet Monte Carlo sample, is shown in blue. The green distribution is the two-dimensional distribution of background electrons from heavy flavour hadronic decays, selected from a $t\bar{t}$ Monte Carlo sample. There is

Operating Point	Efficiency [%]			Discriminant Cut	
	Signal	LF	HF	LFLH	HFLH
Light Flavour Likelihood Discriminant Cut					
Loose	95.0	2.0	22.9	0.17	-
Medium	90.0	0.7	13.3	0.36	-
Tight	80.0	0.2	5.9	0.55	-
Heavy Flavour Likelihood Discriminant Cut					
Loose	95.0	8.2	13.9	-	0.01
Medium	90.0	3.2	7.7	-	0.17
Tight	80.0	1.2	3.2	-	0.33
Optimal Two-Dimensional Likelihood Discriminant Cut					
Loose	95.0	1.4	14.1	0.19	-0.13
Medium	90.0	0.6	9.0	0.35	-0.05
Tight	80.0	0.1	4.4	0.55	0.09

Table 5.5: The top and middle parts of this table show the optimal cuts placed on the light flavour and heavy flavour likelihood discriminants, integrated over all $|\eta|$ and E_T bins. The bottom part of this table shows the optimal two-dimensional discriminant cuts placed on both the light flavour and heavy flavour likelihood discriminants, integrated over all $|\eta|$ and E_T bins. The corresponding efficiency is shown for each operating point for each category of electrons (Signal, LF and HF). It is assumed that the fraction of background electrons from light flavour hadronic decays to background electrons from heavy flavour hadronic decays is the same as the nominal background Monte Carlo sample (0.99 : 0.01).

some overlap between the three regions, but the separation is good enough to distinguish between each category.

If only the inequalities, given in Equations 5.11 and 5.12, are considered to make the classification decision, then there are an infinite number of combinations of cuts on the light flavour and heavy flavour likelihood discriminants, for a given signal efficiency. The optimal two-dimensional likelihood discriminant cut can be found by altering the Neyman-Pearson Lemma to also include information on the composition of the background sample.

5.3.4 The Optimisation of Cuts Placed on the Two-Dimensional Likelihood Discriminant

Starting from first principles, the total probability is given by the sum of the probability of a signal electron and the probability of a background electron:

$$P(Tot) = P(S) + P(B) \tag{5.13}$$
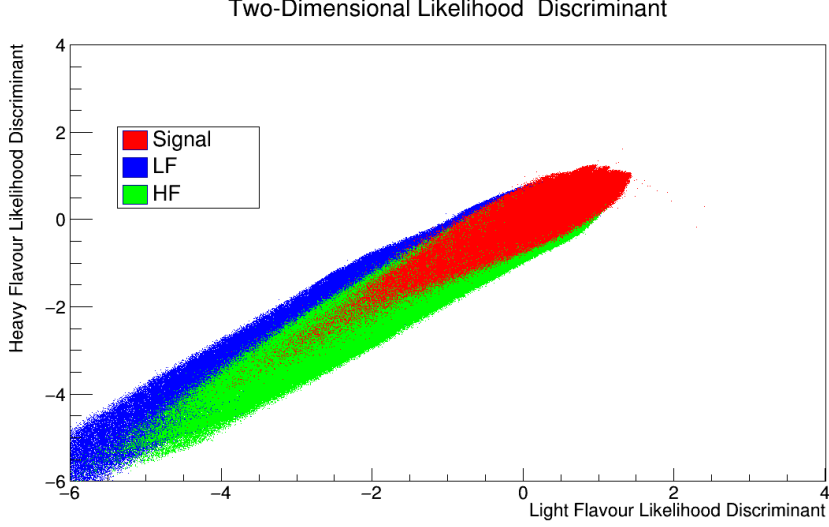
Figure 5.9: This plot shows the two-dimensional likelihood discriminant, integrated over all bins of $|\eta|$ and E_T. The distribution of the heavy flavour likelihood discriminant is plotted against the distribution of the light flavour likelihood discriminant. The distribution of signal electrons (Signal), selected from a $Z \to ee$ Monte Carlo sample, is shown in red. The distribution of background electrons originating from light flavour hadronic decays (LF), selected from the dijet Monte Carlo sample, is shown in blue. The distribution of background electrons originating from heavy flavour hadronic decays (HF), selected from a $t\bar{t}$ Monte Carlo sample, is shown in green.

Using the fraction of signal electrons, f_S, the probability of a signal electron can be written as:

$$P(S) = f_S P(Tot) \tag{5.14}$$

If $f_S + f_B = 1$, then it follows that the probability of background can be written as:

$$P(B) = (1 - f_s)P(Tot) \tag{5.15}$$

If the fraction of background electrons originating from light flavour hadronic decays, f_{LF}, and the fraction of background electrons originating from heavy flavour hadronic decays, f_{HF}, are known, then the probability of a background electron can be given as:

$$P(B) = f_{LF}P(LF) + f_{HF}P(HF) \tag{5.16}$$

Now, Equations 5.11 and 5.12 can be re-written in terms of the fraction of signal electrons, f_S, and the fraction of background electrons from light flavour or heavy flavour hadronic decays, f_{LF} and f_{HF}:

$$\ln P(data|S) - \ln P(data|LF) > \ln\left(\frac{(1 - f_S) \cdot f_{LF}}{f_s}\right) \tag{5.17}$$

$$\ln P(data|S) - \ln P(data|HF) > \ln\left(\frac{(1 - f_S) \cdot f_{HF}}{f_s}\right) \tag{5.18}$$

81
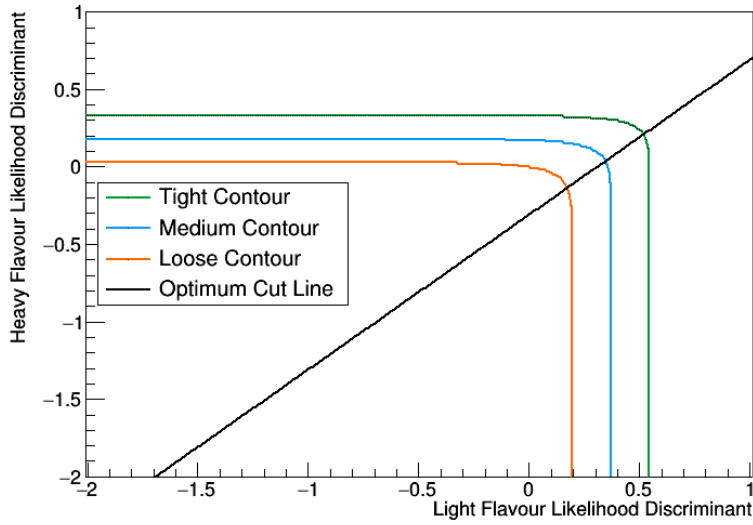
Figure 5.10: Three contour lines are shown on the two dimensional likelihood plane, for the Tight (green), Medium (blue) and Loose (orange) operating points. The straight line (black) shows the relationship between the cut on the light flavour likelihood discriminant and the cut on the heavy flavour likelihood discriminant for the nominal background Monte Carlo sample, which has a ratio of 0.99 : 0.01 of background electrons from light flavour decays to background electrons from heavy flavour decays. The optimal likelihood discriminant cuts for each operating point are taken at the point of intercept between the straight line and the corresponding contour line.

Equations 5.17 and 5.18 can be equated to eliminate f_S [114]. Now the discriminant cut on the light flavour likelihood discriminant and the heavy flavour likelihood discriminant can be related in terms of the fractions of background electrons from light flavour and heavy flavour hadronic decays, f_{LF} and f_{HF}:

$$\text{Cut}_{HF} = \text{Cut}_{LF} - \ln\left(\frac{f_{LF}}{f_{HF}}\right) \tag{5.19}$$

The cut of the heavy flavour likelihood discriminant is dependent on the cut on the light flavour likelihood discriminant, for a sample with a known composition of background electrons. Equation 5.19 can be thought of as a straight line, on the two-dimensional likelihood plane, with an intercept on the axis of the heavy flavour likelihood discriminant, equal to $\ln\frac{f_{LF}}{f_{HF}}$.

A contour of constant signal efficiency can be drawn on the two-dimensional likelihood discriminant plane. The optimal likelihood discriminant cuts are given by the coordinates of the intercept between the straight line, given in Equation 5.19, and the contour of constant signal efficiency. In practice, the optimal two-dimensional likelihood discriminant cut is found using an interpolation method to find the point of intercept between the straight line and contour. Choosing the cuts on the likelihood discriminants in this way ensures the maximum rejection of background electrons, for a given ratio of electrons

originating from light flavour to heavy flavour hadronic decays. Figure 5.10 shows the contours of the Loose, Medium and Tight operating points along with the straight line, from Equation 5.19, for the nominal background Monte Carlo sample, integrated over all bins of pseudorapidity and transverse energy. The nominal background Monte Carlo sample is made up of 99% electrons from light flavour hadronic decays and 1% electrons from heavy flavour hadronic decays. The optimal two-dimensional likelihood discriminant cuts, for each operating point are shown in the bottom part of Table 5.5. Also shown are the corresponding efficiencies for each category of electrons. The efficiencies of both categories of background electrons are smaller than those given by the nominal likelihood discriminant method in Table 5.4 for all operating points. This indicates that the two-dimensional likelihood discriminant method can improve rejection against background electrons. This will be further explored in Section 5.3.5, where the performance of the two-dimensional likelihood discriminant method will be compared to the nominal likelihood discriminant method in bins of pseudorapidity and transverse energy.

5.3.5 Comparisons to the Nominal Likelihood Discriminant Method

The two-dimensional likelihood discriminant method can be compared to the nominal likelihood discriminant method in bins of pseudorapidity and transverse energy. This study follows the binning defined in Tables 5.2 and 5.3, although the highest bins of transverse energy are excluded from the study. This is because some discriminating variables are less effective at distinguishing between signal and background electrons at high energies [86]. Consequently, the list of discriminating variables included in the likelihood is altered for bins of high transverse energy and the workflow of the two-dimensional likelihood discriminant method must be repeated. Since this increases the time taken to run the study for minimal knowledge gain, this study will focus on $E_T < 80$ GeV.

This study compares the level of rejection of background electrons achieved by the nominal likelihood discriminant method and the two-dimensional likelihood discriminant method - where rejection is defined as the inverse of the efficiency - for each of the electron identification operating points. The operating points, listed in Section 5.1.3 give the overall signal efficiencies for all bins of pseudorapidity and transverse energy. However, in practice the signal efficiency varies across the different bins, which is accounted for in this study.

First, the nominal likelihood discriminant cut is found for each electron identification operating point and then the rejection for each category of background electron is calculated. This is done by finding the point on the nominal likelihood discriminant distribution

of signal electrons that yields the desired signal efficiency, for the particular bin of pseudorapidity and transverse energy. Next, the optimal two-dimensional discriminant cut is found for each electron identification operating point and the rejection, R, for each category of background electron is calculated. The optimal two-dimensional likelihood discriminant cut is found for each bin of pseudorapidity and transverse energy using an interpolation method to find the intercept between straight line and constant signal efficiency contour (see Section 5.3.4). The achieved signal efficiency for each bin is held constant across the two methods. The percentage difference between the rejection achieved by the nominal likelihood discriminant method and the new two-dimensional likelihood discriminant method is calculated using the following equation:

$$\%\text{Diff} = \frac{R_{2D} - R_{nom}}{R_{nom}} \times 100 \tag{5.20}$$

Where R_{2D} is the rejection achieved by the new two-dimensional likelihood discriminant method and R_{nom} is the rejection achieved by the nominal likelihood discriminant method.

The percentage difference is calculated for each category of background electron, in each bin of pseudorapidity and transverse energy. The statistical error for the efficiency is calculated using Equation 5.21 [115]:

$$\sigma[\epsilon] = \sqrt{\frac{\epsilon \times (1 - \epsilon)}{N}} \tag{5.21}$$

Where ϵ is the efficiency and N is the total number of events.

Care has to be taken when comparing the rejection achieved by the nominal likelihood discriminant method and the rejection obtained with the new two-dimensional likelihood discriminant method. Both values of rejection are calculated using the same Monte Carlo sample and therefore the associated uncertainties are highly correlated. A simplification is used in the calculation of the statistical uncertainty in order to provide an estimate of the size of the statistical component, but without having to explicitly calculate correlations or track single events. The statistical error associated with the rejection is derived using Gaussian error propagation, making use of the fact that rejection is defined as the inverse of efficiency. This technique only uses the statistical uncertainty of the nominal rejection and the statistical uncertainty on the new rejection is set to zero. Therefore, this method only provides an estimate of the size of the uncertainty on the percentage difference figure.

Comparisons to the nominal likelihood discriminant method are performed for different relative fractions of background electrons. First, the achieved signal efficiency, measured using the $Z \rightarrow ee$ Monte Carlo samples, will be compared between the two methods.

Followed by a comparison between the rejection of background electron from light and heavy flavour hadronic decays.

A like-for-like comparison is performed between the nominal likelihood discriminant method and the two-dimensional likelihood discriminant method, assuming the same ratio of background electrons from light flavour hadronic decays to background electrons from heavy flavour hadronic decays, as found in the nominal background Monte Carlo sample. This ratio is 0.99 : 0.01 electrons from light hadronic decays to electrons from heavy flavour hadronic decays, therefore the optimum two-dimensional cut is found by substituting $f_{LF} = 0.99$ and $f_{HF} = 0.01$ into Equation 5.19 and finding the intercept across a contour of constant efficiency. Then, the comparison is performed for two additional reference points. The first of which, compares the nominal likelihood discriminant method to the two-dimensional likelihood discriminant method assuming the same ratio of background electrons from light flavour and heavy flavour hadronic decays as found in the $t\bar{t}$ dilepton Monte Carlo sample, used to derive the heavy flavour likelihood discriminant. This corresponds to an admixture of 0.96 : 0.04 of background electrons from light flavour hadronic decays to background electrons from heavy flavour hadronic decays. Thus, the optimum two-dimensional discriminant cut for this reference point, is found by substituting $f_{LF} = 0.96$ and $f_{HF} = 0.04$ into Equation 5.19 and finding the intercept across a contour of constant efficiency. The second reference point compares the nominal likelihood discriminant method to the two-dimensional likelihood discriminant method for an admixture that has equal proportions of background electrons from light flavour and heavy flavour hadronic decays. As for the previous two comparisons, the optimum two-dimensional cut is found by substituting $f_{LF} = 0.50$ and $f_{HF} = 0.50$ into Equation 5.19 and finding the intercept across a contour of constant efficiency.

For each comparison study, the change in rejection of background electrons from light flavour hadronic decays is measured using the nominal dijet Monte Carlo background sample (see Section 5.1.2), and the change in rejection of background electrons from heavy flavour hadronic decays is measured using the $t\bar{t}$ dilepton Monte Carlo sample (see Section 5.3.1). A detailed list of the Monte Carlo samples used in this study is given in Appendix A.

5.3.5.1   Results for 0.99:0.01 Admixture

A comparison between the signal efficiency achieved by the two methods is shown in bins of pseudorapidity and transverse energy in Figure 5.11, for the Tight operating point. The absolute value of the signal efficiency achieved by the new two-dimensional likelihood discriminant method is required to be within ± 0.01 of the nominal signal efficiency.

Comparison of Z→ ee Efficiency
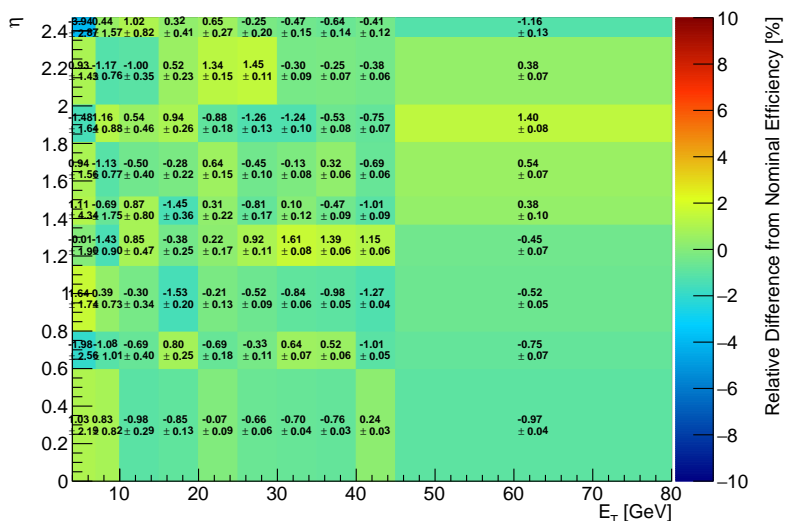
Figure 5.11: The relative difference in efficiency of signal electrons, measured in $Z \to ee$ events, as calculated by the nominal likelihood discriminant method and the two-dimensional likelihood discriminant method, for each $|\eta| - E_T$ bin at the Tight operating point. The fraction of background electrons from light flavour hadronic decays to heavy flavour hadronic decays is assumed to be 0.99:0.01.

Figure 5.11 shows the relative change across the bins of pseudorapidity and transverse energy. There are some small fluctuations which arise as a result of the interpolation method used to find optimum two-dimensional likelihood discriminant cut and due to the relative size of the nominal target efficiency of the Tight operating point varying across the bins. However, generally speaking, the signal efficiency is constant between the two methods.

Figure 5.12 shows a comparison of the rejection of background electrons achieved by the two likelihood discriminant methods. Figure 5.12(a) shows the relative difference in rejection of background electrons originating from heavy flavour hadronic decays. It illustrates that there is a large increase in rejection, particularly in the barrel region of the ATLAS detector ($|\eta| < 1.37$). The improvement is not as stark in the transition region of the ATLAS detector ($1.37 < |\eta| < 1.52$), but this is not unexpected, as performance is typically lower in this region due to large amounts of inactive material in this region [86].

Figure 5.12(b) shows that the relative difference in rejection of background electrons originating from light flavour hadronic decays remains broadly constant, when considering the statistical uncertainties, for bins with a transverse energy, $E_T > 25$ GeV. For bins of low transverse energy, $E_T < 25$ GeV, there is an improvement in the rejection of background electrons from light flavour hadronic decays. This improvement can be
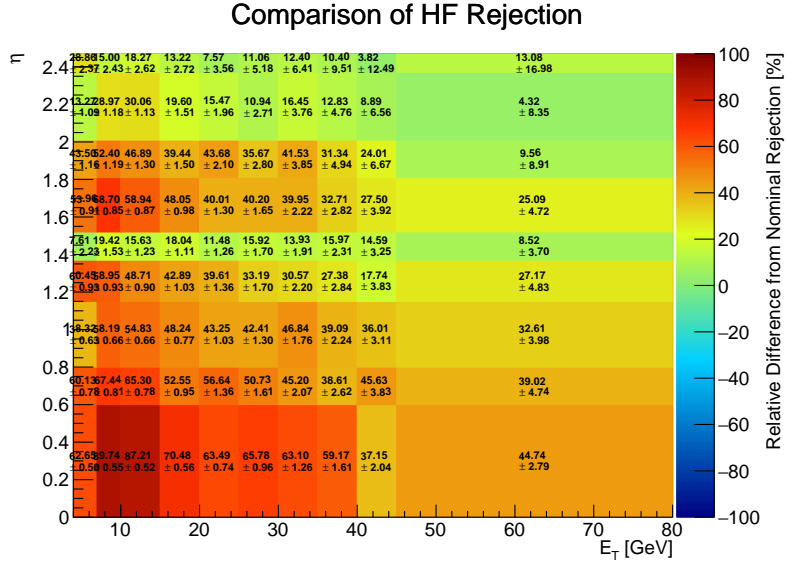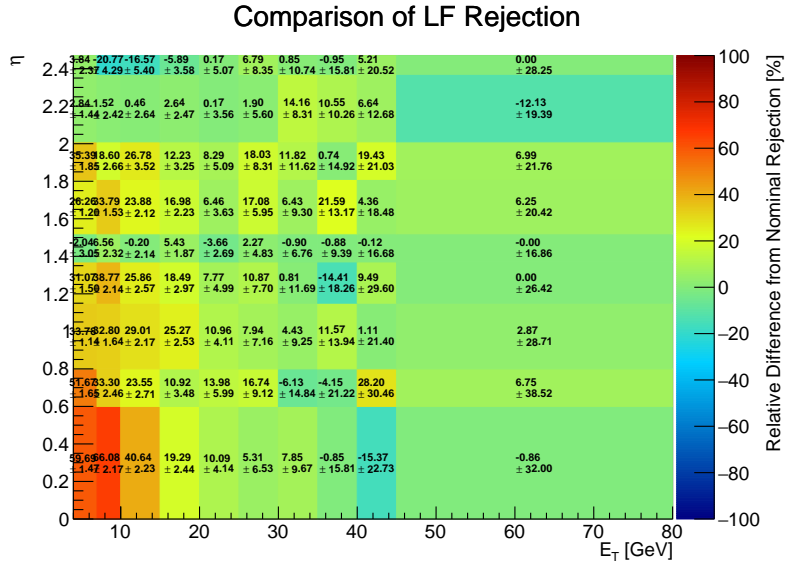
Figure 5.12: The relative difference in rejection of background electrons from a) heavy flavour hadronic decays and b) light flavour hadronic decays, as calculated by the nominal likelihood discriminant method and the two-dimensional likelihood discriminant method, for each $|\eta| - E_T$ bin at the Tight operating point. The fraction of background electrons from light flavour hadronic decays to heavy flavour hadronic decays is assumed to be 0.99:0.01.

explained by two factors. The first contributing factor, is that this study assumes the ratio of background electrons from light flavour and heavy flavour hadronic decays is evenly distributed across all bins of pseudorapidity and transverse energy, for the nominal background sample. Figure 5.13(a) shows that this is not the case and that for regions of low transverse energy, or high pseudorapidity, there are fewer than 1 in 99 electrons that originate from heavy flavour hadronic decays. The optimal two-dimensional likelihood discriminant cut depends on the fraction of electrons from light flavour hadronic decays to electrons from heavy flavour hadronic decays. For bins where this fraction varies from 1 in 99 ($= 0.\dot{0}\dot{1}$), the cut is not optimally placed. Figure 5.13(b) provides additional information about the distribution of the total number events in the nominal background sample, across all bins of pseudorapidity and transverse energy. It illustrates that most events are found in the region of low transverse energy, where the ratio of electrons from heavy flavour hadronic decays to electrons from light flavour hadronic decays is small.

The second factor, is that some electrons from light flavour hadronic decays, with a low transverse energy, have a smaller heavy flavour likelihood discriminant value than light flavour likelihood discriminant value. This means that these electrons pass both the nominal likelihood discriminant cut and the light flavour likelihood discriminant cut, but are rejected by the heavy flavour likelihood discriminant cut. This is illustrated in Figure 5.14, which shows the distribution of the light flavour and the heavy flavour likelihood discriminants for background electrons from light flavour hadronic decays that pass the nominal likelihood discriminant cut but fail the heavy flavour likelihood discriminant cut. The distributions are shown for four bins of pseudorapidity and transverse energy: Figures 5.14(b) and 5.14(a) show these distributions for $E_T = 4$ GeV, $|\eta| = 0.00$, Figures 5.14(d) and 5.14(c) show $E_T = 4$ GeV, $|\eta| = 2.01$ bin, Figures 5.14(f) and 5.14(e) show the $E_T = 30$ GeV, $|\eta| = 0.00$ bin, and Figures 5.14(h) and 5.14(g) show these distributions for the $E_T = 30$ GeV, $|\eta| = 2.01$ bin. The heavy flavour likelihood discriminant adds rejection power as it can fail some background electrons that pass the nominal likelihood discriminant cut. This effect seems more prominent for low transverse energies than high transverse energies.

The light flavour likelihood discriminant does not add any additional rejection of background electrons from light flavour hadronic decays, that is already achieved by the nominal likelihood discriminant method. However, the heavy flavour likelihood discriminant does improve the rejection of background electrons from light flavour hadronic decays with low transverse energy. It is this that can explain the increase in background rejection at low transverse energy, seen in Figure 5.12(b).

A study of the discriminating variables, for electrons that pass the nominal likelihood discriminant cut but fail the heavy flavour likelihood discriminant cut, showed there
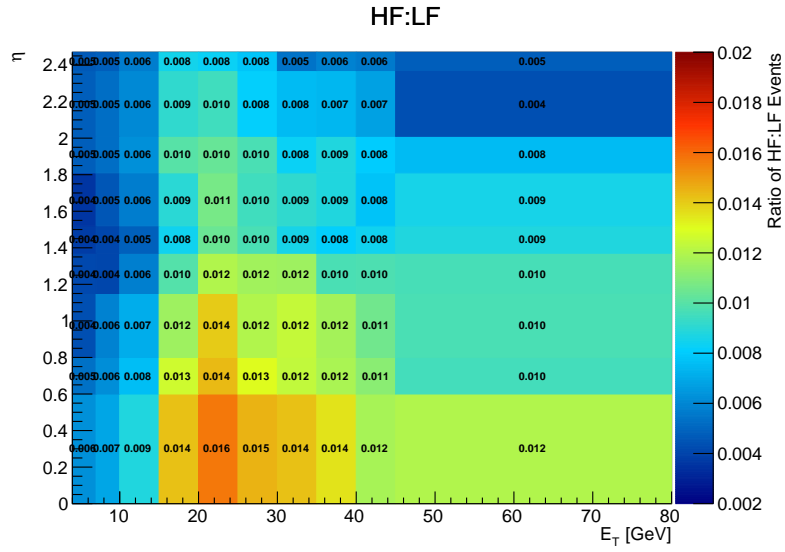
(a)
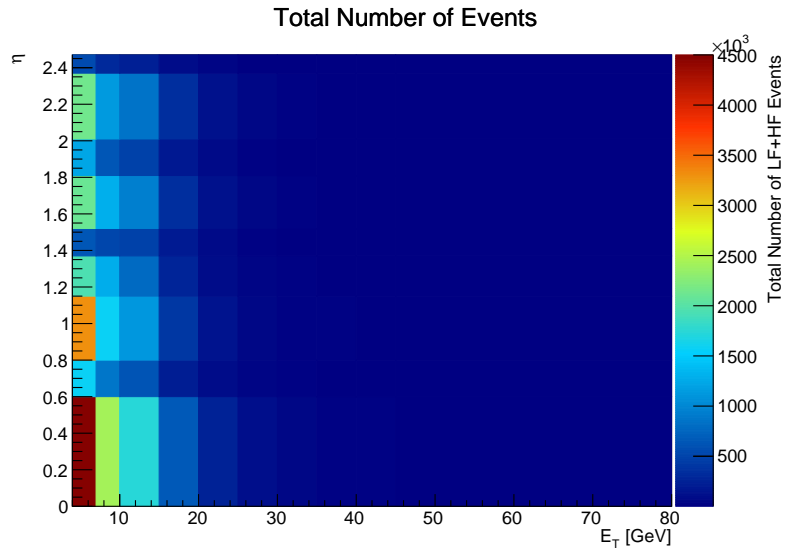
(b)

Figure 5.13: a) Shows the number of background electrons from heavy flavour hadronic decays over the number of background electrons from light flavour hadronic decays, for each $|\eta| - E_T$ bin of the nominal background Monte Carlo sample. b) Illustrates the distribution of the total number of events in the nominal background Monte Carlo sample, for each $|\eta| - E_T$ bin.
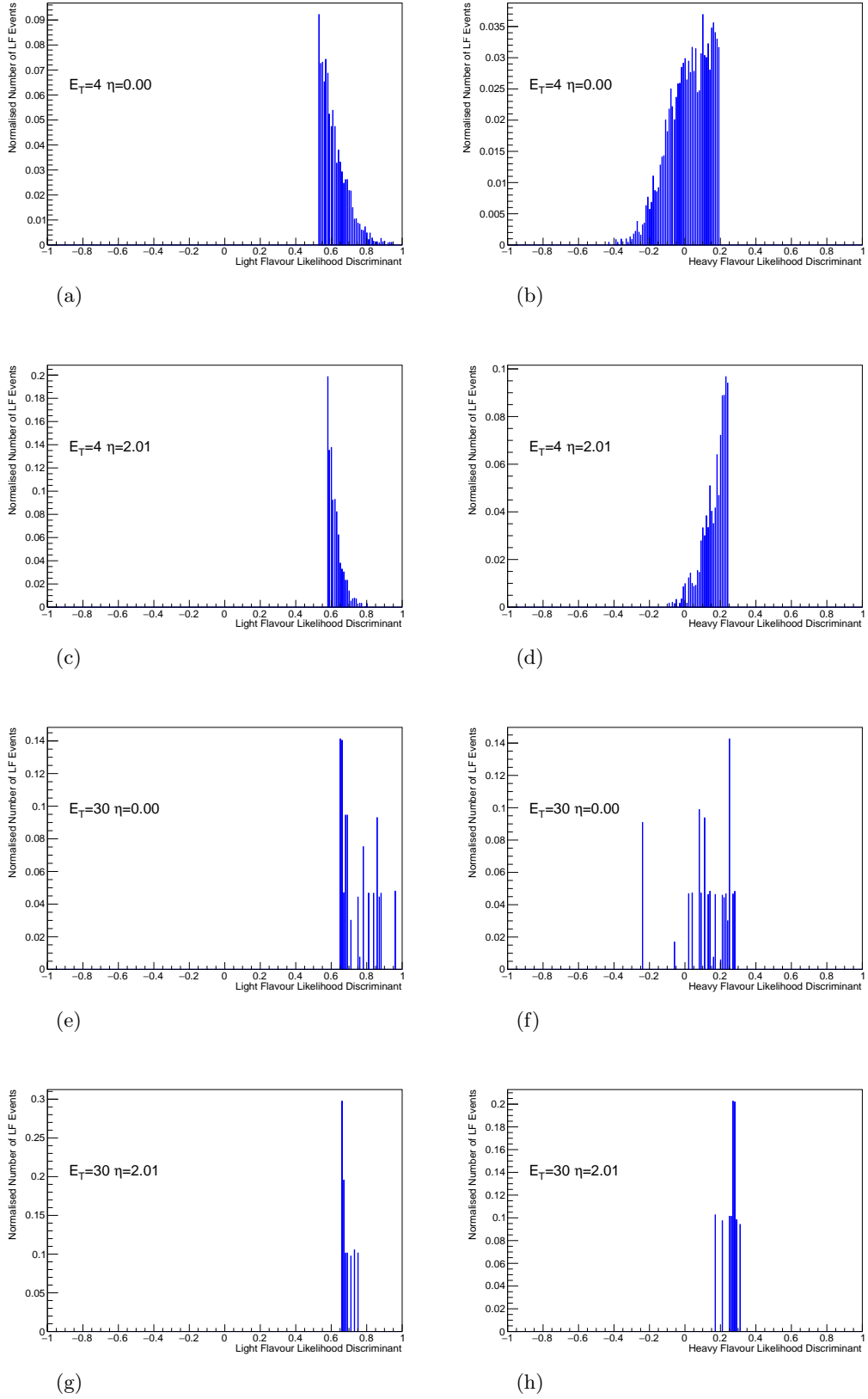
Figure 5.14: The one-dimensional distributions of the light flavour likelihood discriminant (left) and and heavy flavour likelihood discriminant (right) for background electrons from light flavour hadronic decays that pass the nominal likelihood discriminant cut but fail the heavy flavour likelihood discriminant cut for a 0.99 : 0.01 admixture. Four $|\eta| - E_T$ bins are shown.

was very little separation between all three categories of electrons, for most of the discriminating variables. An example of this is given in Figure 5.15, which shows the probability density functions of the f_1 variable across four bins of pseudorapidity and transverse energy, for all three categories of electrons. Figures 5.15(a), 5.15(c), 5.15(e) and 5.15(g) show the distributions for all electrons before any likelihood discriminant cuts have been applied. These are the distributions used to construct the light flavour and heavy flavour likelihood discriminants. They show that for low transverse energies, the f_1 variable is good at distinguishing background electrons from light flavour hadronic decays, from both prompt signal electrons and background electrons from heavy flavour hadronic decays. However, this discriminating power is reduced for the sub-set of electrons that pass the nominal likelihood discriminant cut but fail the heavy flavour likelihood discriminant cut, as shown in Figures 5.15(b), 5.15(d), 5.15(f) and 5.15(h)[9]. These figures illustrate that for low transverse energies, the shape of the distributions of electrons from light flavour and heavy flavour hadronic decays is very similar, as too is the shape of the distribution of prompt signal electrons.

However, some separation remained with the $d_0/\sigma(d_0)$ variable. Figure 5.16 shows the probability density functions of the $d_0/\sigma(d_0)$ variable across four bins of pseudorapidity and transverse energy, for all three categories of electrons. The probability density functions for all electrons before any likelihood discriminant cuts have been applied are shown in Figures 5.16(a), 5.16(c), 5.16(e) and 5.16(g). These distributions are used in the construction of the likelihood discriminants, and they show that the $d_0/\sigma(d_0)$ variable is very good at distinguishing background electrons from heavy flavour hadronic decays from the two other categories. It also shows very little discrimination between prompt signal electrons and background electrons from light flavour hadronic decays. Figures 5.16(b), 5.16(d), 5.16(f) and 5.16(h) show the distributions for electrons that pass the nominal likelihood discriminant cut but fail the heavy flavour likelihood discriminant cut. The distributions for this sub-set of electrons show that the background electrons from light flavour hadronic decays have a $d_0/\sigma(d_0)$ distribution that resembles the distribution for background electrons from heavy flavour hadronic decays. Both the distributions of electrons from light flavour and heavy flavour hadronic decays, look different to the distribution of prompt signal electrons. This explains the additional rejection achieved by the heavy flavour likelihood discriminant.

Another variable of note is the d_0 variable, as shown in Figure 5.17. Figure 5.17 shows the probability density functions of the d_0 variable across four bins of pseudorapidity and transverse energy, for all three categories of electrons. The probability density

---

[9]The distributions of the f_1, $d_0/\sigma(d_0)$ and d_0 variables, for electrons that pass the nominal likelihood discriminant cut but fail the heavy flavour likelihood discriminant cut, have not undergone the kernel density estimation smoothing process.
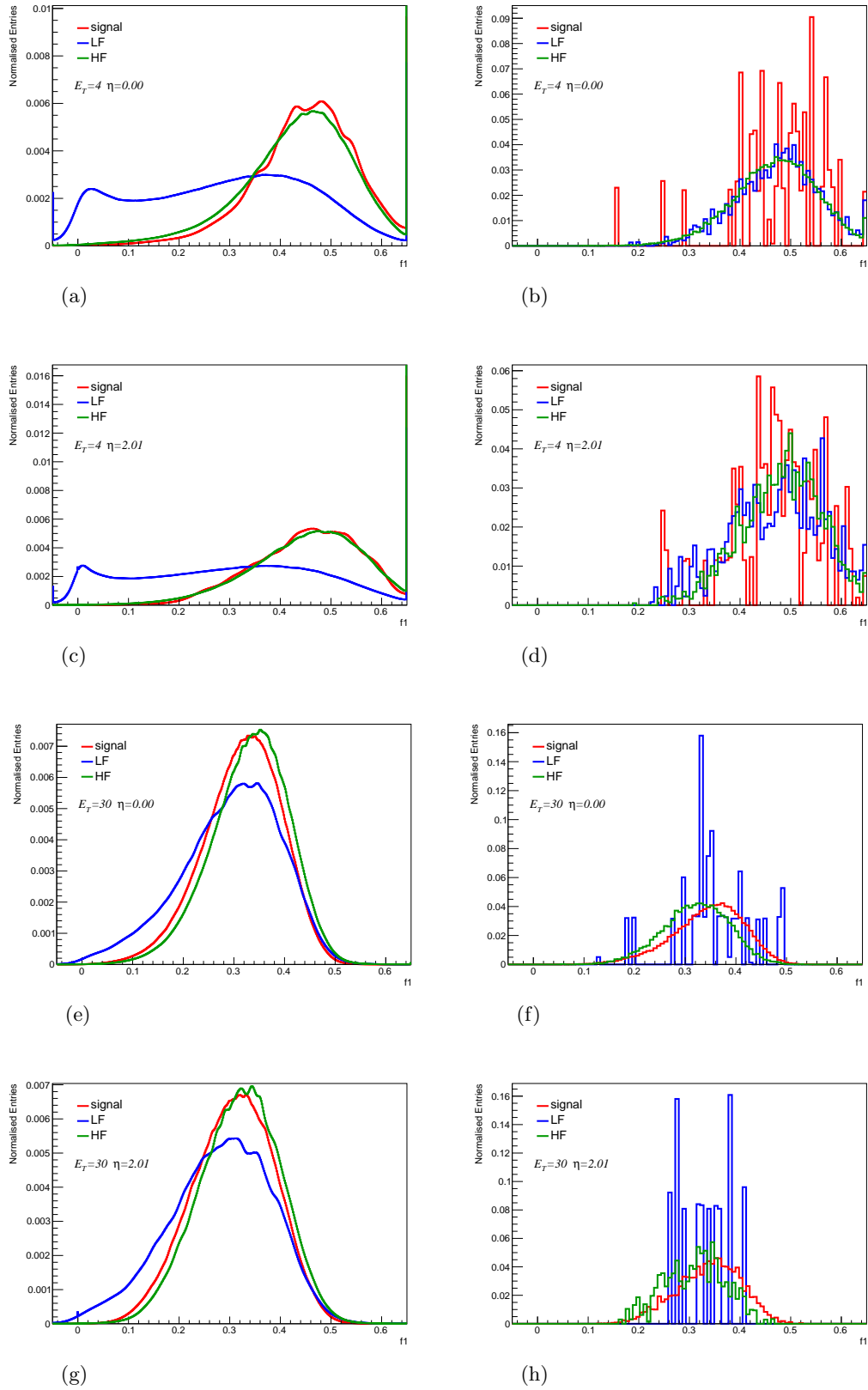
Figure 5.15: Probability density distributions of the f_1 variable across four $|\eta| - E_T$ bins for signal, LF and HF electrons. The plots on the left show the distributions used to construct the light flavour and heavy flavour likelihood discriminants. The plots on the right show the distributions for the sub-set of electrons that pass the nominal likelihood discriminant cut but fail the heavy flavour likelihood discriminant cut.
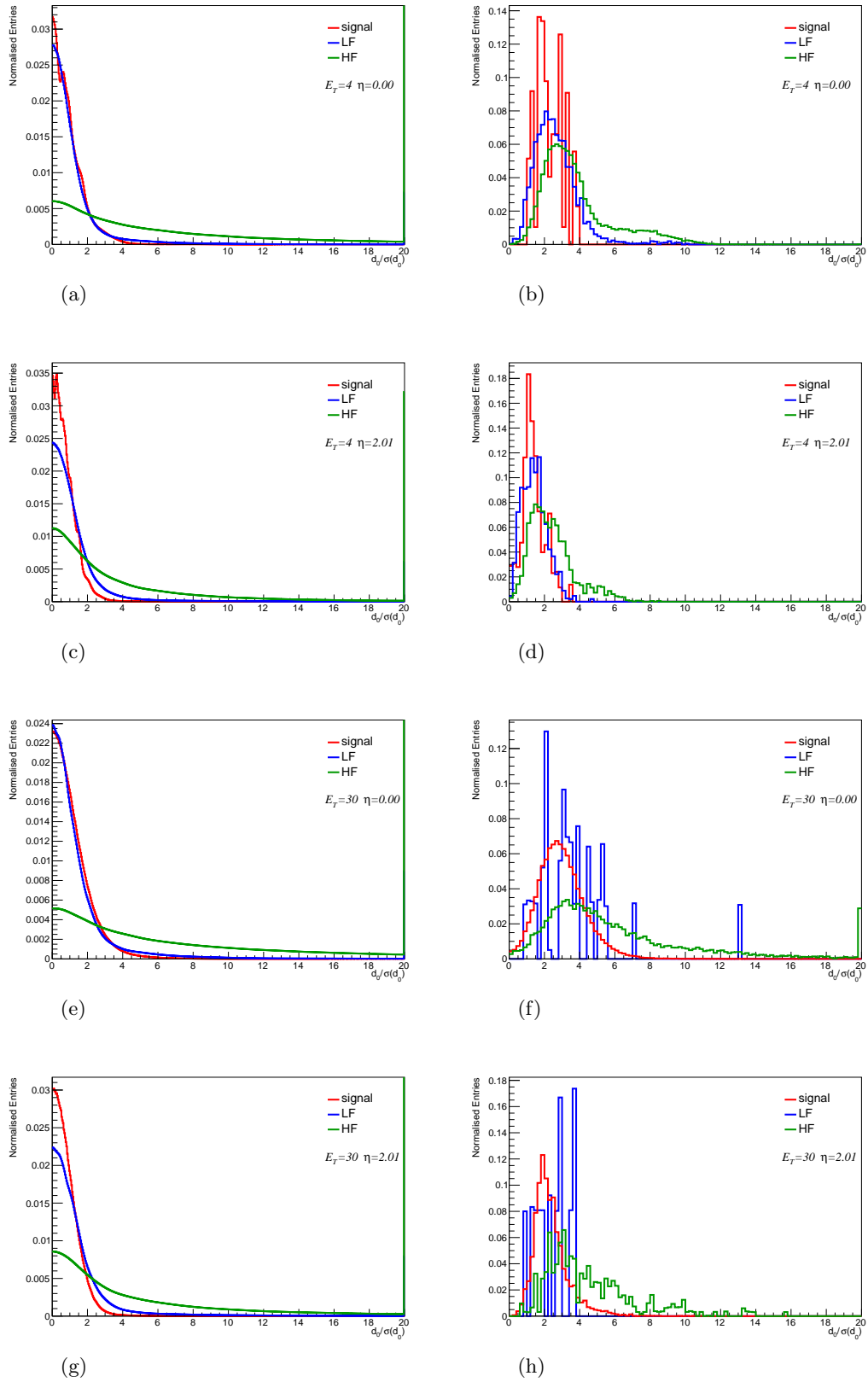
Figure 5.16: Probability density distributions of the $d_0/\sigma(d_0)$ variable across four $|\eta|-E_T$ bins for signal, LF and HF electrons. The plots on the left show the distributions used to construct the light flavour and heavy flavour likelihood discriminants. The plots on the right show the distributions for the sub-set of electrons that pass the nominal likelihood discriminant cut but fail the heavy flavour likelihood discriminant cut.

93

functions for all electrons before any likelihood discriminant cuts have been applied are shown in Figures 5.17(a), 5.17(c), 5.17(e) and 5.17(g). These distributions are used in the construction of the light flavour and heavy flavour likelihood discriminants. They show very little discrimination between prompt signal electrons and background electrons from light flavour hadronic decays but some discrimination between prompt signal electrons and those from heavy flavour hadronic decays. However, for the sub-set of electrons that pass the nominal likelihood discriminant cut but fail the heavy flavour likelihood discriminant cut, the distribution of background electrons from light flavour hadronic decays is more similar to that of electrons from heavy flavour hadronic decays. Figures 5.17(b), 5.17(d), 5.17(f) and 5.17(h) show that for this sub-set of electrons, a double peaked structure occurs for all three categories of electrons. This double peak structure arises due to the fact that most of events are found close to $d_0 = 0$, and most of these events do not fall into the small sub-set of events that pass the nominal likelihood discriminant cut but fail the heavy flavour likelihood discriminant cut. This is true for each of the three categories of electrons. In addition to the double peak structure, it can be seen that the shape of the distribution of background electrons from light flavour hadronic decays is broader than the shape of the distribution of prompt signal electrons or from background electrons from heavy flavour hadronic decays. This leads to a gain in discriminating power against background electrons from light flavour hadronic decays.

Additionally, the Monte Carlo sample used to select background electrons from light flavour hadronic decays, has a filter applied for events with a transverse energy greater than 17 GeV (see Section 5.1.2). This means that the Monte Carlo sample is adapted for background electrons with energies greater than 17 GeV. Therefore a bias is induced for background electrons from light flavour hadronic decays with a transverse energy less than 17 GeV. It is unclear if the bias of the electrons causes the shape differences in the discriminating variables.

It can be concluded that the optimum cut placed on the heavy flavour likelihood discriminant offers some additional rejection of background electrons from light flavour hadronic decays, than is achieved by the nominal likelihood discriminant cut, especially at low transverse energies. This can be attributed to differences in the transverse impact parameter, between the three categories of electrons.

Table 5.6 summarises the results from the Medium and Loose operating points for four bins of pseudorapidity and transverse energy. The signal efficiency remains very close to the target efficiency of the Medium and Loose operating points. Similar trends, for the rejection of background electrons, are seen for the Medium and Loose operating points as for the Tight operating point. There is an overall increase in rejection of background electrons from heavy flavour hadronic decays. The rejection of background electrons from

(a)

(b)

(c)

(d)

(e)

(f)

(g)

(h)
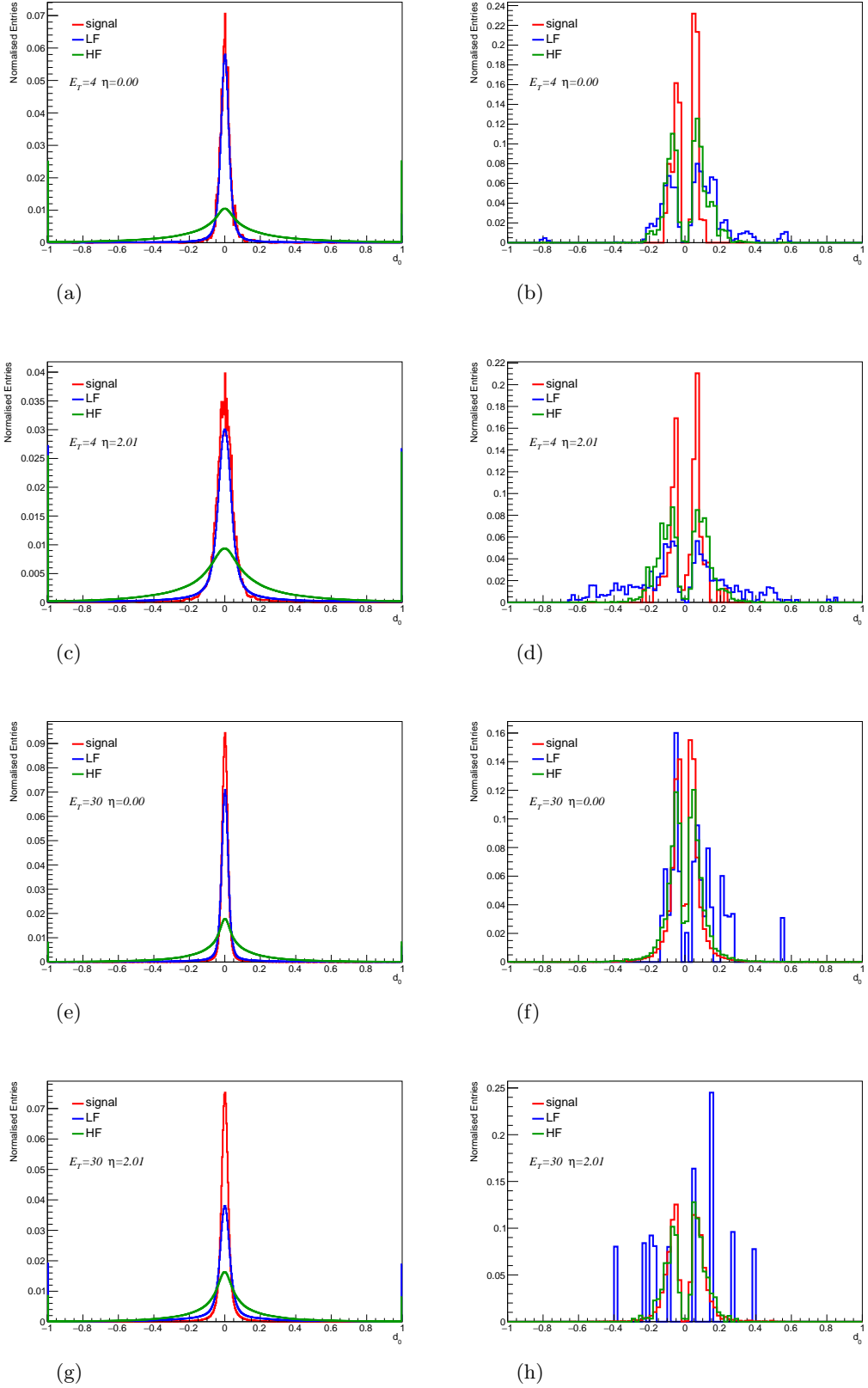
Figure 5.17: Probability density distributions of the d_0 variable across four $|\eta| - E_T$ bins for signal, LF and HF electrons. The plots on the left show the distributions used to construct the light flavour and heavy flavour likelihood discriminants. The plots on the right show the distributions for the sub-set of electrons that pass the nominal likelihood discriminant cut but fail the heavy flavour likelihood discriminant cut.

95

η-E_T bin	Relative Difference From Nominal Efficiency/Rejection [%]					
	Medium			Loose		
	Signal	LF	HF	Signal	LF	HF
$\eta = 0.00$, $E_T = 4$	$+0.35 \pm 1.49$	$+37.32 \pm 0.91$	$+55.27 \pm 0.36$	-1.04 ± 1.01	$+29.91 \pm 0.60$	$+53.40 \pm 0.27$
$\eta = 0.00$, $E_T = 30$	-0.95 ± 0.03	$+6.10 \pm 6.73$	$+58.67 \pm 0.90$	-0.87 ± 0.02	-2.44 ± 5.37	$+57.50 \pm 0.73$
$\eta = 2.01$, $E_T = 4$	-1.45 ± 0.96	$+8.98 \pm 0.92$	$+25.39 \pm 0.75$	-0.50 ± 0.65	$+6.24 \pm 0.62$	$+26.55 \pm 0.54$
$\eta = 2.01$, $E_T = 30$	$+1.20 \pm 0.06$	-3.15 ± 6.28	$+10.63 \pm 2.87$	-0.58 ± 0.06	$+5.45 \pm 5.52$	$+20.22 \pm 2.58$

Table 5.6: A summary of the relative difference in efficiency of prompt signal electrons and rejection of background electrons from light flavour hadronic decays (LF) and heavy flavour hadronic decays (HF) between the nominal likelihood discriminant method and the new two-dimensional likelihood discriminant method, shown for the Medium and Loose operating points. The fraction of background electrons from light flavour hadronic decays to heavy flavour hadronic decays is assumed to be 0.99:0.01.

light flavour hadronic decays has very little change for bins of high transverse energy. However, there is some improvement at low values of transverse energy due to the extra discriminating power gained from the heavy flavour likelihood discriminant. In general, the improvement in rejection is slightly worse for the Loose operating point than the Medium operating point.

5.3.5.2   Results for 0.96:0.04 Admixture

A comparison between the signal efficiency achieved by the two methods is shown in bins of pseudorapidity and transverse energy in Figure 5.18, for the Tight operating point with a $0.96 : 0.04$ admixture. As for the $0.99 : 0.01$ admixture, the absolute value of the signal efficiency achieved by the new two-dimensional likelihood discriminant method is required to be within ± 0.01 of the nominal signal efficiency and Figure 5.18 shows the relative change across the bins of pseudorapidity and transverse energy is approximately constant. There are some small fluctuations, occurring due to the interpolation method used to find the optimum two-dimensional discriminant cut and also due to the varying nominal target efficiency of the Tight operating point across the bins of pseudorapidity and transverse energy.

A comparison for the background rejection at the Tight operating point is shown in Figure 5.19. Figure 5.19(a) shows that there is an even greater improvement in rejection of background electrons from heavy flavour hadronic decays than shown for the $0.99 : 0.01$ admixture. Similar patterns are seen as for Figure 5.12(a), with the greatest improvement seen in the central barrel region of the ATLAS detector and for low transverse energies. The improvement is not as strong for the outer edges of the detector $|\eta| > 2.01$ and in the transition region of the detector ($1.37 < |\eta| < 1.52$).

Comparison of Z→ ee Efficiency

η (vertical axis), E_T [GeV] (horizontal axis), Relative Difference from Nominal Efficiency [%] (colour axis)

(a)

Figure 5.18: The relative difference in efficiency of signal electrons, measured in $Z \rightarrow ee$ events, as calculated by the nominal likelihood discriminant method and the two-dimensional likelihood discriminant method, for each $|\eta| - E_T$ bin at the Tight operating point. The fraction of background electrons from light flavour hadronic decays to heavy flavour hadronic decays is assumed to be 0.96:0.04.

The relative difference in the rejection of background electrons originating from heavy flavour hadronic decays is shown in Figure 5.12(b). There is little difference, when considering the statistical uncertainties, between the nominal likelihood discriminant method and the two-dimensional likelihood discriminant method with an assumed admixture of $0.96 : 0.04$, for the region with transverse energy $E_T > 25$ GeV. There is some increase in rejection of background electrons from light flavour hadronic decays for low values of transverse energy. As was described for Section 5.3.5.1, this can be attributed to a gain in discriminating power, from the heavy flavour likelihood discriminant, against background electrons from light flavour hadronic decays at low transverse energies.

Table 5.7 summarises the results from the Medium and Loose operating points for four bins of pseudorapidity and transverse energy. The signal efficiency is very similar to the target efficiency of the Medium and Loose operating points. Similar trends, for the rejection of background electrons, are seen for the Medium and Loose operating points as for the Tight operating point. The trends for the $0.96 : 0.04$ admixture, also follow the trends for the $0.99 : 0.01$ admixture, shown in Table 5.6. There is a greater improvement of rejection of background electrons from heavy flavour hadronic decays than light flavour hadronic decays. Furthermore, the two-dimensional likelihood discriminant cut based on the $0.96 : 0.04$ admixture outperforms the two-dimensional likelihood discriminant cut based on the $0.99 : 0.01$ admixture, when it comes to rejecting against background electrons from heavy flavour hadronic decays.

97

(a)

(b)

Figure 5.19: The relative difference in rejection of background electrons from a) heavy flavour hadronic decays and b) light flavour hadronic decays, as calculated by the nominal likelihood discriminant method and the two-dimensional likelihood discriminant method, for each $|\eta| - E_T$ bin at the Tight operating point. The fraction of background electrons from light flavour hadronic decays to heavy flavour hadronic decays is assumed to be 0.96:0.04.

η-E_T bin	Relative Difference From Nominal Efficiency/Rejection [%]					
	Medium			Loose		
	Signal	LF	HF	Signal	LF	HF
$\eta = 0.00$, $E_T = 4$	$+0.85 \pm 1.49$	$+39.34 \pm 0.91$	$+74.08 \pm 0.39$	-1.13 ± 1.01	$+25.27 \pm 0.59$	$+68.12 \pm 0.29$
$\eta = 0.00$, $E_T = 30$	-1.07 ± 0.03	-7.26 ± 6.73	$+69.69 \pm 0.94$	-0.88 ± 0.02	-9.91 ± 5.39	$+65.81 \pm 0.76$
$\eta = 2.01$, $E_T = 4$	-0.25 ± 0.96	$+1.45 \pm 0.91$	$+27.33 \pm 0.76$	-0.82 ± 0.65	$+2.88 \pm 0.61$	$+35.02 \pm 0.56$
$\eta = 2.01$, $E_T = 30$	-0.91 ± 0.06	$+4.27 \pm 6.29$	$+30.80 \pm 2.99$	-0.29 ± 0.06	$+3.08 \pm 5.51$	$+28.23 \pm 2.62$

Table 5.7: A summary of the relative difference in efficiency of prompt signal electrons and rejection of background electrons from light flavour hadronic decays (LF) and heavy flavour hadronic decays (HF) between the nominal likelihood discriminant method and the new two-dimensional likelihood discriminant method, shown for the Medium and Loose operating points. The fraction of background electrons from light flavour hadronic decays to heavy flavour hadronic decays is assumed to be 0.96:0.04.
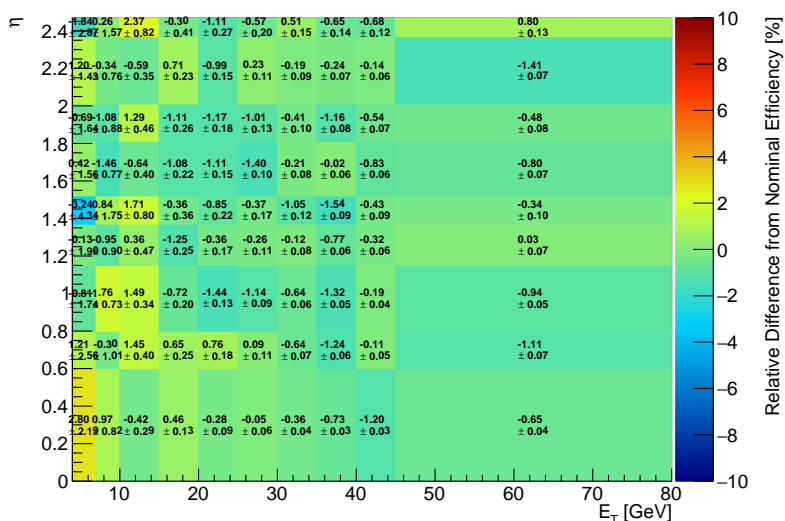
5.3.5.3 Results for 0.50:0.50 Admixture

A comparison between the signal efficiency achieved by the two methods for the $0.50 : 0.50$ admixture, at the Tight operating point, is shown in Figure 5.20 for bins of pseudorapidity and transverse energy. As for the previous two admixtures, the absolute value of the signal efficiency achieved by the new two-dimensional likelihood discriminant method is required to be within ± 0.01 of the nominal signal efficiency. Figure 5.20 shows the relative change across the bins of pseudorapidity and transverse energy is approximately constant with some small fluctuations due to the interpolation method used to find the optimum two-dimensional discriminant cut and also due to the varying nominal target efficiency of the Tight operating point across the bins of pseudorapidity and transverse energy.

Figure 5.21 shows a comparison for the background rejection at the Tight operating point for the $0.50 : 0.50$ admixture. Figure 5.21(b) shows that there is a strong increase in the rejection of background electrons from heavy flavour hadronic decays, across all bins of pseudorapidity and transverse energy. For this admixture, there is now a large decrease in the rejection of background electrons from light flavour hadronic decays in most bins, as shown in Figure 5.21(a). This is because the optimum two-dimensional likelihood discriminant cut is now much looser on the light flavour likelihood discriminant and much stricter on the heavy flavour likelihood discriminant.

It must be noted that even for a $0.50 : 50$ admixture, there is a small increase in rejection of background electrons from light flavour hadronic decays for the very first bin ($E_T = 4$ GeV, $|\eta| = 0.00$). This effect is due to the additional discriminating power provided by the heavy flavour likelihood discriminant at low values of transverse energy. There is not the same improvement as seen for the $0.99 : 0.01$ and $0.96 : 0.04$ admixtures (see Figures 5.12(b) and 5.19(b)), however some additional discriminating power is still seen. The additional rejection against background electrons from light flavour hadronic
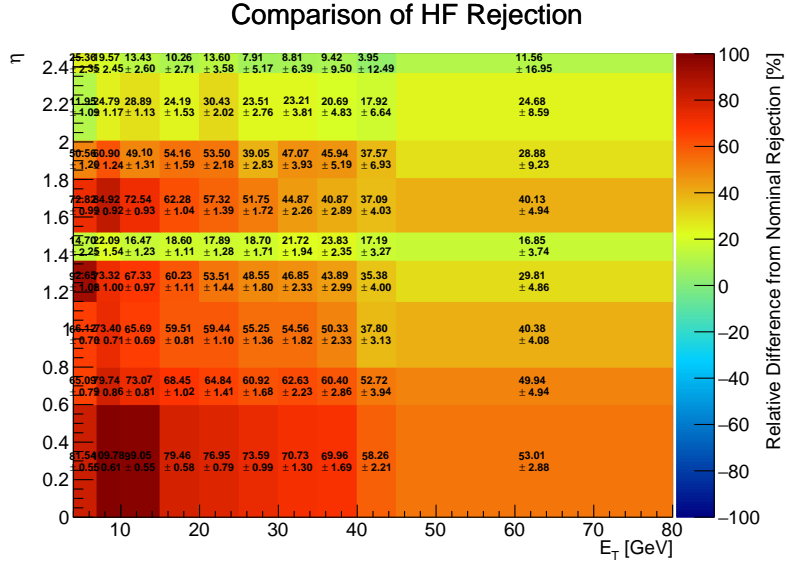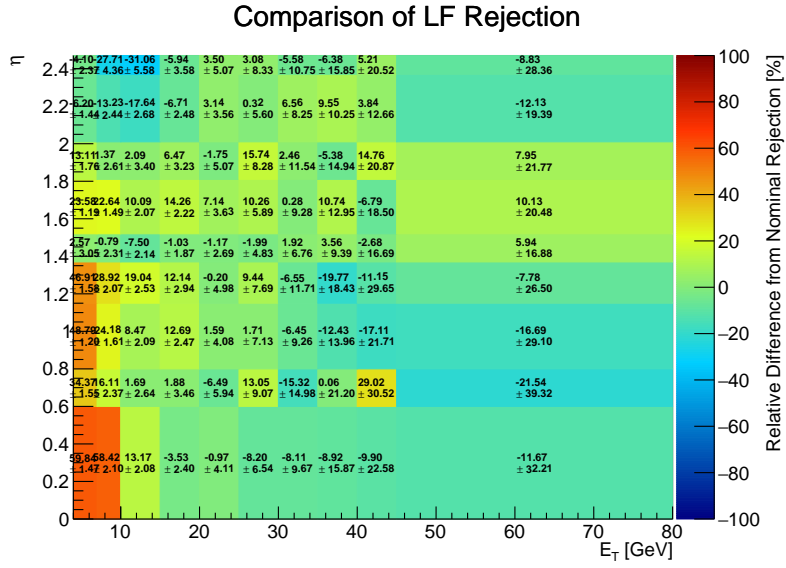
Figure 5.20: The relative difference in efficiency of signal electrons, measured in $Z \rightarrow ee$ events, as calculated by the nominal likelihood discriminant method and the two-dimensional likelihood discriminant method, for each $|\eta| - E_T$ bin at the Tight operating point. The fraction of background electrons from light flavour hadronic decays to heavy flavour hadronic decays is assumed to be 0.50:0.50.

decays, can be attributed to a gain in discriminating power by the heavy flavour likelihood discriminant, as explained in Section 5.3.5.1.

Table 5.8 summarises the results from the Medium and Loose operating points for four bins of pseudorapidity and transverse energy. The signal efficiency for the Medium and Loose operating points is very similar to the target efficiency of the Tight operating point. Similar trends, for the rejection of background electrons, are seen for the Medium and Loose operating points as for the Tight operating point. There is a decrease in the rejection of background electrons from light flavour hadronic decays, and a strong increase in the rejection of background electrons from heavy flavour hadronic decays, across all bins of pseudorapidity and transverse energy for the Medium and Loose operating points.

5.4 Conclusions

The rejection of background electrons achieved by the two-dimensional likelihood discriminant method depends on the fraction of background electrons from light and heavy flavour hadronic decays. Consequently the ability of the two-dimensional likelihood discriminant method to reject background electrons varies depending on the composition of the background sample. For the case of a background sample composed of 99% electrons from light flavour hadronic decays and 1% electrons from heavy flavour decays,
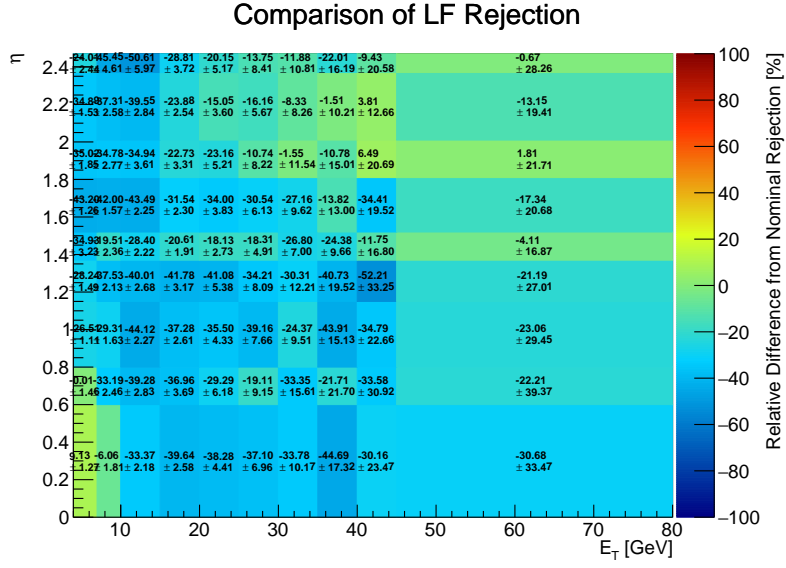
(a)
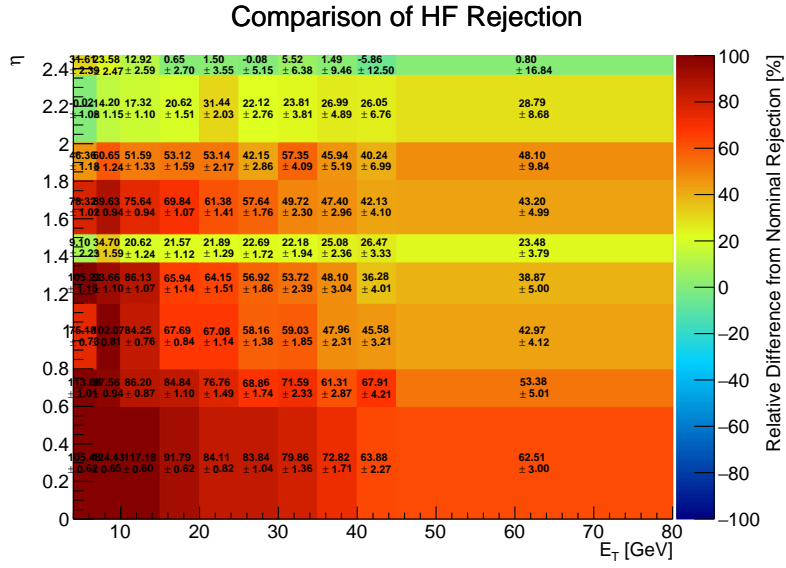
(b)

Figure 5.21: The relative difference in rejection of background electrons from a) light flavour hadronic decays and b) heavy flavour hadronic decays, as calculated by the nominal likelihood discriminant method and the two-dimensional likelihood discriminant method, for each $|\eta| - E_T$ bin at the Tight operating point. The fraction of background electrons from light flavour hadronic decays to heavy flavour hadronic decays is assumed to be 0.50:0.50.

| η-E_T bin | Relative Difference From Nominal Efficiency/Rejection [%] | | | | | |
| | Medium | | | Loose | | |
	Signal	LF	HF	Signal	LF	HF
$\eta = 0.00$, $E_T = 4$	-1.38 ± 1.49	-9.92 ± 0.85	$+93.08 \pm 0.43$	-0.86 ± 1.01	-20.26 ± 0.58	$+83.69 \pm 0.31$
$\eta = 0.00$, $E_T = 30$	-0.85 ± 0.03	-33.87 ± 7.09	$+74.80 \pm 0.97$	-0.93 ± 0.02	-31.91 ± 5.63	$+74.38 \pm 0.79$
$\eta = 2.01$, $E_T = 4$	-1.17 ± 0.96	-25.08 ± 0.94	$+20.08 \pm 0.75$	-1.13 ± 0.65	-20.94 ± 0.63	$+33.35 \pm 0.55$
$\eta = 2.01$, $E_T = 30$	-0.28 ± 0.06	-11.23 ± 6.32	$+31.67 \pm 3.00$	-0.91 ± 0.06	-7.92 ± 5.53	$+36.57 \pm 2.69$

Table 5.8: A summary of the relative difference in efficiency of prompt signal electrons rejection of background electrons from light flavour hadronic decays (LF) and heavy flavour hadronic decays (HF) between the nominal likelihood discriminant method and the new two-dimensional likelihood discriminant method, shown for the Medium and Loose operating points. The fraction of background electrons from light flavour hadronic decays to heavy flavour hadronic decays is assumed to be 0.50:0.50.
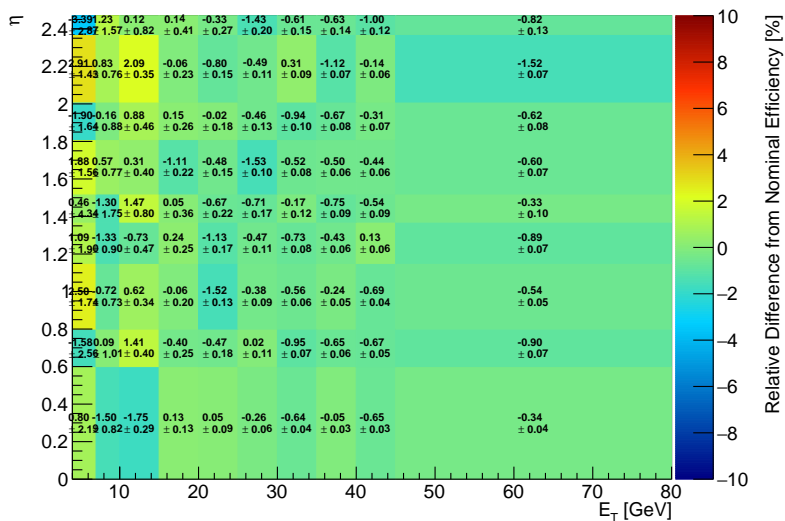
the two-dimensional likelihood discriminant method offers similar or better rejection of background electrons from light flavour hadronic decays, as the nominal likelihood discriminant method. There is some additional discriminating power gained from the heavy flavour likelihood discriminant which helps to increase rejection of background electrons from light flavour hadronic decays, at low values of transverse energy. This can be attributed to differences of the transverse impact parameter between the three categories of electrons.

The two-dimensional likelihood discriminant method can better reject against background electrons originating from heavy flavour hadronic decays in most bins of pseudorapidity and transverse energy; although the performance drops in the transition region of the detector ($1.37 < |\eta| < 1.52$) and in the outer regions of the detector ($|\eta| > 2.01$), in comparison to the central region of the detector.

As the fraction of background electrons from heavy flavour hadronic decays increases, the two-dimensional likelihood discriminant method shows a relative reduction in the rejection of background electrons from light flavour hadronic decays. But, this is countered with a relative increase in the rejection of background electrons from heavy flavour hadronic decays.

The two-dimensional likelihood discriminant method can provide a better rejection of background electrons than the nominal likelihood discriminant method, when the composition of background electrons differs to that of the nominal background Monte Carlo sample. For cases with a higher fraction of background electrons originating from heavy flavour hadronic decays, greater background rejection can be achieved with the two-dimensional likelihood discriminant method. The two-dimensional likelihood discriminant method has the potential to be utilised in physics analyses with at least one electron in the final state. Additionally, the same principles could be used to better reject against background electrons originating from other sources such as photon conversions

or Dalitz decay. More work, such as performing the studies with Monte Carlo samples with correction factors applied, is still needed to validate the method. However, these proof-of-principle studies have encouraged the ATLAS collaboration to consider the role that multi-class classification can play in the future of electron identification.

Chapter 6

Studying photon-induced W^+W^- Boson Production

This chapter will first discuss the motivations for studying photon-induced W^+W^- production before moving on to discuss some of the key concepts behind studying this process at the LHC in Section 6.2. Then there will be a brief summary of previous measurements by both the ATLAS and CMS collaborations in Section 6.3. The photon-induced W^+W^- analysis approach, used by the ATLAS experiment with the full Run 2 data set will be described in detail in Section 6.4. Section 6.4.4 will discuss the background processes that contribute to this analysis and how they are understood with the use of kinematic control regions.

6.1   Introduction and Motivation

The interaction of two incoming photons to produce a W-boson pair has long been predicted by the Standard Model. However, it was not until the LHC was built, that physicists could reach the high energies required to study this process. Since such photon-induced processes typically have small cross-sections, it has taken the ATLAS and CMS collaborations almost 10 years to collect sufficient data in order to perform detailed studies.

Photon-induced processes, such as the $\gamma\gamma \rightarrow WW$ process, are interesting to study because they are instances of triple and quartic gauge boson interactions. Such interactions occur due to the non-abelian SU(2) × U(1) structure of the Standard Model. Figure 6.1 shows the leading-order Feynman diagrams for the $\gamma\gamma \rightarrow WW$ process. The quartic $\gamma\gamma WW$ coupling is shown in Figure 6.1(a), whilst the exchange of a W boson between
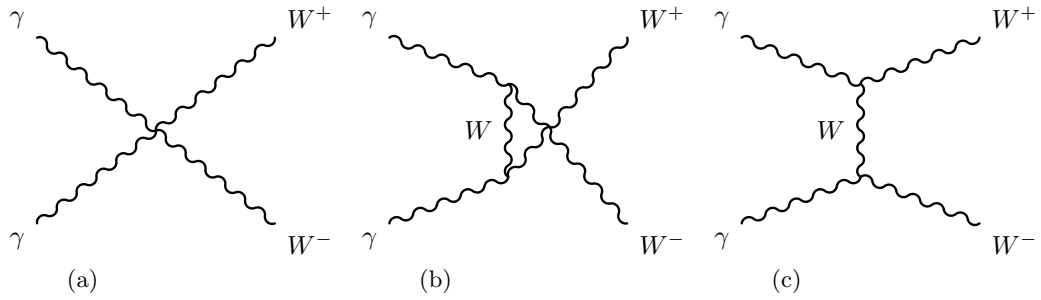
Figure 6.1: These Feynman diagrams show the leading order contributions to the $\gamma\gamma \rightarrow WW$ process. a) Shows the quartic $\gamma\gamma WW$ coupling. The process also occurs via the t- and u- channels in which a W boson is exchanged between two γWW vertices, as shown in b) and c), respectively.

two γWW vertices, via the t- and u-channels, is shown Figure 6.1(b) and Figure 6.1(c), respectively. At high energies the scattering amplitudes diverge as a result of the linear energy dependence of the longitudinal polarisation of the W boson. However, the t- and u-channel γWW coupling cancels with the quartic $\gamma\gamma WW$ coupling, hence conserving unitarity and ensuring the behaviour of the Standard Model at high energies [118]. The study of photon-induced W^+W^- production can provide a crucial test of the Standard Model, as any deviation from Standard Model predictions could reveal the presence of new physics.

Photon-induced W^+W^- boson production is, by its nature, an entirely QED process, and therefore it is sensitive to the anomalous gauge-boson interactions that arise in physics beyond the Standard Model. EFT extends the Standard Model Lagrangian with the use of dimension-6 and dimension-8 operators to parameterise the anomalous gauge-boson interactions. A measurement of the $\gamma\gamma \rightarrow WW$ cross-section can be used in further studies of global EFT fits to constrain the value of the anomalous couplings [29, 119]. This topic will be discussed further in Chapter 10.

6.2 Photon-induced W^+W^- Boson Production at the LHC

Inside the LHC, photon-induced W^+W^- boson production occurs when a photon is radiated off each of the incoming protons. The manner in which the incoming photons are radiated off the initial state protons can be described as either elastic or inelastic:

Elastic production - In the elastic production mechanism, the photons are coherently radiated off the incoming protons as a whole (see Section 2.4.2). The protons remain intact and their trajectories continue along the beam-axis, or are deflected by a very

small angle and typically fall outside of the acceptance region of the inner detector[1]. A diagram illustrating elastic production is shown in Figure 6.2(a). Approximately 80% of elastic events produce a W boson pair with no additional final state particles. For the remaining $\sim 20\%$ of elastic events, the protons can scatter with a very small impact parameter and some hadronic activity can be found in the final state as a result of additional soft QCD interactions [120].

Inelastic Production - Inelastic production is a term which encompasses two mechanisms of photon production from the incoming protons. The first such mechanism occurs when an excited hadronic state of the proton is produced that later decays into a low-multiplicity final state. Photons created via this mechanism have low virtualities. Where virtuality is defined by the four-momentum squared, and is used to quantify how much a particle is off its mass shell. In this context, "low virtualities" refers to photons with $Q^2 < 5$ GeV.

The second kind of inelastic production occurs when a photon is radiated directly off one of the constituent partons of the proton. Known as quark splitting, this process produces photons with higher virtualities. In both mechanisms, the incoming proton breaks up and hadronic interactions are initiated in the forward direction, in a process known as dissociation. Often the proton remnants fall outside of the acceptance region of the inner detector. For dissociative events there is a higher probability of the protons breaking up causing a higher track multiplicity around the interaction vertex. Of course, photon-induced W^+W^- production requires two incoming photons, both of which have the independent potential to scatter inelastically. Thus inelastic production can be further divided into two categories: single-dissociation - where just one proton dissociates - and double-dissociation - where both protons dissociate. Single dissociative production is illustrated in Figure 6.2(b) and double dissociative production is illustrated in Figure 6.2(c).

The photon-induced W^+W^- process can be written as: $pp(\gamma\gamma) \rightarrow p^{(*)}W^+W^-p^{(*)}$ - where $p^{(*)}$ denotes the final state proton remaining intact or fragmenting depending on if the photon is produced elastically or inelastically. The lack of proton remnants within the central detector contrasts the many totally inelastic collisions, that are often measured at the LHC. It means that photon-induced W^+W^- production can be selected by requiring no additional charged particles originating from underlying event activity. Known as the *exclusivity* requirement, it is implemented by ensuring there are no additional charged particles in a window around the interaction vertex.

---

[1]For the elastic production mechanism there is the potential for the final state protons to be detected by the ATLAS forward detectors. However the available data set recorded by the ATLAS Forward Proton detector, is not yet large enough to enable an observation of the $\gamma\gamma \rightarrow WW$ process.
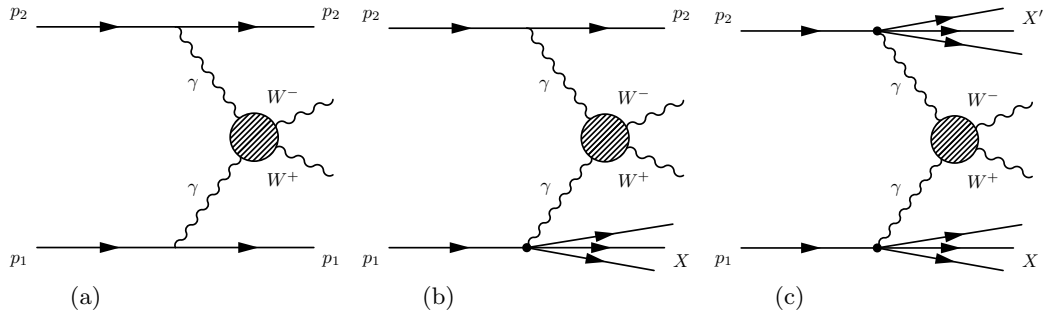
Figure 6.2: These diagrams show the different production mechanism of the photon-induced W^+W^- process. a) Shows the elastic production mechanism. b) Shows a case of inelastic production, where one if the initial protons dissociates into any additional final state, known as single-dissociation. c) Shows a second case of inelastic production, where both of the initial protons dissociate into any additional final state, known as double-dissociation [2].

6.2.1 The Survival Factor and Impact Parameter Dependence

The Equivalent Photon Approximation (see Section 2.4.2) provides a good basis for calculating the cross section of photon-induced processes, however it does not fully account for any additional proton-proton rescattering effects that may arise after the QED interaction. When the two incoming protons are in close proximity to one another there can be soft QCD interactions between the partons in addition to the hard QED interaction responsible for the photon emission. The soft QCD interactions can produce additional hadrons with low momentum, as well as affecting the kinematics of the final state protons. Consequently, events with proton-proton rescattering activity are associated with a high particle multiplicity and can be very difficult to distinguish from other background processes, leading to an effective reduction of the measured cross section. This is because events with proton-proton rescattering have charged particles close to the W^+W^- production vertex and are removed by the exclusivity requirement. The proton-proton rescattering activity is an effect of soft QCD interactions so cannot be calculated via perturbation theory. The survival factor, S^2, is the probability that proton-proton rescattering does not occur. The survival factor gives the probability that the two incoming protons remain intact and do not break up as a result of additional soft QCD interactions. The difference between the measured cross section and the theoretical cross section, that arises from the Equivalent Photon Approximation, can be accounted for by the survival factor:

$$\sigma_{meas} = S^2 \cdot \sigma_{EPA} \tag{6.1}$$

Figure 6.3 shows two Feynman diagrams illustrating a photon-induced process. The diagram on the left shows a photon-induced process with no additional proton-proton rescattering activity. This is known as the bare amplitude and is equivalent to the
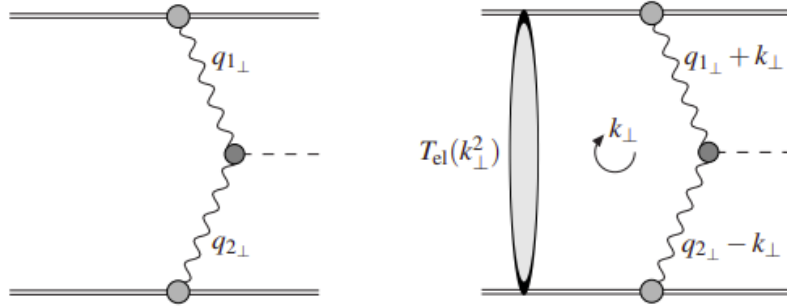
Figure 6.3: Feynman diagrams showing the amplitudes for the photon-induced exclusive processes. The left figure shows the bare amplitude, with no rescattering effects considered; and the right figure shows the screened amplitude, which does consider an additional proton-proton scatter [121].

prediction made by the Equivalent Photon Approximation. The diagram on the right shows a photon-induced process with the effects of additional proton-proton rescattering, this is known as the screened amplitude. The grey area represents the soft QCD interactions that occur between the two protons, and transverse momentum is exchanged between the two protons, via the loop. The corrected cross section of a photon-induced process is proportional to the square of sum of the bare and screened amplitudes:

$$\sigma \propto |T^{bare}(p_1, p_2) + T^{screened}(p_1, p_2)|^2 \tag{6.2}$$

The survival factor quantifies the extent to which the theoretical cross section, calculated using the Equivalent Photon Approximation, is reduced when additional proton-proton rescattering effects are taken into account. Therefore, the survival factor is constructed to be less than unity. The survival factor is equal to the corrected cross section divided by the theoretical cross section:

$$S^2 = \frac{\int d^2 p_1, d^2 p_2 |T^{bare}(p_1, p_2) + T^{screened}(p_1, p_2)|^2}{\int d^2 p_1 d^2 p_2 |T^{bare}(p_1, p_2)|^2} \tag{6.3}$$

It has been established that the survival factor depends on the transverse momenta of the protons. Performing a Fourier transform enables the survival factor to be expressed in terms of the transverse distance between the incoming protons:

$$S^2 = \frac{\int d^2\vec{b}_{1t} d^2\vec{b}_{2t} |T(s, \vec{b}_{1t}, \vec{b}_{2t})|^2 \exp(-\Omega(s, b_t))}{\int d^2\vec{b}_{1t} d^2\vec{b}_{2t} |T(s, \vec{b}_{1t}, \vec{b}_{2t})|^2} \tag{6.4}$$

The transverse distance between the two protons is given by $\vec{b}_t = \vec{b}_{1t} + \vec{b}_{2t}$, and $b_t = |\vec{b}_t| \cdot T(s, \vec{b}_{1t}, \vec{b}_{2t})$ gives the amplitude in impact parameter space. $\Omega(s, b_t)$ is the proton opacity and $\exp(-\Omega(s, b_t))$ is the probability of no inelastic scattering [122].

Hence, the survival factor depends upon the impact parameter of the two incoming protons. The closer the protons are to one another, the larger the suppression of the cross section and the greater the proton-proton rescattering effects. For a purely QED-induced event, the quasi-real photons that are radiated off the protons have a low virtuality. This in turn, leads to photons with low transverse momenta and larger impact parameters between the incoming protons, therefore the resulting survival factor is close to one [121, 123].

It is challenging to calculate the survival factor due to the intricacies of the transverse momentum exchanged between the incoming protons. As a consequence, the survival factor is not modelled in the studies presented in this thesis. Instead, it is accounted for by a data-driven scale factor[2], derived in Chapter 8. Estimates of the survival factor can be obtained by comparing the measured cross section of a photon-induced process with the theoretical prediction.

For the interested reader, some phenomenological predictions of the survival factor for different photon-induced processes are given in reference [124]. These predictions utilise eikonal models to approximate the rescattering process. The eikonal models assume the additional rescattering effects are uncorrelated [125].

6.2.2 General Analysis Strategy

For photon-induced W^+W^- production, the leptonic decay channel offers the cleanest event signature because in this decay channel there are only two tracks left in the detector. The hadronic and semi-hadronic decay channels of the W boson pair have much larger branching ratios than the leptonic decay channel [20], however the former channels leave a much busier signature in the detector, making it harder to identify from background processes. In addition to studying this process in the leptonic decay channel, the photon-induced W^+W^- signal is typically studied in the $e^{\pm}\mu^{\mp}$ final state in order to better distinguish from other background processes that generally have a same flavour dilepton final state - background processes will be discussed in more detail in Section 6.4.4. This is the general analysis strategy that has been used by both the ATLAS and CMS collaborations when studying photon-induced W^+W^- production at the LHC.

---

[2]This scale factor accounts for both the survival factor and the contributions from the inelastic production mechanisms.
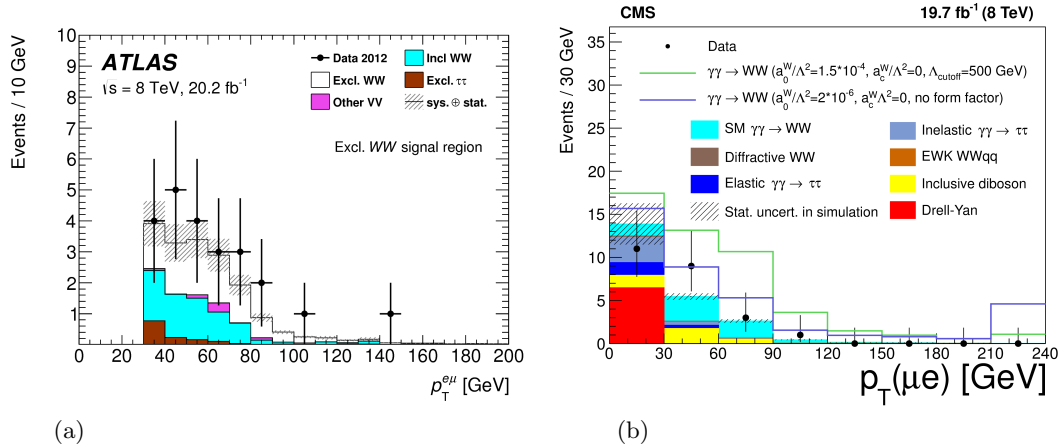
Figure 6.4: The distribution of the transverse momentum of the electron-muon pair for events with no associated tracks for $p_T^{\mu e} > 30$ GeV. a) Shows the results achieved by the ATLAS experiment in 2016 using the 8 TeVdata set [2] and b) Shows the results achieved by the CMS experiment in the same year using the combined $7 + 8$ TeVdata set [3]

6.3 Previous Measurements

Photon-induced W^+W^- production from two incoming photons was first studied by both the ATLAS and CMS collaborations during Run 1 of the LHC. In 2016, the ATLAS collaboration studied this process with 20.2 fb^{-1} of proton-proton collision data at $\sqrt{s} = 8$ TeV, and found evidence for photon-induced W^+W^- production with a significance of $3\,\sigma$ significance [2]. The CMS collaboration combined the $\sqrt{s} = 7$ TeV and $\sqrt{s} = 8$ TeV proton-proton collision data sets to find a 3.4 σ excess over the background-only hypothesis [3], see Figure 6.4. Both experiments also used their measurements to place limits on the effective coupling constants, α_c/Λ^2 and α_0/Λ^2 as shown in Figure 6.5. α_c/Λ^2 and α_0/Λ^2 can be converted to the formalism of EFT used in the rest of this thesis, using the equations given in Reference [126].

6.4 The photon-induced W^+W^- Analysis

The topic of photon-induced W^+W^- boson production was revisited by the ATLAS experiment, with the use of the full Run 2 data set. This section will now describe the event samples and the analysis approach in more detail.
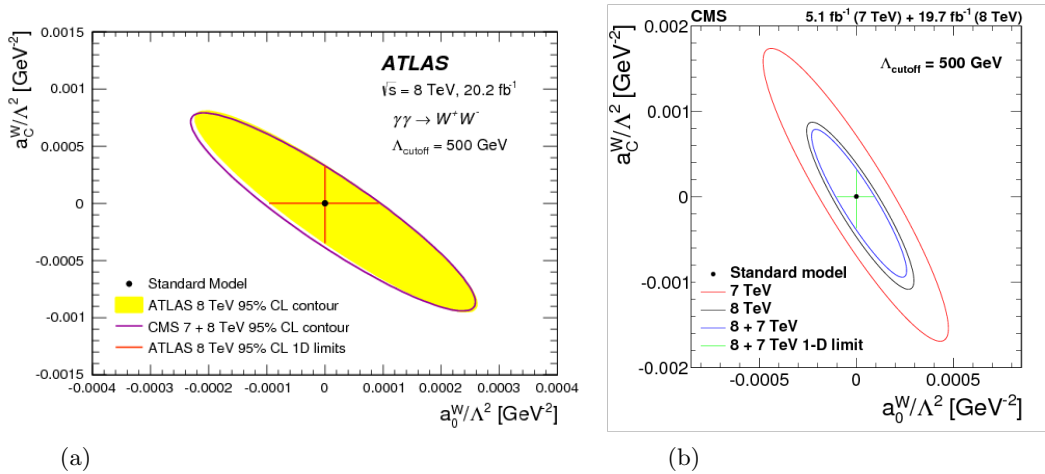
Figure 6.5: The excluded values of the anomalous coupling parameters with $\Lambda_{cutoff} = 500$ GeV (applied to conserve unitarity). a) Shows the 95% confidence limits set by the ATLAS collaboration [1]. The yellow area indicates the log-likelikelihood 95% CL contour and 1D limits are illustrated by the red cross. Also included on this figure is the CMS combined $7+8$ TeV result for comparison. b) Shows the CMS result for Run 1 in more depth [3]. This plot includes the 95% confidence level for the measurement at 7 TeV, 8 TeV and $7+8$ TeV. The one-dimensional limits for each parameter, with the second parameter set to 0, is shown by the cross for the $7+8$ TeV data set.

6.4.1 Event Samples from Data and Monte Carlo

6.4.1.1 Data Samples

This analysis makes use of proton-proton collision data, collected by the ATLAS detector during Run 2. The Run 2 data taking period had a centre-of-mass energy $\sqrt{s} = 13$ TeV and amounts to an integrated luminosity of $\mathcal{L} = 139$ fb$^{-1} \pm 2.4$ fb^{-1}. Only data events that pass the data quality assessments are used [62]. This selection ensure only stable proton-proton collision events with all detector components functional are included in the study [62]. The number of interactions per bunch crossing for the Run 2 data taking period varies from $\mu = 10$ to $\mu = 60$, with an average value of $\mu = 33.7$ [84].

6.4.1.2 Monte Carlo samples

Monte Carlo samples were used to model the signal and background processes. The simulations helped to provide insight into the interplay between signal and background processes and helped to interpret the physics results. Feynman diagrams of the most common background processes are shown in Figure 6.6. By studying the kinematic distributions of the Monte Carlo samples, event selections could be validated and any short-falls of the modelling could be understood, with the aid of control regions.
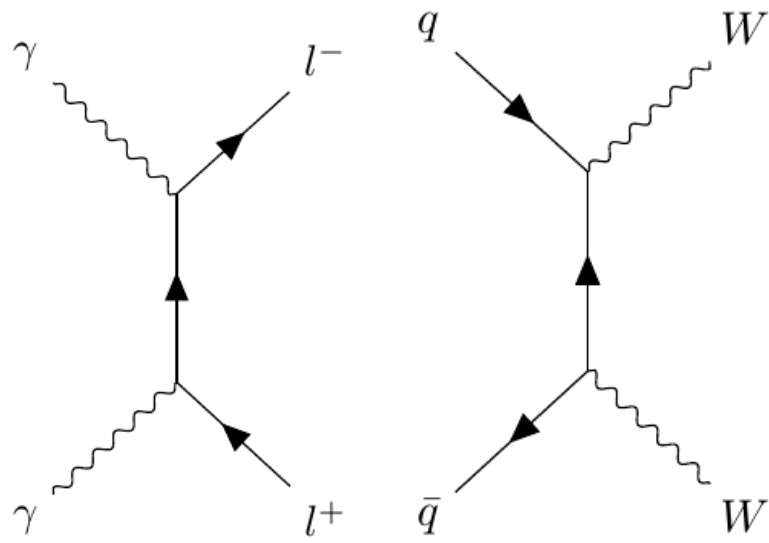
(a) Photon-induced dilepton production.

(b) Inclusive WW production.
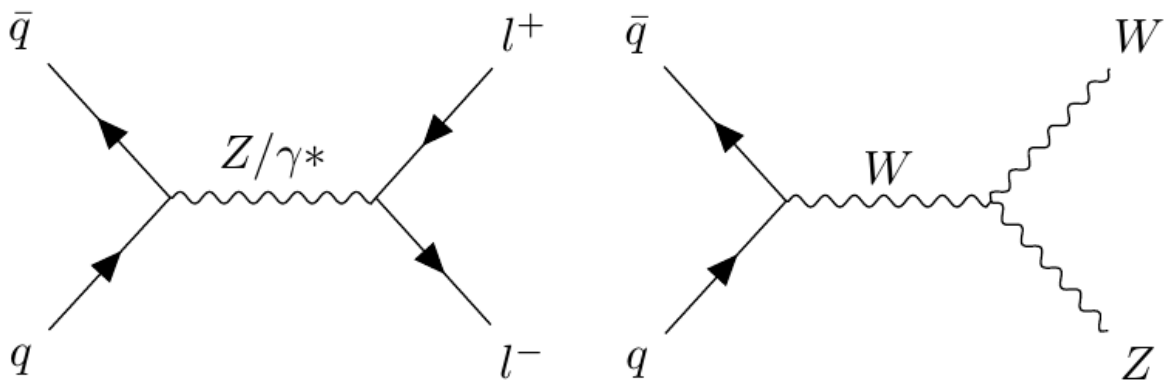
(c) Drell-Yan production.

(d) WZ production.
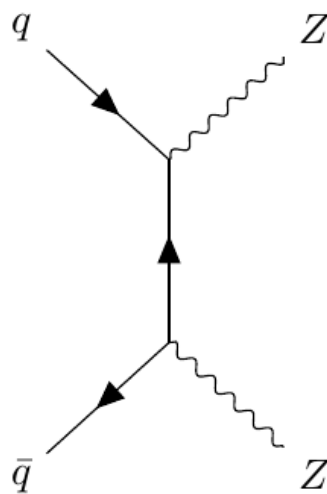
(e) ZZ production.

Figure 6.6: Feynman diagrams of the most common background processes in the $\gamma\gamma \to WW$ analysis.

Inelastic proton-proton collisions were generated with PYTHIA 8.186 [116] using the tuned A3 parameters [127] and the NNPDF2.3LO parton distribution functions [128]. The QCD interactions in all samples using either PYTHIA8 or HERWIG7, originating from parton showering, the underlying event and hadronisation, or the decay of bottom and charm hadrons, are modelled using EvtGen 1.2.0 [129].

The elastic production of the $\gamma\gamma \rightarrow WW$ process was modelled at leading order using HERWIG 7.1.5 [130, 131] and the BudnevQED photon flux [42] by the THEPEG software [132]. This sample uses a photon flux to model the photon-induced processes and is corrected to the cross section to include the dissociative and non-perturbative components, with the use of a data-driven scale factor (explained in more detail in Chapter 8). The data-driven scale factor is validated with Monte Carlo samples that simulate both the elastic and dissociative components of the $\gamma\gamma \rightarrow WW$ process. These samples are produced using MG_AMC@NLO [133] interfaced with PYTHIA 8.243. These samples were not used as the primary elastic production samples as they do not model the proton-proton rescattering and hence do not account for the survival factor [1].

The elastic production of the $\gamma\gamma \rightarrow ll$ process, illustrated in Figure 6.6(a), was modelled with the same generator as for the $\gamma\gamma \rightarrow WW$ process. However the dissociative components of $\gamma\gamma \rightarrow ll$ were modelled using LPAIR 4.0 [134] for the single-dissociative channel and PYTHIA 8.240 using NNPDF3.1NLOluxQED parton distribution functions [135] for the double-dissociative channel.

The most dominant background to the signal process is inclusive W^+W^- production, which arises as a direct result of a proton-proton collision, $qq \rightarrow WW$. Figure 6.6(b) shows the leading order Feynman diagram for this process. Inclusive WW production was modelled at next-to-leading-order accuracy using the POWHEG-BOX v2 [103, 104, 105, 136, 137] generator interfaced to PYTHIA8, and alternatively to HERWIG7, with the CT10 [109] parton distribution function, for the matrix element calculation. The POWHEG-BOX v2 sample was interfaced with PYTHIA 8.212, with the AZNLO tune [110] and the CTEQ6L1 [111] parton distribution functions, in order to model the parton showering and hadronisation. An alternative parton shower was also produced using HERWIG7.1.6 using the H7UE tune [131] and the MMHT2014LO parton distribution functions [138]. Finally, the modelling uncertainties were evaluated with the help of an inclusive W^+W^- sample, produced using the SHERPA 2.2.2 [139, 140] event generator [1].

Another background process is Drell-Yan production, $pp \rightarrow Z/\gamma^* \rightarrow ll$, shown in Figure 6.6(c). This process was modelled using identical generator settings as for the inclusive W^+W^- sample [1]. The $Z/\gamma^* \rightarrow \tau\tau$ channel was modelled with POWEHEG interfaced with Pythia8.186 using the NNPDF3.0NLO parton distribution functions [112]

and the AZNLO tune. The parton showering and hadronisation is modelled with CTEQ6L1 parton distribution functions.

The WZ and ZZ diboson processes are illustrated in Figures 6.6(d) and 6.6(e). These processes were modelled at next-to-leading-order using the same settings, as for the W^+W^- samples, for SHERPA and POWHEGBOX v2 interfaced with PYTHIA8.212. The SHERPA2.2.2 generator was used with the NNPDF3.0NLO parton distribution functions to model $W\gamma$ production, gluon-induced W^+W^- prodcution[3] and $WWjj$ production, produced in vector boson scattering. POWHEGBOX v2 [103, 104, 105, 106, 141] generator was used to model the $t\bar{t}$ and Wt processes. These samples were modelled at next-to-leading-order with NNPDF3.0NLO parton distribution functions, interfaced with PYTHIA8.230 using the A14 tune [117], and the NNPDF2.3LO parton distribution functions [1].

A full list of the Monte Carlo samples used in this analysis can be found in Appendix B.

6.4.2 Event Selection

Events are selected based on an initial preselection criteria, which constrains the properties of reconstructed tracks and leptons. All events used in this analysis must meet the preselection criteria. Additional selections based on the kinematics and flavours of the dilepton pair are used to distinguish between signal and background events (this will be detailed further in Section 6.4.4).

The reconstructed tracks(see Chapter 4, Section 4.1.2) must meet the Tight Primary selection criteria. The transverse impact parameter is required to be less than 1 mm as this helps to reject tracks from secondary interactions. Tracks passing these selection requirements are reconstructed with an efficiency of 75-80%, depending on the transverse momentum of the track. In simulated events, the reconstructed origin of the reconstructed tracks can be traced back to either the hard scatter or from pile-up. This is done by matching the number of hits contributing to the track fit, to the energy deposited by the simulated charged particle. The number of tracks in each category are denoted by n_{trk}^{HS} and n_{ntrk}^{PU} [1].

Leptons are reconstructed as discussed in Sections 4.3.2 and 4.4 of Chapter 4. Reconstructed electrons are required to pass the Medium likelihood selection and have a transverse energy greater than 20 GeV. Only electrons with a pseudorapidity of $|\eta| < 2.47$ and do not fall in the transition region ($1.37 < |\eta| < 1.52$) of the electromagnetic calorimeter are selected. The electrons must also pass isolation requirements which select events

---

[3]this includes both resonant and non-resonant contributions

based on information from the inner detector tracks and the calorimeter energy deposits, in a cone with a fixed size of $\Delta R = 0.2$ surrounding the electron. Electrons passing these selections are typically reconstructed with an efficiency of 75-85%. Finally a cut is placed on the significance of transverse impact parameter with respect to the the beam line, $d_0/\sigma_{d_0} < 5.0$.

Reconstructed muons must pass the medium quality requirement (as described in Chapter 4 Section 4.4.2) and the Loose isolation requirement [92]. Muons passing these requirements are reconstructed with an efficiency of 95%. The muons must also have a transverse momentum greater than 20 GeV and a pseudorapidity of $|\eta| < 2.4$. Lastly, a cut of $d_0/\sigma_{d_0} < 3.0$ is placed on the muon.

Events are triggered using the either a single-muon or single-electron trigger, which have identification and isolation requirements comparable to those applied in offline reconstruction. Each trigger has a transverse momentum threshold which varies for each data-taking period. In 2015 the single-electron trigger required 24 GeV [90] and the single-muon trigger required 20 GeV [94], however in 2016-2018, both thresholds were increased to 26 GeV and the identification and isolation requirements were tightened. At least one of the selected leptons must pass a trigger and have a transverse momentum greater than the trigger's threshold. The single-electron triggers used are summarised in Table 6.1, and the single-muon triggers used are summarised in Table 6.2.

Also included in the preselection are kinematic cuts on the transverse momentum of each lepton and their invariant mass. The leading lepton must have a transverse momentum greater than 27 GeV and the sub-leading lepton must have a transverse momentum greater than 20 GeV. The dilepton pair must have an invariant mass greater than 20 GeV [1].

6.4.3 Selecting Signal Events

As described in Section 6.2.2, photon-induced W^+W^- production is studied in the $e^\pm\mu^\mp$ leptonic decay channel and there must be no additional charged particle tracks associated with the interaction vertex [1]. The latter requirement exploits the elastic production mechanism of photon-induced W^+W^- boson production and is known as the exclusivity requirement. Additionally, the vector sum of dilepton pair's transverse momentum must be greater than 30 GeV.

The exclusivity requirement stipulates that there must be no additional charged tracks, other than the dilepton pair, associated with the interaction vertex. The interaction vertex is found as the weighted average z-position of each leptons' track, extrapolated

Data Taking Period	Single-Electron Trigger Name	p_T [GeV]	Description
2015	HLT_e24_lhmedium_L1EM20vH	24	An electron of interest is identified using the L1EM20vH level 1 trigger, calibrated at the EM scale and with 20 GeV threshold. The electron must pass medium ID quality.
	HLT_e60_lhmedium	60	The electron must pass medium ID quality.
	HLT_e120_lhloose	120	The electron must pass loose ID quality.
2016 − 2018	HLT_e26_lhtight_nod0 _ivarloose	26	The electron is required to pass the tight likelihood ID and a variable loose isolation is also required.
	HLT_e60_lhmedium _nod0	60	The electron is required to pass the medium likelihood ID.
	HLT_e140_lhloose _nod0	140	The electron is required to pass the loose likelihood ID.

Table 6.1: A summary of the single-electron triggers used to select electrons in the $\gamma\gamma \rightarrow WW$ analysis.

back to the beam line:

$$z_{vtx}^{ll} = \frac{z_{l_1} \sin^2 \theta_{l_1} + z_{l_2} \sin^2 \theta_{l_2}}{\sin^2 \theta_{l_1} + \sin^2 \theta_{l_2}} \qquad (6.5)$$

In this instance, $\sin^2 \theta_l$ is used as an approximation of the resolution of the z-position [76].

Defining the interaction vertex with respect to the weighted average z-position of each track, prevents a bias induced by the presence of additional tracks from either pile-up interactions or from hadronic activity from the underlying event. This definition results in a 30% increase in the vertex reconstruction efficiency, when compared to a vertex selection based only of the sum of the squared track transverse momenta [1]. The reconstructed leptons also have a cut placed on their longitudinal impact parameter, with respect to the interaction vertex: $|(z_l - z_{vtx}^{ll}) \sin \theta| < 0.5$ mm.

The number of tracks within a window of $\Delta z = \pm 1$ mm around the interaction vertex, excluding the reconstructed dilepton pair, is denoted by the track multiplicity, n_{trk}. For the exclusivity requirement, used to select signal events, $n_{\mathrm{trk}} = 0$ [1].

Data Taking Period	Single-Muon Trigger Name	p_T [GeV]	Description
2015	HLT_mu20_iloose_L1MU15	20	A muon of interest is identified using the L1MU15 level 1 trigger, with a threshold of 15 GeV. The muon must pass loose isolation requirements.
	HLT_mu50	50	There are no isolation requirements placed on the muon.
2016 − 2018	HLT_mu26_ivarmedium	26	A variable cone isolation requirement is placed on the muon.
	HLT_mu50	50	There are no isolation requirements placed on the muon.

Table 6.2: A summary of the single-muon triggers used to select muons in the $\gamma\gamma \to WW$ analysis.

Region	Kinematic Selection	Purpose
SR	$p_T^{e\mu} > 30$ GeV $n_{\mathrm{trk}} = 0$	Region used to select signal events
CR1	$p_T^{e\mu} < 30$ GeV $1 \leq n_{\mathrm{trk}} \leq 4$	Region used to constrain the $Z/\gamma* \to \tau\tau$ normalisation and also provides insight into inclusive W^+W^- production
CR2	$p_T^{e\mu} > 30$GeV $1 \leq n_{\mathrm{trk}} \leq 4$	Region enriched in inclusive W^+W^- events, $qq \to WW$, and used to check the n_{ch} reweighting
CR3	$p_T^{e\mu} < 30$ GeV $n_{\mathrm{trk}} = 0$	Region used to understand modelling of events with no associated tracks such as $\gamma\gamma \to ll$

Table 6.3: This table summarises the kinematic selections used to define the signal and control regions. In each region events are selected with the nominal pre-selection and then selections on the number of charged tracks and the transverse momentum of the dilepton pair, vary between regions. Each region is designed to enhance a particular physics process in order to check the modelling of background processes.

6.4.4 Background Estimation

Events are selected as described in Section 6.4.2, with the key kinematic selections, which allow for signal to be distinguished from background processes, being $n_{\mathrm{trk}} = 0$ and $p_T^{e\mu} > 30$ GeV. Additional control regions, with alternate selections of the charged track distribution and transverse momenta of the dilepton pair, are defined in order to verify the modelling of the background processes. In total there are three control regions in addition to the signal region; with the kinematic selection of each region specifically designed to enhance a particular physics process. The selection regions are summarised in Table 6.3.

In the signal region, $\gamma\gamma \to WW$ events account for 57% of selected and the largest source of background contamination comes from W^+W^- production initiated by the interaction between two quarks, which account for 33% of selected events [1]. The first control region is designed to enhance the selection of Drell-Yan events with two final state τ leptons, which amount to 75% of events selected in this region. In this region there are also notable contributions from inclusive W^+W^- events and from non-prompt leptons. Control region two enhances the selection of inclusive W^+W^- events, which total to 70% of events contributing in this region. Drell-Yan processes and non-prompt lepton events also contribute in this control region. The final control region is constructed such that background processes with no associated tracks can be assessed. This control region is particularly useful for understanding the modelling of $\gamma\gamma \to \tau\tau$ events, however 10% of events in this control region originate from signal events [1].

6.4.4.1 Misidentified Leptons

Background events originating from non-prompt leptons contribute towards 6% of events selected in the signal region [1]. The main source of these misidentified leptons are events from the W+jets process, which produces one prompt lepton and one non-prompt lepton. In this case, the non-prompt lepton originates from either light flavour or heavy flavour hadronic decays and are generally accompanied by additional activity around the candidate lepton. Since this analysis places strict requirements on the number of additional charged tracks, most misidentified lepton arise as a result of track reconstruction inefficiencies or if the additional activity mainly consists of neutral particles.

Other members of the analysis team estimated the contribution from misidentified leptons using the so-called fake factor method. This method provides an estimate of the number of misidentified leptons by finding a transfer factor, known as the fake factor, to translate the yield of misidentified leptons between two orthogonal selection regions. In this method, a same sign $e^{\pm}\mu^{\pm}$ pair is selected using the nominal pre-selection (as described in Section 6.4.2) and $1 \leq n_{\mathrm{trk}} \leq 4$ in data. However one lepton is required to fail the nominal lepton identification criteria. The ratio of the number of non-prompt leptons passing all identification requirements to those failing some of the requirements is used as a scaling factor to estimate the contribution from misidentified leptons. The estimate of the contribution is then extrapolated into the signal region with an assigned uncertainty [1].

6.4.5 Modelling Corrections

The Monte Carlo samples, described in Section 6.4.1.2, do not always accurately reflect data. Adjustments must be made to the lepton trigger, identification and isolation efficiencies, and the momentum resolutions, to ensure agreement between data and Monte Carlo samples.

There are three categories of data-driven corrections which are applied to simulated samples in this analysis:

1. Corrections applied to the beam spot size (as defined in Chapter 4 Section 4.2) in order to correct for the mismodelling of additional proton-proton interactions.

2. Corrections applied to the charged track multiplicity in order to correct for the mismodelling of the underlying event activity in background processes.

3. Corrections applied to the signal to account for dissociative and non-perturbative contributions.

The first correction was extracted by other members of the $\gamma\gamma \to WW$ analysis team, and will be summarised below in Section 6.4.6. The second correction was also extracted by other members of the analysis team, however, the author made direct contributions towards the validation this correction. The correction applied to the charged track multiplicity will be summarised in Chapter 7, along with the authors efforts to validate this correction. The final correction was derived by the author and will be described in detail in Chapter 8.

6.4.6 Corrections Applied to the Beam Spot

In some cases, tracks originating from proton-proton interactions can be found in a close proximity to the photon-photon interaction vertex. This is most likely to happen when there is a high density of proton-proton interactions and has implications on the efficiency of the exclusivity requirement. In order to ensure that the Monte Carlo samples accurately reflect the data, two independent data-driven correction factors are applied to all Monte Carlo samples used in the analysis.

The first relates to density of proton-proton interactions and the second to the number of tracks per interaction [1]. The average number of proton-proton interactions per bunch crossing, also known as pile-up, in Monte Carlo is reweighted to the data. The average density of additional proton-proton interactions in close proximity to the interaction vertex is determined by the longitudinal width of the beam spot, σ^{BS}.
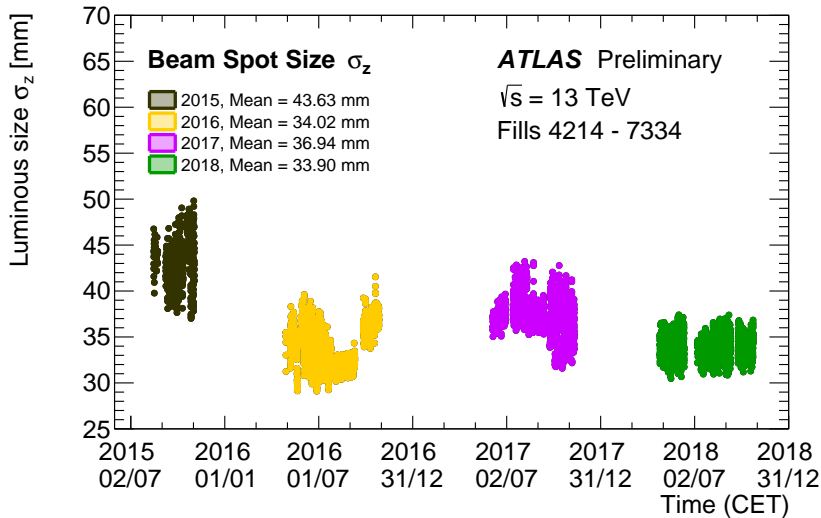
Figure 6.7: The average longitudinal width of the beam spot as a function of time. The four colours correspond to each year of data taking during Run 2 [142].

The beam spot size recorded in the data samples used in this analysis, varied over the course of the Run 2 data taking period. This is an effect of changes to the LHC beam optics. Figure 6.7 shows how the longitudinal width of the beam spot varied for each data taking year. The longitudinal beam spot size varied between 33.90 mm and 43.63 mm. The longitudinal size of the beam spot determines the density of the proton-proton interactions along the beam-axis and is therefore of particular importance to the photon-induced WW analysis [84].

Monte Carlo samples are produced with a nominal value of the longitudinal beam spot size; since they are often made before the data is recorded, when the exact beam parameters are not known. Nominally, simulated samples are produced with $\sigma^{BS} = 42$ mm, however photon-induced Monte Carlo samples were also requested with $\sigma_z^{BS} = 35$ mm which were then used in the analysis. The difference in the densities of the additional proton-proton interactions, in data and Monte Carlo, are dealt with by altering the number of tracks matched to the interaction vertex in the simulation. Any simulated tracks that originate from pile-up interactions, are only counted towards the track multiplicity if $|z_0^{trk} - z_{vtx}^{ll}| < 1$ mm $\times \sigma_{MC}^{BS}/\sigma_{Data}^{BS}$. All Monte Carlo samples are corrected to the beam conditions of the data [1].

The second correction applied, addresses the number of tracks from pile-up interactions, $n_{\mathrm{trk}}^{\mathrm{PU}}$, that are randomly matched to the interaction vertex. This correction is extracted using same flavour $Z \to ll$ events and finds the number of tracks passing the nominal track selection criteria, relative to the number of tracks at a random z-position, that is far away from the interaction vertex, $|z_{vtx}^{ll} - z| > 10$ mm. This process is done in

120

multiple distinct z-regions per event, in order to enhance its statistical power. However this induces a bias in $n_{\text{trk}}^{\text{PU}}$ since the distribution of z_{vtx}^{ll} along z is not accounted for. To overcome this, the bias is studied as a function of the z-coordinate and then weighted with the normalised beam spot distribution [1].

Additional tracks from pile-up interactions can inadvertently cause the rejection of signal events. This can be quantified by the signal efficiency of the exclusivity requirement which makes use of the distribution of $n_{\text{trk}}^{\text{PU}}$ and depends on both the pile-up and beam conditions. For the Run 2 data-taking period, with an average pile-up equal to 33.7, the average signal efficiency was found to be 52.6% [1].

Chapter 7

Corrections Applied to the Charged Track Multiplicity

The correction applied to the charged track multiplicity, in order to correct for the mismodelling of the underlying event activity in background processes, will be outlined in Section 7.1. Then, studies performed by the author of this thesis, on the validity of applying the charged track multiplicity reweighting factor to diboson processes, will be presented in Section 7.2.

7.1 The Charged Track Multiplicity Reweighting Method

One of the most important distributions in the photon-induced W^+W^- analysis, is the charged particle multiplicity, n_{ch}, which gets reconstructed as a number of tracks, n_{trk} in the detector. These quantities are crucial for the accurate selection of signal events. Quark-induced background processes can be accompanied by additional charged particles produced as a result of the proton-proton rescattering effects, which are attributed to the underlying event activity. Therefore the modelling of the underlying event can be assessed indirectly through the charged particle distribution. In Monte Carlo samples, the distribution of the number of charged particles at low multiplicities is not well modelled and must be corrected for using a data-driven method [1].

The underlying event activity depends on the transverse momenta transferred from the incoming protons to the final state particles. Quark-induced production of different colourless diboson final states are taken to be analogous to Drell-Yan production, if the transverse momenta of the different final state particles are equivalent. With this in

mind, the correcting weights are extracted from measurements of Drell-Yan production in data and then applied to other quark-induced diboson processes.

The charged particle multiplicity reweighting factors are extracted from same flavour Drell-Yan events that have passed the preselection requirements, as described in Section 6.4.2. Additionally, requirements are placed on the charged track multiplicity and the invariant mass. Events must have between one and four associated charged tracks ($1 \leq n_{\mathrm{trk}} \leq 4$) and an invariant mass similar to the mass of the Z boson (70 GeV $< m_{ll} <$ 105 GeV). These requirements suppress the contribution from other processes and ensure that a high purity of Drell-Yan events are selected.

Any events selected that are not Drell-Yan events, will be dominated by photon-induced dilepton production. Photon-induced dilepton production has a different dependence on the transverse momenta of the dilepton pair than is seen for Drell-Yan events. The contributions from photon-induced dilepton production and from pile-up interactions are subtracted so that only the contribution from the Drell-Yan events remain. A D'Agostini [143, 144] unfolding technique is used iteratively to unfold the distribution of reconstructed charged tracks, n_{trk}, into the number of charged particles, n_{ch}. And then the charged particle multiplicity is found a function of the transverse momenta of the dilepton pair in bins of $p_T^{ll} = 5$ GeV.

A reweighting factor is given by the ratio of the unfolded data to the unfolded Monte Carlo simulation, as a function of both the charged particle multiplicity and the transverse momenta of the dilepton system. It is defined as [1]:

$$w(n_{\mathrm{ch}}) = \frac{f^{data}(n_{\mathrm{ch}}; p_T^{ll})}{f^{MC}(n_{\mathrm{ch}}; p_T^{ll})} \qquad (7.1)$$

Where $f^{data}(n_{\mathrm{ch}}; p_T^{ll})$ and $f^{MC}(n_{\mathrm{ch}}; p_T^{ll})$ refer to the charged particle multiplicity distribution for a specific p_T^{ll} bin, for data and Monte Carlo respectively. No analytical formula can be used to defined these distributions, although they are shown in Figure 7.1, along with the corrected distribution. Figure 7.1 shows the good agreement between data and Monte Carlo after the charged particle multiplicity reweighting has been applied.

7.2 Validation of the Charged particle multiplicity reweighting in Diboson Events

This section will detail the studies, performed by the author of this thesis, on the validity of applying the charged particle multiplicity reweighting to diboson Monte Carlo samples. The charged particle multiplicity reweighting is a data-driven correction factor extracted
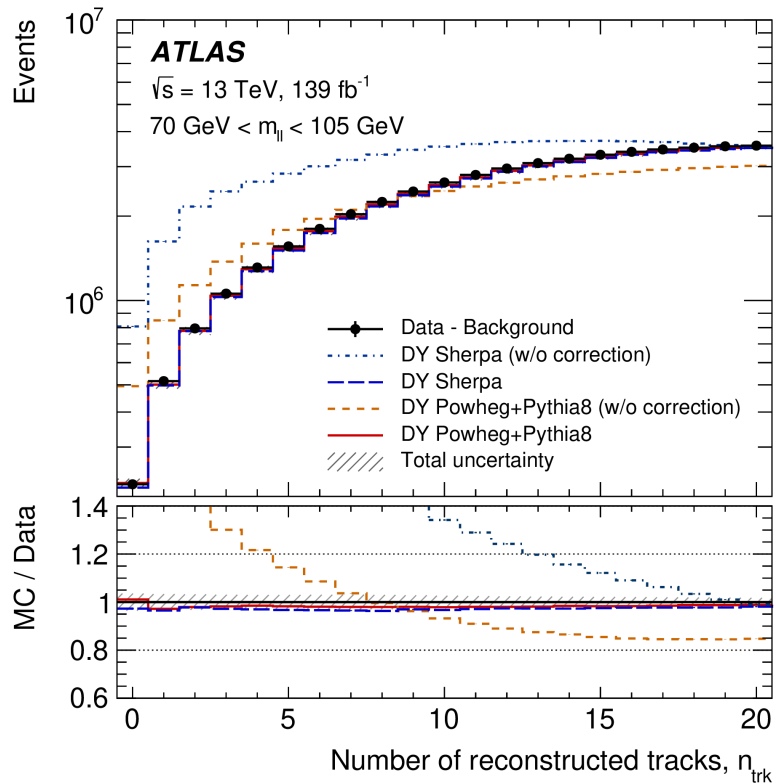
Figure 7.1: A comparison between data, and the POWHEG+PYTHIA8 and SHERPA Monte Carlo samples before and after the charged particle multiplicity correction is applied, for the charged track multiplicity distribution of Drell-Yan events. The total uncertainty of the charged particle multiplicity correction is indicated in the upper panel for the POWHEG+PYTHIA8 sample. Additionally, it is shown as a band around unity in the lower panel. The total uncertainty for the SHERPA sample is very similar to that of the POWHEG+PYTHIA8 sample [1].

from Drell-Yan events and applied to other quark-induced diboson processes, under the assumption that the transverse momenta of the produced bosons, such as inclusive W^+W^-, VBS, WZ and ZZ events, are equivalent. The studies presented in this section use the POWHEGBOX v2 diboson samples, and the SHERPA2.2.2 VBS samples, listed in Chapter 6 Section 6.4.1.2.

The primary motivation for these studies is to ensure that the inclusive W^+W^- process, which is the largest source of background in the $\gamma\gamma \rightarrow WW$ analysis, is well modelled. It is important to ensure the underlying event, and subsequently, the charged particle multiplicity is correctly modelled since the exclusivity selection, used to define the $\gamma\gamma \rightarrow WW$ signal region, depends on this distribution. However, it is difficult to select a pure sample of inclusive W^+W^- events with a low charged multiplicity in data that is not contaminated with signal events. For this reason, the charged particle multiplicity reweighting is validated using WZ and ZZ events, which have more leptons in their final states.

7.3   Studies of ZZ Events using a Four Lepton Selection

First, the application of the charged particle multiplicity reweighting to ZZ events will be examined. The Standard Model does not include neutral gauge boson self-interactions therefore it does not predict a contribution from photon-induced ZZ production. This means there are no other processes with a four lepton final state that can contribute at low track multiplicities, and so a pure sample of ZZ events can be selected in data.

The ZZ events are selected by requiring two pairs of same-flavour opposite-sign leptons that have passed the event preselection as described in Chapter 6 Section 6.4.2. Additionally, all other corrections used in the $\gamma\gamma \rightarrow WW$ analysis, such as the events weights and pile-up corrections, have been applied. Only on-mass shell Z bosons are considered in this study, therefore the invariant mass of each dilepton pair must be within 15 GeV of the Z mass. To increase the sample size, the second dilepton pair may have the same or different flavour as the first dilepton pair. If all four final state leptons are of the same flavour, then the combination of leptons with an invariant mass closest to the mass of the Z boson, are chosen to be a pair. Then, the remaining two leptons are also paired together. A cut of $1 \leq n_{trk} \leq 4$ is also applied since it is the charged track distribution at low multiplicities that is most relevant to this study.

Figure 7.2 shows the comparison between data and Monte Carlo for the distribution of the charged track multiplicity of the four lepton system. Figure7.2(a) shows the distribution before the charged particle multiplicity reweighting has been applied and Figure 7.2(b) shows the distribution after the charged particle multiplicity reweighting has been applied, with the systematic uncertainty on the charged particle multiplicity reweighting included in the error band on the Monte Carlo. Before the charged particle multiplicity reweighting is applied, the reduced chi-squared statistic is equal to $\chi^2/\text{NDF} = 0.57$. After the reweighting has been applied the reduced chi-squared statistic is equal to $\chi^2/\text{NDF} = 0.69$. Applying the charge particle multiplicity reweighting factor to the charged track multiplicity distribution leads to a small reduction in the agreement between Monte Carlo and data, however it is still acceptable.

Figure 7.3 shows the comparison between data and Monte Carlo for the transverse momentum of the four lepton system. Figure 7.3(a) shows the distribution before the charged particle multiplicity reweighting has been applied and Figure 7.3(b) shows the distribution after the charged particle multiplicity reweighting has been applied, with the systematic uncertainty on the charged particle multiplicity reweighting included in the error band on the Monte Carlo. These plots show that before the charged particle multiplicity reweighting is applied, the Monte Carlo typically overestimates the data.

Figure 7.2: Comparison plots between data and Monte Carlo for the charged track multiplicity of the four lepton selection. a) Shows the distribution before the charged particle multiplicity reweighting has been applied. b) Shows the distribution after the charged particle multiplicity reweighting has been applied.
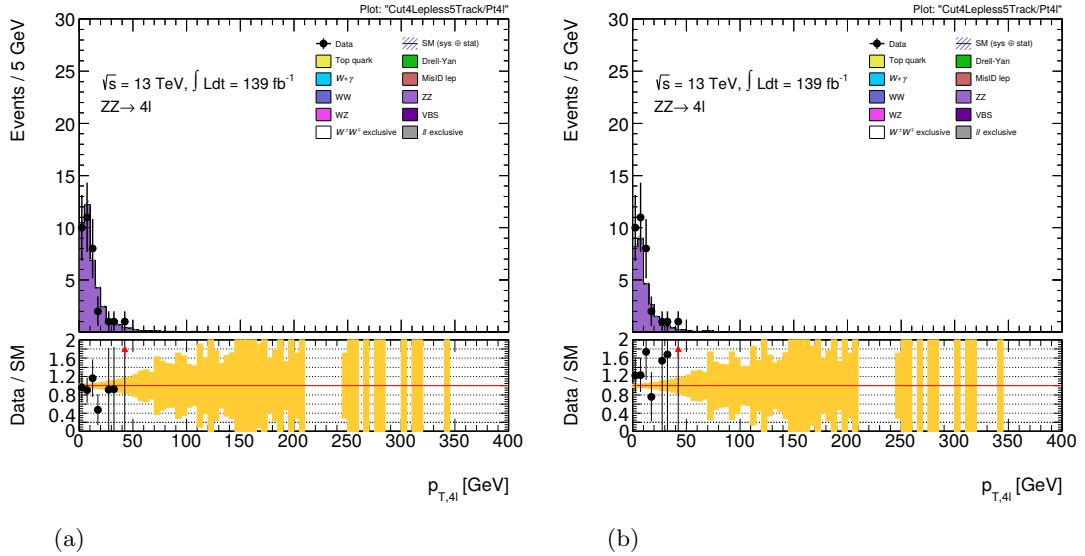
Figure 7.3: Comparison plots between data and Monte Carlo for the transverse momentum of the four lepton selection. a) Shows the distribution before the charged particle multiplicity reweighting has been applied. b) Shows the distribution after the charged particle multiplicity reweighting has been applied.

Once the charged particle multiplicity reweighting has been applied, the Monte Carlo typically underestimates the data.

The four lepton selection region has a fairly small event count, which means the conclusions drawn from this study are somewhat limited by statistical precision. Nonetheless, this

study shows that the agreement between data and Monte Carlo does not drastically deteriorate after the charged particle multiplicity reweighting has been applied.

Other members of the analysis team are performing an on-going analysis, focussing on the purely electromagnetic production of $\gamma\gamma \to 4l$. This on-going analysis does not have an on shell Z mass requirement and studies leptons with a lower transverse momentum, than the study presented in this section. Early indicators from this analysis suggest that significant improvements are seen for the data Monte Carlo agreement, when the charged particle multiplicity reweighting is applied in the $n_{trk} < 10$ region. This provides some encouragement that the charged particle multiplicity reweighting can be applied to ZZ events.

7.4   Studies of WZ Events using a Three Lepton Selection

The charge particle multiplicity reweighting is also applied to WZ events which has a final state of three leptons and one neutrino. As is the case for ZZ events, the Standard Model does not predict photon-induced WZ production, therefore there are no exclusive production processes with three leptons in the final state that can contribute at low track multiplicities. WZ events can be selected from data with a higher purity than inclusive W^+W^- events, but with a lower purity than ZZ events.

WZ diboson events are selected by requiring three final state leptons, that have passed the event preselection as described in Chapter 6 Section 6.4.2. Additionally, all other corrections used in the $\gamma\gamma \to WW$ analysis, such as the events weights and pile-up corrections, have been applied. One lepton originates from a W decay, while the other two originate from a Z decay. The two leptons originating from the Z decay are required to be the same flavour and have opposite signs. In addition, Z boson must be on-mass shell, so the invariant mass of the same flavour dilepton pair must be within 15 GeV of the Z mass. The lepton originating from the W boson decay is selected with Tight isolation requirements and with either the Tight electron likelihood or muon quality applied. To increase the sample size, there is no restriction applied on the flavour of the lepton originating from the W boson. As is the case for the ZZ study, a cut of $1 \le n_{trk} \le 4$ is applied since it is the charged track distribution at low multiplicities that is most relevant.

Figure 7.4 shows a comparison between the data and Monte Carlo for the charged track multiplicity distribution. Figure7.4(a) shows the distribution before the charged particle multiplicity reweighting has been applied and Figure 7.4(b) shows the distribution after the charged particle multiplicity reweighting has been applied, with the systematic
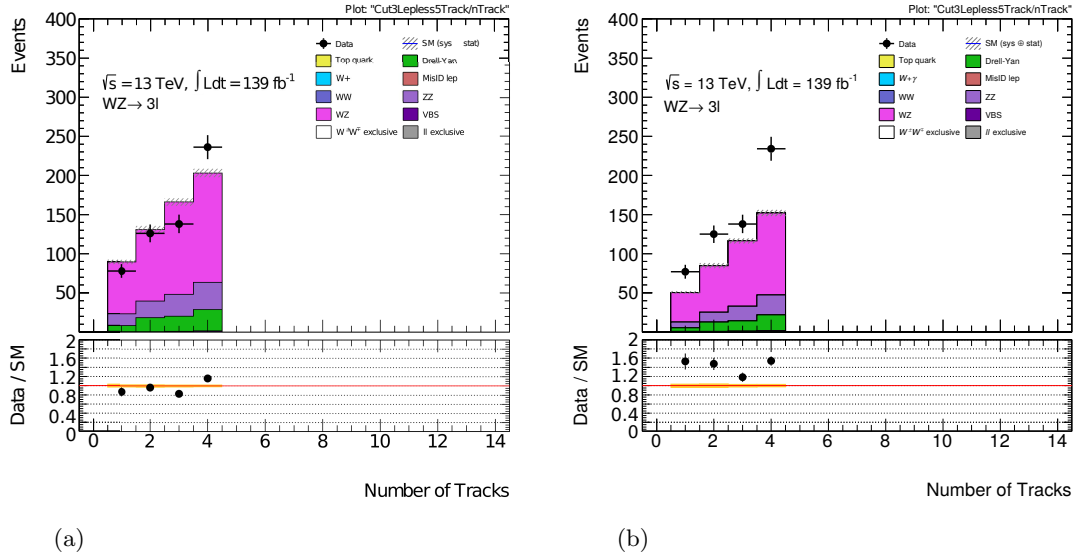
Figure 7.4: Comparison plots between data and Monte Carlo for the charged track multiplicity of the three lepton selection. a) Shows the distribution before the charged particle multiplicity reweighting has been applied. b) Shows the distribution after the charged particle multiplicity reweighting has been applied.

uncertainty on the charged particle multiplicity reweighting included in the error band on the Monte Carlo. Before the charged particle multiplicity reweighting is applied, the reduced chi-squared statistic is equal to $\chi^2/\text{NDF} = 0.17$. After the charged particle multiplicity reweighting has been applied, the reduced chi-squared statistic is equal to $\chi^2/\text{NDF} = 1.15$. This indicates that applying the charged particle reweighing to the three lepton selection, reduces the agreement between data and Monte Carlo.

Now, the data and Monte Carlo is compared for the transverse momentum of the three lepton system in Figure 7.5. Figure 7.5(a) shows the distribution before the charged particle multiplicity reweighting has been applied and Figure 7.5(b) shows the distribution after the charged particle multiplicity reweighting has been applied, with the systematic uncertainty on the charged particle multiplicity reweighting included in the error band on the Monte Carlo. These plots show that before the charged particle multiplicity reweighting is applied, the modelling typically overestimates the amount of data. After the charged particle multiplicity reweighting has been applied, the agreement between data and Monte Carlo has worsened, with the Monte Carlo now underestimating the data in nearly all bins.

It is possible that this disagreement between data and Monte Carlo could arise from misidentified leptons. Any misidentified leptons are more likely to have a low transverse momentum and will have originated either from charged hadrons, photon conversion semi-leptonic heavy flavour decays, or from in-flight meson decays. Misidentified muons are most likely to originate from semi-leptonic heavy flavour decays. Misidentified electrons
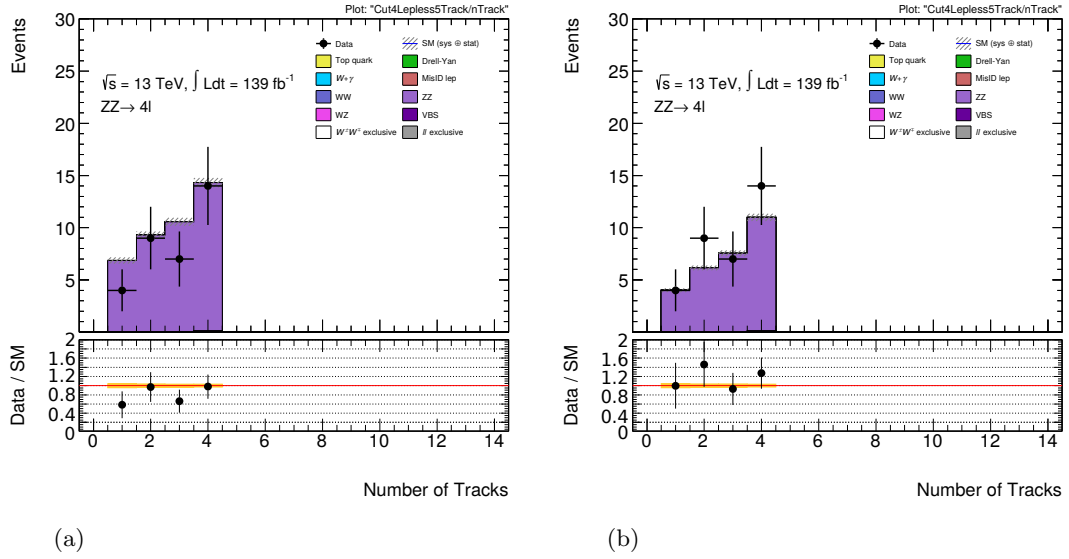
128
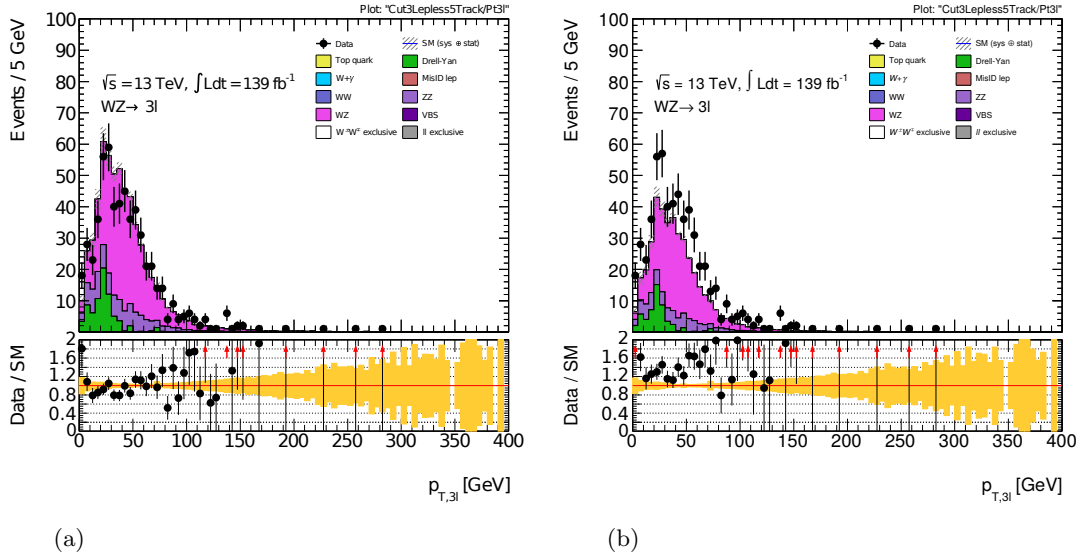
Figure 7.5: Comparison plots between data and Monte Carlo for the transverse momentum of the three lepton selection. a) Shows the distribution before the charged particle multiplicity reweighting has been applied. b) Shows the distribution after the charged particle multiplicity reweighting has been applied.

with low values of transverse momentum are dominated by charged hadrons and photon conversions.

A data-driven estimate of the contribution from misidentified leptons is obtained using a similar method to the fake factor method, described in Chapter 6 Section 6.4.4.1. The number of misidentified leptons is estimated with the use of a transfer factor, known as a fake factor, to translate the yield of misidentified leptons between two orthogonal selection regions. A control sample is used to obtain an estimate of the number of misidentified leptons. The control sample has the same kinematic selections as the nominal WZ selection but there are no isolation criteria applied to the leptons. The fake factor, f_{Fake} is defined as the ratio of the number of leptons satisfying the nominal three lepton selection criteria, N_{3l}^{pass} to the number of leptons failing the same criteria, N_{3l}^{fail}:

$$f_{Fake} = \frac{N_{3l}^{pass}}{N_{3l}^{fail}} \tag{7.2}$$

The estimate of the number of misidentified leptons is obtained by applying the fake factor to the number of leptons in the control sample that originate from a W boson and fail the selection criteria.

For WZ events, where the Z boson is on-shell, the transverse momentum of the dilepton pair is likely to be high. Therefore it is more likely that the lepton from the W decay could manifest as a misidentified lepton. For this reason, the estimate of misidentified leptons is only performed on the lepton originating from the W boson.
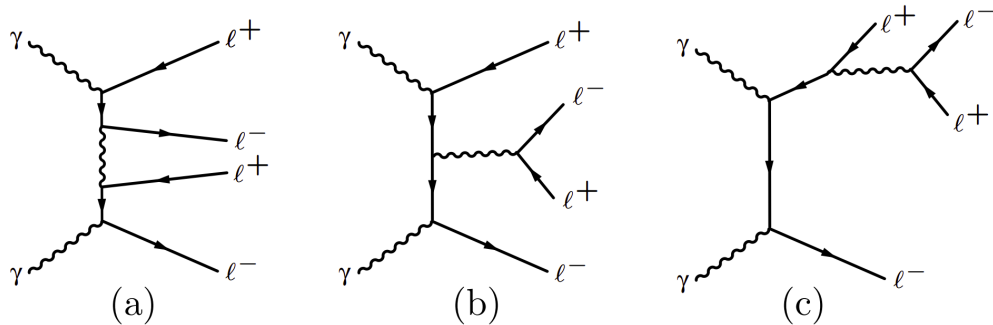
Figure 7.6: Leading order Feynman diagrams of the $\gamma\gamma \rightarrow 4l$ process [145].

The contribution from misidentified leptons is very small and cannot provide a full explanation of discrepancy seen between data and Monte Carlo. Another member of the $\gamma\gamma \rightarrow WW$ analysis team performed studies where the the charged multiplicity reweighting was applied at truth-level and the effects were studied at reco-level. These studies indicated that the charged particle multiplicity reweighting behaved as expected, and concluded that the difference between data and Monte Carlo must originate from an unknown source of background. Furthermore, other distributions were investigated and they showed a flat ratio of data to Monte Carlo. It is possible that the discrepancy arises from photon-induced dilepton production with a W boson radiated off or from low mass WZ events. It is also possible that the difference between data and Monte Carlo could be attributed to virtual $W\gamma^*/Z$ events or from ZZ events with some leptons falling outside of the acceptance region of the detector.

Alternatively, it is possible that there is some contribution from $\gamma\gamma \rightarrow 4l$ events with some leptons falling outside of the acceptance region of the detector [145]. Figure 7.6 shows the Feynman diagrams of the $\gamma\gamma \rightarrow 4l$ process at leading order. There is no contribution from $ZZ \rightarrow 4l$ with two on-shell Z bosons at tree-level, therefore the $\gamma\gamma \rightarrow 4l$ process does not contribute towards the four lepton selection described in Section 7.3. This explains why the charged particle multiplicity reweighting works better for the four lepton selection than the three lepton selection.

7.5 Conclusions

The studies of applying the charged particle multiplicity reweighting to ZZ events indicate that applying the charged particle multiplicity reweighting slightly reduces the agreement between data and Monte Carlo. Applying the charged particle multiplicity reweighting to ZZ events does not cause a drastic deterioration of the agreement between data and Monte Carlo, providing some encouragement that the reweighting factor can

be applied to diboson events. However, it is hard to draw concrete conclusions due to limitations from statistical sample size in this selection region.

The studies of applying the charged particle multiplicity reweighting to WZ events did not yield more conclusive answers. Applying the charged particle multiplicity reweighting to WZ events shows some deterioration between the data and Monte Carlo agreement. These studies indicate there is some additional background contributing in this region that is not well understood. Further studies are needed with additional photon-induced Monte Carlo samples to fully understand the reason behind the difference between data and Monte Carlo in this selection region. The studies presented in Sections 7.3 and 7.4 did not help to validate the application of the charged particle multiplicity reweighting to diboson events.

With this in mind, a truth-level systematic uncertainty was assigned to the application of the charged particle multiplicity reweighting to diboson samples. The truth-level systematic uncertainty was taken to be the difference between the charged particle multiplicity distributions of the inclusive W^+W^- and Drell-Yan Monte Carlo samples, at truth-level.

Figure 7.7 shows the normalised charged track multiplicity distribution for inclusive W^+W^- production as predicted by the POWHEG+PYTHIA8 Monte Carlo sample with the AZNLO eigentunes[1]. Also plotted are the predictions by the POWHEG+HERWIG and SHERPA Monte Carlo samples. In general, the track multiplicity distribution is modelled consistently across the generators, however a large variation is seen in the $n_{trk} = 0$ bin. The total systematic uncertainty is taken to be the full range of the Monte Carlo predictions, shown by the grey hatched band in Figure 7.7 [1].

Additionally, Figure 7.1 shows a comparison between data, POWHEG+PYTHIA8 and SHERPA Monte Carlo samples, before and after the reweighting has been applied to the charged track multiplicity distribution of Drell-Yan events. The Drell-Yan events shown in this figure are required to satisfy 70 GeV $< m_{ll} < 105$ GeV to ensure a pure sample and that the Z boson is on-mass shell. This figure illustrates how poorly the underlying event is modelled in Drell-Yan events before the charged particle multiplicity is applied. Applying the charged particle multiplicity to Drell-Yan events brings the two Monte Carlo samples into agreement with each other and into agreement with data, within the associated systematic uncertainty.

---

[1]The AZNLO eigentunes are a set of variations parton shower settings of the Monte Carlo generator [146]
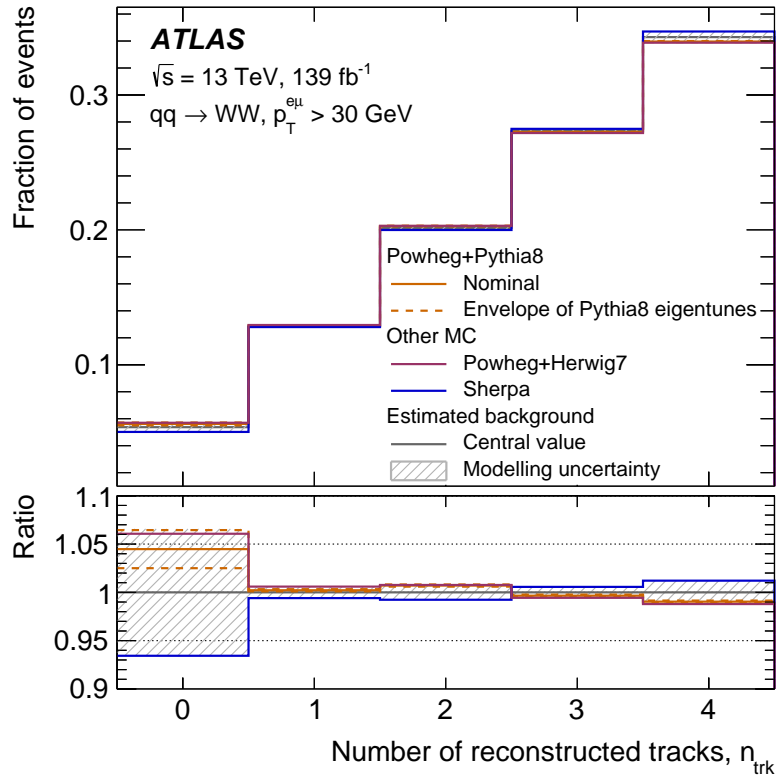
Figure 7.7: The normalised charged track multiplicity distribution for inclusive W^+W^- production, as predicted by Powheg+Pythia8, Powheg+Herwig and Sherpa Monte Carlo samples, with the charged track multiplicity reweighting applied. The Powheg+Pythia8 sample includes the envelope from the AZNLO eigentunes. Good agreement is seen for the $0 < n_{trk} < 5$ region, however a large variation is seen for the $n_{trk} = 0$ bin. The $\gamma\gamma \to WW$ analysis takes the average value of the predictions to be the background contribution form inclusive W^+W^- production (dark grey line) and the total systematic uncertainty is taken to be the full range of the Monte Carlo predictions (grey hatched band). The lower pannel shows the ratio of each Monte Carlo sample to the estimated value of inclusive W^+W^- [1].

Figure 7.8 shows the difference between the diboson Powheg+Pythia8 and Sherpa samples (listed in Chapter 6 Section 6.4.1) before and after the charged particle multiplicity reweighting is applied. Figure 7.8(a) shows the comparison for the nominal dilepton selection in the $e\mu$ channel. Whilst Figures 7.8(b) and 7.8(c) show the comparison for the three and four lepton selections, respectively. The bottom panel in each figure shows the ratio of Sherpa to Powheg+Pythia8. The black lines indicate the ratio before the reweighting has been applied and the red lines indicate the ratio after the reweighting has been applied. These figures illustrate that there is a large disagreement between the Monte Carlo generators before the charged particle multiplicity reweighting is applied. The agreement between the Monte Carlo generators improves after the reweighting has been applied. This trend is seen for both the two, three and four lepton selections. It mirrors the trend seen for the selection of Drell-Yan events in Figure 7.1, which shows that after the charged particle multiplicity reweighting has been applied, the agreement

between the Monte Carlo generators improves and also that that the agreement between Monte Carlo and data improves. It is assumed that with the addition of the missing background contribution (see Section 7.4), the modelling of the three and four lepton selections would also move towards the data, after the application of charged particle multiplicity reweighting.
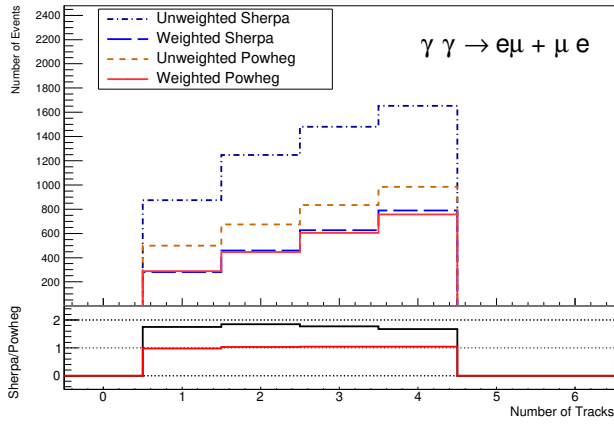
(a)
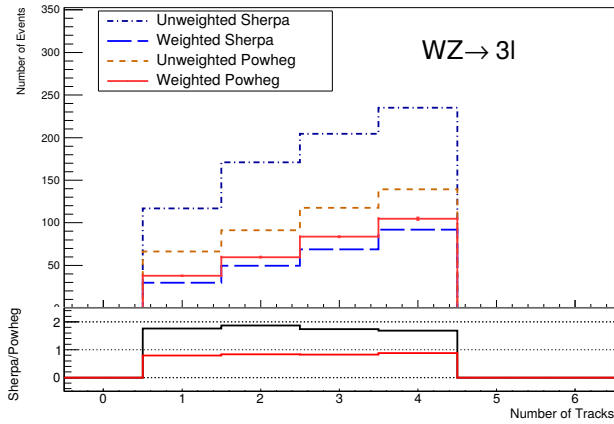
(b)
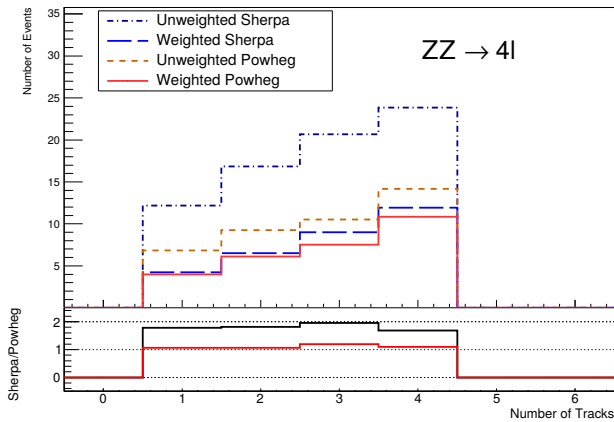
(c)

Figure 7.8: The normalised distribution of the charged track multiplicity before and after the charged particle multiplicity reweighting is applied. The figures show the comparison between the Powheg+Pythia8 and Sherpa Monte Carlo samples and the bottom panel displays the ratio between the two samples before (black) and after (red) the reweighting has been applied. a) Shows the comparison for the nominal dilepton selection in the $e\mu$ channel. b) Shows the comparison for the three lepton selection. c) Shows the comparison for the four lepton selection.

134

Chapter 8

Determining the Exclusivity Scale Factor

This chapter will describe the final data-driven correction applied in the $\gamma\gamma \to WW$ analysis - the exclusivity scale factor, S_{Excl}. The exclusivity scale factor is applied to the simulated HERWIG7 signal samples, which do not account for contributions from the inelastic production mechanisms. Contributions from the inelastic production mechanisms produce additional charged particles, causing the event to be rejected by the exclusivity requirement and therefore a subsequent reduction of the measured cross section, compared to what is expected theoretically.

The exclusivity scale factor is derived using a $\gamma\gamma \to ll$ sample collected from data. It is calculated by the ratio of the number of exclusive events in data to the number of predicted exclusive events. This is realised by studying the invariant mass distribution and then subtracting the yield in background from the yield in data, divided by the yield of signal, as shown in Equation 8.1.

$$S_{Excl} = \frac{N_{data} - N_{bkg}}{N_{Excl}} \tag{8.1}$$

The data-driven approach used to calculate the exclusivity scale factor estimates N_{bkg} using a template model in data and N_{Excl} is given by simulated photon-induced events.

By its essence, the exclusivity scale factor accounts for the contribution to the observed events from semi- and double-dissociative events, where the incoming photon is radiated off the partons inside the proton, as well as for additional proton-proton rescatterring effects that occur after the photons have been emitted. The probability that the incoming protons remain intact and do not break up as a result of additional soft QCD rescattering

effects is given by the survival factor, as described in Chapter 6 Section 6.2.1. The survival factor cannot be calculated from first principles but its physical effects are included in the exclusivity scale factor. There is no way to experimentally distinguish the two contributions to the exclusivity scale factor and therefore there is no analytical way of relating the survival factor to the exclusivity factor.

This chapter describes the techniques used by the author of this thesis to determine the exclusivity scale factor.

8.1 Control Sample Selection

The exclusivity scale factor is derived from a control sample using photon-induced dilepton production. At the LHC, this process occurs when a photon is radiated off each of the incoming protons, $pp(\gamma\gamma) \to p^{(*)}l^+l^-p^{(*)}$ - where $p^{(*)}$ denotes the final state proton remaining intact or fragmenting, after it has emitted a photon. This process can occur via elastic or dissociative production mechanisms, thus is very similar to photon-induced W^+W^- production [44]. The exclusivity scale factor is derived using photon-induced dilepton events so that the final scale factor is as unbiased as possible.

Events are selected using the same preselection as detailed in Chapter 6 Section 6.4.2, with only same flavour final states considered. To increase the sample size, the exclusivity scale factor is studied in the combined ee and $\mu\mu$ channel. The exclusivity requirement is applied and the dilepton invariant mass is required to be greater than 160 GeV in order to resemble the kinematic threshold of $\gamma\gamma \to WW$ production. The selection requirements for the preselection and control sample are summarised in Table 8.1

Where simulated $\gamma\gamma \to ll$ samples are used, all corrections used in the nominal event selection are applied (as described in Chapter 6 Section 6.4.5). This control sample is considered to be independent from the $\gamma\gamma \to WW$ signal sample since the predicted event count of the $\gamma\gamma \to ll$ process is approximately 66 times greater than the predicted event count for the $\gamma\gamma \to WW$ process with same flavour final states.

8.2 The Estimation of Background Contributions in the $\gamma\gamma \to ll$ Control Region

A template method is used to estimate the contribution of background processes in the control sample by employing the distribution of the invariant mass of the dilepton pair. Figure 8.1 shows the invariant mass distribution of the control sample in data and Monte

Reconstructed Object	Selection
	Preselection
Tracks	Tight Primary
	$d0 < 1mm$
electrons	Medium Likelihood
	Loose Isolation
	$|\eta| < 2.47$ (excluding $1.37 < |\eta| < 1.52$)
	$E_T > 20$ GeV
	$d_0/\sigma_{d_0} < 5.0$
muons	Medium Quality
	Loose Isolation
	$|\eta| < 2.5$
	$E_T > 20$ GeV
	$d_0/\sigma_{d_0} < 3.0$
p_T^l	leading lepton > 27 GeV
	sub-leading lepton > 20 GeV
m_{ll}	> 20 GeV
	Control Sample Selection
Dilepton Charge	Opposite Charge
Dilepton Flavour	Same Flavour
m_{ll}	> 160 GeV

Table 8.1: A summary of the preselection requirements and control sample requirements, used to select events for determining the exclusivity scale factor.

Carlo with the exclusivity requirement applied[1]. Figure 8.1 shows that some Drell-Yan events are still select with the control sample selection, however the contribution from these events falls off steeply with increased values of invariant mass. For higher values of invariant mass, the $\gamma\gamma \to ll$ process becomes the largest contribution in the control sample selection. Furthermore, Figure 8.1 shows that the agreement between data and Monte Carlo is good around the Z mass peak, where Drell-Yan events dominate; however it worsens for higher values of invariant mass. the exclusivity scale factor aims to correct for this discrepancy.

In order to construct the background template, the processes that contribute to the control sample must be considered. The primary source of background in the control region is Drell-Yan production. Since Drell-Yan production is a quark-induced process, it is usually associated with a large track multiplicity and so is suppressed when the exclusivity requirement is applied. Relaxing the selection on the number of additional charged tracks therefore leads to an increase in the number of background Drell-Yan events and a decrease in the number of exclusive signal events.

---

[1]The exclusivity requirement stipulates no charged tracks in addition to the tracks of the selected leptons, $n_{\text{trk}} = 0$. This requirement, first introduced in Chapter 6 Section 6.4.3, helps to select photon-induced events.
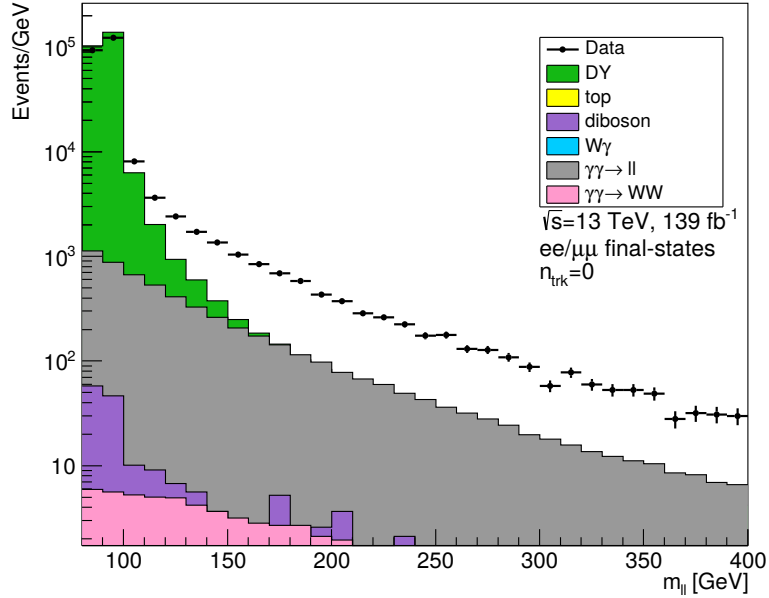
Figure 8.1: The distribution of the invariant mass with the exclusivity requirement applied shown for the control sample selection in data and Monte Carlo, in the combined ee and $\mu\mu$ channel. The distributions are normalised to the Z mass peak (83.5 GeV < m_{ll} < 98.5 GeV).

An estimate of the background can be extracted for a selection on the track multiplicity, $n_{\text{trk}} > 0$, if the number of exclusive events is adequately small and the shape of the invariant mass distribution is still representative of that when the exclusivity requirement is applied.

First the shape of the invariant mass distribution is studied, in bins of charged track multiplicity, to establish if this distribution is suitable for the basis of the template model. Then the relative contributions of signal and background processes are studied, also in bins of charged track multiplicity, in order to find a selection that enhances the background sufficiently.

8.2.1 The Shape of the Invariant Mass Distribution

The exclusivity scale factor is extracted using the invariant mass distribution, under the assumption that the shape of this distribution in background is independent of the charged track multiplicity. Figure 8.2 shows the invariant mass distribution for the $n_{\text{trk}} = 0, 2, 5, 7, 10$ selections for all Monte Carlo background samples[2] (Figure 8.2(a)) and for data (Figure 8.2(b)). Both plots show the invariant mass distribution for the combined ee and $\mu\mu$ channel.

---

[2]A list of the Monte Carlo background samples can be found in Chapter 6, Section 6.4.1.
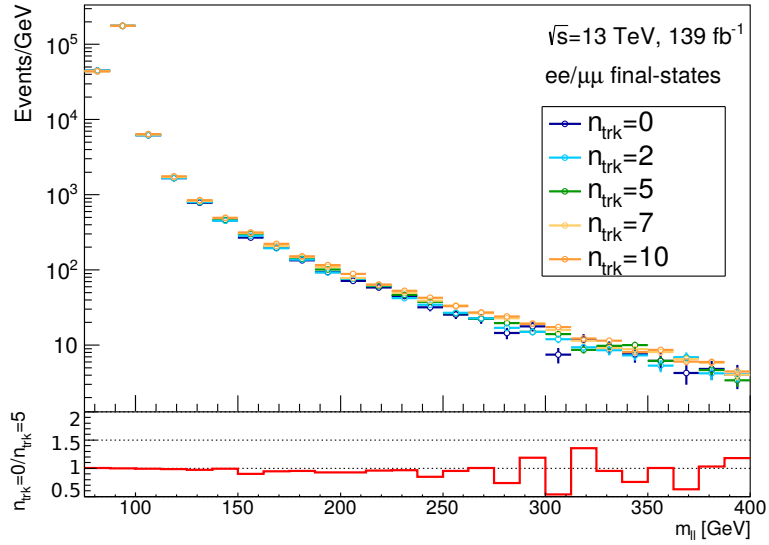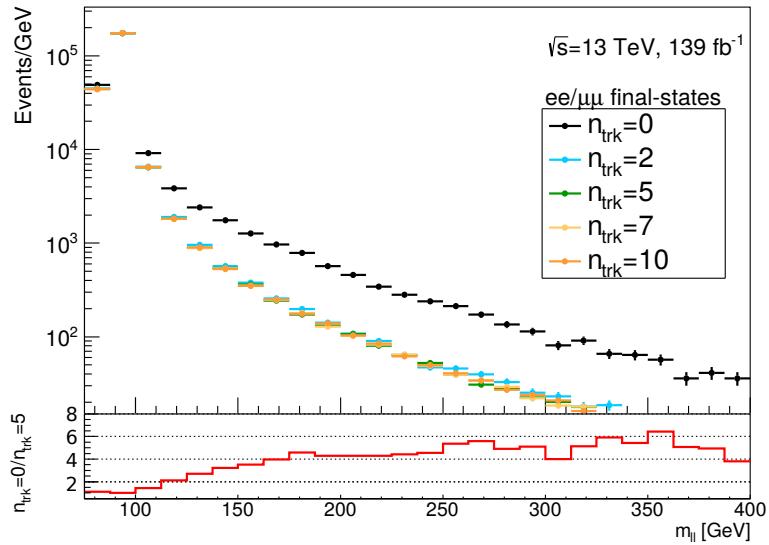
Figure 8.2: The invariant mass distribution with the exclusivity requirement applied in the combined ee and $\mu\mu$ channel and normalised to the Z mass peak (83.5 GeV $< m_{ll} < 98.5$ GeV). The plots show the shape of the distribution for different selections on the charged track multiplicity. a) shows the distribution for all Monte Carlo samples and b) shows the distribution for data. The lower panel shows the ratio of the $n_{\mathrm{trk}} = 0$ selection to the $n_{\mathrm{trk}} = 5$ selection.

Process	Percentage Contribution [%]										
	$n_{\text{trk}}=0$	$n_{\text{trk}}=1$	$n_{\text{trk}}=2$	$n_{\text{trk}}=3$	$n_{\text{trk}}=4$	$n_{\text{trk}}=5$	$n_{\text{trk}}=6$	$n_{\text{trk}}=7$	$n_{\text{trk}}=8$	$n_{\text{trk}}=9$	$n_{\text{trk}}=10$
$\gamma\gamma \to ll$	53.20	9.27	3.29	1.73	1.07	0.72	0.51	0.37	0.30	0.24	0.20
$\gamma\gamma \to WW$	1.37	0.21	0.07	0.04	0.03	0.02	0.01	0.01	0.01	0.01	0.01
$Z \to ll$	43.90	88.08	93.80	95.04	95.55	96.02	96.31	96.47	96.49	96.43	96.16
$Z \to \tau\tau$	0.04	0.06	0.08	0.09	0.07	0.07	0.04	0.03	0.01	0.01	0.00
Inclusive WW	1.27	1.73	1.97	2.07	2.18	1.76	1.58	1.15	0.81	0.52	0.24
$W\gamma$	0.03	0.12	0.06	0.18	0.10	0.07	0.03	0.04	0.10	0.09	0.10
Others	0.19	0.53	0.73	0.86	1.00	1.34	1.52	1.93	2.28	2.70	3.29
Signal Contamination	54.57	9.48	3.36	1.77	1.10	0.74	0.52	0.38	0.31	0.25	0.20

Table 8.2: The relative contributions of each physics process for different selections on the charged track multiplicity. The figures in this table were obtained using all available Monte Carlo samples in the combined ee and $\mu\mu$ channel and for $m_{ll} > 160$ GeV.

The distribution in Monte Carlo shows a similar shape for all five track selections. In comparison, the distribution in data shows a difference in shape between the exclusive track selection ($n_{\text{trk}} = 0$) and track selections of higher multiplicity. This difference can be attributed to the contributions from dissociative channels, which are not modelled in the Monte Carlo samples (see Chapter 6 Section 6.4.1).

The consistency of the shape of the invariant mass distribution for higher values of charged track multiplicity validates the assumption that the shape of this distribution is independent of the number of additional charged tracks. Consequently, the template model of background in data can be constructed using the invariant mass distribution for a given track multiplicity selection.

8.2.2 The Relative Contributions of Signal and Background Processes

An estimate of the background contribution in data can be extracted using a data template of the invariant mass distribution only if the number of photon-induced events is adequately small. In order to find this point, all available Monte Carlo samples are used to study the relative contributions for each process as a function of the number of tracks. Table 8.2 shows the relative contributions as predicted by the Monte Carlo in the combined ee and $\mu\mu$ channel for $m_{ll} > 160$ GeV. In this table the category *Others* refers to small contributions from hWW, ZZ, WZ, $t\bar{t}$ and Wt events. Table 8.2 illustrates the how the number of exclusive events rapidly falls with an increasing number of tracks.

The relative contributions as predicted by the Monte Carlo, for each physics process contributing to the control sample, are used to define a selection for data in which background processes will dominate. The background estimation is derived from data

Process	Percentage Contribution [%]							
	88.5−93.5 GeV	86−96 GeV	83.5−98.5 GeV	81−101 GeV	78.5−103.5 GeV	76−106 GeV	73.5−108.5 GeV	71−111 GeV
$\gamma\gamma \to ll$	0.35	0.49	0.66	0.83	1.01	1.20	1.39	1.58
$\gamma\gamma \to WW$	0.00	0.00	0.00	0.01	0.01	0.01	0.01	0.01
$Z \to ll$	96.61	99.47	99.30	99.12	98.93	98.74	98.54	98.34
$Z \to \tau\tau$	0.00	0.00	0.00	0.01	0.01	0.01	0.02	0.02
Inclusive WW	0.00	0.01	0.01	0.01	0.01	0.01	0.01	0.01
$W\gamma$	0.00	0.00	0.00	0.00	0.00	0.00	0.00	0.00
Others	0.04	0.03	0.03	0.02	0.03	0.03	0.03	0.04
Signal Contamination	0.35	0.49	0.66	0.84	1.02	1.21	1.40	1.59

Table 8.3: The relative contributions of each physics process within windows of varying size, centred around the Z mass peak. The figures in this table were obtained using all available Monte Carlo samples in the combined ee and $\mu\mu$ channel with the exclusive track selection applied.

that passes the control sample selection but with the exclusivity requirement replaced by a condition of $n_{\mathrm{trk}} = 5$. The 5-track selection is the first point at which the signal contamination drops below 1% and it is used as the nominal selection for the background contribution in the calculation of the exclusivity scale factor.

8.2.3   Normalisation of the Background Template

The next step in this data-driven method for the estimation of background is to normalise the dilepton invariant mass distribution of the chosen background data selection, to the Z mass peak of the exclusive track selection, $n_{\mathrm{trk}} = 0$, in data. Table 8.3 shows the relative contributions for each physics process for varying normalisation windows, all centred around the Z mass peak. As is the case for Table 8.2, the *Others* category in Table 8.3 refers to small contributions from hWW, ZZ, WZ, $t\bar{t}$ and Wt events.

A normalisation window of ± 5 GeV of the Z mass, 83.5 GeV$< m_{ll} < 98.5$ GeV, is chosen, because this in this mass region there is a very high prevalence of the dominant source of background events - 99.30% of events originate from Drell-Yan production. Additionally, the Monte Carlo predicts no contribution from photon-induced W^+W^- events in this mass region and the contribution from exclusive dilepton events is less than 1%.

The invariant mass distribution for the background track selection, $n_{\mathrm{trk}} = 5$, is normalised to the Z mass peak of the exclusive track selection in data. The exclusivity scale factor is evaluated for the region of $m_{ll} \geq 160$ GeV, as this is the threshold for WW production. Figure 8.3 shows the normalised invariant mass distributions for both data and Monte Carlo. The normalisation and evaluation mass regions are indicated by the dashed vertical lines.
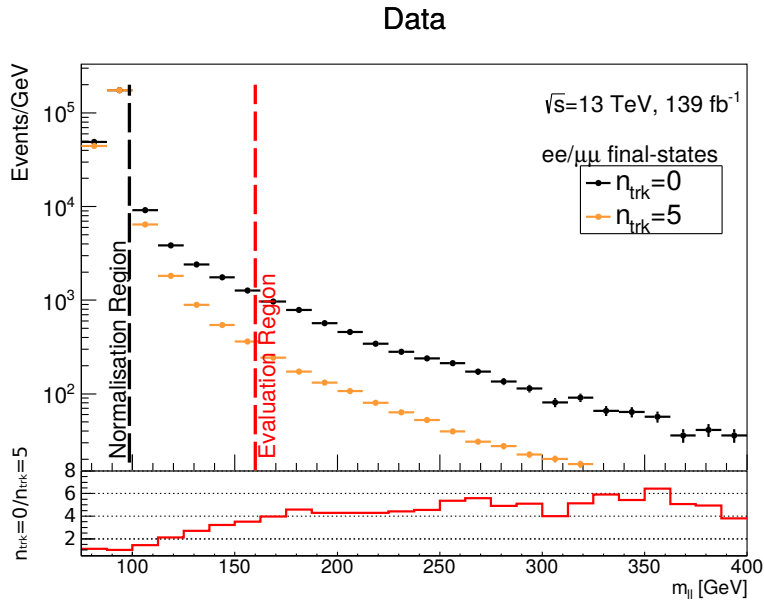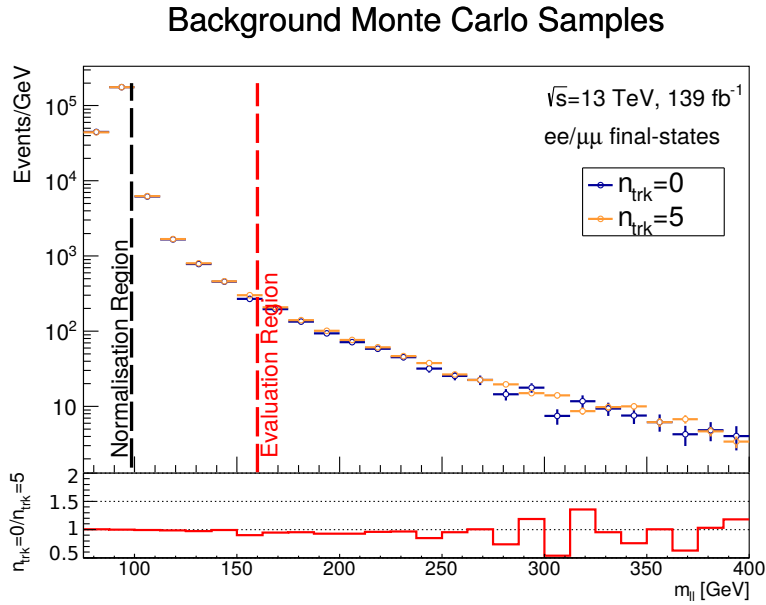
Figure 8.3: Shown are the invariant mass distributions of the exclusive and background track selections in the combined ee and $\mu\mu$ channel. Each distribution is normalised to a region of ± 5 GeV of the Z mass peak for the exclusive track selection in data. The normalisation region is indicated by the black dashed vertical line, whilst the evaluation region is on the threshold of WW production as indicated by the red dashed vertical line. a) shows the distributions in data and b) shows the distributions in Monte Carlo. The shape of the background selection in data matches the shape of the Monte Carlo distributions. The lower panel shows the ratio of the $n_{\mathrm{trk}} = 0$ selection to the $n_{\mathrm{trk}} = 5$ selection.

8.3 Extracting the Exclusivity Scale Factor Using the Template Model

Now that a template model for the contribution of background processes in data has been found, Equation 8.1 can be adjusted as follows:

$$S_{Excl} = \frac{1}{N_{Excl}^{MC}} \left(N_{data}(n_{\text{trk}} = 0) - N_{data}(n_{\text{trk}} = 5) \cdot \frac{N(n_{\text{trk}} = 0, Z_{\text{window}})}{N(n_{\text{trk}} = 5, Z_{\text{window}})} \right) \quad (8.2)$$

Where N_{Excl}^{MC} is the number of exclusive events predicted by the Monte Carlo and Z_{window} is the normalisation region of 83.5 GeV$< m_{ll} <$ 98.5 GeV. The normalisation factor is denoted by $\frac{N(n_{\text{trk}}=0,Z\text{window})}{N(n_{\text{trk}}=5,Z\text{window})}$. The nominal normalisation factor is equal to 0.16.

8.4 Systematics

It is important to note that the data-driven method has a number of sources of systematic error that will now be addressed. For instance, the nominal background selection has some contribution from exclusive processes as shown in Table 8.2. In order to quantify this source of systematic error, the exclusivity scale factor is studied for an alternate track selection, $n_{\text{trk}} = 2$. A 2-track systematic selection is chosen since this is approximately half-way between the exclusive track selection and the nominal background track selection used in the template model. The contribution from exclusive processes amounts to 3.36% of events for the systematic background track selection. This is approximately 4.5 times more signal contamination than for the nominal background track selection. The systematic uncertainty associated with the track selection of the background template is calculated as the relative difference between the exclusivity scale factor given by the nominal and systematic track selections. The systematic track selection yields an uncertainty of ±3.61%.

Varying the track selection alone does not account for the contribution of exclusive events in the normalisation range. Therefore a further source of systematic error originates from the width of the normalisation window. The systematic error associated with the normalisation region can be understood by studying the relative contributions of the Monte Carlo with the exclusive track selection applied, for varying normalisation windows centred around the Z mass peak as shown in Table 8.3. A systematic normalisation region of ±15 GeV of the Z mass, $73.5 < m_{ll} < 108.5$ GeV, is chosen. The systematic normalisation factor is equal to 0.31. 1.40% of events in this mass region originate from exclusive events. This figure is about twice as large as the number of exclusive events contributing in the nominal normalisation region. The systematic uncertainty associated

with the normalisation of the background template is calculated as the relative difference between the exclusivity scale factor given by the nominal and systematic normalisation regions. The systematic normalisation region yields an uncertainty of $\pm 1.11\%$.

The dilepton invariant mass distribution for both the exclusive and systematic background track selections are shown in Figure 8.4 for both Monte Carlo and data. The systematic normalisation region is indicated by the dashed vertical black line. For the systematic variations, the exclusivity scale factor is still evaluated for $m_{ll} \geq 160$ GeV.

Finally, an additional transfer uncertainty must be considered to represent any potential differences between $\gamma\gamma \to ll$ events, used to derive the exclusivity scale factor, and $\gamma\gamma \to WW$ events, for which the exclusivity scale factor is applied. Differences between these two exclusive processes may occur due to the mass-dependence of rescattering effects. Nominally, the exclusivity scale factor is evaluated at the threshold of WW boson production, $m_{ll} \geq 160$ GeV. The transfer uncertainty is computed by varying the lower bound on the evaluation region of the exclusivity scale factor and taking the value that produces the largest variation from the nominal exclusivity scale factor. The lower bound of the dilepton invariant mass was varied from 100 GeV to 400 GeV in steps of 10 GeV. Table 8.4 shows how the exclusivity scale factor varies for the different evaluation regions. The ensuing transfer uncertainty is found to be $\pm 11.20\%$. The maximal value of the exclusivity scale factor is found near to the threshold of WW boson production. This is an expected effect, as studies of the exclusivity scale factor have shown that its value typically decreases with energy. This is effect is likely to be caused by a combination of kinematic effects, an increases of WW contribution, and the difference between the photon parton distribution function and the Equivalent Photon Approximation. Further studies are needed to fully understand how each of these factors affect the value of the exclusivity scale factor.

The transfer uncertainty is only applicable to the scaling of the $\gamma\gamma \to WW$ process and consequently affects the measured signal strength and any cross-section predictions made using the exclusivity scale factor. It does however, cancel out in the measurement of the fiducial cross-section because the fiducial cross section is obtained from the product of the signal strength parameter and the predicted cross-section [1].

The uncertainties from the track selection and normalisation region are added together in quadrature along with the statistical uncertainty of the exclusivity scale factor to give a total uncertainty of $\pm 4.19\%$.
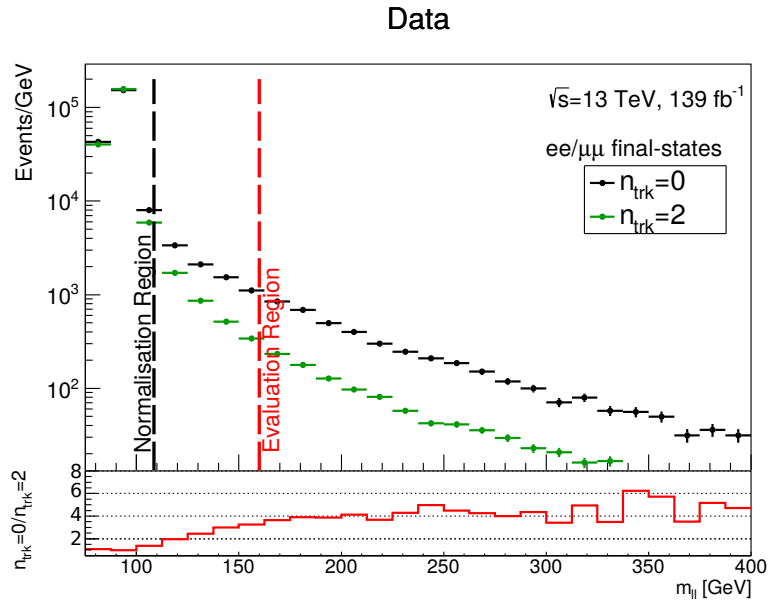
(a)
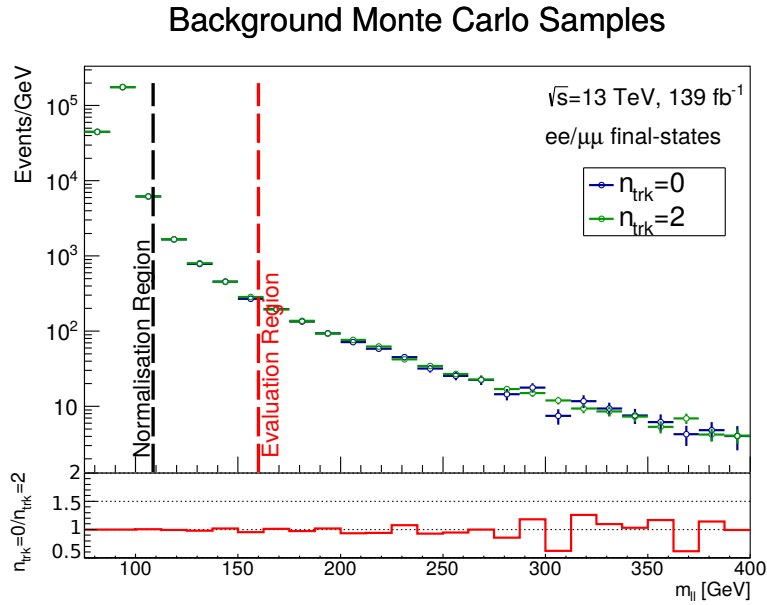
(b)

Figure 8.4: Shown are the invariant mass distributions of the exclusive and systematic background track selections in the combined *ee* and *μμ* channel. Each distribution is normalised to a systematic normalisation region of ±15 GeV of the *Z* mass peak for the exclusive track selection in data. The systematic normalisation region is indicated by the black dashed vertical line, whilst the evaluation region is on the threshold of *WW* production as indicated by the red dashed vertical line. a) shows the distributions in data and b) shows the distributions in Monte Carlo. The lower panel shows the ratio of the $n_{\mathrm{trk}} = 0$ selection to the $n_{\mathrm{trk}} = 5$ selection.

m_{ll} Lower Bound [GeV]	Exclusivity Scale Factor	Variation From Nominal Value [%]
100	3.52 ± 0.05	-1.90
110	3.55 ± 0.04	-1.13
120	3.57 ± 0.05	-0.42
130	3.58 ± 0.05	-0.03
140	3.60 ± 0.06	$+0.37$
150	3.58 ± 0.06	-0.07
160	3.59 ± 0.06	0.00
170	3.56 ± 0.07	-0.76
180	3.52 ± 0.07	-1.81
190	3.44 ± 0.08	-4.03
200	3.43 ± 0.09	-4.24
210	3.39 ± 0.09	-5.37
220	3.42 ± 0.10	-4.58
230	3.42 ± 0.10	-4.71
240	3.39 ± 0.11	-5.40
250	3.42 ± 0.12	-4.58
260	3.35 ± 0.12	-6.53
270	3.35 ± 0.13	-6.61
280	3.31 ± 0.14	-7.65
290	3.25 ± 0.14	-9.25
300	3.23 ± 0.15	-9.97
310	3.33 ± 0.16	-7.15
320	3.26 ± 0.16	-9.03
330	3.24 ± 0.17	-9.78
340	3.22 ± 0.18	-10.30
350	3.23 ± 0.19	-9.84
360	3.18 ± 0.19	-11.20
370	3.21 ± 0.20	-10.44
380	3.22 ± 0.21	-10.15
390	3.19 ± 0.22	-11.10
400	3.19 ± 0.22	-10.94

Table 8.4: This table shows the value of the exclusivity scale factor and associated statistical uncertainty for varying values of the lower bound of the evaluation region and the variation as a percentage from the nominal value of the exclusivity scale factor.

8.5   Results

The data-driven technique to calculate the exclusivity scale factor yields:

$$S_{Excl} = 3.59 \pm 0.06(\text{stat.}) \pm 0.14(\text{syst.})$$

This value agrees with the expected value calculated using the MG_AMC@NLO Monte Carlo samples, which include contributions from both the elastic and dissociative channels (see Chapter 6 Section 6.4.1.2). Figure 8.5 shows the invariant mass distributions of the combined ee and $\mu\mu$ channel for the exclusive selection in data and the background track
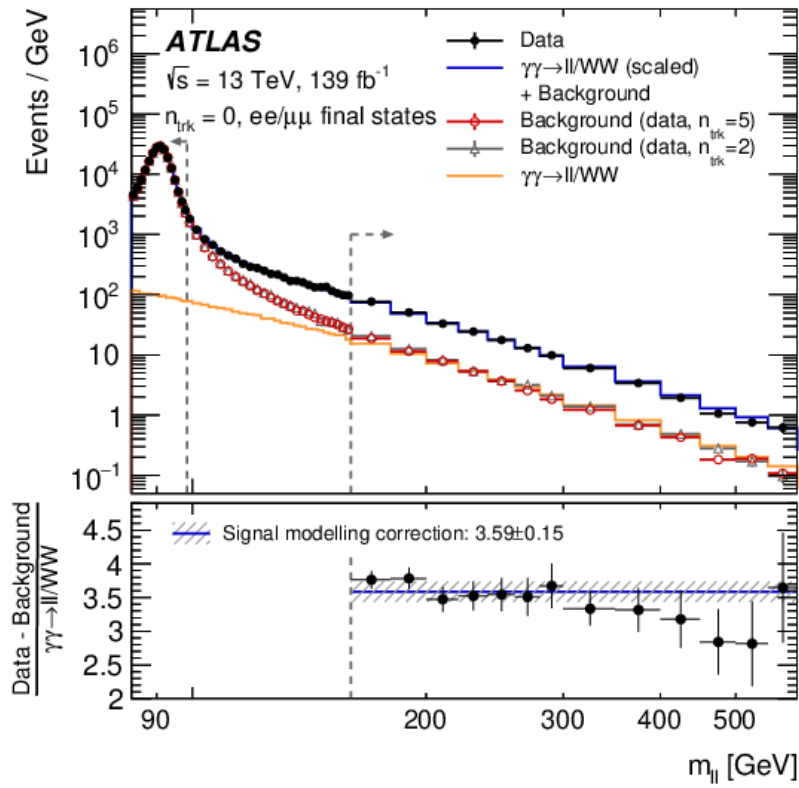
Figure 8.5: The invariant mass distribution, normalised to the Z mass peak, shown for the control sample selection for data (black markers), simulated exclusive events (orange line) and for the nominal (red markers) and systematic (grey markers) track selections in data. The normalisation and evaluation regions are indicated by the dashed vertical lines. The simulated exclusive sample, scaled by the exclusivity scale factor is shown by the dark blue line. The lower panel shows the exclusivity scale factor as a function the lower limit of the invariant mass [1].

selections in data. Also shown are the distributions of the simulated exclusive processes both before and after the exclusivity scale factor is applied. There is a lower panel which illustrates how the exclusivity scale factor varies as a function of the invariant mass.

Chapter 9

Signal Extraction and Cross Section Measurement

The fiducial cross section of the photon-induced W^+W^- process is found by performing a profile likelihood fit to the estimated signal and background event yields. The likelihood of observing signal events for a particular distribution, x, is constructed using a Poisson distribution:

$$L(\boldsymbol{x}; \mu, s, b) = \frac{(\mu s + b)^N}{N!} e^{-(\mu s + b)} \prod_{i}^{N} \left(f_s P_s(x_i; \boldsymbol{\theta}) + f_b P_b(x_i; \boldsymbol{\theta}) \right) \qquad (9.1)$$

where s and b represent the predicted signal and background event yields; and f_s and f_b are the fraction of signal and background events. P_s and P_b correspond to the probability density functions of the distribution x. Finally, μ is the signal strength parameter:

$$s = \mu s_{theory} \qquad (9.2)$$

The signal strength parameter defines how strong the observed signal is compared to the theoretical prediction [147].

The estimated signal and background yields, and the normalisation of the dominant background processes are left to be free parameters. The remaining background processes are fixed. The systematic uncertainties associated with the analysis, along with any other parameters not directly related to the cross section measurement, are viewed as nuisance parameters (denoted by $\boldsymbol{\theta} = (\theta_1...\theta_n)$). A profile likelihood ratio can be constructed

$$\lambda(\mu) = \frac{L(\boldsymbol{x}; \mu, \hat{\hat{\boldsymbol{\theta}}})}{L(\boldsymbol{x}; \hat{\mu}, \hat{\boldsymbol{\theta}})} \qquad (9.3)$$

	SR	CR1	CR2	CR3
Kinematic Selection	$p_T^{e\mu} > 30$ GeV $n_{\mathrm{trk}} = 0$	$p_T^{e\mu} < 30$ GeV $1 \leq n_{\mathrm{trk}} \leq 4$	$p_T^{e\mu} > 30$GeV $1 \leq n_{\mathrm{trk}} \leq 4$	$p_T^{e\mu} < 30$ GeV $n_{\mathrm{trk}} = 0$
$\gamma\gamma \to WW$	174 ± 20	24 ± 5	95 ± 19	45 ± 6
$\gamma\gamma \to ll$	5.5 ± 0.3	32 ± 7	5.6 ± 1.2	39.6 ± 1.9
Drell-Yan	4.5 ± 0.9	4700 ± 400	105 ± 19	280 ± 40
$qq \to WW$ (including gg and VBS)	101 ± 17	970 ± 150	1700 ± 270	55 ± 10
Non-prompt Leptons	14 ± 14	500 ± 400	220 ± 220	36 ± 25
Other Backgrounds	7.1 ± 1.7	81 ± 15	311 ± 76	1.9 ± 0.4
Total	305 ± 18	6320 ± 130	2460 ± 60	459 ± 19
Data	307	6332	2458	449

Table 9.1: This table shows a summary of the predicted signal and background event yields and the data event yields after the profile likelihood fit, for each kinematic region. The total uncertainties are shown and they include both systematic and statistical uncertainties. The event yields from the "Other Backgrounds" category include WZ and ZZ diboson production, top-quark production and other gluon-induced processes [1].

The numerator in equation 9.3 is the value of the likelihood maximised for the number of observed events in data. Here, the signal strength parameter is fixed and the likelihood is maximised by the conditional maximum likelihood estimator, $\hat{\hat{\boldsymbol{\theta}}}$. In the denominator, both the signal strength parameter and the nuisance parameters are fitted simultaneously, and the likelihood is maximised for the number of events observed in data without constraint. Here, the likelihood is maximised by likelihood estimators for both the signal strength parameter, $\hat{\mu}$, and the nuisance parameters, $\hat{\boldsymbol{\theta}}$ [113, 115].

The integrated event yield for the signal region and four control regionsThe first three control regions are described in Chapter 6 Section 6.4.4 and the final control region is the region used to calculate the exclusivity scale factor in Chapter 8. are used in the fit. The event yield for the $\gamma\gamma \to WW$ process is scaled by a signal strength parameter, in addition to the exclusivity scale factor. The resulting fit rejects the background-only hypothesis with a significance of 6.7 standard deviations [1].

Table 9.1 summarises the predicted number of events for signal and background, for each kinematic region, after the profile likelihood fit has been performed. A total uncertainty, including both statistical and systematic uncertainties, is given for each event yield. The best fit results indicate 132 background events are predicted in the signal region. Also shown is the number of observed data events observed for each kinematic region. A total of 307 events were observed in data in the signal region. The normalisation of the inclusive WW background process is constrained and found to be $1.21^{+0.19}_{-0.23}$ (tot.). The normalisation of the Drell-Yan background process is constrained and found to be $1.16^{+0.10}_{-0.12}$ (tot.).
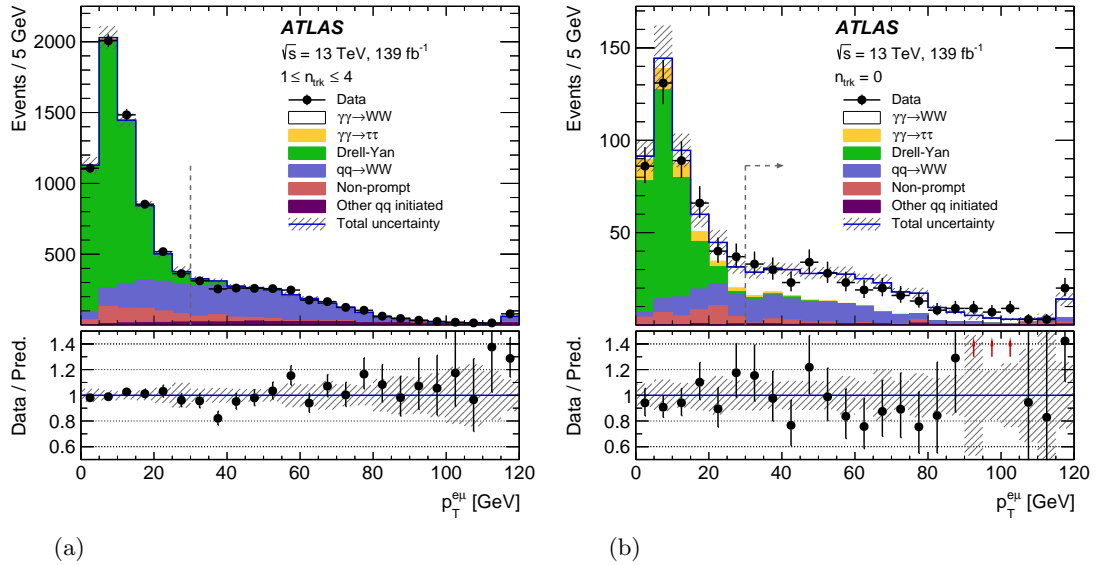
Figure 9.1: The distribution of the transverse momentum of the dilepton pair. a) Shows this distribution for $1 \leq n_{\text{trk}} \leq 4$ tracks and b) shows this distribution for $n_{\text{trk}} = 0$. The dashed vertical line on each plot indicates the transition between the different control regions, and the signal region is shown by the dashed horizontal arrow. The normalisation factors and nuisance parameters extracted from the profile likelihood fit have been applied. The ratio of data to prediction is shown in the lower panel and the total uncertainties are indicated by the hatched band. The final bin in each distribution includes the overflow [1].

Next a fit to data is performed and the background-only hypothesis is rejected with a significance of 8.4 standard deviations and a signal strength of $1.33^{+0.14}_{-0.14}(\text{stat.})^{+0.22}_{-0.17}(\text{syst.})$ is measured relative to the yield of simulated $\gamma\gamma \rightarrow WW$ events, scaled by the exclusivity scale factor. The significance of this fit is enough to establish the observation of photon-induced W^+W^- production in proton-proton collisions.

Two distributions of the transverse momentum of the dilepton pair, with the fitted nuisance parameters and background normalisations, are shown in Figure 9.1. Figure 9.1(a) shows this distribution with a requirement of $1 \leq n_{\text{trk}} \leq 4$ applied, and Figure 9.1(b) shows this distribution with a requirement of $n_{\text{trk}} = 0$ applied. The boundary between the different control regions and the signal regions is indicated by the vertical dashed lines at $p_T^{e\mu} = 30$ GeV.

Figure 9.2 shows the distribution of the number of reconstructed tracks with the requirement that the transverse momentum of the dilepton pair is greater than 30 GeV. The signal region is indicated by the dashed line and arrow on the figure. The background normalisations and the fitted nuisance parameters are included in this figure.

The cross section measurement of the $\gamma\gamma \rightarrow WW$ process is performed in a fiducial region that is similar to the acceptance of the detector. The leptons must originate from

150
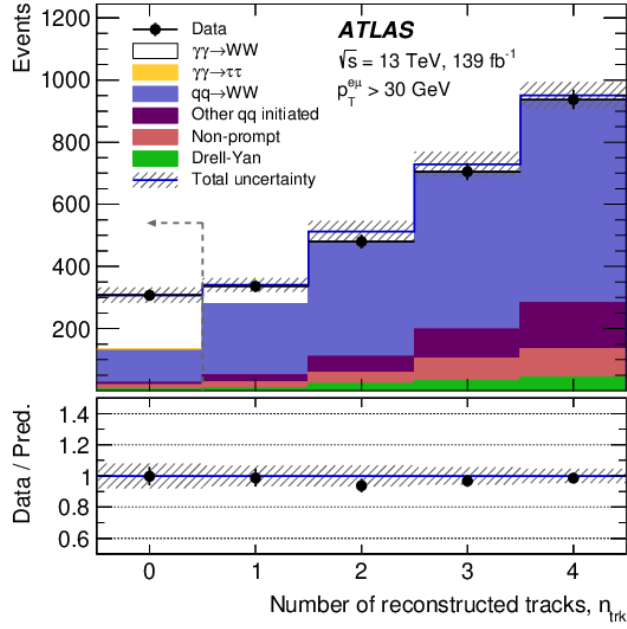
Figure 9.2: This figure shows the distribution of the number of charged tracks associated with the dilepton interaction vertex. The signal region of the photon-induced W^+W^- analysis requires $n_{\mathrm{trk}} = 0$ and is indicated by the dashed line on the plot. Data is shown by the black markers and the simulated processes are shown by the coloured areas. The normalisation factors and nuisance parameters extracted from the profile likelihood fit have been applied. The ratio of data to prediction is shown in the lower panel and the total uncertainties are indicated by the hatched band [1].

W decays, and they are required to have a pseudorapidity less than 2.5 at particle level. The leading lepton is required to have a transverse momentum greater than 27 GeV and the sub-leading lepton must have a transverse momentum greater than 20 GeV. If there are any photons that do not originated from a hadronic decay, in a cone of $\Delta R = 0.1$, around a given lepton, then it is added to the four-momentum of that lepton. Events are selected with two leptons of opposite-sign and different-flavour final states, however W decays into a τ-lepton are not included in the event selection. The selected dilepton pair must have an invariant mass greater than 20 GeV and a transverse momentum greater than 30 GeV. Finally, there can be no additional charged particles with a transverse momentum greater than 500 MeV and with a pseudorapidity less than 2.5 at particle level.

The fiducial cross section of $pp(\gamma\gamma) \rightarrow p^{(*)}W^+W^-p^{(*)}$, with $W^+W^- \rightarrow e^\pm\nu\mu^\mp\nu$, is retrieved from the observed signal strength [1]:

$$\sigma_{meas} = 3.13 \pm 0.31(\text{stat.}) \pm 0.28(\text{syst.}) \text{ fb}$$

The measured cross section from data can be compared to the cross section predicted by the simulated $\gamma\gamma \to WW$ samples, scaled by the exclusivity scale factor [1]:

$$\sigma_{theo} \times (3.59 \pm 0.15(\text{exp.}) \pm 0.39(\text{trans.})) = 2.34 \pm 0.27 \text{ fb}$$

where the uncertainties include all experimental uncertainties and an additional transfer uncertainty, which accounts for the application of the exclusivity scale factor to $\gamma\gamma \to WW$ despite being calculated from $\gamma\gamma \to ll$ events. Chapter 8 Section 8.4 describes how the transfer uncertainty is calculated.

Additionally, a theoretical prediction of the fiducial cross-section can be calculated using MG5_AMC@NLO+PYTHIA8 and the appropriate MMHT2015qed parton distribution functions [37], for either the elastic or inelastic channels. Fiducial requirements are then applied to the output to generate a cross section of $4.3 \pm 1.0(\text{scale}) \pm 0.12(\text{PDF})$ fb. Where the uncertainties relate to the factorisation scale and to the parton distribution functions.

The cross section predicted by MG5_AMC@NLO+PYTHIA8 does not include the additional proton-proton rescattering effects that are quantified by the survival factor and are understood to reduce the fiducial cross-section. Previous measurements of the survival factor have estimated $S^2 = 0.65$ for elastic $\gamma\gamma \to WW$ production [120] and $S^2 = 0.82$ for a two channel eikonal model [148]. Applying these estimations of the survival factor to the cross section predicted by MG5_AMC@NLO+PYTHIA8 gives a new theoretical prediction of 2.8 ± 0.8 fb and 3.15 ± 1.0 fb, respectively. The total uncertainty of each prediction is given by the quadratic sum of the scale and PDF uncertainties. The theoretical predictions are in agreement with the measurement in data.

Chapter 10

Preliminary Studies on New Physics using Effective Field Theory

This chapter discusses how the results from the $\gamma\gamma \to WW$ analysis can be used to constrain extensions of the Standard Model, with the use of EFT (described in Chapter 2 Section 2.3). The studies presented in this chapter are preliminary since they only make use of simulated events at truth-level. This is because Monte Carlo samples that had been passed through detector simulation and reconstruction algorithms, were not available when the study took place. Obtaining such samples required more time and resources than were available to the author. These preliminary EFT studies are intended to identify which EFT operators the $\gamma\gamma \to WW$ analysis is most sensitive to, in order to validate the Monte Carlo generation settings for future, more detailed studies.

Section 10.1 describes how an initial estimate can be placed on the limits of dimension-6 and dimension-8 EFT operators using a naive event counting method. Then, Section 10.2 presents a study of the kinematic distributions of the EFT operators. The results presented in this chapter can be used to guide the direction of a future differential shape analysis, in order to set more stringent limits on the EFT operators.

10.1   An Initial Estimate of Limits on New Physics

Limits can be placed on EFT operators that are sensitive to the $\gamma\gamma \to WW$ process, by calculating the maximum number of possible EFT events that agree with the observed data, when considering the statistical and experimental uncertainties. This section will

describe the method used to calculate an initial estimate of the limits on dimension-6 and dimension-8 EFT operators. The following method does not account for the fiducial cuts applied in the $\gamma\gamma \to WW$ analysis, nor does it account for the shape of the kinematic distributions. The effective Lagrangian can be written as the sum of the Standard Model Lagrangian plus the Lagrangians of the dimension-6 and dimension-8 operators:

$$\mathcal{L}_{eff} = \mathcal{L}_{SM} + \mathcal{L}_{D-6} + \mathcal{L}_{D-8} \tag{10.1}$$

For a given EFT operator, the measured $\gamma\gamma \to WW$ cross section, can be approximated as the square of the effective Lagrangian:

$$\sigma_{meas} \sim (\mathcal{L}_{eff})^2 = (\mathcal{L}_{SM})^2 + (\mathcal{L}_{SM}\frac{c_i}{\Lambda_i^{d-4}}\mathcal{O}_i) + (\frac{c_i}{\Lambda_i^{d-4}}\mathcal{O}_i)^2 \tag{10.2}$$

Where d refers to either dimension-6 or dimension-8.

Equation 10.2 features an interference term between the Standard Model Lagrangian and the EFT Lagrangian, which has a linear dependence on the EFT term, $\frac{c_i}{\Lambda_i^{d-4}}\mathcal{O}_i$. There is also a term with a quadratic dependence on the EFT term, $(\frac{c_i}{\Lambda_i^{d-4}}\mathcal{O}_i)^2$.

The effect a specific operator has on the overall cross section, can be calculated from Equation 10.2 for different values of the free EFT parameter, c_i. Consequently, the measured $\gamma\gamma \to WW$ cross section can also be written in the form of a second order polynomial, with a constant term corresponding to the Standard Model cross section, and a linear and quadratic term for the free EFT parameter:

$$\sigma_{meas} + \delta_{meas} = (\sigma_{SM} + \delta_{SM}) + \frac{c_i}{\Lambda_i^{d-4}} \cdot (\sigma_i + \delta_i) + (\frac{c_i}{\Lambda_i^{d-4}})^2 \cdot (\sigma_i + \delta_i)^2 \tag{10.3}$$

Where δ_x corresponds to the experimental or theoretical uncertainty. The Standard Model is recovered when $c_i = 0$.

The calculation of the naive limits of the anomalous couplings begins by using the MG_AMC@NLO [133] generator with the SMEFTsim package to calculate the theoretical cross section for each sensitive EFT operator, for a given value of the free EFT parameter [149, 150]. The theoretical cross sections are predicted using the SMEFTsim package are given for truth-level, with only parton-level cuts applied. As a result, the theoretical cross sections do not account for detector effects, fiducial cuts or reconstruction efficiencies, but the theoretical cross sections can be used to identify which operators are affected most by the anomalous couplings.

A parton-level cut of $p_T > 20$ GeV is applied to each generated lepton. The truth-level cross sections are converted into an event count using the relation:

$$N = \sigma \cdot L \tag{10.4}$$

Where $L = 139\text{fb}^{-1}$ and equates to the total luminosity recorded by the ATLAS experiment in Run 2.

The reconstruction efficiencies are naively accounted for by scaling the number of events at truth-level to match the number of simulated reconstructed events in the $\gamma\gamma \to WW$ Run 2 analysis, given in Table 9.1. Scaling the truth-level event count in this way, accounts for the reconstruction efficiencies and means the figures can be compared more directly to the actual expectation on the number of reconstructed events[1].

A profile likelihood technique can be used to set initial limits of a free EFT parameter [113]. The expected number of events for each EFT operator, N_{EFT}, is treated as signal in the profile likelihood fit and the number of events predicted by the Standard Model, N_{SM}, is treated as background. The likelihood of observing the measured number of events in data, N_{obs}, can be constructed following a Poisson distribution:

$$L(N_{obs}; \mu) = \frac{(\mu N_{EFT} + N_{SM})^{N_{obs}}}{N_{obs}!} e^{-(\mu N_{EFT} + N_{SM})} \tag{10.5}$$

Where the signal strength parameter, μ is the signal strength of the cross section of the EFT operator. As such, μ is directly related to the free EFT parameter. The profile likelihood is constructed independently for each sensitive EFT operator.

If there are EFT events contributing, their event count must lie within the uncertainty on the agreement between data and the number of events predicted by the Standard Model. The number of events predicted by the Standard Model is allowed to vary between a minimum and maximum values and it is summed with the number of events arising from the EFT operator, to give a total number of expected events.

A constraint on the contribution from the Standard Model is included in the profile likelihood fit, via the use of a nuisance parameter, $\boldsymbol{\theta}$. The constraint follows a Gaussian distribution, $f(\boldsymbol{\theta})$, and is also allowed to vary between the same minimum and a maximum value, as is the case for the number of events predicted by the Standard Model. The mean of the Gaussian constraint is equal to the number of events predicted by the Standard Model and the width of the Gaussian constraint is given by the total uncertainty on the $\gamma\gamma \to WW$ measurement. The total uncertainty includes the statistical error on the

---

[1]This method is approximate and the kinematic cuts applied in the $\gamma\gamma \to WW$ analysis are not implemented in the calculation of the truth-level cross sections.

number of events and the relative systematic uncertainty, which is equal to 8.95%. The final model is the product of the Poisson probability density function and the Gaussian constraint:

$$L(N_{obs}; \mu\boldsymbol{\theta}) = \frac{(\mu N_{EFT} + N_{SM}(\boldsymbol{\theta}))^{N_{obs}}}{N_{obs}!} e^{-(\mu N_{EFT} + N_{SM}(\boldsymbol{\theta}))} f(\boldsymbol{\theta}) \qquad (10.6)$$

The constructed model is tested against the number of observed events in data, based on the principle of rejecting the null hypothesis, H_0. In this context, the null hypothesis includes the predictions of both the Standard Model and new physics from EFT operators, whilst the alternative hypothesis is the background-only hypothesis, H_1, and only contains the predictions of the Standard Model [32].

A profile likelihood ratio can be used to test the agreement between two hypotheses. The profile likelihood ratio tests the likelihood for a hypothesised value of the signal strength parameter, against alternative values. The profile likelihood ratio is given by:

$$\lambda(\mu) = \frac{L(\mu, \hat{\hat{\boldsymbol{\theta}}})}{L(\hat{\mu}, \hat{\boldsymbol{\theta}})} \qquad (10.7)$$

Where $L(\mu, \hat{\hat{\boldsymbol{\theta}}})$ is the likelihood maximised for the number of events observed in data for the hypothesised value of the signal strength parameter. It is maximised by the conditional maximum likelihood estimator, $\hat{\hat{\boldsymbol{\theta}}}$. $L(\hat{\mu}, \hat{\boldsymbol{\theta}})$ is the likelihood maximised for the number of events in observed data without a constraint, it maximised by likelihood estimators for both the nuisance parameter, $\hat{\boldsymbol{\theta}}$, and the signal strength parameter, μ.

The profile likelihood ratio yields a value between 0 and 1. A value of 1 indicates that the hypothesised signal strength parameter, μ, agrees with the maximised likelihood estimator, $\hat{\mu}$, and therefore shows agreement between the data and the hypothesis. Conversely, a value of 0 indicates that the value of the hypothesised signal strength parameter, μ, does not agree with the maximised likelihood estimator, $\hat{\mu}$, and therefore shows poor agreement between data and the hypothesis [115].

In this naive example, the limits on the EFT contribution are calculated in terms of the number of events. The number of EFT events can be fitted directly by setting the signal strength parameter to unity $\mu = 1$. This can be done because the signal strength parameter is intrinsically linked to the free EFT parameter, and hence the number of EFT events.

A test statistic, q is used to decide if new physics is present:

$$q = \begin{cases} -2\ln\frac{L(N_{EFT},\hat{\boldsymbol{\theta}})}{L(\hat{N}_{EFT},\hat{\boldsymbol{\theta}})}, & \text{if } \hat{N}_{EFT} \leq 0 \\ 0, & \hat{N}_{EFT} > N_{EFT} \end{cases} \tag{10.8}$$

The test statistic can be used to find the probability of obtaining results that are at least as incompatible with the hypothesis as the observed data set, under the assumption that the hypothesis is true [151]. This is known as the p-value and can be used to exclude hypotheses if their p-values are below a certain value, α. A confidence interval, with a confidence level of $1 - \alpha$, can be placed on the number of EFT events using the p-value:

$$p = \int_{q,obs}^{\infty} f(q|N_{EFT})dq = \alpha \tag{10.9}$$

A confidence interval is defined as the region in which the target value of the number of signal events is contained. When the p-value of the number of signal events is equal to or less than a value, α. The confidence interval then is defined for a given certainty, $1 - \alpha$, which expresses how likely this result will be reproduced for a repeated experiment. If the null hypothesis is rejected, then an alternative hypothesis is used to explain the data. In this study, the p-value is chosen to be 0.05^2, which corresponds to a confidence level of 95%. The confidence interval in the number of EFT events can be calculated for both the linear and quadratic terms in Equation 10.3. The linear and quadratic confidence intervals can be converted from a number of events into a value of the free EFT parameter using the following relations:

$$c_{lim}^{lin} = c_i \times \frac{N_{lim}}{N_{EFT}} \tag{10.10}$$

$$c_{lim}^{quad} = c_i \times \sqrt{\frac{N_{lim}}{N_{EFT}}} \tag{10.11}$$

Where c_i is the initial value of the free EFT parameter, used to generate the EFT effects at truth-level. N_{EFT} is the number of EFT events, scaled to reco-level. N_{lim} stands for the upper or lower bound of the confidence interval given for the number of signal events. The upper or lower bound of the confidence interval in terms of the free EFT parameter is given by c_{lim}. Equation 10.10 is used to transform the limits from the linear contribution, whilst Equation 10.11 is used to transform the limits from the quadratic contribution.

---

[2]Usually in particle physics a significance of 5σ is needed to declare a discovery, corresponding to a p-value of 2.87×10^{-7}. However, it is standard practice to reject a null hypothesis based on a p-value of 0.05.

10.1.1 Results

A summary of the initial estimates of the limits calculated for a confidence level of 95%, is shown in Figure 10.1 for the dimension-6 and dimension-8 EFT operators that describe the $WW\gamma$ and $WW\gamma\gamma$ vertices (see Chapter 2 Section 2.3). The contribution from the linear EFT term is shown in red and the contribution from the quadratic EFT term is shown in blue. The limits on the $c_{H\square}$ parameter are excluded from the list of dimension-6 operator results because it is highly suppressed and consequently, this method yields very large limits. The $c_{H\square}$ operator is better constrained by other processes, such as Higgs production and decay [152], and therefore will not be discussed further in this thesis.

The 95% confidence limits on the dimension-6 free parameters are shown in Figure 10.1(a). The limits calculated using the linear terms of the EFT operators are shown in red and the limits calculated using the quadratic terms of the EFT operators are shown in blue. The confidence limits calculated using the quadratic terms of the c_W, c_{HDD}, c_{WWW} and c_{HB} parameters are much smaller than the limits calculated using the respective linear terms. However, this is not the case for the c_{HWB}, c_{Hl3} and c_{ll3} parameters, which see smaller limits when the linear term is used in the calculation than for the quadratic term. This effect can be explained by the helicity selection rules that govern the interference between the Standard Model and EFT operators [153]. The helicity constraints mean that for some operators, the linear terms are highly suppressed and it is only the quadratic terms that contribute.

The 95% confidence limits on the dimension-8 free parameters are shown in Figure 10.1(b). The confidence limits calculated using the linear terms of the EFT operators are shown in red and the limits calculated using the quadratic terms of the EFT operators are shown in blue. The black arrows indicate limits that are larger than the scale used in the plot, however the numerical value of these limits are shown in the right-hand column on the plot. For dimension-8 operators, the contribution from the quadratic term dominates across all of the dimension-8 parameters and therefore the limits calculated using the quadratic terms are much smaller than those calculated for the linear terms, as illustrated in Figure 10.1(b). The results of the naive calculation indicate that the $\gamma\gamma \rightarrow WW$ process is most sensitive to the $f_{M,2}$ and $f_{T,5}$ parameters. .

For EFT theories with weak couplings, the contribution from dimension-8 operators is larger than the contribution from dimension-6 operators [153, 154]. The $WW\gamma$ and $WW\gamma\gamma$ vertices are most sensitive to the dimension-8 operators. Therefore, the remaining studies presented in this chapter will focus on the dimension-8 operators and will use 95% confidence limits calculated using the quadratic term.
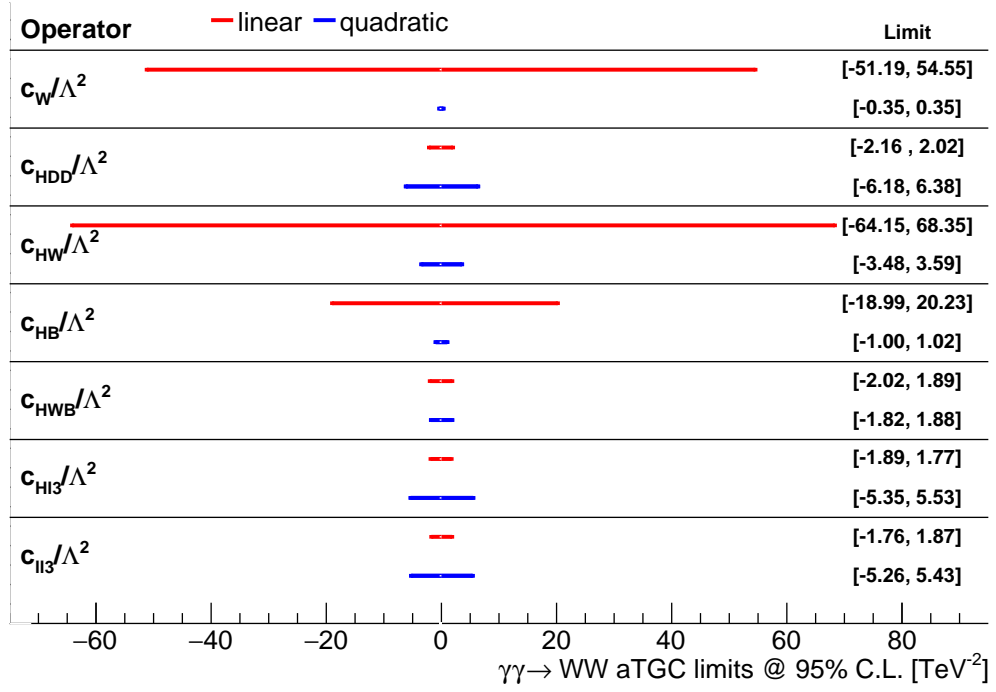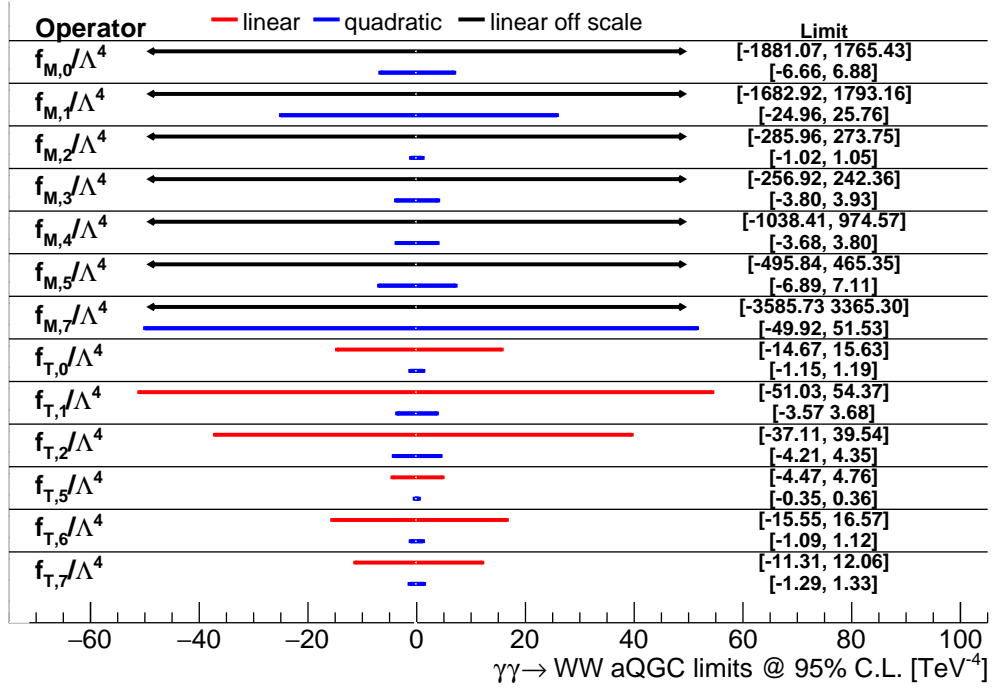
Figure 10.1: A plot summarising the initial estimates of the limits placed on the free EFT parameters using the naive event counting method. The contribution from the linear terms are shown in red and the contribution from the quadratic terms are shown in blue. The black arrows indicate limits calculated using linear terms that are too large for the scale of the plot. a) shows the dimension-6 operators. b) shows the dimension-8 operators.

10.2 Moving Towards A Differential Analysis

The kinematic distributions of the sensitive EFT operators can be studied in an endeavor to improve the initial estimates of the limits on the free EFT parameters. Events are now generated using the MG_AMC@NLO +PYTHIA8 parton shower and processed using a particle-level code [133, 116]. Generating events in this way allows for the kinematic distributions to be studied, and for kinematic cuts, corresponding to those used to define the $\gamma\gamma \to WW$ signal region (see Chapter 6, Section 6.4.2), to be applied. The events are scaled to reco-level, following the same methods used in initial estimates. The fiducial region of the $\gamma\gamma \to WW$ Run 2 data set is replicated by applying kinematic cuts and scaling to reco-level.

The generated kinematic distributions, associated with the quadratic contribution from the dimension-8 operators, are scaled to the initial limits, as calculated in Section 10.1, and then summed with the expected Standard Model distribution. Figure 10.2 shows a comparison of the invariant mass distribution for the Standard Model combined with the effects of the $\mathcal{O}_{M,2}$ and $\mathcal{O}_{T,5}$ operators (plotted in blue), with the nominal Standard Model distribution (plotted in red). The invariant mass distribution of the quadratic contribution from the $\mathcal{O}_{M,2}$ operator is shown in Figure 10.2(a). The distribution is scaled to the naive limit of the $f_{M,2}$ parameter, $c_{lim} = 1.05$ TeV^{-4}. Similarly, the invariant mass distribution of the quadratic contribution from the $\mathcal{O}_{T,5}$ operator is shown in Figure 10.2(b). This distribution is also scaled to the naive limit on the $f_{T,5}$ parameter, derived in Section 10.1, such that $c_{lim} = 0.36$ TeV^{-4}. Both the distributions from the $\mathcal{O}_{M,2}$ and $\mathcal{O}_{T,5}$ operators illustrate that the most of the events arising as a result of EFT, occur in the high mass region of $m_{ll} > 400$ GeV. The invariant mass distributions shown in Figure 10.2 has been re-binned to emphasise the increased number of EFT events in the high mass region.

Similar trends are seen across all 13 of the sensitive dimension-8 operators - there is a general increase in the number of events arising as a result of higher order operators at higher values of invariant mass and transverse momentum. This is because EFT events are suppressed by the energy scale, therefore moving to higher energies, and thus higher invariant masses, leads to increased production.

The rise in the number of EFT events at high energies can be used to define a selection region with an enhanced number of EFT events, in an attempt to improve upon the initial estimates of the limits on the free EFT parameters found in Section 10.1. New limits can be set by studying the event count in the high mass region, $m_{ll} > 400$ GeV, making use of the coarse binning shown in Figure 10.2. The new limits are calculated in this high mass region, following the same naive event counting method detailed in
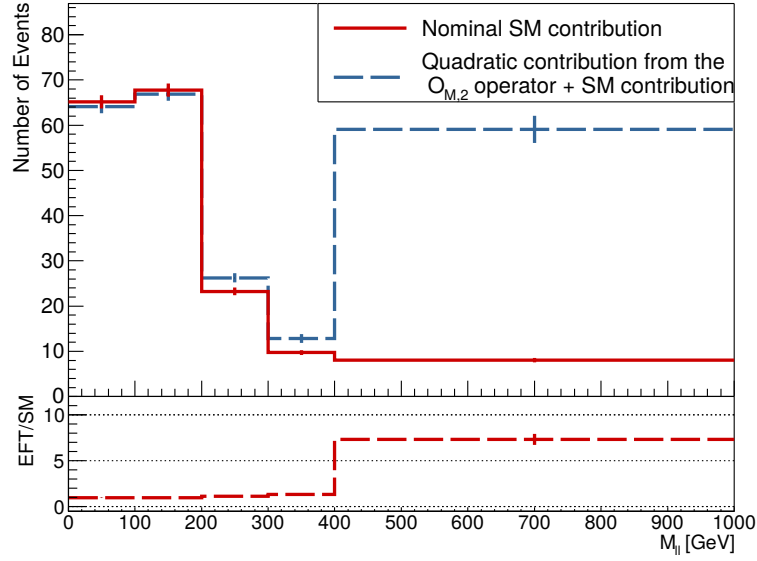
(a)
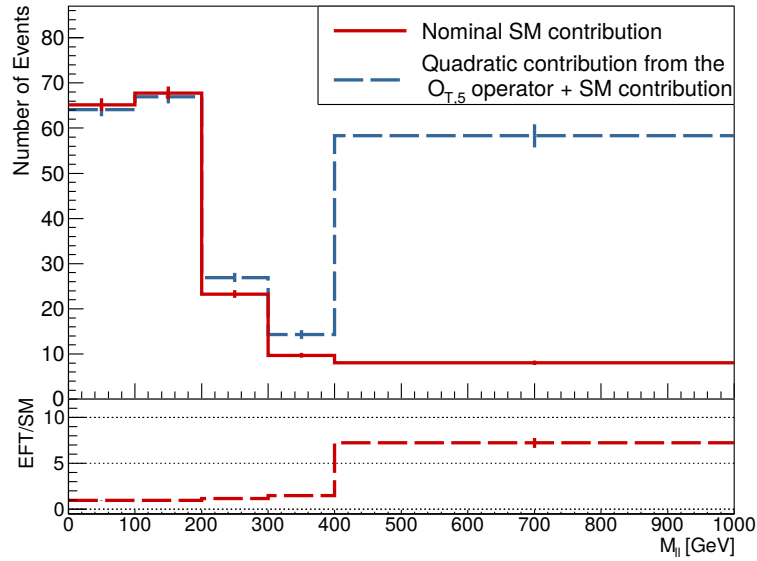
(b)

Figure 10.2: The re-binned invariant mass distribution. a) shows the $\mathcal{O}_{M,2}$ operator summed with the Standard Model distribution (blue), compared to the nominal Standard Model distribution (red). b) shows the $\mathcal{O}_{T,5}$ operator summed with the Standard Model distribution (blue), compared to the nominal Standard Model distribution (red). The bottom panel on each plot shows the ratio of the effect of the EFT operator summed with the Standard Model over the nominal Standard Model distribution.

161
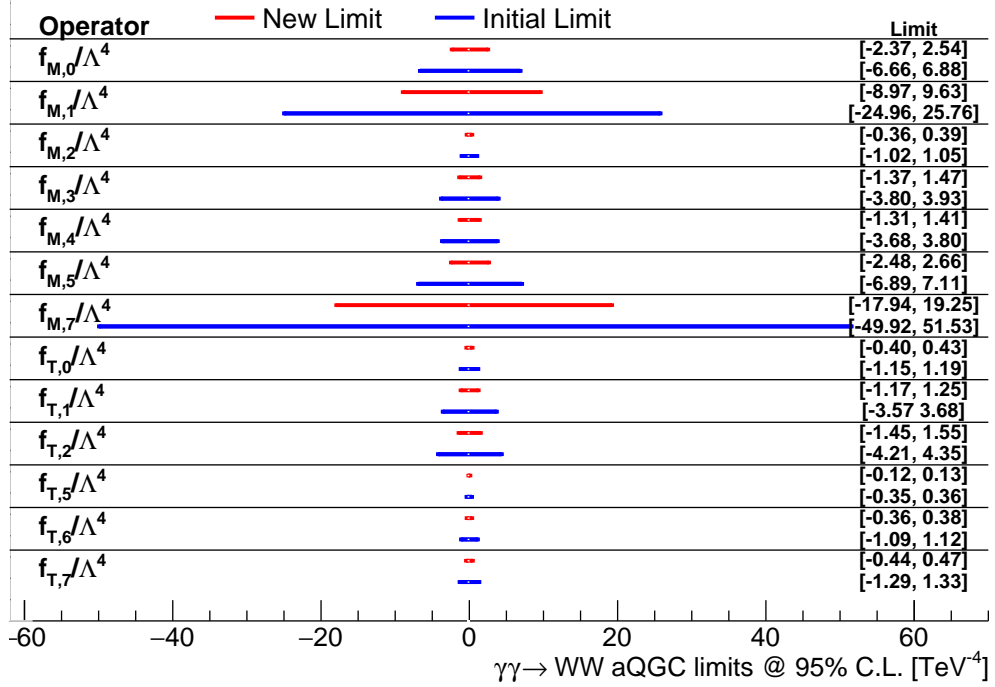
Figure 10.3: A plot comparing the new limits calculated in the high mass region (red) to the initial limits (blue) placed on the dimension-8 parameters using the naive event counting method. Only the limits calculated using the quadratic contribution from the dimension-8 EFT operators are shown.

Section 10.1. The new limits also account for the fiducial cuts of the $\gamma\gamma \to WW$ analysis, unlike the initial estimates calculated in Section 10.1.

Additionally, the cross section of the high mass region is smaller than the cross section used to produce the total invariant mass distribution. The relative reduction of the cross section is also accounted for when calculating the limits in the high mass region. This method is an improvement on the initial method, however it is still an approximation and its purpose is to understand how the initial limits can be constrained by considering the shape of kinematic distributions.

10.2.1 Results

The new limits are compared to the initial limits (from Section 10.1.1) in Figure 10.3. Only limits calculated using the quadratic contribution from the dimension-8 EFT operators are shown. Figure 10.3 illustrates that the limits on free EFT parameters are reduced by approximately a factor of 3, when calculated in the high mass region.

Operator — $\gamma\gamma \to$ WW Run2 — Other Processes   Channel   Reference

c_W/Λ^2 — VBS+diboson (Marginalised) Eur.Phys.J.C 81 (2021) 6, 560 — VBS+diboson (Individual) Eur.Phys.J.C 81 (2021) 6, 560 — diboson Eur.Phys.J.C 81 (2021) 6, 560 — $\gamma\gamma \to$ WW

c_{HDD}/Λ^2 — VBS+diboson (Marginalised) Eur.Phys.J.C 81 (2021) 6, 560 — VBS+diboson (Individual) Eur.Phys.J.C 81 (2021) 6, 560 — diboson Eur.Phys.J.C 81 (2021) 6, 560 — $\gamma\gamma \to$ WW

c_{HW}/Λ^2 — VBS+diboson (Marginalised) Eur.Phys.J.C 81 (2021) 6, 560 — VBS+diboson (Individual) Eur.Phys.J.C 81 (2021) 6, 560 — diboson Eur.Phys.J.C 81 (2021) 6, 560 — $\gamma\gamma \to$ WW

c_{HB}/Λ^2 — VBS+diboson (Marginalised) Eur.Phys.J.C 81 (2021) 6, 560 — VBS+diboson (Individual) Eur.Phys.J.C 81 (2021) 6, 560 — $\gamma\gamma \to$ WW

c_{HWB}/Λ^2 — VBS+diboson (Marginalised) Eur.Phys.J.C 81 (2021) 6, 560 — VBS+diboson (Individual) Eur.Phys.J.C 81 (2021) 6, 560 — diboson Eur.Phys.J.C 81 (2021) 6, 560 — $\gamma\gamma \to$ WW

c_{Hl3}/Λ^2 — VBS+diboson (Marginalised) Eur.Phys.J.C 81 (2021) 6, 560 — VBS+diboson (Individual) Eur.Phys.J.C 81 (2021) 6, 560 — diboson Eur.Phys.J.C 81 (2021) 6, 560 — $\gamma\gamma \to$ WW

c_{ll1}/Λ^2 — VBS+diboson (Marginalised) Eur.Phys.J.C 81 (2021) 6, 560 — VBS+diboson (Individual) Eur.Phys.J.C 81 (2021) 6, 560 — diboson Eur.Phys.J.C 81 (2021) 6, 560 — $\gamma\gamma \to$ WW

15   −10   −5   0   5   10   15   20

aTGC limits @ 95% C.L. [TeV^{-2}]

Figure 10.4: Summary plots showing a comparison between the limits set on dimension-6 EFT parameters by the CMS and ATLAS collaborations. Limits shown in red are the initial estimate of the limits produced using the quadratic contribution from each operator, Run 2 data set.

10.3   Comparisons to Previously Published Results

The estimates of the limits on the dimension-6 and dimension-8 free parameters can be compared to previously published results, in order to see what could be gained by a future, more in-depth analysis.

Figure 10.4 shows a comparison of the initial estimate on the limits of dimension-6 parameters, with previously published results using combined data sets from both the ATLAS and CMS collaborations [155]. The comparison shows results for VBS+diboson events and for diboson only processes. The VBS+diboson limits are further categorised into marginalised - which refers to a global fit of all dimension-6 EFT parameters - and individual - which only varies one parameter at a time whilst the others are set equal to the prediction of the Standard Model. The estimates of the dimension-6 parameters made using the $\gamma\gamma \to WW$ Run 2 data set are performed at an individual level. Figure 10.4 shows that the initial estimates of the limits on the dimension-6 are not very competitive with previous results. The limits on dimension-6 free parameters can be better constrained by other processes.

Figure 10.5 shows a comparison of the initial limits calculated for the dimension-8 EFT

operators, with previously published limits by the ATLAS and CMS collaborations[3][156, 157, 158, 159, 160, 161]. The blue lines indicate the limits extracted by the $\gamma\gamma \to WW$ Run 1 analyses. Both the ATLAS and CMS collaborations extracted these limits from the distribution of the transverse momentum of the dilepton pair [4] [2, 3] and the limits published using other processes are shown in black. The limits shown in red are the limits calculated using the $\gamma\gamma \to WW$ Run 2 data set for the quadratic contribution of EFT operators in the high mass region (see Section 10.2). The latest estimates on the limits of the $f_{M,0}$, $f_{M,1}$, $f_{M,2}$ and $f_{M,3}$ parameters are at least as stringent as the limits set by the $\gamma\gamma \to WW$ Run 1 analyses. Furthermore, the initial estimates indicate that stricter limits could be set on the $f_{M,4}$, $f_{M,5}$, $f_{T,5}$ and $f_{T,7}$ operators.

The estimates of limits on the free EFT parameters show encouraging signs that the $\gamma\gamma \to WW$ Run 2 data set can be used to set new stringent limits that help to progress what is known about EFT. The results presented in this chapter are the product of approximate methods and only provide an indication of what could be achieved by a more in-depth analysis. The estimates were made using only the quadratic EFT contributions, but a more in-depth analysis would also consider the effects of the linear contributions, which would further improve upon the estimates presented here. Additionally, the initial estimates have shown that the limits on the free EFT parameters can be reduced by considering the shape of the kinematic distributions. Crude studies of the invariant mass distribution indicated the limits could be reduced by a factor of 3. With further iteration and refinement, the kinematic distributions can be used to set more stringent limits on the free EFT parameters by using a binned profile likelihood fit of the invariant mass distribution.

---

[3]The limits set by the $W\gamma$, $Z\gamma$ and ZZ processes, include an energy dependent cut-off to ensure unitarity is conserved. This means these limits are larger than if no energy dependent cut-off is applied.

[4]The ATLAS collaboration placed a cut of $p_T^{e,\mu} > 120$ GeV when calculating the limits on the EFT parameters for $\sqrt{s} = 8$ TeV. The CMS collaboration placed a cut of $p_T^{e,\mu} > 100$ GeV and $p_T^{e,\mu} > 130$ GeV when calculating the limits on the EFT parameters for $\sqrt{s} = 7$ TeV and $\sqrt{s} = 8$ TeV, respectively.

(a)

Operator	Channel	L	$\sqrt{s}$	Reference
$f_{M,0}/\Lambda^4$	WZjj	35.9 fb⁻¹	13 TeV	PLB 809 (2020) 135710
	Wγ	35.9 fb⁻¹	13 TeV	PLB 811 (2020) 135988
	W±W±jj	35.9 fb⁻¹	13 TeV	PRL 120 (2018) 081801
	ssWW	137 fb⁻¹	13 TeV	PLB 809 (2020) 135710
	WZ	137 fb⁻¹	13 TeV	PLB 809 (2020) 135710
	VVjj	35.9 fb⁻¹	13 TeV	PLB 798 (2019)134985
	γγ → WW	20.2 fb⁻¹	8 TeV	PRD 94 (2016) 032011
	γγ → WW	24.7 fb⁻¹	7,8 TeV	JHEP 08 (2016) 119
	γγ→ WW	139 fb⁻¹	13 TeV	
$f_{M,1}/\Lambda^4$	Wγ	35.9 fb⁻¹	13 TeV	PLB 811 (2020) 135988
	WZjj	35.9 fb⁻¹	13 TeV	PLB 809 (2020) 135710
	W±W±jj	137 fb⁻¹	13 TeV	PLB 809 (2020) 135710
	VVjj	35.9 fb⁻¹	13 TeV	PLB 798 (2019)134985
	ssWW	137 fb⁻¹	13 TeV	PLB 809 (2020) 135710
	WZ	137 fb⁻¹	13 TeV	PLB 809 (2020) 135710
	γγ → WW	20.2 fb⁻¹	8 TeV	PRD 94 (2016) 032011
	γγ → WW	24.7 fb⁻¹	7,8 TeV	JHEP 08 (2016) 119
	γγ→ WW	139 fb⁻¹	13 TeV	
$f_{M,2}/\Lambda^4$	Wγ	35.9 fb⁻¹	13 TeV	PLB 811 (2020) 135988
	γγ → WW	20.2 fb⁻¹	8 TeV	PRD 94 (2016) 032011
	γγ → WW	24.7 fb⁻¹	7,8 TeV	JHEP 08 (2016) 119
	γγ→ WW	139 fb⁻¹	13 TeV	
$f_{M,3}/\Lambda^4$	Wγ	35.9 fb⁻¹	13 TeV	PLB 811 (2020) 135988
	γγ → WW	24.7 fb⁻¹	7,8 TeV	JHEP 08 (2016) 119
	γγ→ WW	139 fb⁻¹	13 TeV	
$f_{M,4}/\Lambda^4$	Wγ	35.9 fb⁻¹	13 TeV	PLB 811 (2020) 135988
	γγ → WW	139 fb⁻¹	13 TeV	
$f_{M,5}/\Lambda^4$	Wγ	19.7 fb⁻¹	8 TeV	JHEP 06 (2017) 106
	γγ → WW	139 fb⁻¹	13 TeV	
$f_{M,7}/\Lambda^4$	Wγ	35.9 fb⁻¹	13 TeV	PLB 811 (2020) 135988
	ssWW	137 fb⁻¹	13 TeV	PLB 809 (2020) 135710
	WZ	137 fb⁻¹	13 TeV	PLB 809 (2020) 135710
	W±W±jj	137 fb⁻¹	13 TeV	PLB 809 (2020) 135710
	VVjj	35.9 fb⁻¹	13 TeV	PLB 798 (2019)134985
	γγ→ WW	139 fb⁻¹	13 TeV	

Legend: γγ→ WW Run2 (red), γγ→ WW Run1 (blue), Other Processes (black)

x-axis: aQGC limits @ 95% C.L. [TeV⁻⁴], range −100 to 300

(a)

(b)

Operator	Channel	L	$\sqrt{s}$	Reference
$f_{T,0}/\Lambda^4$	WWW	35.9 fb⁻¹	13 TeV	100 (2019) 012004
	Zγ	35.9 fb⁻¹	13 TeV	JHEP 06 (2020) 076
	Wγ	35.9 fb⁻¹	13 TeV	PLB 811 (2020) 135988
	ssWW	137 fb⁻¹	13 TeV	PLB 809 (2020) 135710
	WZ	137 fb⁻¹	13 TeV	PLB 809 (2020) 135710
	ZZ	137 fb⁻¹	13 TeV	PLB 812 (2020) 135992
	VVjj	35.9 fb⁻¹	13 TeV	PLB 798 (2019) 134985
	γγ→ WW	139 fb⁻¹	13 TeV	
$f_{T,1}/\Lambda^4$	WWW	35.9 fb⁻¹	13 TeV	100 (2019) 012004
	Wγ	35.9 fb⁻¹	13 TeV	PLB 811 (2020) 135988
	ssWW	137 fb⁻¹	13 TeV	PLB 809 (2020) 135710
	WZ	137 fb⁻¹	13 TeV	PLB 809 (2020) 135710
	ZZ	137 fb⁻¹	13 TeV	PLB 812 (2020) 135992
	VVjj	35.9 fb⁻¹	13 TeV	PLB 798 (2019) 134985
	γγ→ WW	139 fb⁻¹	13 TeV	
$f_{T,2}/\Lambda^4$	WWW	35.9 fb⁻¹	13 TeV	100 (2019) 012004
	Zγ	35.9 fb⁻¹	13 TeV	JHEP 06 (2020) 076
	Wγ	35.9 fb⁻¹	13 TeV	PLB 811 (2020) 135988
	ssWW	137 fb⁻¹	13 TeV	PLB 809 (2020) 135710
	WZ	137 fb⁻¹	13 TeV	PLB 809 (2020) 135710
	ZZ	137 fb⁻¹	13 TeV	PLB 812 (2020) 135992
	VVjj	35.9 fb⁻¹	13 TeV	PLB 798 (2019) 134985
	γγ→ WW	139 fb⁻¹	13 TeV	
$f_{T,5}/\Lambda^4$	Zγ	35.9 fb⁻¹	13 TeV	JHEP 06 (2020) 076
	Wγ	35.9 fb⁻¹	13 TeV	PLB 811 (2020) 135988
	γγ→ WW	139 fb⁻¹	13 TeV	
$f_{T,6}/\Lambda^4$	Zγ	35.9 fb⁻¹	13 TeV	JHEP 06 (2020) 076
	Wγ	35.9 fb⁻¹	13 TeV	PLB 811 (2020) 135988
	γγ→ WW	139 fb⁻¹	13 TeV	
$f_{T,7}/\Lambda^4$	Zγ	35.9 fb⁻¹	13 TeV	JHEP 06 (2020) 076
	Wγ	35.9 fb⁻¹	13 TeV	PLB 811 (2020) 135988
	γγ→ WW	139 fb⁻¹	13 TeV	

Legend: γγ→ WW Run2 (red), Other Processes (black)

x-axis: aQGC limits @ 95% C.L. [TeV⁻⁴], range −4 to 12

(b)

Figure 10.5: Summary plots showing a comparison between the limits set on dimension-8 EFT parameters ($f_{M,i}$ and $f_{T,i}$) by the CMS and ATLAS collaborations. Limits shown in blue are previous limits set by the $\gamma\gamma \to WW$ Run 1 analyses, whilst limits shown in red are the initial limits produced from the Run 2 data set. a) shows the comparison for the mixed operators, $\mathcal{O}_{M,i}$ and b) shows the comparison for the transverse operators, $\mathcal{O}_{T,i}$.

Chapter 11

Summary

This thesis has presented work that examines the electroweak sector of physics, using the ATLAS detector at CERN. Chapter 5 examined the methods used to identify electrons within the ATLAS detector. Electrons are one of the fundamental particles that can be directly detected by the ATLAS detector. They interact via both the electromagnetic and weak forces, hence are good candidates for measuring electroweak interactions inside the detector. The importance of being able to distinguish prompt electrons from non-prompt background electrons was discussed, before moving on to discuss how the Neyman-Pearson Lemma can be altered to encapsulate information from electrons of different background sources.

The so called "two-dimensional" likelihood discriminant method was developed in an effort to improve rejection against electrons originating from heavy flavour hadronic decays. This technique constructed two individual likelihood discriminants: the first discriminated against electrons from light flavour hadronic decays whilst the second discriminated against electrons from heavy flavour hadronic decays. Both likelihood discriminants were plotted as a two-dimensional distribution, illustrating the separation between prompt electrons and electrons from light flavour hadronic decays or heavy flavour hadronic decays. An optimum two-dimensional likelihood discriminant cut was found from the Neyman-Pearson Lemmas that offered the maximum amount of rejection of background electrons for a given signal efficiency. The optimum two-dimensional likelihood discriminant cut depends on the ratio of the fraction of electrons from light flavour hadronic decays to the fraction of electrons from heavy flavour hadronic decays. This was studied for different operating points and for different compositions of background electrons. The new two-dimensional likelihood discriminant method showed an increase in the rejection of background electrons from heavy flavour hadronic decays. By improving the rejection of background electrons from heavy flavour hadronic decays, the two-dimensional likelihood

discriminant method improves the purity of prompt signal electrons; an effect that increases as the fraction of background electrons from heavy flavour hadronic decays increases.

The two-dimensional likelihood discriminant method was also studied in bins of pseudorapidity and transverse energy. This study showed that the rejection of background electrons from heavy flavour hadronic decays improved across all bins of pseudorapidity and transverse energy. It also showed that there was some increase in the rejection of background electrons from light flavour hadronic decays at low transverse energies. This effect was attributed to some electrons, from light flavour hadronic decays, that pass the nominal likelihood discriminant cut, failing the heavy flavour likelihood discriminant cut. A study of the distributions of the discriminating variables used to construct the likelihood, showed that the transverse impact parameter added some additional discriminating power; enabling the heavy flavour likelihood discriminant to differentiate between some background electrons from light flavour hadronic decays and prompt signal electrons.

Photon-induced W^+W^- production was introduced in Chapter 6 and previous measurements of this process by both the ATLAS and CMS collaborations were summarised. Then, the general analysis strategy, used to analyse the full Run 2 data set, was outlined. The $\gamma\gamma \to WW$ process was studied in the $e^\pm\mu^\mp$ channel. Signal events were required pass the exclusivity requirement, which means there could be no additional charged particle tracks in a window of $\Delta z = \pm 1$ around the interaction vertex. Additionally, events were selected with a transverse momentum greater than 30 GeV. Three modelling corrections were applied to the Monte Carlo samples used in the $\gamma\gamma \to WW$ analysis. The first, corrected the beam spot size and was used to correct the modelling of additional proton-proton interactions. The second, corrected for the mismodelling of the charged track multiplicity, and the third correction accounted for dissociative and non-perturbative contributions.

The application of the charged particle multiplicity reweighting was discussed in more detail in Chapter 7. This chapter outlined the motivation behind the charged particle multiplicity reweighting factor and described how it is extracted from Drell-Yan events. Then, two studies were presented with the motivation of validating the application of the charged particle multiplicity reweighting to diboson events. It is challenging to validate the application of the charged particle reweighting to the main background in the $\gamma\gamma \to WW$ analysis, inclusive W^+W^-. This is because it is difficult to select a pure sample of inclusive W^+W^- events, with a low charged track multiplicity, in data, that is not contaminated with signal events. Studies were shown of the application of the charged particle reweighting to ZZ and WZ events, which have four and three leptons in their final states. The Standard Model does not predict photon-induced ZZ or WZ

production, therefore it is easier to select a pure sample in data. New four lepton and three lepton selections were developed to study these events. The agreement between data and Monte Carlo was assessed before and after the application of the charged particle multiplicity reweighting. The four lepton selection was limited by statistical sample size, however it showed that applying the charged particle multiplicity reweighting did not drastically deteriorate the agreement between data and Monte Carlo. The three lepton selection showed a considerable deterioration in the agreement between data and Monte Carlo after the charged particle multiplicity reweighting was applied. This difference could be attributed to contributions from the purely electromagnetic $\gamma\gamma \rightarrow 4l$ process that does not have an on-mass shell Z boson requirement. Further studies with additional Monte Carlo samples are needed for more conclusive results. These studies did not help to validate the application of the charged particle multiplicity reweighting to inclusive WW events. As a result, a systematic uncertainty was applied to account for the inconclusive results. The systematic uncertainty assigned is equal to the difference between the distribution of the charged particle multiplicity at truth-level for the inclusive W^+W^- and Drell-Yan Monte Carlo samples, was assigned.

The exclusivity scale factor, which accounts for dissociative and non-perturbative contributions not modelled in the Monte Carlo, was described in Chapter 8. It is defined as the ratio of the number of exclusive events in data to the number of exclusive events predicted by the Monte Carlo. A data-driven method was used to construct a template of the background contributions in data. The background contribution was subtracted from the measured data to find the exclusive contribution in data. The exclusivity scale factor was calculated to be $3.59 \pm 0.06(\text{stat.}) \pm 0.14(\text{syst.})$.

The results of the $\gamma\gamma \rightarrow WW$ Run 2 analysis were presented in Chapter 9. The $\gamma\gamma \rightarrow WW$ process was observed with a significance of 6.7σ and the fiducial cross section was measured to be $3.13 \pm 0.31(\text{stat.}) \pm 0.28(\text{syst.})$ fb.

Finally, Chapter 10 discussed how the results from the $\gamma\gamma \rightarrow WW$ Run 2 analysis can be used to set limits on new physics using EFT. A naive event counting method was used to set initial limits on the free parameters of sensitive dimension-6 and dimension-8 operators using a profile likelihood fit. The initial limits do not account for the fiducial cuts applied in the $\gamma\gamma \rightarrow WW$ analysis, or for the shape of kinematic distributions. Next, the technique was refined to include features of the invariant mass distribution of EFT events. The EFT events are suppressed by the energy scale and as a consequence, the production of EFT events increases at higher energies and therefore higher masses. The limits on free EFT parameters were calculated using the same event counting technique for a high mass region of $m_{ll} > 400$ GeV. This study was only performed using the quadratic contribution from dimension-8 EFT operators but it indicated the initial

estimates on the limits could be improved by a factor of 3. The results from this study showed highlighted the sensitivities of $\gamma\gamma \to WW$ process to EFT operators and indicated that with some refinement, the $\gamma\gamma \to WW$ Run 2 data set could be used to set stringent limits that are competitive with previously published results.

x

Appendix A

Monte Carlo Samples used in Two-Dimensional Likelihood Discriminant Studies

This appendix provides a full list of the Monte Carlo samples used in the two-dimensional likelihood discriminant studies, presented in Chapter 5. These studies used the MC16e Monte Carlo campaign, which corresponds to the AMI tag r10724.

DSID	σ, pb	filter ϵ	AMI Tag
$Z \rightarrow ee$ samples			
361106	1.90×10^3	1.0	e3601_e5984_s3126_s3136_r10724_p4089
dijet samples			
423300	2.43×10^9	0.0742	e3848_e5984_s3126_s3136_r10724_p4191
$t\bar{t}$ samples			
410472	730	0.1055	e6348_s5984_s3126_r10724_p4189

Table A.1: A list of the Monte Carlo samples used in the two-dimensional likelihood discriminant studies. These studies were performed using the MC16e Monte Carlo campaign.

x

Appendix B

Monte Carlo Samples used in the $\gamma\gamma \rightarrow WW$ Run 2 Analysis

This appendix provides a full list of the Monte Carlo samples used in the Run 2 $\gamma\gamma \rightarrow WW$ analysis. This analysis used the full Run 2 data set, and as a consequence, all three of ATLAS' Monte Carlo campaigns (MC16a, MC16d and MC16e) were used. The AMI tag rX is used in the tables below to reflect this. For the MC16a samples, rX takes the value r9364. For MC16d, rX takes the value r10201, and for MC16e, rX takes the value r10724.

DSID	σ, pb	k-fac.	filter ϵ	AMI Tag
Nominal signal samples				
$\gamma\gamma \to WW$, exclusive production				
363761	0.014942	1.0	0.31438	e7184_e5984_rX_rX_p3714
exclusive di-lepton production				
$\gamma\gamma \to ee$				
363750	0.6003	1.0	0.43128	e7880_e7400_s3482_rX_p3714
363751	0.079051	1.0	0.43838	e7880_e7400_s3482_rX_p3714
363752	0.032657	1.0	0.40615	e7880_e7400_s3482_rX_p3714
$\gamma\gamma \to \mu\mu$				
363753	2.3577	1.0	0.20598	e7880_e7400_s3482_rX_p3714
363754	0.600021	1.0	0.43134	e7880_e7400_s3482_rX_p3714
363755	0.078800	1.0	0.43800	e7880_e7400_s3482_rX_p3714
363756	0.032661	1.0	0.40669	e7880_e7400_s3482_rX_p3714
single dissociative di-lepton production				
$\gamma\gamma \to ee$				
363694	9.95054	1.0	1.0	e7546_e5984_a875_rX_rX_p3712
363695	1.4797	1.0	1.0	e7546_e5984_a875_rX_rX_p3712
363696	0.078420	1.0	1.0	e7546_e5984_a875_rX_rX_p3712
$\gamma\gamma \to \mu\mu$				
363697	17.28	1.0	1.0	e7546_e5984_a875_rX_rX_p3712
363698	7.34	1.0	1.0	e7546_e5984_a875_rX_rX_p3712
363699	0.582	1.0	1.0	e7546_e5984_a875_rX_rX_p3712
363700	0.026284	1.0	1.0	e7546_e5984_a875_rX_rX_p3712
double dissociative di-lepton production				
$\gamma\gamma \to ee$				
363672	17.493	1.0	0.11605	e7546_e5984_a875_rX_rX_p3712
363673	1.7919	1.0	0.31442	e7546_e5984_a875_rX_rX_p3712
363674	0.1386	1.0	0.37826	e7546_e5984_a875_rX_rX_p3712
$\gamma\gamma \to \mu\mu$				
363675	109.16	1.0	0.073246	e7546_e5984_a875_rX_rX_p3712
363676	17.477	1.0	0.26493	e7546_e5984_a875_rX_rX_p3712
363677	1.7906	1.0	0.34242	e7546_e5984_a875_rX_rX_p3712
363678	0.13883	1.0	0.38223	e7546_e5984_a875_rX_rX_p3712
$\gamma\gamma \to \tau\tau$				
363679	61.64	1.0	0.00083596	e7546_e5984_a875_rX_rX_p3712
363680	14.264	1.0	0.010507	e7546_e5984_a875_rX_rX_p3712
363681	1.6267	1.0	0.031995	e7546_e5984_a875_rX_rX_p3712
363682	0.12993	1.0	0.050452	e7546_e5984_a875_rX_rX_p3712

Table B.1: A list of the exclusive and dissociative Monte Carlo samples used in the $\gamma\gamma \to WW$ analysis Run 2 analysis. The AMI tag rX corresponds to the reconstruction of each Monte Carlo campaign.

DSID	σ, pb	k-fac.	filter ϵ	AMI Tag
Inclusive $pp \rightarrow WW$ production				
361600	10.636	1.115	1.0	e4616_e5984_s3126_rX_rX_p3712
Alternative WW samples				
364254	12.501	1.0	1.0	e5916_s3126_rX_rX_p3712
$H \rightarrow WW$ production				
345324	1.102	1.0	0.49374	e5769_e5984_s3126_rX_rX_p3712
Other diboson production processes				
361601	4.4821	1.18	1.0	e4475_e5984_s3126_rX_rX_p3712
364250	1.2523	1.0	1.0	e5984_e5984_s3126_rX_rX_p3712
364288	1.4496	1.0	1.0	e6096_e5984_s3126_rX_rX_p3712
Alternative diboson production processes				
364253	4.579	1.0	1.0	e5916_s3126_rX_rX_p3712
364289	2.9599	1.0	1.0	e5984_s3126_rX_rX_p3712
$W\gamma$ production				
$W\gamma \rightarrow e\nu_\tau\gamma$				
364521	199.27	1.0	1.0	e5928_e5984_s3126_rX_rX_p3712
364522	134.38	1.0	1.0	e5928_e5984_s3126_rX_rX_p3712
364523	19.074	1.0	1.0	e5928_e5984_s3126_rX_rX_p3712
364524	1.9215	1.0	1.0	e5928_e5984_s3126_rX_rX_p3712
364525	0.29803	1.0	1.0	e5928_e5984_s3126_rX_rX_p3712
$W\gamma \rightarrow \mu\nu_\tau\gamma$				
364526	199.44	1.0	1.0	e5928_e5984_s3126_rX_rX_p3712
364527	134.45	1.0	1.0	e5928_e5984_s3126_rX_rX_p3712
364528	19.108	1.0	1.0	e5928_e5984_s3126_rX_rX_p3712
364529	1.9249	1.0	1.0	e5928_e5984_s3126_rX_rX_p3712
364530	0.2987	1.0	1.0	e5928_e5984_s3126_rX_rX_p3712
$W\gamma \rightarrow \tau\nu_\tau\gamma$				
364531	199.4	1.0	1.0	e5928_e5984_s3126_rX_rX_p3712
364532	134.43	1.0	1.0	e5928_e5984_s3126_rX_rX_p3712
364533	19.115	1.0	1.0	e5928_e5984_s3126_rX_rX_p3712
364534	1.9288	1.0	1.0	e5928_e5984_s3126_rX_rX_p3712
364535	0.29827	1.0	1.0	e5928_e5984_s3126_rX_rX_p3712
Nominal top production				
410472	729.77	1.1398	0.10546	e6348_e5984_s3126_rX_rX_p3712
Alternative top production				
410648	3.997	0.9451	1.0	e6348_e5984_s3126_rX_rX_p3712
410649	3.9939	0.9458	1.0	e6615_e5984_s3126_rX_rX_p3712

Table B.2: A list of the diboson and top Monte Carlo samples used in the $\gamma\gamma \rightarrow WW$ analysis. The AMI tag rX corresponds to the reconstruction of each Monte Carlo campaign.

DSID	σ, pb	k-fac.	filter ϵ	AMI Tag

DSID	σ, pb	k-fac.	filter ϵ	AMI Tag
Nominal inclusive Z production				
$Z \to ee$				
361106	1901.1	1.0260	1.0	e3601_e5984_s3126_rX_rX_p3712
361664	13960.0	1.0	0.051411	e4770_e5984_s3126_rX_rX_p3712
361665	6621.5	1.0	0.26642	e4770_e5984_s3126_rX_rX_p3712
$Z \to \mu\mu$				
361107	1898.5	1.026	1.0	e3601_e5984_s3126_rX_rX_p3712
361666	13960.0	1.0	0.054481	e4770_e5984_s3126_rX_rX_p3712
361667	6621.5	1.0	0.27369	e4770_e5984_s3126_rX_rX_p3712
$Z \to \tau\tau$				
361108	1898.0	1.026	1.0	e3601_e5984_s3126_rX_rX_p3712
361668	13960.0	1.0	0.00059244	e4784_e5984_s3126_rX_rX_p3712
361669	6621.8	1.0	0.015147	e4770_e5984_s3126_rX_rX_p3712
filtered $Z \to \tau\tau$				
344772	246.053	0.9751	0.203784	e5585_e5984_s3126_rX_rX_p3712
344776	13.7241	0.9751	0.28202	e5585_e5984_s3126_rX_rX_p3712
Alternative inclusive Z production				
colspan $Z \to ee$				
364204	2415.3	0.9751	0.9652	e5421_s3126_rX_rX_p3712
364205	2415.5	0.9751	0.034696	e5421_s3126_rX_rX_p3712
364206	50.354	0.9751	0.8932	e5421_s3126_rX_rX_p3712
364207	50.487	0.9751	0.1087	e5421_s3126_rX_rX_p3712
364208	3.2539	0.9751	0.85485	e5421_s3126_rX_rX_p3712
364209	3.2526	0.9751	0.15351	e5421_s3126_rX_rX_p3712
364114	1981.6	0.9751	0.82133	e5299_s3126_rX_rX_p3712
364115	1981.5	0.9751	0.11386	e5299_s3126_rX_rX_p3712
364116	1982.0	0.9751	0.065756	e5299_s3126_rX_rX_p3712
364117	110.64	0.9751	0.69426	e5299_s3126_rX_rX_p3712
364118	110.5	0.9751	0.18855	e5299_s3126_rX_rX_p3712
364119	110.46	0.9751	0.11827	e5299_s3126_rX_rX_p3712
364120	40.645	0.9751	0.61615	e5299_s3126_rX_rX_p3712
364121	40.671	0.9751	0.23291	e5299_s3126_rX_rX_p3712
364122	40.675	0.9751	0.15332	e5299_s3126_rX_rX_p3712
364123	8.6703	0.9751	0.56739	e5299_s3126_rX_rX_p3712
364124	8.6668	0.9751	0.2662	e5299_s3126_rX_rX_p3712
364125	8.6809	0.9751	0.17655	e5299_s3126_rX_rX_p3712
364126	1.8092	0.9751	1.0	e5299_s3126_rX_rX_p3712
364127	0.14875	0.9751	1.0	e5299_s3126_rX_rX_p3712

Table B.3: A list of Drell-Yan Monte Carlo samples used in the $\gamma\gamma \to WW$ analysis. The AMI tag rX corresponds to the reconstruction of each Monte Carlo campaign.

DSID	σ, pb	k-fac.	filter ϵ	AMI Tag
Alternative inclusive Z production continued
$Z \to \mu\mu$
364198	2414.3	0.9751	0.96536	e5421_s3126_rX_rX_p3712
364199	2414.2	0.9751	0.034445	e5421_s3126_rX_rX_p3712
364200	50.33	0.9751	0.89306	e5421_s3126_rX_rX_p3712
364201	50.29	0.9751	0.11212	e5421_s3126_rX_rX_p3712
364202	3.2398	0.9751	0.85373	e5421_s3126_rX_rX_p3712
364203	3.2813	0.9751	0.16027	e5421_s3126_rX_rX_p3712
364100	1982.5	0.9751	0.82172	e5271_s3126_rX_rX_p3712
364101	1982.2	0.9751	0.11355	e5271_s3126_rX_rX_p3712
364102	1981.5	0.9751	0.06589	e5271_s3126_rX_rX_p3712
364103	109.14	0.9751	0.68992	e5271_s3126_rX_rX_p3712
364104	108.98	0.9751	0.19665	e5271_s3126_rX_rX_p3712
364105	109.09	0.9751	0.11701	e5271_s3126_rX_rX_p3712
364106	39.87	0.9751	0.59942	e5271_s3126_rX_rX_p3712
364107	39.857	0.9751	0.23527	e5271_s3126_rX_rX_p3712
364108	39.888	0.9751	0.1557	e5271_s3126_rX_rX_p3712
364109	8.5256	0.9751	0.56023	e5271_s3126_rX_rX_p3712
364110	8.5259	0.9751	0.26641	e5271_s3126_rX_rX_p3712
364111	8.5281	0.9751	0.17674	e5271_s3126_rX_rX_p3712
364112	1.787	0.9751	1.0	e5271_s3126_rX_rX_p3712
364113	0.1476	0.9751	1.0	e5271_s3126_rX_rX_p3712

Table B.4: A continued list of the alternative Drell-Yan Monte Carlo samples used in the $\gamma\gamma \to WW$ analysis. The AMI tag rX corresponds to the reconstruction of each Monte Carlo campaign.

Bibliography

[1] The ATLAS Collaboration, "Observation of photon-induced W^+W production in pp collisions at $\sqrt{s} = 13$ TeV using the ATLAS detector," *Physics Letters B*, p. 136190, 2021. https://doi.org/10.1016/j.physletb.2021.136190.

[2] The ATLAS Collaboration, "Measurement of exclusive $\gamma\gamma \to W^+W^-$ production and search for exclusive Higgs boson production in pp collisions at $\sqrt{s} = 8$ TeVusing the ATLAS detector," *Phys. Rev. D*, vol. 94, p. 032011, Aug 2016. 10.1103/PhysRevD.94.032011.

[3] The CMS Collaboration, "Evidence for exclusive $\gamma\gamma \to W^+W^-$ production and constraints on anomalous quartic gauge couplings in pp collisions at $\sqrt{s} = 7$ and 8 TeV," *Journal of High Energy Physics*, vol. 2016, p. 119, Aug 2016. 10.1007/JHEP08(2016)119.

[4] M. Osler, *Reconfiguring the World: Nature, God, and Human Understanding from the Middle Ages to Early Modern Europe*. History of science, Johns Hopkins University Press, 2010. ISBN:9780801896552.

[5] I. Falconer, "J J Thomson and the discovery of the electron," *Physics Education*, vol. 32, pp. 226–231, jul 1997. 10.1088/0031-9120/32/4/015.

[6] M. Zoli, "Particle scattering in the Thomson and Rutherford atomic models," *European Journal of Physics*, vol. 19, pp. 187–193, mar 1998. 10.1088/0143-0807/19/2/013.

[7] P. Dirac, "The quantum theory of the electron," *Royal Society*, vol. 117, Feb 1928. `https://doi.org/10.1098/rspa.1928.0023`.

[8] C. N. Yang and R. L. Mills, "Conservation of Isotopic Spin and Isotopic Gauge Invariance," *Phys. Rev.*, vol. 96, pp. 191–195, Oct 1954. 10.1103/PhysRev.96.191.

[9] S. L. Glashow, "Partial-symmetries of weak interactions," *Nuclear Physics*, vol. 22, no. 4, pp. 579–588, 1961. `https://doi.org/10.1016/0029-5582(61)90469-2`.

[10] P. Higgs, "Broken symmetries, massless particles and gauge fields," *Physics Letters*, vol. 12, no. 2, pp. 132–133, 1964. `https://doi.org/10.1016/0031-9163(64)91136-9`.

[11] F. Englert and R. Brout, "Broken symmetry and the mass of gauge vector mesons," *Phys. Rev. Lett.*, vol. 13, pp. 321–323, Aug 1964. 10.1103/PhysRevLett.13.321.

[12] G. S. Guralnik, C. R. Hagen, and T. W. B. Kibble, "Global conservation laws and massless particles," *Phys. Rev. Lett.*, vol. 13, pp. 585–587, Nov 1964. 10.1103/PhysRevLett.13.585.

[13] H. Fritzsch and P. Minkowski, "Unified interactions of leptons and hadrons," *Annals of Physics*, vol. 93, no. 1, pp. 193–266, 1975. `https://doi.org/10.1016/0003-4916(75)90211-0`.

[14] M. Gell-Mann, "A schematic model of baryons and mesons," *Physics Letters*, vol. 8, no. 3, pp. 214–215, 1964. `https://doi.org/10.1016/S0031-9163(64)92001-3`.

[15] A. Pais and S. B. Treiman, "How many charm quantum numbers are there?," *Phys. Rev. Lett.*, vol. 35, pp. 1556–1559, Dec 1975. 10.1103/PhysRevLett.35.1556.

[16] A. Arbuzov, "Quantum field theory and the electroweak standard model," *Proceedings of the 2017 European School of High-Energy Physics*, vol. 3, 2018. `https://doi.org/10.23730/CYRSP-2018-003.1`.

[17] M. Thomson, *Modern particle physics*. New York: Cambridge University Press, 2013. ISBN:978-1-107-03426-6.

[18] "CKM Quark-Mixing Matrix," *Progress of Theoretical and Experimental Physics*, vol. 2020, Aug 2020. 10.1093/ptep/ptaa104.

[19] W. N. Cottingham and D. A. Greenwood, *An Introduction to the Standard Model of Particle Physics*. Cambridge University Press, 2 ed., 2007. 10.1017/CBO9780511791406.

[20] "Review of particle physics," *Phys. Rev. D*, vol. 98, Aug 2018. 10.1103/PhysRevD.98.030001.

[21] M. E. Peskin and D. V. Schroeder, *An Introduction to quantum field theory*. Reading, USA: Addison-Wesley, 1995. ISBN:978-0-201-50397-5.

[22] The ATLAS Collaboration, "Summary plots from the ATLAS standard model physics group," 2018. `https://atlas.web.cern.ch/Atlas/GROUPS/PHYSICS/CombinedSummaryPlots/SM/`.

[23] D. G. Cerdeno, "Dark matter: From production to detection," *Lecture Notes for the 2017 School for Experimental High Energy Physics Students*, 2017.

[24] R. N. R. N. Mohapatra, *Massive Neutrinos In Physics And Astrophysics [electronic resource]*. World Scientific lecture notes in physics ; v. 72, Singapore: World Scientific Publishing Company, 3rd ed. ed., 2004. ISBN: 1-281-87220-2.

[25] Gounaris and et al, "Triple gauge boson couplings," 1996. 10.5170/CERN-1996-001-V-1.525.

[26] S. Godfrey, "Quartic gauge boson couplings," May 1995. `https://cds.cern.ch/record/281467`.

[27] O. J. P. Éboli, M. C. Gonzalez-Garcia, and S. M. Lietti, "Bosonic quartic couplings at CERN LHC," *Physical Review D*, vol. 69, May 2004. 10.1103/physrevd.69.095005.

[28] C. Degrande, N. Greiner, W. Kilian, O. Mattelaer, H. Mebane, T. Stelzer, S. Willenbrock, and C. Zhang, "Effective field theory: A modern approach to anomalous couplings," *Annals of Physics*, vol. 335, p. 21–32, Aug 2013. 10.1016/j.aop.2013.04.016.

[29] B. Grzadkowski, M. Iskrzyński, M. Misiak, and J. Rosiek, "Dimension-six terms in the Standard Model Lagrangian," *Journal of High Energy Physics*, vol. 2010, Oct 2010. 10.1007/jhep10(2010)085.

[30] O. Éboli and M. Gonzalez–Garcia, "Classifying the bosonic quartic couplings," *Physical Review D*, vol. 93, May 2016. 10.1103/physrevd.93.093013.

[31] J. D. Bjorken, "Asymptotic sum rules at infinite momentum," *Phys. Rev.*, vol. 179, pp. 1547–1553, Mar 1969. 10.1103/PhysRev.179.1547.

[32] D. Kar, *Experimental particle physics: understanding the measurements and searches at the Large Hadron Collider*. IOP expanding physics, Bristol: IOP, 2019. ISBN: 978-0-7503-2110-5.

[33] D. E. Soper, "Parton distribution functions," *Nuclear Physics B - Proceedings Supplements*, vol. 53, p. 69–80, Feb 1997. 10.1016/s0920-5632(96)00600-7.

[34] G. Altarelli and G. Parisi, "Asymptotic freedom in parton language," *Nuclear Physics B*, vol. 126, no. 2, pp. 298–318, 1977. https://doi.org/10.1016/0550-3213(77)90384-4.

[35] V. Gribov and L. Lipatov, "Deep inelastic electron scattering in perturbation theory," *Physics Letters B*, vol. 37, no. 1, pp. 78–80, 1971. https://doi.org/10.1016/0370-2693(71)90576-4.

[36] "Review of Particle Physics," *Progress of Theoretical and Experimental Physics*, vol. 2020, 08 2020. 10.1093/ptep/ptaa104.

[37] L. A. Harland-Lang, A. D. Martin, R. Nathvani, and R. S. Thorne, "Ad Lucem: QED parton distribution functions in the MMHT framework," *The European Physical Journal C*, vol. 79, Oct 2019. 10.1140/epjc/s10052-019-7296-0.

[38] R. Brock *et al.*, "Handbook of perturbative QCD: Version 1.0,"

[39] K. Melnikov, "Lectures on QCD for hadron colliders," *Proceedings of the 2017 European School of High-Energy Physics*, vol. 3, 2018. `https://doi.org/10.23730/CYRSP-2018-003.37`.

[40] T. Plehn, "Lectures on LHC Physics," *Lecture Notes in Physics*, 2012. 10.1007/978-3-642-24040-9.

[41] E. Fermi, "On the theory of collisions between atoms and electrically charged particles," *Nuovo Cimento*, vol. 2, pp. 143–158, 1925. https://doi.org/10.1142/9789812704214$_0$026.

[42] V. Budnev, I. Ginzburg, G. Meledin, and V. Serbo, "The two-photon particle production mechanism. physical problems. applications. equivalent photon approximation," *Physics Reports*, vol. 15, no. 4, pp. 181 – 282, 1975. https://doi.org/10.1016/0370-1573(75)90009-5.

[43] F. Krauss, M. Greiner, and G. Soff, "Photon and gluon induced processes in relativistic heavy-ion collisions," *Progress in Particle and Nuclear Physics*, vol. 39, pp. 503 – 564, 1997. https://doi.org/10.1016/S0146-6410(97)00049-5.

[44] The ATLAS Collaboration, "Measurement of exclusive $\gamma\gamma \rightarrow l^{\pm} + l^{\pm}$ production in proton–proton collisions at $\sqrt{s} = 7$ TeVwith the ATLAS detector," *Physics Letters B*, vol. 749, p. 242–261, Oct 2015. 10.1016/j.physletb.2015.07.069.

[45] The ATLAS Collaboration, "Measurement of fiducial and differential W^+W^- production cross-sections at $\sqrt{s} = 13$ TeV with the ATLAS detector," *The European Physical Journal C*, vol. 79, Oct 2019. 10.1140/epjc/s10052-019-7371-6.

[46] A. Buckley, J. Butterworth, S. Gieseke, D. Grellscheid, S. Höche, H. Hoeth, F. Krauss, L. Lönnblad, E. Nurse, P. Richardson, and et al., "General-purpose event generators for LHC physics," *Physics Reports*, vol. 504, p. 145–233, Jul 2011. 10.1016/j.physrep.2011.03.005.

[47] T. Gleisberg, S. Höche, F. Krauss, M. Schönherr, S. Schumann, F. Siegert, and J. Winter, "Event generation with SHERPA 1.1," *Journal of High Energy Physics*, vol. 2009, p. 007–007, Feb 2009. 10.1088/1126-6708/2009/02/007.

[48] S. Agostinelli and et al., "Geant4—a simulation toolkit," *Nuclear Instruments and Methods in Physics Research Section A: Accelerators, Spectrometers, Detectors and Associated Equipment*, vol. 506, no. 3, pp. 250–303, 2003. https://doi.org/10.1016/S0168-9002(03)01368-8.

[49] The ATLAS Collaboration, "The ATLAS simulation infrastructure," *The European Physical Journal C*, vol. 70, p. 823–874, Sep 2010. 10.1140/epjc/s10052-010-1429-9.

[50] The LHCb Collaboration *JINST*, vol. 3, pp. S08005–S08005, aug 2008. 10.1088/1748-0221/3/08/s08005.

[51] The ALICE Collaboration *Journal of Physics G: Nuclear and Particle Physics*, vol. 3, pp. S08002–S08002, aug 2008. 10.1088/1748-0221/3/08/s08002.

[52] The ATLAS Collaboration, "The ATLAS experiment at the cern large hadron collider," *Journal of Instrumentation*, vol. 3, pp. S08003–S08003, aug 2008. 10.1088/1748-0221/3/08/s08003.

[53] The CMS Collaboration *JINST*, vol. 3, pp. S08004–S08004, aug 2008. 10.1088/1748-0221/3/08/s08004.

[54] R. Amann, M. Lamont, and S. Myers, "A brief history of the LEP collider," *Nuclear Physics B - Proceedings Supplements*, vol. 109, no. 2, pp. 17 – 31, 2002. Proceedings of the 7th Topical Seminar.

[55] O. S. Brüning, P. Collier, P. Lebrun, S. Myers, R. Ostojic, J. Poole, and P. Proudlock, *LHC Design Report*. CERN Yellow Reports: Monographs, Geneva: CERN, 2004. 10.5170/CERN-2004-003-V-1.

[56] E. Mobs, "The CERN accelerator complex. complexe des accélérateurs du cern," Jul 2016. `https://cds.cern.ch/record/2197559`.

[57] The ATLAS Collaboration, "Linear accelerator 2," Sep 2012. `https://cds.cern.ch/record/1997427`.

[58] The ATLAS Collaboration, "The Proton Synchrotron Booster," Jul 2012. `https://cds.cern.ch/record/1997372`.

[59] The ATLAS Collaboration, "The Proton Synchrotron," Jan 2012. `https://cds.cern.ch/record/1997189`.

[60] The ATLAS Collaboration, "The Super Proton Synchrotron," Jan 2012. `https://cds.cern.ch/record/1997188`.

[61] R. Schmidt, "Accelerator physics and technology of the LHC," 1999. 10.5170/CERN-1999-001.7.

[62] The ATLAS Collaboration, "ATLAS data quality operations and performance for 2015–2018 data-taking," *Journal of Instrumentation*, vol. 15, p. P04003–P04003, Apr 2020. 10.1088/1748-0221/15/04/p04003.

[63] The ATLAS Collaboration, "Charged-particle distributions at low transverse momentum in $\sqrt{s} = 13$ TeVpp interactions measured with the ATLAS detector at the LHC," *The European Physical Journal C*, vol. 76, Sep 2016. 10.1140/epjc/s10052-016-4335-y.

[64] K. Potamianos, "The upgraded Pixel detector and the commissioning of the Inner Detector tracking of the ATLAS experiment for Run-2 at the Large Hadron Collider," *EPS-HEP 2015 Proceedings*, 2016. `https://arxiv.org/pdf/1608.07850.pdf`.

[65] N. Hessey, "Building a Stereo-angle into strip-sensors for the ATLAS-Upgrade Inner-Tracker Endcaps," Tech. Rep. ATL-UPGRADE-PUB-2013-002, CERN, Geneva, Feb 2013. `https://cds.cern.ch/record/1514636`.

[66] The ATLAS Collaboration, "The ATLAS transition radiation tracker (TRT) proportional drift tube: design and performance," *Journal of Instrumentation*, vol. 3, pp. P02013–P02013, feb 2008. 10.1088/1748-0221/3/02/p02013.

[67] R. Wigmans, "Calorimetry," *Acta Scientific*, vol. 2, no. 1, pp. 18–55, 2008. `http://siba.unipv.it/fisica/ScientificaActa/volume_2_1/Wigmans.pdf`.

[68] B. Aubert and et al, "Construction, assembly and tests of the ATLAS electromagnetic barrel calorimeter," *Nuclear Instruments and Methods in Physics Research Section A: Accelerators, Spectrometers, Detectors and Associated Equipment*, vol. 558, no. 2, pp. 388–418, 2006. https://doi.org/10.1016/j.nima.2005.11.212.

[69] W. Bonivento, "Overview of the ATLAS electromagnetic calorimeter," *Nuclear Physics B - Proceedings Supplements*, vol. 78, no. 1, pp. 176–181, 1999.

[70] *ATLAS tile calorimeter: Technical Design Report*. Technical design report. ATLAS, Geneva: CERN, 1996. `https://cds.cern.ch/record/331062`.

[71] S. Palestini, "The muon spectrometer of the ATLAS experiment," *Nuclear Physics B - Proceedings Supplements*, vol. 125, pp. 337–345, 2003. https://doi.org/10.1016/S0920-5632(03)91013-9.

[72] The ATLAS Collaboration, "Performance of the ATLAS trigger system in 2015," *The European Physical Journal C*, vol. 77, May 2017. 10.1140/epjc/s10052-017-4852-3.

[73] The ATLAS Collaboration, "Performance of the reconstruction of large impact parameter tracks in the ATLAS inner detector," Tech. Rep. ATL-PHYS-PUB-2017-014, CERN, Geneva, Jul 2017. `https://cds.cern.ch/record/2275635`.

[74] T. G. Cornelissen, N. Van Eldik, M. Elsing, W. Liebig, E. Moyse, N. Piacquadio, K. Prokofiev, A. Salzburger, and A. Wildauer, "Updates of the ATLAS tracking event data model (release 13)," tech. rep., CERN, Geneva, Jun 2007. `http://cds.cern.ch/record/1038095`.

[75] A. Abdesselam and T. Akimoto, "The barrel modules of the ATLAS semiconductor tracker," Tech. Rep. ATL-INDET-PUB-2006-005. ATL-COM-INDET-2006-009.CERN-ATL-COM-INDET-2006-009, CERN, Geneva, Jul 2006. 10.1016/j.nima.2006.08.036.

[76] The ATLAS Collaboration, "Performance of the ATLAS track reconstruction algorithms in dense environments in LHC Run 2," *The European Physical Journal C*, vol. 77, p. 673, Oct 2017. 10.1140/epjc/s10052-017-5225-7.

[77] The ATLAS Collaboration, "Track reconstruction performance of the ATLAS inner detector at $\sqrt{s} = 13$ TeV," Tech. Rep. ATL-PHYS-PUB-2015-018, CERN, Geneva, Jul 2015. `https://cds.cern.ch/record/2037683`.

[78] R. Frühwirth, "Application of Kalman filtering to track and vertex fitting," *Nuclear Instruments and Methods in Physics Research Section A: Accelerators, Spectrometers, Detectors and Associated Equipment*, vol. 262, no. 2, pp. 444 – 450, 1987. https://doi.org/10.1016/0168-9002(87)90887-4.

[79] The ATLAS Collaboration, "Measurements of b-jet tagging efficiency with the ATLAS detector using $t\bar{t}$ events at $\sqrt{s} = 13$ TeV," *Journal of High Energy Physics*, vol. 2018, Aug 2018. 10.1007/jhep08(2018)089.

[80] The ATLAS Collaboration, "Performance of the ATLAS Inner Detector Track and Vertex Reconstruction in the High Pile-Up LHC Environment," Tech. Rep. ATLAS-CONF-2012-042, CERN, Geneva, Mar 2012. ATLAS-CONF-2012-042.

[81] The ATLAS Collaboration, "Early Inner Detector Tracking Performance in the 2015 data at $\sqrt{s} = 13$ TeV," tech. rep., CERN, Geneva, Dec 2015. ATL-PHYS-PUB-2015-051.

[82] The ATLAS Collaboration, "Reconstruction of primary vertices at the ATLAS experiment in Run 1 proton–proton collisions at the LHC," 10.1140/epjc/s10052-017-4887-5.

[83] The ATLAS Collaboration, "Vertex Reconstruction Performance of the AT-LAS Detector at $\sqrt{s} = 13\ TeV$," Tech. Rep. ATL-PHYS-PUB-2015-026, CERN, Geneva, Jul 2015. `https://cds.cern.ch/record/2037717/files/ATL-PHYS-PUB-2015-026.pdf`.

[84] The ATLAS Collaboration, "Luminosity determination in pp collisions at $\sqrt{s} = 13$ TeV using the ATLAS detector at the LHC," Tech. Rep. ATLAS-CONF-2019-021, CERN, Geneva, Jun 2019. ATLAS-CONF-2019-021.

[85] H. Wiedemann, *Particle Accelerator Physics.* Cham: Springer International Publishing, 2015. ISBN: 978-3-319-18317-6.

[86] The ATLAS Collaboration, "Electron reconstruction and identification in the ATLAS experiment using the 2015 and 2016 lhc proton–proton collision data at $\sqrt{s} = 13$ TeV," *The European Physical Journal C*, vol. 79, p. 639, Aug 2019. 10.1140/epjc/s10052-019-7140-6.

[87] The ATLAS Collaboration, "Topological cell clustering in the ATLAS calorimeters and its performance in LHC Run 1," *The European Physical Journal C*, vol. 77, Jul 2017. 10.1140/epjc/s10052-017-5004-5.

[88] The ATLAS Collaboration, "Electron and photon energy calibration with the ATLAS detector using 2015-2016 LHC proton-proton collision data," *Journal of Instrumentation*, vol. 14, pp. P03017–P03017, mar 2019. 10.1088/1748-0221/14/03/p03017.

[89] The ATLAS Collaboration, "Electron and photon performance measurements with the ATLAS detector using the 2015–2017 LHC proton-proton collision data," *Journal of Instrumentation*, vol. 14, pp. P12006–P12006, dec 2019. 10.1088/1748-0221/14/12/p12006.

[90] The ATLAS Collaboration, "Performance of electron and photon triggers in AT-LAS during LHC Run 2," *The European Physical Journal C*, vol. 80, Jan 2020. 10.1140/epjc/s10052-019-7500-2.

[91] The ATLAS Collaboration, "Electron and photon energy calibration with the ATLAS detector using data collected in 2015 at $\sqrt{s} = 13$ TeV," Tech. Rep. ATL-PHYS-PUB-2016-015, CERN, Geneva, Aug 2016. `https://cds.cern.ch/record/2203514`.

[92] The ATLAS Collaboration, "Muon reconstruction goal performance of the ATLAS detector in proton–proton collision data at $\sqrt{s}=13$ TeV," *The European Physical Journal C*, vol. 76, May 2016. 10.1140/epjc/s10052-016-4120-y.

[93] The ATLAS Collaboration, "Muon reconstruction and identification efficiency in ATLAS using the full Run 2 pp collision data set at $\sqrt{s} = 13$ TeV," 2020. https://arxiv.org/pdf/2012.00578.pdf.

[94] The ATLAS Collaboration, "Performance of the ATLAS muon triggers in Run 2," *JINST*, vol. 15, p. P09015. 60 p, Apr 2020. 10.1088/1748-0221/15/09/p09015.

[95] K. Assamagan, D. Barberis, D. Constanzo, E. Moyse, G. Polesello, D. Quarrie, D. Rousseau, R. Schaffer, and P. Sherwood, "Final report of the ATLAS AOD/ESD Definition Task Force," 2004. http://cds.cern.ch/record/810339/files/soft-2004-006.pdf.

[96] M. Beckingham, M. Duehrssen, E. Schmidt, M. Shapiro, M. Venturi, J. Virzi, I. Vivarelli, M. Werner, S. Yamamoto, and T. Yamanaka, "The simulation principle and performance of the ATLAS fast calorimeter simulation FastCaloSim," 10 2010. https://inspirehep.net/literature/1194623.

[97] J. Catmore, "The ATLAS data processing chain: from collisions to papers." Joint Oslo/Bergen/NBI ATLAS Software Tutorial, Feb 2016. https://indico.cern.ch/event/472469/contributions/1982677/attachments/1220934/1785823/intro_slides.pdf.

[98] K. Koeneke, "Distributing and storing required data efficiently by means of specifically tailored data formats in the ATLAS collaboration," Jan 2011.

[99] ATLAS Collaboration, "Athena," May 2021. 10.5281/zenodo.4772550.

[100] J. Fulachier, J. Odier, and F. Lambert, "Atlas metadata interface (ami), a generic metadata framework," *Journal of Physics: Conference Series*, vol. 898, p. 062001, 10 2017.

[101] The ATLAS Collaboration, "Electron efficiency measurements with the ATLAS detector using the 2015 LHC proton-proton collision data," Tech. Rep. ATLAS-CONF-2016-024, CERN, Geneva, Jun 2016. https://cds.cern.ch/record/2157687.

[102] A. Hoecker, P. Speckmayer, J. Stelzer, J. Therhaag, E. von Toerne, and H. Voss, "TMVA: Toolkit for Multivariate Data Analysis," *PoS*, vol. ACAT, p. 040, 2007. https://arxiv.org/pdf/physics/0703039.pdf.

[103] P. Nason, "A new method for combining nlo qcd with shower monte carlo algorithms," *Journal of High Energy Physics*, vol. 2004, p. 040–040, Nov 2004. 10.1088/1126-6708/2004/11/040.

[104] S. Frixione, P. Nason, and C. Oleari, "Matching nlo qcd computations with parton shower simulations: the powheg method," *Journal of High Energy Physics*, vol. 2007, p. 070–070, Nov 2007. 10.1088/1126-6708/2007/11/070.

[105] S. Alioli, P. Nason, C. Oleari, and E. Re, "A general framework for implementing NLO calculations in shower Monte Carlo programs: the POWHEG BOX," *Journal of High Energy Physics*, vol. 2010, Jun 2010. 10.1007/jhep06(2010)043.

[106] S. Frixione, G. Ridolfi, and P. Nason, "A positive-weight next-to-leading-order Monte Carlo for heavy flavour hadron production," *Journal of High Energy Physics*, vol. 2007, p. 126–126, Sep 2007. 10.1088/1126-6708/2007/09/126.

[107] S. Alioli, P. Nason, C. Oleari, and E. Re, "NLO vector-boson production matched with shower in POWHEG," *Journal of High Energy Physics*, vol. 2008, Jul 2008. 10.1088/1126-6708/2008/07/060.

[108] T. Sjöstrand, S. Mrenna, and P. Skands, "A brief introduction to pythia 8.1," *Computer Physics Communications*, vol. 178, Jun 2008. 10.1016/j.cpc.2008.01.036.

[109] H.-L. Lai, M. Guzzi, J. Huston, Z. Li, P. M. Nadolsky, J. Pumplin, and C.-P. Yuan, "New parton distributions for collider physics," *Physical Review D*, vol. 82, Oct 2010. 10.1103/physrevd.82.074024.

[110] G. Aad, B. Abbott, J. Abdallah, S. Abdel Khalek, O. Abdinov, R. Aben, B. Abi, M. Abolins, O. S. AbouZeid, and et al., "Measurement of the Z/$\gamma*$ boson transverse momentum distribution in pp collisions at s = 7 $\sqrt{s} = 7$ TeVwith the ATLAS detector," *Journal of High Energy Physics*, vol. 2014, Sep 2014. 10.1007/jhep09(2014)145.

[111] J. Pumplin, D. R. Stump, J. Huston, H.-L. Lai, P. Nadolsky, and W.-K. Tung, "New generation of parton distributions with uncertainties from global qcd analysis," *Journal of High Energy Physics*, vol. 2002, p. 012–012, Jul 2002. 10.1088/1126-6708/2002/07/012.

[112] R. D. Ball, V. Bertone, S. Carrazza, C. S. Deans, L. Del Debbio, S. Forte, A. Guffanti, N. P. Hartland, J. I. Latorre, and et al., "Parton distributions for the LHC run ii," *Journal of High Energy Physics*, vol. 2015, Apr 2015. 10.1007/jhep04(2015)040.

[113] G. Cowan, *Statistical Data Analysis*. New York, USA: Oxford University Press, 1998. ISBN: 9780198501558.

[114] S. Theodoridis and K. Koutroumbas, *Pattern Recognition*. 01 2003. ISNB: 0-12-685875-6.

[115] O. Behnke, K. Kröninger, G. Schott, and T. Schörner-Sadenius, *Data Analysis in High Energy Physics: A Practical Guide to Statistical Methods*. Weinheim, Germany: John Wiley & Sons Incorporated, 2013. ISBN: 978-3-527-41058-3.

[116] T. Sjöstrand, S. Ask, J. R. Christiansen, R. Corke, N. Desai, P. Ilten, S. Mrenna, S. Prestel, C. O. Rasmussen, and P. Z. Skands, "An introduction to PYTHIA 8.2," *Computer Physics Communications*, vol. 191, p. 159–177, Jun 2015. 10.1016/j.cpc.2015.01.024.

[117] The ATLAS Collaboration, "ATLAS Pythia 8 tunes to 7 TeV data," Tech. Rep. ATL-PHYS-PUB-2014-021, CERN, Geneva, Nov 2014. `https://cds.cern.ch/record/1966419`.

[118] E. Chapon, C. Royon, and O. Kepka, "Anomalous quartic $WW\gamma\gamma$, $ZZ\gamma\gamma$, and trilinear $WW\gamma$ couplings in two-photon processes at high luminosity at the LHC," *Phys. Rev. D*, vol. 81, p. 074003, Apr 2010. 10.1103/PhysRevD.81.074003.

[119] O. J. P. Éboli, M. C. Gonzalez-García, S. M. Lietti, and S. F. Novaes, "Anomalous quartic gauge boson couplings at hadron colliders," *Phys. Rev. D*, vol. 63, p. 075008, Mar 2001. 10.1103/PhysRevD.63.075008.

[120] M. Dyndal and L. Schoeffel, "The role of finite-size effects on the spectrum of equivalent photons in proton–proton collisions at the LHC," *Physics Letters B*, vol. 741, pp. 66 – 70, 2015. https://doi.org/10.1016/j.physletb.2014.12.019.

[121] L. A. Harland-Lang, V. A. Khoze, and M. G. Ryskin, "The production of a diphoton resonance via photon-photon fusion," *Journal of High Energy Physics*, vol. 2016, Mar 2016. 10.1007/jhep03(2016)182.

[122] L. Frankfurt, C. E. Hyde, M. Strikman, and C. Weiss, "Generalized parton distributions and rapidity gap survival in exclusive diffractive pp scattering," *Physical Review D*, vol. 75, no. 5, 2007. 10.1103/physrevd.75.054009.

[123] L. A. Harland-Lang, V. A. Khoze, and M. G. Ryskin, "The photon PDF in events with rapidity gaps," *The European Physical Journal C*, vol. 76, May 2016. 10.1140/epjc/s10052-016-4100-2.

[124] M. Dyndal and L. Schoeffel, "The role of finite-size effects on the spectrum of equivalent photons in proton–proton collisions at the LHC," *Physics Letters B*, vol. 741, p. 66–70, Feb 2015. 10.1016/j.physletb.2014.12.019.

[125] J. Butterworth, J. R. Forshaw, M. Seymour, J. Storrow, and R. Walker, "Multiple hard interactions in $\gamma\gamma$ and γp physics at LEP and HERA," pp. 175–180. 7 p, Jun 1995. `https://cds.cern.ch/record/282962`.

[126] C. Degrande, O. Eboli, B. Feigl, B. Jäger, W. Kilian, O. Mattelaer, M. Rauch, J. Reuter, M. Sekulla, and D. Wackeroth, "Monte Carlo tools for studies of non-standard electroweak gauge boson interactions in multi-boson processes: A Snowmass White Paper," in *Community Summer Study 2013: Snowmass on the Mississippi*, 9 2013. `https://arxiv.org/pdf/1309.7890.pdf`.

[127] The ATLAS Collaboration, "The Pythia 8 A3 tune description of ATLAS minimum bias and inelastic measurements incorporating the Donnachie-Landshoff diffractive model," Tech. Rep. ATL-PHYS-PUB-2016-017, CERN, Geneva, Aug 2016. `https://cds.cern.ch/record/2206965`.

[128] R. D. Ball, V. Bertone, S. Carrazza, C. S. Deans, L. Del Debbio, S. Forte, A. Guffanti, N. P. Hartland, J. I. Latorre, J. Rojo, and et al., "Parton distributions with LHC data," *Nuclear Physics B*, vol. 867, p. 244–289, Feb 2013. 10.1016/j.nuclphysb.2012.10.003.

[129] D. J. Lange, "The EvtGen particle decay simulation package," *Nuclear Instruments and Methods in Physics Research Section A: Accelerators, Spectrometers, Detectors and Associated Equipment*, vol. 462, no. 1, pp. 152–155, 2001. https://doi.org/10.1016/S0168-9002(01)00089-4.

[130] M. Bähr, S. Gieseke, M. A. Gigg, D. Grellscheid, K. Hamilton, O. Latunde-Dada, S. Plätzer, P. Richardson, M. H. Seymour, A. Sherstnev, and et al., "Herwig++ physics and manual," *The European Physical Journal C*, vol. 58, p. 639–707, Nov 2008. 10.1140/epjc/s10052-008-0798-9.

[131] J. Bellm, S. Gieseke, D. Grellscheid, S. Plätzer, M. Rauch, C. Reuschle, P. Richardson, P. Schichtel, M. H. Seymour, A. Siódmok, and et al., "Herwig 7.0/herwig++ 3.0 release note," *The European Physical Journal C*, vol. 76, Apr 2016. 10.1140/epjc/s10052-016-4018-8.

[132] H. Jung et al, "Proceedings of the workshop: HERA and the LHC workshop series on the implications of HERA for LHC physics," 2009. `https://arxiv.org/pdf/0903.3861.pdf`.

[133] J. Alwall, R. Frederix, S. Frixione, V. Hirschi, F. Maltoni, O. Mattelaer, H.-S. Shao, T. Stelzer, P. Torrielli, and M. Zaro, "The automated computation of tree-level and next-to-leading order differential cross sections, and their matching to parton shower simulations," *Journal of High Energy Physics*, vol. 2014, Jul 2014. 10.1007/jhep07(2014)079.

[134] J. Vermaseren, "Two-photon processes at very high energies," *Nuclear Physics B*, vol. 229, no. 2, pp. 347–371, 1983. https://doi.org/10.1016/0550-3213(83)90336-X.

[135] V. Bertone, S. Carrazza, N. Hartland, and J. Rojo, "Illuminating the photon content of the proton within a global pdf analysis," *SciPost Physics*, vol. 5, Jul 2018. 10.21468/scipostphys.5.1.008.

[136] T. Melia, P. Nason, R. Röntsch, and G. Zanderighi, "W^+W, WZ and ZZ production in the POWHEG BOX," *Journal of High Energy Physics*, vol. 2011, Nov 2011. 10.1007/jhep11(2011)078.

[137] P. Nason and G. Zanderighi, "W^+W^-, WZ and ZZ production in the POWHEG-BOX-V2," *The European Physical Journal C*, vol. 74, Jan 2014. 10.1140/epjc/s10052-013-2702-5.

[138] L. A. Harland-Lang, A. D. Martin, P. Motylinski, and R. S. Thorne, "Parton distributions in the LHC era: MMHT 2014 PDFs," *The European Physical Journal C*, vol. 75, May 2015. 10.1140/epjc/s10052-015-3397-6.

[139] S. Höche, F. Krauss, S. Schumann, and F. Siegert, "QCD matrix elements and truncated showers," *Journal of High Energy Physics*, vol. 2009, p. 053–053, May 2009. 10.1088/1126-6708/2009/05/053.

[140] E. Bothmann, G. Singh Chahal, S. Höche, J. Krause, F. Krauss, S. Kuttimalai, S. Liebschner, D. Napoletano, M. Schönherr, H. Schulz, and et al., "Event generation with sherpa 2.2," *SciPost Physics*, vol. 7, Sep 2019. 10.21468/scipostphys.7.3.034.

[141] E. Re, "Single-top Wt-channel production matched with parton showers using the POWHEG method," *The European Physical Journal C*, vol. 71, Feb 2011. 10.1140/epjc/s10052-011-1547-z.

[142] The ATLAS Collaboration, "Beam Spot Public Results," 2019. `https://twiki.cern.ch/twiki/bin/view/AtlasPublic/BeamSpotPublicResults#2015_25ns_pp_Collisions_s_13_TeV`.

[143] G. D'Agostini, "A multidimensional unfolding method based on Bayes' theorem," *Nuclear Instruments and Methods in Physics Research Section A: Accelerators, Spectrometers, Detectors and Associated Equipment*, vol. 362, no. 2, pp. 487–498, 1995. https://doi.org/10.1016/0168-9002(95)00274-X.

[144] G. D'Agostini, "Improved iterative bayesian unfolding," 2010. `https://arxiv.org/pdf/1010.0632.pdf`.

[145] M. Dyndal and L. Schoeffel, "Four-lepton production from photon-induced reactions in pp collisions at the lhc," *Acta Physica Polonica B*, vol. 47, no. 6, p. 1645, 2016. 10.5506/aphyspolb.47.1645.

[146] L. C. S. Amaroso, "Towards common LHC tune: discussion on parameterisation of energy dependence." LHC-EW WG:Jets and EW bosons, May 2019. https://indico.cern.ch/event/820080/contributions/3427411/attachments/1844116/3024883/LHCEWWG_Tuning-14-05-2019.pdf.

[147] L. Lista, "Practical statistics for particle physicists," *Proceedings of the 2016 European School of High-Energy Physics*, vol. 5, 2017.

[148] L. A. Harland-Lang, V. A. Khoze, and M. G. Ryskin, "Exclusive physics at the LHC with superchic 2," *The European Physical Journal C*, vol. 76, Jan 2016. 10.1140/epjc/s10052-015-3832-8.

[149] I. Brivio, Y. Jiang, and M. Trott, "The SMEFTsim package, theory and tools," *JHEP*, vol. 12, p. 070, 2017. 10.1007/JHEP12(2017)070.

[150] O. Eboli and M. Gonzalez-Garcia, "Anomalous quartic electroweak gauge-boson interactions," 2020. [Online]. https://feynrules.irmp.ucl.ac.be/wiki/AnomalousGaugeCoupling.

[151] G. Cowan, K. Cranmer, E. Gross, and O. Vitells, "Asymptotic formulae for likelihood-based tests of new physics," *The European Physical Journal C*, vol. 71, Feb 2011. 10.1140/epjc/s10052-011-1554-0.

[152] J. Ellis, M. Madigan, K. Mimasu, V. Sanz, and T. You, "Top, Higgs, diboson and electroweak fit to the Standard Model effective field theory," *Journal of High Energy Physics*, vol. 2021, Apr 2021. 10.1007/jhep04(2021)279.

[153] A. Azatov, R. Contino, C. S. Machado, and F. Riva, "Helicity selection rules and noninterference for BSM amplitudes," *Physical Review D*, vol. 95, Mar 2017. 10.1103/physrevd.95.065014.

[154] D. Liu, A. Pomarol, R. Rattazzi, and F. Riva, "Patterns of strong coupling for LHC searches," *Journal of High Energy Physics*, vol. 2016, Nov 2016. 10.1007/jhep11(2016)141.

[155] J. J. Ethier, R. Gomez-Ambrosio, G. Magni, and J. Rojo, "SMEFT analysis of vector boson scattering and diboson data from the LHC Run II," *Eur. Phys. J. C*, vol. 81, no. 6, p. 560, 2021. 10.1140/epjc/s10052-021-09347-7.

[156] A. M. Sirunyan, A. Tumasyan, W. Adam, F. Ambrogi, T. Bergauer, J. Brandstetter, M. Dragicevic, J. Erö, A. Escalante Del Valle, and et al., "Measurement of the cross section for electroweak production of a Z boson, a photon and two jets in proton-proton collisions at $\sqrt{s} = 13$ TeV and constraints on anomalous quartic couplings," *Journal of High Energy Physics*, vol. 2020, Jun 2020. 10.1007/jhep06(2020)076.

[157] The CMS Collaboration , "Observation of electroweak production of $W\gamma$ with two jets in proton-proton collisions at $\sqrt{s} = 13$ TeV," *Physics Letters B*, vol. 811, p. 135988, 2020. `https://doi.org/10.1016/j.physletb.2020.135988`.

[158] The CMS Collaboration, "Evidence for electroweak production of four charged leptons and two jets in proton-proton collisions at $\sqrt{s} = 13$ TeV," *Physics Letters B*, vol. 812, p. 135992, Jan 2021. 10.1016/j.physletb.2020.135992.

[159] The CMS Collaboration, "Measurements of production cross sections of wz and same-sign ww boson pairs in association with two jets in proton-proton collisions at s=13tev," *Physics Letters B*, vol. 809, p. 135710, Oct 2020. 10.1016/j.physletb.2020.135710.

[160] The CMS Collaboration, "Observation of electroweak production of same-sign w boson pairs in the two jet and two same-sign lepton final state in proton-proton collisions at $\sqrt{s} = 13$ TeV," *Phys. Rev. Lett.*, vol. 120, p. 081801, Feb 2018. 10.1103/PhysRevLett.120.081801.

[161] The CMS Collaboration, "Search for anomalous electroweak production of vector boson pairs in association with two jets in proton-proton collisions at 13 TeV," *Phys. Lett. B*, vol. 798, p. 134985, 2019. `https://doi.org/10.1016/j.physletb.2019.134985`.